CHARACTERISTIC STRUCTURAL FEATURES OF TALL BUILDINGS IN TURKEY AND THEIR DYNAMIC BEHAVIOR

by

Ömer Odabaşı

B.S., Civil Engineering, Kocaeli University, 2014

Submitted to Kandilli Observatory and Earthquake Research Institute
in partial fulfillment of the requirements for the degree of
Master of Science

Graduate Program in Earthquake Engineering

Boğaziçi University

2016

ACKNOWLEDGEMENTS

I would first like to thank my thesis advisor Prof. Dr. Sinan Akkar. I have gained valuable experiences in both structural and earthquake engineering fields as a researcher and in life as a person thanks to him. In pursuit of constant improvement, I can't be thankful enough to him for pushing me towards developing a better grasp in many aspects.

I would also like to thank dear fellow researchers and colleagues who were involved in various parts of this work: Dr. Cüneyt Tüzün and Nilgün Merve Çağlar. I am indebted to them for their valuable input.

It is of importance to note that a part of this thesis was supported by the Ministry of Environment and Urbanization (ÇvŞB) of Turkey, which is gratefully acknowledged.

Finally, I must express my deepest gratitude towards, my mom, dad, sisters and friends for their unfailing support and encouragements.

ABSTRACT

CHARACTERISTIC STRUCTURAL FEATURES OF TALL BUILDINGS IN TURKEY AND THEIR DYNAMIC BEHAVIOR

High-rise reinforced concrete (RC) shear wall buildings having 10 to 30 stories in metropolitan cities of Turkey are investigated under the systematic framework of Performance Based Earthquake Engineering (PBEE). A building inventory is compiled entailing blueprints of tall buildings in densely populated areas of the cities: Istanbul, Ankara, Bursa and Mersin primarily to represent the tall building stock. These buildings are thoroughly investigated via statistical methods to develop six reference building models. The recently proposed Conditional Spectrum (CS) is used as a tool to scale the selected ground motions which provided the link between the target hazard at the reference site (represents high seismicity) and structural responses. It is concluded that the high-rise RC shear wall buildings designed by Turkish engineering practice in metropolitan areas show satisfactory performance up to 475-year return period ground motions. However, the increase in ground motion hazard (e.g., 2475-year, maximum considered) may result in irreparable and severe damage states for these buildings, which may be mostly critical in terms of economic losses. The results obtained from this study can be used as reference source for future studies on several other research topics on tall buildings such as estimating cost-effectiveness and vulnerability functions of high-rise building stock in earthquake-prone regions of Turkey.

ÖZET

TÜRKİYE'DEKİ YÜKSEK BİNALARIN KARAKTERİSTİK YAPISAL ÖZELLİKLERİ VE DİNAMİK DAVRANIŞI

Türkiye'nin büyük şehirlerinde bulunan 10 ve 30 kat arası betonarme perde duvarlı yüksek binalar, Performansa Dayalı Deprem Mühendisliği (PDDM) sistematik çerçevesi altında incelenmiştir. Istanbul, Ankara, Bursa ve Mersin şehirleri başta olmak üzere yüksek binaların yoğunca bulunduğu şehirlerinden teknik çizimler içeren bir bina envanteri derlenmiştir. Envanterdeki binalar detaylı bir biçimde istatistiksel yöntemler aracılığıyla incelenip altı referans bina modeli üretilmiştir. Yapısal davranış ile belirlenen referans sahasındaki (yüksek deprem tehlikesi teşkil eden) deprem tehlikesinin ilişkilendirilmesi için Koşullu Spektrum yöntemi kullanılarak yer hareketi seçim ve ölçeklendirmeleri yapılmıştır. Büyük şehirlerdeki perde duvarlı betonarme yüksek binaların 475-yıl dönüş periyoduna sahip (tasarım depremi) deprem senaryosuna kadar tatmin edici performans göstermiştir. Fakat deprem tehlike seviyesindeki artışın (örneğin, 2475-yıl dönüş periyoduna sahip beklenen en büyük deprem) binalarda *onarılamaz* veya *ileri hasar* seviyelerinin gözlenmesine sebep olabileceği gözlenmiştir. Bu durum olası maddi kayıplar açısından büyük önem taşımaktadır. Bu çalışmada elde edilen sonuçlar, Türkiye'nin sismik tehlike teşkil eden bölgelerindeki yüksek bina envanterinin maliyet açısından etkinlik, hasar görebilirlik fonksiyonlarının araştırılması gibi çalışma konularında ön-bilgi olarak kullanılabilecek niteliktedir.

to my family…

TABLE OF CONTENTS

LIST OF FIGURES

LIST OF TABLES

LIST OF SYMBOLS

A_{cv}	Effective cross-section are of a shear wall section
A_{ch}	Gross shear wall cross-section area
A_g	Gross cross-section area
$[C]$	Damping matrix
b_w	Thickness of a shear wall section
$[c_i]$	Diagonal matrix of damping coefficients for each mode
E_c	Modulus of elasticity of concrete
f_c'	Specified compressive strength of concrete
f_{cd}	Design compressive strength of concrete
f_{sy}	Yield strength of reinforcing steel
f_u	Specified ultimate tensile strength of reinforcing steel
$f_{u,exp}$	Expected ultimate tensile strength of reinforcing steel
f_y	Nominal yield strength of reinforcing steel
$f_{y,exp}$	Expected yield strength of reinforcing steel
G	Total dead load of structre
G_c	Shear modulus
H_w	Total height of building
I_g	Gross moment of inertia
$[K]$	Stiffness matrix
L_{exp}	Live load reduction factor
l_{be}	Boundary element width
$ln\hat{\theta}$	Logarithmic mean estimate
l_w	Width of a shear wall cross section
M_w	Moment magnitude
$[M]$	Mass matrix
n_j	Number of ground motions in an analysis suite
P_u	Axial load on member
Q	Total live load on a structure

R	Earthquake's distance
R_{rup}	The shortest distance from a site to a rupture surface
S_a	Spectral acceleration
$S_a(T_i)$	Spectral acceleration at i'th period
$S_a(T^*)$	Spectral acceleration at the conditional period
S_d	Spectral displacement
T_{1x}	1st mode period in translational *x* direction
T_{1y}	1st mode period in translational *y* direction
T_n	Nth mode period
T^*	Conditioning period
v_{cr}	Cracking strength
v_{cu}	Increased shear strength considering axial load effects
v_n	Nominal shear strength
V	Shear force
V_{cr}	Cracking strength in force units
V_e	Design shear force in a member
V_n	Ultimate shear force
V_r	Residual strength
V_{s30}	The average shear-wave velocity between 0 and 30-meters depth
V_y	Yield strength
W	Total weight of structure
z_y	Number of observed damage level exceedence
x_m	Logarithmic mean of data
α_c	Constant for shear wall heigh-to-width ratio
α_K	Proportionality constant (stiffness proportional)
α_M	Proportionality constant (mass proportional)
β	Logarithmic standart deviation
$\hat{\beta}$	Logarithmic standart deviation estimate
γ_{cr}	Cracking shear strain of a shear wall section
γ_y	Yield shear strain of a shear wall section

δ_{avg}	Average of the displacements at extreme corners of a structure under earthquake excitation
Δ_y	Yield deformation
ε	Flexural strain
ε_{cc}	Associated strain value at the compressive strength of concrete
ε_{cu}	Ultimate compressive strain of concrete
ε_{sy}	Yield strain of reinforcing steel
ε_{sh}	Strain at the onset of strain hardening in reinforcing steel
ε_{su}	Ultimate tensile strain of reinforcing steel
η_t	Torsional irregularity constant
θ	Other seismilogical parameters such as rupture mechanism,
λ_{IM}	Mean annual rate of exceedence of a ground-motion intensity measure, *IM*
μ	Mean value
μ_{lnSa}	Logarithmic mean of spectral accelerations
ν	Poisson ratio
ξ_n	Nth mode critical damping
ρ	Correlation coefficient
ρ_{bottom}	Longitudinal reinforcement ratio of bottom half of the member cross-section
ρ_n	Transverse reinforcement ratio in the web of a shear wall section
ρ_{top}	Longitudinal reinforcement ratio of top half of the member cross-section
$\rho_{transverse}$	Transverse reinforcement ratio in the direction of interest
σ	Standart deviation
σ_{lnSa}	Logarithmic standart deviation of spectral accelerations
$\phi(.)$	Standart normal cumulative distribution function
ϕ_n	Nth mode eigenvector
$[\phi^T]$	Matrix of eigenvectors

LIST OF ACRONYMS/ABBREVIATIONS

2D	Two dimensional
3D	Three dimensional
BZ	Boundary zone
C	Collapse
CDF	Cummulative distribution function
CMS	Conditional Mean Spectrum
CP	Collapse prevention
CS	Conditional Spectrum
CWF	Core wall-frame
DBE	Design based earthquake
D/C	Demand/Capacity
DV	Decision variable
EDP	Engineering demand parameter
F-D	Force-deformation
GMPE	Groudn motion prediction equation
HSC	High-strength concrete
IDR	Interstory drift ratio
IM	Intensity measure
IO	Immediate occupancy
KN	Kilonewton
LS	Life safety
MCE	Maximum considered earthquake
MPA	Megapascal
MRF	Moment-resisting frame
MIDR	Maximum interstory drift ratio
MLE	Maximum likelihood method
MSA	Multiple stripes analysis
MVLEM	Multiple vertical line element model
NGA	Next generation attenuation

NRHA	Nonlinear response history analysis
NSC	Normal-strength concrete
PBEE	Performance-based earthquake engineering
PDF	Probability density function
PFA	Peak floor acceleration
PGA	Peak ground acceleration
PSHA	Probabilistic seismic hazard assessment
RC	Reinforced concrete
RP	Return period
SI	Super-imposed
SRSS	Square root of sum of squares
SSE	Sum of squared roots
SW	Shear wall
UHS	Uniform hazard spectrum
US	United States

1. INTRODUCTION

1.1. General

Over the last two decades, the design and construction of tall buildings speeded up as a consequence of economic growth in Turkey. A recent study in Turkey (GRM İletişim ve Bilişim, 2015) indicated that as of 2015, there are 1593 tall buildings with 20 or more stories, from which 565 are still under construction. The metropolitan cities such as Istanbul, Ankara, Bursa and İzmir constitute the areas where high-rise buildings are densely populated (Figure 1.1). Among these tall buildings, 99.3% comprises reinforced concrete (RC) buildings, 0.45% comprises RC-Steel buildings and 0.25% comprises steel buildings. These numbers indicate that a vast majority of the high-rise building stock is RC buildings.

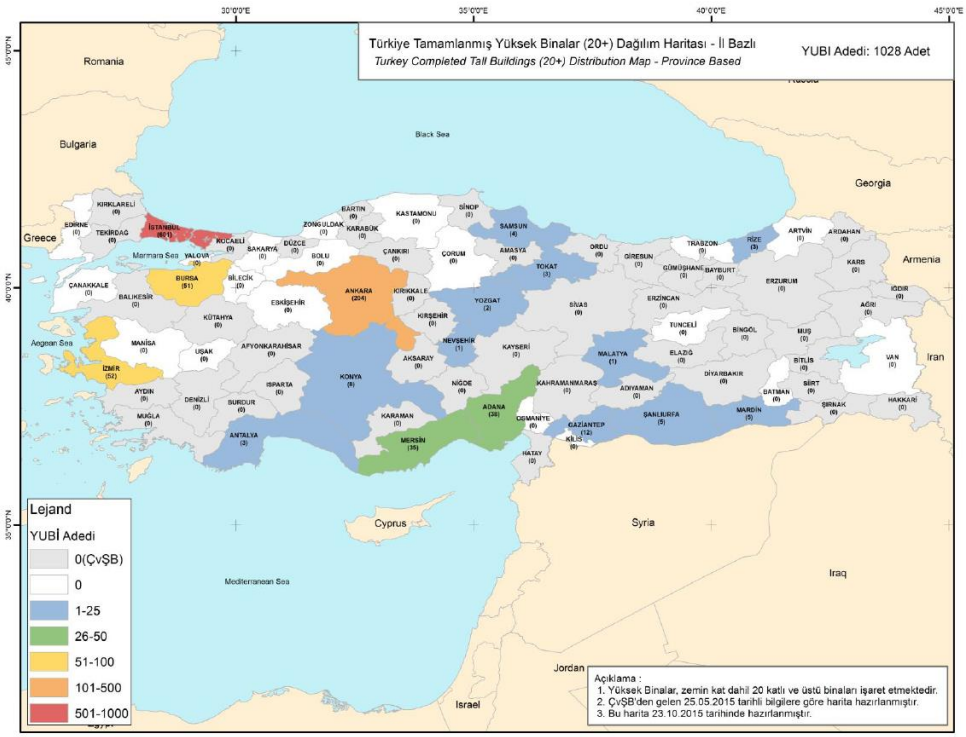

Figure 1.1. Distribution of tall buildings across Turkey. Color codes represent different density levels (GRM İletişim ve Bilişim, 2015)

Due to the increasing demands, structural engineering in Turkey has started to more frequently engage in designing tall buildings. However, most of the time the calculations for these complicated systems bear on simplified linear analysis methods. Given the lack of

implementing proper analysis and design rationale adopted by performance-based seismic design methodology in these designs, a recent concern has arisen among eminent structural engineers and policy makers regarding the safety of tall buildings under various levels of seismic hazard. Therefore, a comprehensive assessment of the seismic vulnerability of this building stock is of growing importance to estimate possible losses that the future earthquakes are likely to induce. Outcomes of such a study can be used to develop strategies regarding mitigation of losses. The studies presented in this thesis partially addresses these concerns by following the probabilistic framework of performance-based earthquake engineering (PBEE). The thesis aims at providing some meaningful information and insight about the earthquake response of RC core-wall-frame tall building stock in Turkey that may guide decision makers and stakeholders towards more proper decisions.

Performance based earthquake engineering (PBEE) has become an indispensable concept for seismic design and assessment of structures for more than a decade. The probabilistic seismic assessment framework of PBEE was first proposed by the *Pacific Earthquake Engineering Research* (PEER) *Center* (Cornell 2004; Deierlein 2004; Krawinkler et al. 2004; Miranda et al. 2004). Within the context of the PBEE framework, various guidelines and handbooks are published with the objective of improving the practice in performance-based seismic design of tall buildings (e.g. Tall Buildings Initiative/PEER, 2010; Los Angeles Tall Buildings Structural Design Council, 2014). PBEE seeks to provide delicate, all encompassing sets of data to the decision-maker through its rigorous probabilistic framework. However the step-by-step nature of this cumulative process requires a significant effort to be invested. The methodology can be broken down into four main steps (Cornell and Krawinkler, 2000):

1. Seismic Hazard Analysis
2. Demand Analysis
3. Damage Analysis
4. Loss Estimation

The first step defines the level of target ground-motion intensity measure (IM) and it is usually the product of a probabilistic approach (i.e., probabilistic seismic hazard aassessment, PSHA). The most commonly used IM for structural design and performance

assessment is spectral acceleration. As a product of PSHA, IM is described through a mean annual rate of exceedence, λ_{IM}, which is specific to the site of interest and design (or assessment) objectives. The second step includes calculation of the structural response parameters, or the so called engineering demand parameters (EDPs) such as interstory drift ratio (definition; IDR) and peak floor accelerations (definition; PFA). Other common EDPs may come in the forms of inelastic component deformations and strains. In the third step, the EDP distributions are used in connection with the damage level criteria set for the target building class to predict damage state probabilities. The final step of the assessment is to determine decision variables (DV) in terms of quantities that are meaningful for decision-makers such as, monetary losses, down time or casualties. This study elaborates on the first three step of the PBEE framework.

1.2. Literature Survey

Performance-based seismic design concept is a rapidly growing idea that can be viewed as a process prior to an assessment procedure in which the performance of structural systems are evaluated. Researchers in the past have studied many different aspects of such framework and contributed to the establishment of novel guidelines such as: Vision 2000 (1995), ATC40 (ATC, 1996), SAC/FEMA350 (FEMA, 2000), FEMA-440 (ATC, 2005) and more recent ATC 72-1 (2010), TBI (2011) and LATBSDC (2014). These handbooks and guidelines helped many other researchers to embark on performance-based seismic assessment of structures.

Moehle and Dierlein (2004) along with several other studies (e.g., Cornell 2004; Deierlein 2004; Krawinkler et al. 2004) aimed to develop the rigorous PBEE framework by breaking down the design and assessment processes into logical elements as explained in the previous section. The adoption of a consistent probabilistic framework gave rise to the development of more reliable, transparent rationale for establishing simpler performance metrics and acceptance criteria for performance-based design.

The comprehensive study of Ji et al. (2007) was among the first that aimed to address the seismic performance and fragility assessment of high-rise building population. Special emphasis is given to the derivation of probabilistic fragility functions to assess the overall

seismic vulnerability of a 54-story RC dual core wall system. The inelastic response history analyses were performed using simplified lumped-parameter models derived from complex finite element models by utilizing genetic algorithms. Within the scope of that study, new performance limit states based on detailed pushover analyses were proposed. The overall framework suggested a generic approach that is computationally efficient and capable of presenting probabilistic seismic fragility relationships for RC high-rise buildings of different configurations.

Following the recent developments in PBEE framework, several studies about analytical fragility functions were conducted. Akkar et *al.* (2005) investigated the general characteristics of 2-5 story Turkish substandard RC building inventory and used 32 representative sample buildings. Field data were employed in this study to attain structure capacity metrics to evaluate seismic vulnerability of conventional RC buildings in Turkey. The later studies (Baykal and Kırçıl, 2006; Kırçıl and Polat, 2006) concerned with the vulnerability of the Turkish building stock were carried out aiming to obtain fragility information of mid-rise RC frame buildings in Istanbul by using MDOF models of 3,5 and 7-story structures.

Ay and Erberik (2006) studied structural vulnerability of RC frame structures by establishing 2D structural models of target low-rise and mid-rise buildings that constitute approximately 75% of the conventional building stock in Turkey. The frame structures are categorized as poor, typical or superior depending on certain characteristics of construction practice and observed performances after major earthquakes in Turkey. Limit states for fragility assessments are determined from pushover procedures. Moreover, the study delivered a probabilistic fragility database that can later be used for damage and loss estimation of the target building stock.

Although details of structural anaysis or performance assessment procedures were not emphasized, Bal et *al.* (2008) provided valuable statistical information that can be used in urban/regional-scale earthquake protection strategies by investigating geometrical, functional and material properties of the RC building stock in the northern Marmara Region. The existing RC stock was classified as ‘compliant’ or ‘non-compliant’ buildings; shear wall-frame or frame structures and emergent or embedded-beam systems. A fairly large

number of actual structres were investigated in computing general building block statistics for the Marmara region. Similarly, Azak et *al.* (2012) presented a statistical study on geometrical properties of Turkish RC building stock. These authors used the results of a statistical building inventory survey undertaken in several districts of İstanbul as well as Bolu and Düzce. Their study presented statistical parameters in terms of mean and standart deviation of examined geometrical properties (x, y and z). Durukal et *al.* (2006) carried out a building loss estimation study to have a clearer vision on earthquake risk mitigation management via insurance schemes.

Moreover, as a result of growing concerns about the seismic vulnerability of various building stocks worldwide, the Global Earthquake Model (GEM) Foundation has supported the development of an online platform to explore a multitude of models that were required in characterization of the physical vulnerability of assets. Outcomes of the Global Vulnerability Consortion (GVC) project (Porter et al. 2012) aided strongly the growth of this database. The later European collaborative research project SYNER-G (Pitilakis et *al.*, 2014) also contributed significantly in creation of this database. Maio and Tsionis (2015) has recently presented a technical report that comprises a review of analytical fragility functions and selection of these fragility curves for a given geographical location to provide a clear insight on the existing literature concerned with seismicly vulnerable assets.

The literature survey suggests that there is a clear lack of studies concerning characteristics and dynamic behavior of the high-rise building stock in seismicly vulnerable regions of Turkey. This can be attributed to reasons such as: (1) the challenging procedure of compiling a tall building database; (2) the fact that a proper representation of a rare building class requires making carefully thought decisions; (3) the technical difficulties lie under the subsequent steps of PBEE framework which involves, appropriate analytical modelling of high-rise structures considering its major pitfalls, seismic hazard assessment, selecting and scaling of ground motions, the processing of mass generated structural analysis data to derive meaningful information which can be used for decision making purposes. For these reasons, this thesis aims to provide a valuable insight on the unexplored field of characteristics and seismic vulnerability of the high-rise building stock in Turkey.

The above summarized studies assess the structural performance of Turkish building stock but the actual research on developing design guidelines for tall building design is conducted in countries such as United States. PEER/TBI Task 12 (2011) presented an extensive study that covers all aspects of PBEE framework aimed to provide a widespread understanding of: (a) performance objectives, (b) ground motion selection, scaling and application for design, (c) modelling and analysis procedures, and (d) written guidelines for tall building design. Case studies on three different tall building systems with translational vibration periods around 5 sec. were carried out to study their performance. These building types were: (1) RC core-only building with post-tensioned concrete gravity framing; (2) RC core wall building with concrete special moment frames (dual core wall system) and (3) steel buckling-restrained braced frame system. Loss estimation studies were conducted on the case stuctures to predict repair costs for anticipated future earthquakes.

1.3. Objective and Scope

The vulnerability of Turkish building stock in highly seismic regions has already been regarded as an important issue that is partially addressed in the previous section. Earthquake damage and loss estimation studies about the Turkish building block in such regions have aimed to leverage upon the wealth of knowledge that will help mitigate potential losses due to future earthquakes. Although the literature is abundant of studies about characteristics and overall vulnerability of conventional low to mid-rise RC buildings, there is almost no information about the characteristics, seismic vulnerability and dynamic behaviour of high-rise RC building stock in Turkey. This is because of the challenges lie within the task of examining this particular structure class. This study aims to provide information related to (1) the characteristics of RC core wall-frame tall building inventory of 10 to 30 stories; (2) dynamic properties of this target building stock through probabilistic damage assessment framework and (3) the fragility curves for future earthquake damage and loss estimation studies of this stock in Turkey. Series of nonlinear response history analyses (NRHA) are conducted on 3D building models based on a statistical survey undertaken through the high-rise buildings compiled from major cities of Turkey. The PBEE framework is adopted to present a transparent methodology relevant to the current practice.

The studies within the context of this thesis are presented under several chapters. Chapter 2 includes the statistical characterization of the building types studied in the thesis. The following Chapter 3 emphasises the development of analytical models from the statistical studies conducted in Chapter 2. Definition of seismic hazard for the chosen site, as well as the ground motion selection procedure is presented in Chapter 4. The overall structural behaviour of the building models are evaluated in Chapter 5 through statistical studies. Fragility functions are derived for the target building stock and are given in Chapter 6. Discussions and recommendations alongside with the findings and observations in this study are delivered in Chapter 7.

2. HIGH-RISE BUILDING INVENTORY

A tall building inventory was compiled within the framework of this thesis. Confined to the limitations of this study, the compiled database partially represents the RC high-rise buildings that are located in metropolitan cities of Turkey (e.g., Istanbul, Ankara, Bursa and Mersin). It is believed that the presented building inventory, having a fairly large amount of descriptive structural and architectural items, provides significant insight in understanding the key structural properties and design practice of tall buildings in Turkey.

2.1. Inventory Information

A statistical survey is carried out to determine various structural and architectural properties of the tall building inventory. The inventory contains detailed blueprints that provide information regarding:

- Location of the buildings,
- Site conditions,
- Code based design assumptions (e.g. earthquake load reduction factors),
- Material properties,
- All-in geometrical and architectural characteristics,
- Structural detailings of RC elements.

The building inventory consists of 92 RC buildings with 10 or more stories, excluding podium stories. Among these structures however, eliminations are made to establish a pool of high-rise buildings featuring similar structural design and behavior. The main reason for this initial step is to retain a sense of homogeneity among buildings that can be categorized under the same context. Following this idea, only "RC Core Shear Wall-Frame*"* systems (abbreviated as RC-CWF) are evaluated where an RC-CWF system is composed of a central shear wall core that is connected to the frame members such as beams and columns. The second elimination is done by excluding buildings that have unique architectural features because they can not fit into any generalized tall building class. To this end, buildings having more than 30 stories (excluding podium floors) are disregarded in this study.

In essence, 45 RC shear wall-frame high-rise buildings of 10-30 stories constitute the target building stock for statistical inventory evaluation in this study. Note that buildings exhibiting the same structural properties (such as individual buildings in residence blocks as in Figure 2.1) are counted as a single building. Otherwise the inventory parameters would be distorted by stacking up the properties of the same buildings.

Figure 2.1. An illustration of multiple buildings sharing the same geometrical and structural properties (Mall of Istanbul project, residence blocks)

2.2. Evaluation of Parameters

The parameters extracted from the evaluated high-rise buildings are explained in this section. These parameters together with their classifications are given in the following lines.

Geometrical Parameters:

- Floor plan dimentions in both orthogonal directions (the most frequently observed dimensions along the building height are used)
- Span lengths in both orthogonal directions
- Average typical floor heights
- Typical gravity column and gravity beam dimensions
- Typical link beam dimensions
- Gravity beam span-to-height ratios
- Type of slab system used

- Typical floor slab thicknesses
- Shear wall cross-section areas in both orthogonal directions
- The ratio of the total shear wall cross-section area to floor area in both orthogonal directions (abbreviated as SW ratio)

Material and Design Parameters:

- Concrete grade
- Reinforcement steel grade
- Soil type at the building site

Structural Member Parameters:

- Cross-sectional dimension of structural members
- Longitudinal and transverse reinforcement configurations of beams and columns
- Longitudinal and transverse reinforcement configurations of shear walls in web and boundary regions.

2.3. Characterization of Building Subtypes

Six buildings are designed utilizing the inventory information to account for the inherent variations among the buildings in the inventory. A hierarchical methodology is adopted in the categorization of these buildings. Firstly, buildings are separated into two main groups according to number of stories. Group-1 buildings represent 10 to 20 story RC-CWF buildings, while Group-2 represents similar buildings of 20 to 30 stories (Table 2.1). Group-1 buildings are mimicked by 15 stories whereas Group-2 buildings are mimicked by 25 stories. Submodels under each major group are determined by categorizing the buildings according to their shear wall (SW) area / floor plan area ratios (SW ratio). Section 2.3.1 explains this categorization in detail.

Table 2.1. Categorization of tall buildings

Building Type	Group	Submodel (Model Name)	Stories
RC-CWF	1	1A	15
		1B	
		1C	
	2	2A	25
		2B	
		2C	

2.3.1. Categorization of Building Models Using SW Areas

SW configurations are inspected very carefully in the building database because SWs are expected to dominate the structural behaviour as well as damage states of CWF buildings. Statististical evaluations of the building inventory has shown that the SW ratios are related to building dimensions along short and long directions. Figure 2.2 shows the definitions of SW ratio in *short* and *long* directions. These directions represent short and long orthogonal dimensions of floor plans. This information is collected from each building.

The collected SW ratios along short and long directions follow a log-normal distribution as shown in Figure 2.3. The logarithm of a lognormally distributed variate (SW ratio in this case) is normally distributed (Probability Theory: Laplace, 1812). Figure 2.3 shows the empirical cumulative distribution functions (CDFs) of logarithms of SW ratios in short and long distributions together with theoretical normal CDFs. Figure 2.3a shows these distributions for Group-1 buildings in short (left panel) and long (right panel) directons. Figure 2.3b shows the same distribution for Group-2 buildings. The Kolmogorov–Smirnov test (Massey, 1951) (K–S test or KS test) is implemented to the distributions shown in Figure 2.3 to verify the goodness-of-fit. Hypothesis test results returned as a logical value of 1 for all cases which indicates the rejection of the null hypothesis at 0.05 (5%) significance level.

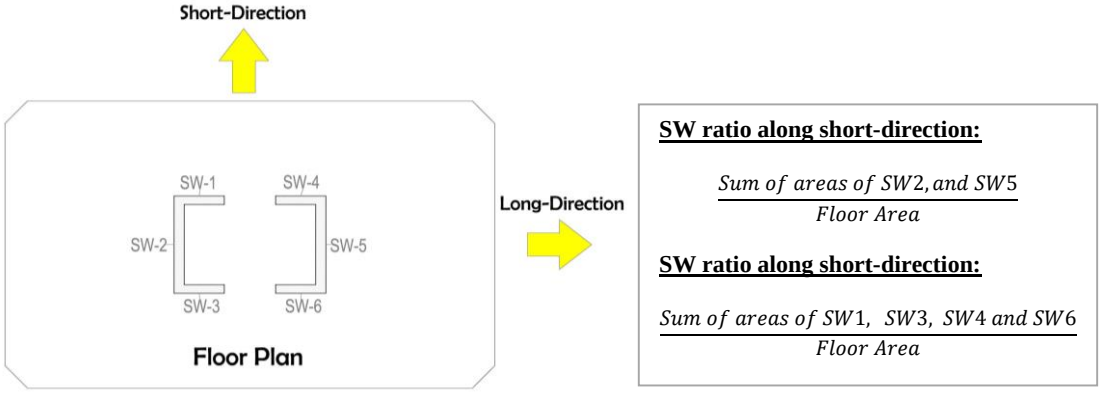

Figure 2.2. Illustration about the computation of SW ratios along short and long directions

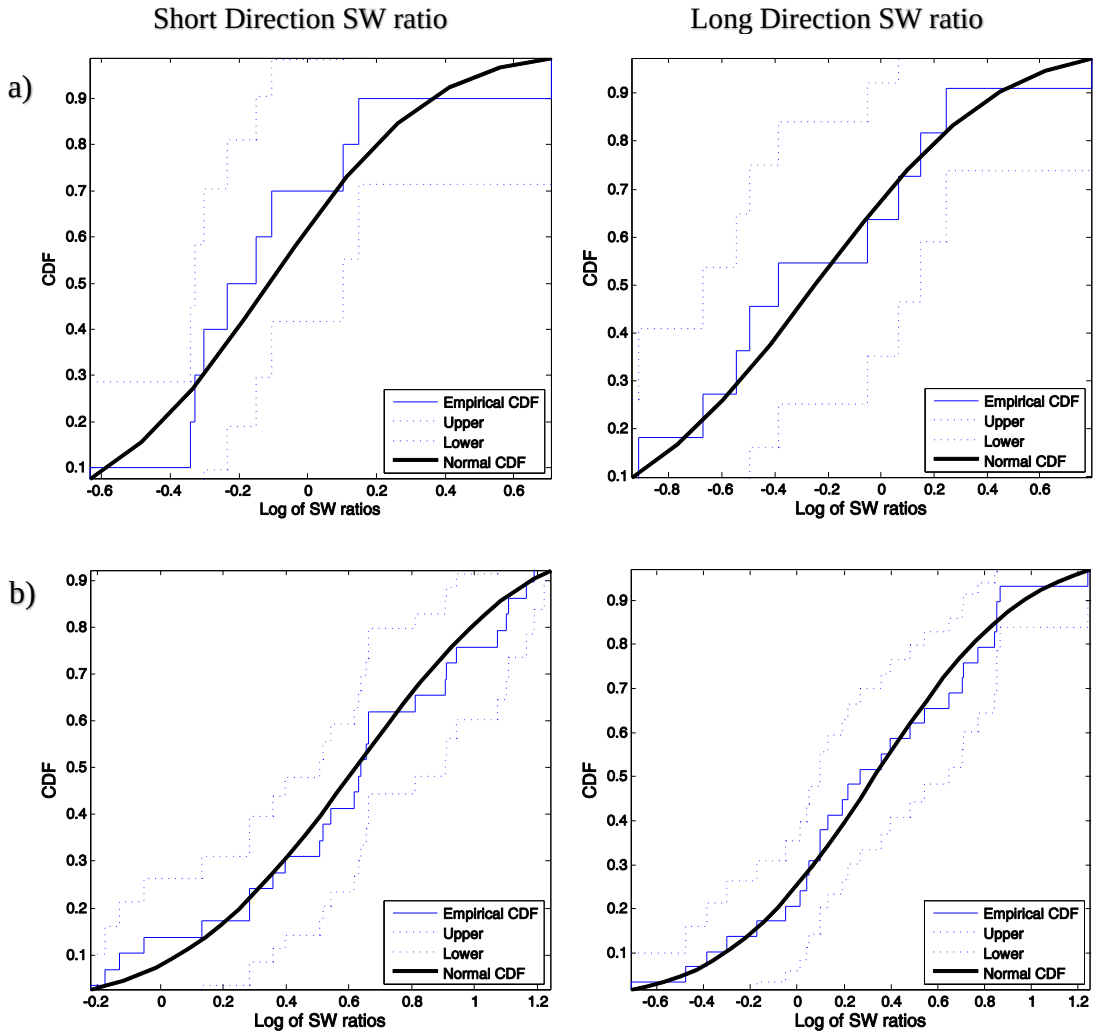

Figure 2.3. Normal cumulative distribution of natural logarithms of shear wall ratios in short and long directions (See Figure 2.2) a) for Group-1 buildings b) for Group-2 buildings

In order to account for the interaction between SW ratios along short and long directions for the submodels, the long-direction SW ratios are divided into 3 regions as given in Figure 2.4. These regions follow the below rules and each delineated region represent a particular submodel as given in Table 2.2 where μ and σ are the mean and standart deviation of SW ratio distributions along the long direction.

Table 2.2. Descriptions for submodel regions

Region	**Rule**
Low-end region	SW ratio ≤ μ-σ
Intermediate region	μ-σ < SW ratio < μ+σ
High-end region	SW ratio ≥ μ+σ

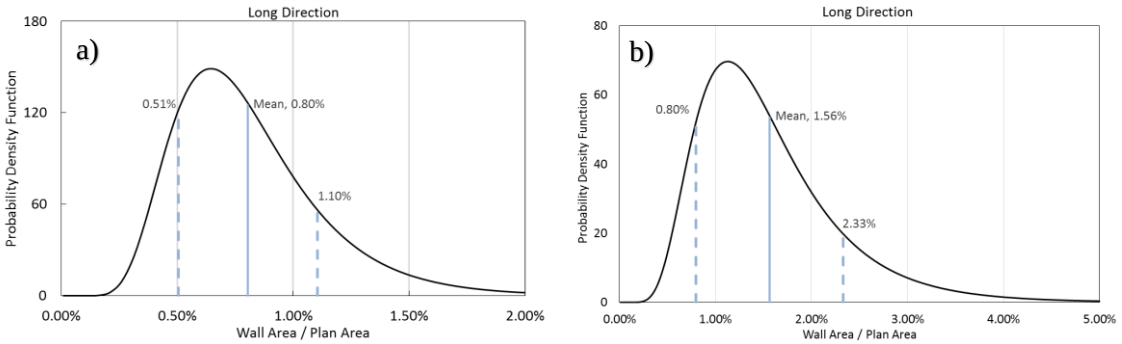

Figure 2.4. Lognormal distributions of SW area ratios a) for Group-1 Buldings, b) for Group-2 Buildings. Solid stripes represent the mean of each data set while dotted stripes mark the minus and plus standart deviation bounds

Submodels having letter “A” (either 1A or 2A) represent low-end SW ratios along long direction. The average of short direction SW ratios of the buildings falling into this region describe the corresponding SW ratio along short direction for this submodel. The same type of classification applies for submodels having letters “B” and “C”. In other words, intermediate and high-end SW ratios along long directions represent “B” and “C” submodels respectively. The averages of short direction SW ratios of the corresponding building falling into these regions define the SW ratios for these submodels. As indicated above, this procedure, in a way, considers the dependency of shear wall area ratios along short and long

directions. Table 2.3 lists the SW ratios as well as the structural wall detailing parameters in plastic hinge regions of three submodels for each major group.

Table 2.3. Shear wall ratios determined from building inventory survey

Group	Subtype (Model Name)	Shear Wall Ratio-Long Direction*	Shear Wall Ratio-Short Direction*	BZ† Vertical Reinf. Ratio	BZ Transverse Reinf. Ratio	Web Vertical Reinf. Ratio	Web Transverse Reinf. Ratio
1	1A	0.45%	0.98%	1.54%	0.64%	1.10%	0.47%
	1B	0.78%	0.83%	1.47%	0.50%	0.91%	0.57%
	1C	1.22%	0.94%	1.93%	0.52%	1.06%	0.31%
2	2A	0.63%	1.40%	1.05%	0.46%	0.88%	0.76%
	2B	1.56%	2.21%	1.19%	0.56%	1.07%	0.58%
	2C	2.93%	2.45%	2.03%	0.39%	0.73%	0.25%

* Shear wall ratio is calculated by dividing the gross cross section area of the shear walls in one direction of the building to the total floor area

† BZ: Boundary zone, where concrete in confined

2.3.2. Beam and Column Members of the Model Buildings

Geometrical properties of the beams for structural models are determined from the most frequently observed cross sections in the buildings in each major group (Group-1 and Group-2). Note that each one of the three building submodels under a major group comprises of the same beam cross-sections. This is because 1) it was observed that the beam cross-sections are not influenced by SW ratios; 2) buildings in the inventory usually have one typical beam cross-section that is most frequently used; 3) having one beam type saves computational effort without affecting the structural behaviour significantly. The geometry of beam cross-sections are summarized in Table 2.4.

Coupling beams (link beams) and their geometrical properties vary across different building submodels depending on the shear wall configuration adopted in the corresponding building model. The most commonly used link beam cross-sections for the coupled shear wall configurations are investigated among the individual buildings in the database to obtain this information. Table 2.4 includes link beam cross-sections used in all building models.

Cross-section geometry of columns for each submodel is determined in view of the following two features:

1. The most frequently observed column cross sections
2. Design and layout of core shear walls of the corresponding submodel

Cross-section dimensions of columns remain constant along the height of all building models as this was the most frequently observed case from the inventory survey. Section geometry of column members are given in Table 2.4.

Table 2.4. Cross-section dimensions of beam and column members

Building Subtype	**Beams**	**Link Beams**	**Columns**
1A	80x60cm	30x60cm	80x80cm
1B	80x60cm	30x60cm 40x60xm	80x80cm
1C	80x60cm	30x60cm 40x60xm	80x80cm
2A	80x60cm	30x60cm 40x60xm	80x80cm
2B	80x60cm	40x60cm 50x60cm	80x80cm
2C	80x60cm	50x60cm 40x60cm	100x100cm

Dimensions are given in the order of ‘width x height’.

Reinforcing steel ratios are investigated by realizing a statistical survey on beams and columns of buildings in the inventory. The mean values of the most commonly observed reinforcement configurations in the beam and column members of individual buildings are taken to represent the reinforcement ratios of structural members in the model buildings. Note that these values are not determined separately for each building submodel and given in Table 2.5. In other words, the whole inventory is considered as one large data set to obtain these mean values. This is because the inventory survey has indicated that the beam and

column reinforcement ratios do not change significantly depending on neither SW ratios nor number or stories in a building (within 10 to 30 story range).

Table 2.5. Reinforcing steel ratios for beam and column sections used in the model buldings

Item	ρ_{top} *	ρ_{bottom} *	$\rho_{transverse}$ †
Gravity Beam 80x60cm	0.49%	0.49%	0.48%
Coupling Beam 25x60cm	0.32%	0.42%	0.52%
Coupling Beam 30x60cm	0.35%	0.41%	0.40%
Coupling Beam 50x60cm	0.35%	0.39%	0.39%
Column 100x100cm	0.50%	0.50%	0.50%
Column 80x80cm	0.50%	0.50%	0.50%

* Top and bottom vertical reinforcement ratios

† Transverse reinforcement in direction of interest (ρ_x or ρ_y)

2.3.3. Material Properties

Statistical survey on the building inventory indicated that only conventional reinforcing steel is used in all structures. The conventional reinforcement refers to a steel rebar with yield stress not greater than 420 MPa (ACI, 2011). The use of high-strength steel bars is still limited even in regions of high seismicity with design service life, i.e. usually assumed to be 50 years for RC residential buildings (Sarja, 1998; Wegen et *al.*, 2012). The most commonly used reinforcing steel grade in the building stock has a nominal yield strength of 420 MPa (S420). The mechanical properties of the S420 grade steel is given in Appendix A.

Normal-strength concrete (NSC) is used in all buildings in the inventory, suggesting that the concrete grade for bulding models are below C55 grade which indicates a specified compressive strength of 55 MPa. According to American Concrete Institute (ACI, 2011),

high-strength concrete (HSC) is defined as the concrete having a specified compressive strength of 55 MPa or greater. This concrete compressive strength value (55 Mpa or above) requires special treatment for its production and testing as well as for the design of structural members (ACI, 2011). For this reason, the use of HSC is limited in the current construction and design practice in Turkey. Concrete cube strength of 35 MPa and 40 MPa are used in Group-1 and Group-2 buildings, respectively. Concrete grades are held constant for all RC members along building height. These decisions are taken by considering the results of the building stock.

2.4. Design Methodology of Model Buildings

Inherently, the design of buildings in the inventory differs from each other. Thus the most frequent design approaches encountered in the building database are adopted to obtain model buildings representing the building inventory. Design approaches for certain structural members pose more importance in terms of overall structural behaviour. To this end, they are studied closely than other secondary members. That being the case, this section only elaborates on structural configurations of coupling beams and shear walls.

2.4.1. Coupling Beam Configurations

The efficiency of a coupled structural wall system can be improved by proper coupling of two consecutive walls through the use of coupling beams (link beams). To achieve satisfactory performance in a coupled wall system during a seismic action, the short coupling beams should retain a significant portion of its initial strength and stiffness through large cyclic displacements. ACI Building Code (ACI, 2008; ACI, 2011) requires that diagonal reinforcement should be provided to withstand large shear and flexural demands (Figure 2.5).

Figure 2.5. Diagonal reinforcement configuration in a coupling beam

Coupling beams in the target building inventory are not only as deep as the coupling beams frequently met in the design practice of the US, they are also poorly designed in diagonal reinforcements. Hence, these beams do not have large shear or bending capacities resulting in a poor dual system behaviour between consecutive shear wall segments. Consequently, this design practice in Turkey may lead to excessive damage in coupling beams, higher period elongation in post-elastic response and larger interstory drift ratios. This observed defficiency is implemented in the building models in order to simulate the actual behaviour in the compiled building stock.

2.4.2. Shear Wall Configurations

In almost all investigated buildings, shear walls are only confined in boundary zones, indicating that the web concrete remains unconfined. The statistical survey on the building inventory has shown that the boundary zones make up 40% (20% at each end) of the SW gross area within the critical height (i.e., the plastic hinge region) and 20% above the plastic hinge region. Boundary zones are located at each opposite end of a SW cross section to provide an increased flexural capacity and ductility. This is usually achieved by employing denser reinforcement detailing (both longitudinal and transverse) in the boundary zones to improve compressive stress-strain relationship of concrete. A typical detailing of a SW cross section is given in Figure 2.6, where l_{be} is the boundary element width, l_w is the width of the wall cross section and b_w is the thickness of the wall section. Note that these observations on boundary zone area ratios are consistent with the design criteria given for the design of “high ductility” SWs in Turkish Earthquake Code (TSC, 2007). The following subsection

describes the observed design practice for SWs above and below critical height of tall buildings.

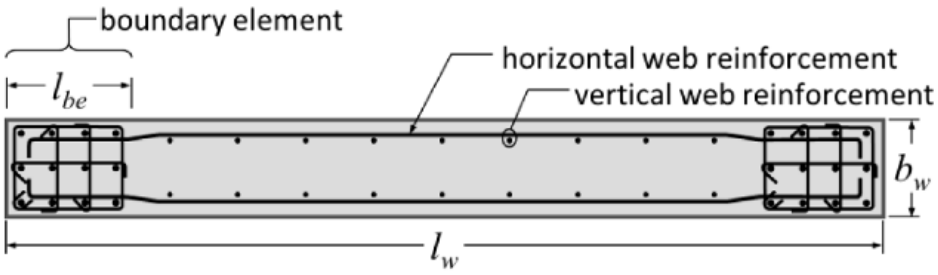

Figure 2.6. A typical reinforcement detailing for rectangular shear wall (NEHRP Seismic Design Technical Brief No. 6, 2012)

2.4.2.1. Reinforecement Configuration of SWs Above and Below Critical Height

Codes recommend denser reinforcement within the SW plastic hinge regions. Strict design provisions apply for these regions to assure a certain level of ductility and moment capacity. These regions are delineated by the term “critical height” (Figure 2.7). Since the core walls would be the dominant lateral load resisting components of the buildings of interest, earthquake induced demands are expected to reach their maxima at lower stories due to cantilever-like behaviour of these members. Well-detailed core SW sections at the base therefore are critical for better seismic behaviour of such buildings. The detailing conditions of core SW sections differ below and above the plastic hinge regions in the investigated building inventory. Critical height is observed to be around 0.25 times the total height of the buildings, H_w. The detailings of the model buildings reflect this observed feature. The longitudinal and transverse reinforcement ratios within the plastic hinge region for model buildings are defined as given in Table 2.3.

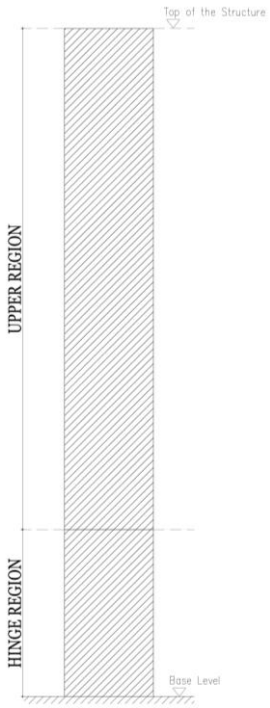

Figure 2.7. Discretization between the hinge region and the upper region

For most cases, structural wall geometry remains constant over the height of the investigated buildings. Above the critical height however, reinforcement configurations change. Longitudinal reinforcement ratios are halved above the critical height of the structures. This reduction in reinforcement, in most cases, is 0.5. Also note that the reduced reinforcement ratios are not observed to be less than 1.0% for boundary zones and 0.25% for the web of the walls i.e., compliant with TSC (2007) provisions. As for the transverse reinforcement ratios, the code minimum of 0.25% is most commonly provided. The following rules are set in view of above expressions to determine the reinforcement ratios in SWs above plastic hinge regions:

1) The longitudinal reinforcement ratio is taken as 0.5 times the value determined for SWs within the critical height as given in Table 2.3. This value is not permitted to be less than 1.0% in boundary zones and 0.25% in web of the SWs
2) The transverse reinforcement ratio of SWs above plastic hinge regions is defined as 0.25%.

2.4.3. Summary of the Model Building Parameters

Table 2.6 lists the model parameters used in the model buildings that are explained throughout this chapter. Parameters that vary from one building model to the other (such as bay widths) are not listed on Table 2.6 but presented in formwork plans of each model building (Figure 2.8, 2.9 and 2.10; Figure 2.11, 2.12 and 2.13). Mode statistics of the investigated inventory are used for building parameters (e.g., building height or concrete grade) that attain specific values. Figures 2.8 to 2.10 represent the typical formwork plans of group-1 model buildings (i.e., 1A, 1B and 1C). Whereas Figures 2.10 to 2.11 show typical formwork plans of group-2 model buildings (i.e., 2A, 2B and 2C).

Table 2.6. Important building parameters used in the model buildings of this study

Parameter	**Group-1 Buildings**	**Group-2 Buildings**
Story #	15	25
Story Height	3.40 m	3.10 m
Plan Dimensions	52 x 25 m	40 x 25 m
Slab Thickness	17 cm	20 cm
Slab Type	Flat RC Slab	Flat RC Slab
Concrete Grade	C35*	C40*
Steel Grade	S420**	S420**
Seismic Zone†	Zone 1	Zone 1
Soil Type†	Z2	Z2

* Concrete grades C35 and C40 indicate that the nominal compressive strength is 35 MPa and 40 MPa, respectively

** S420 steel grade translates into a steel specimen having a nominal yield strength of 420 MPa, and an ultimate tensile strength of 550 MPa

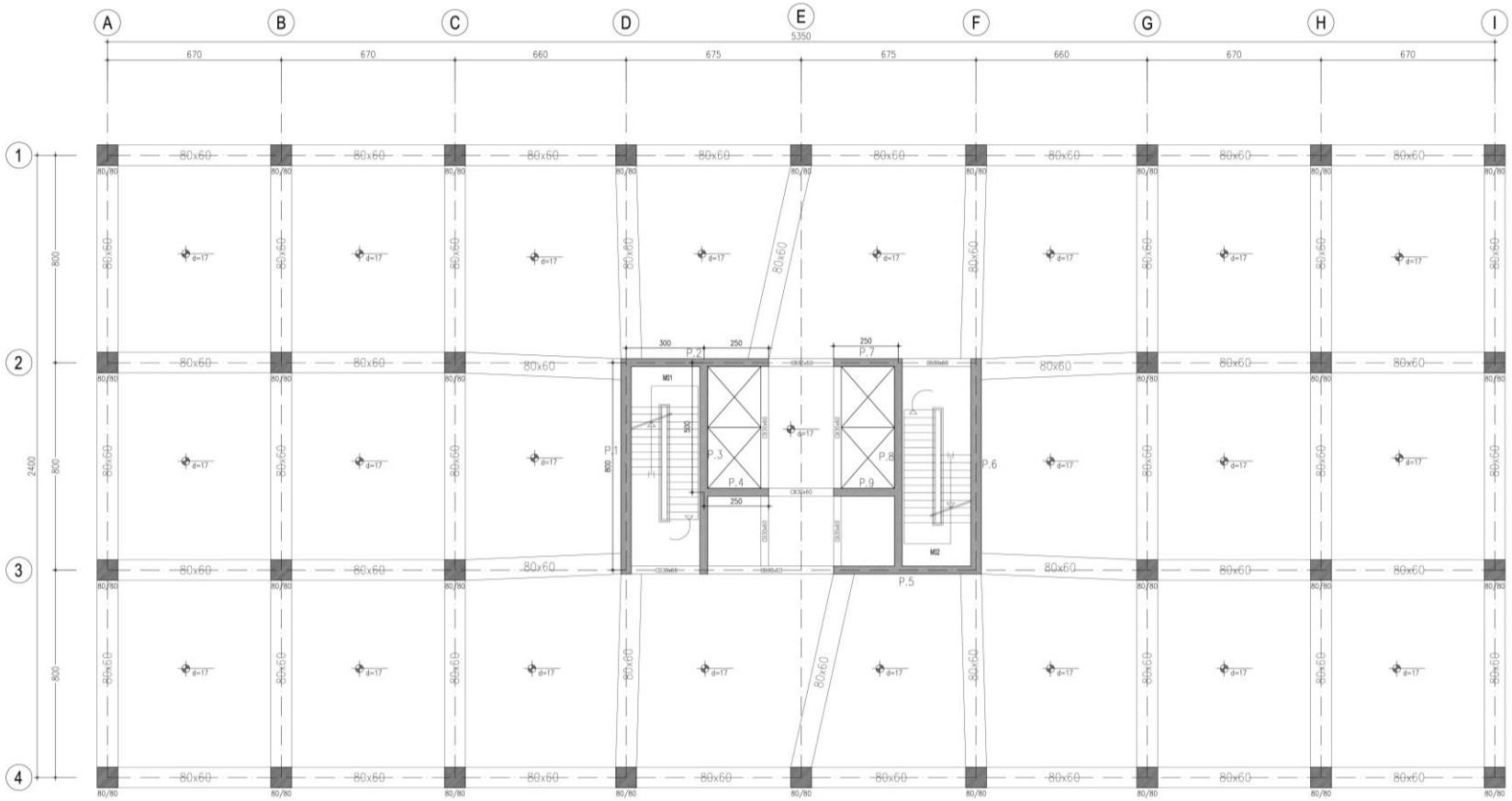

Figure 2.8. Typical floor plan of submodel 1A

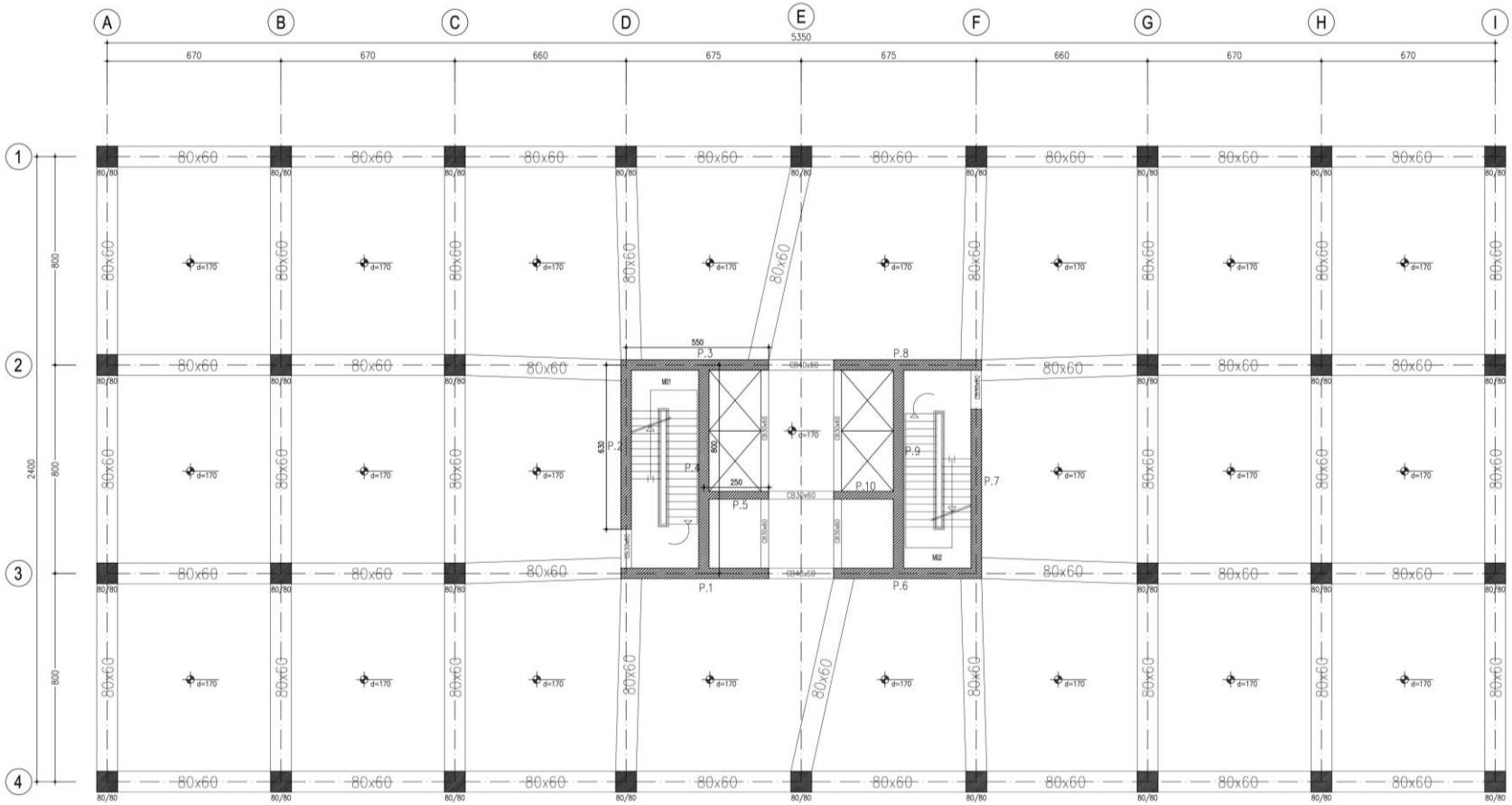

Figure 2.9. Typical floor plan of submodel 1B

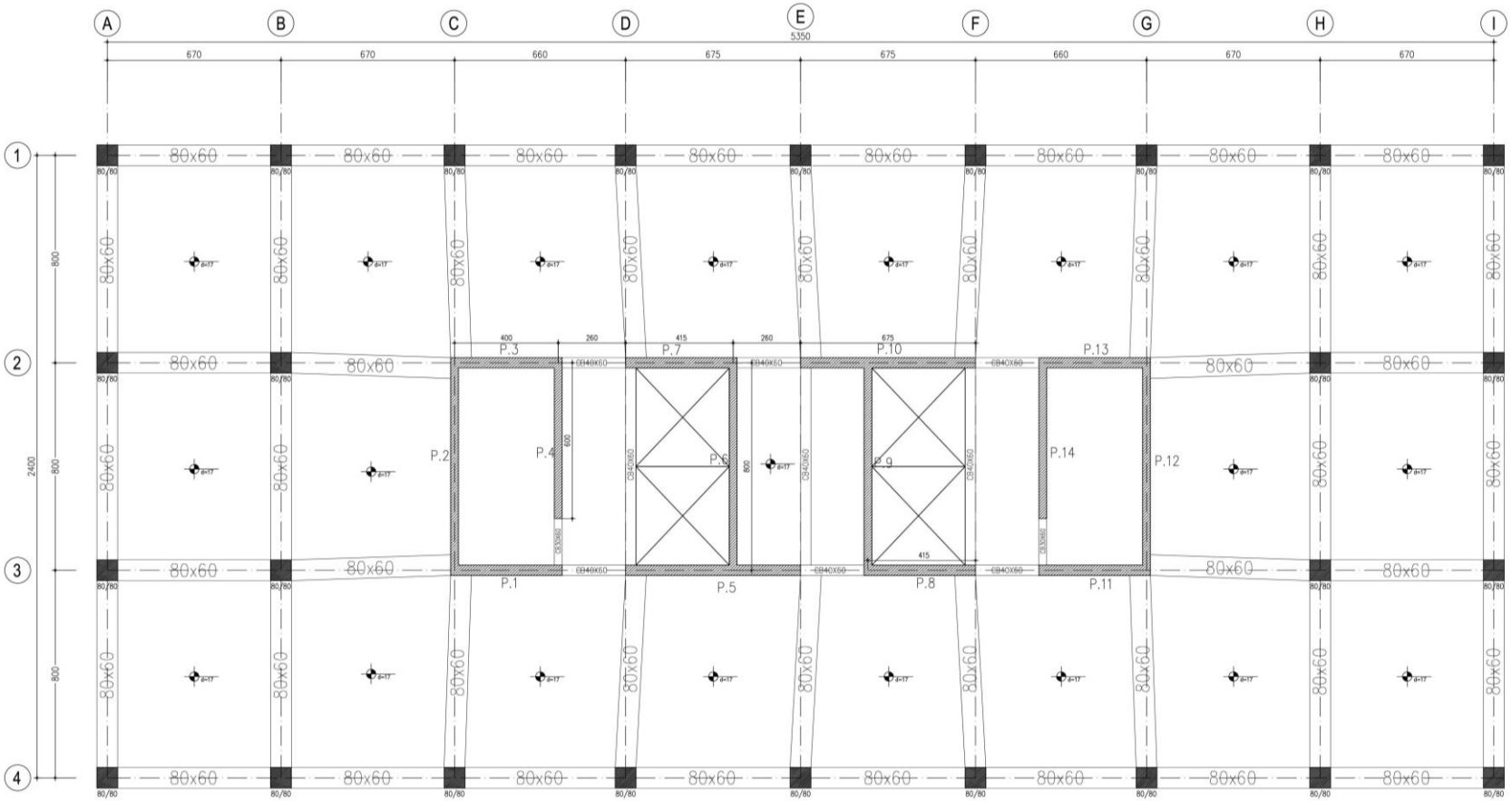

Figure 2.10. Typical floor plan of submodel 1C

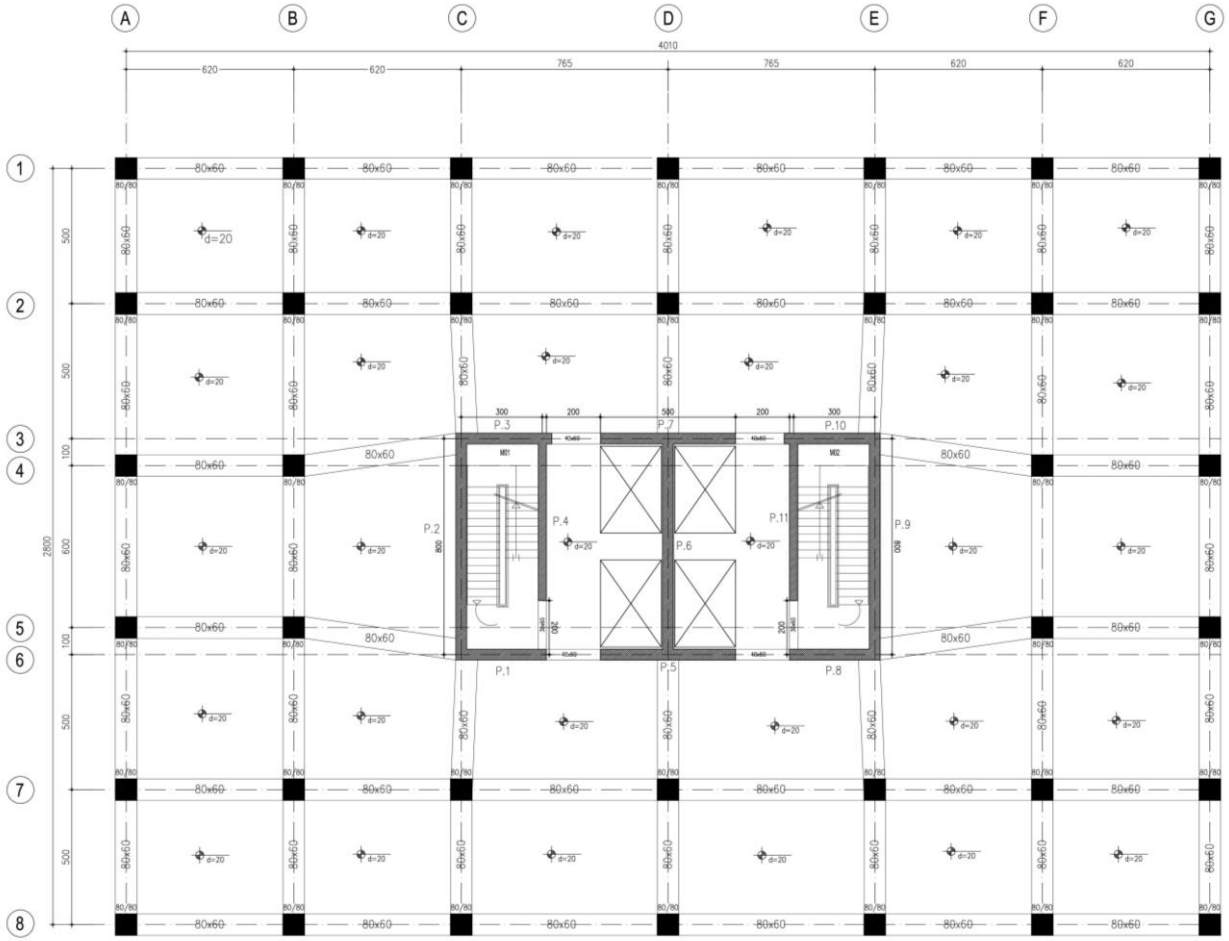

Figure 2.11. Typical floor plan of submodel 2A

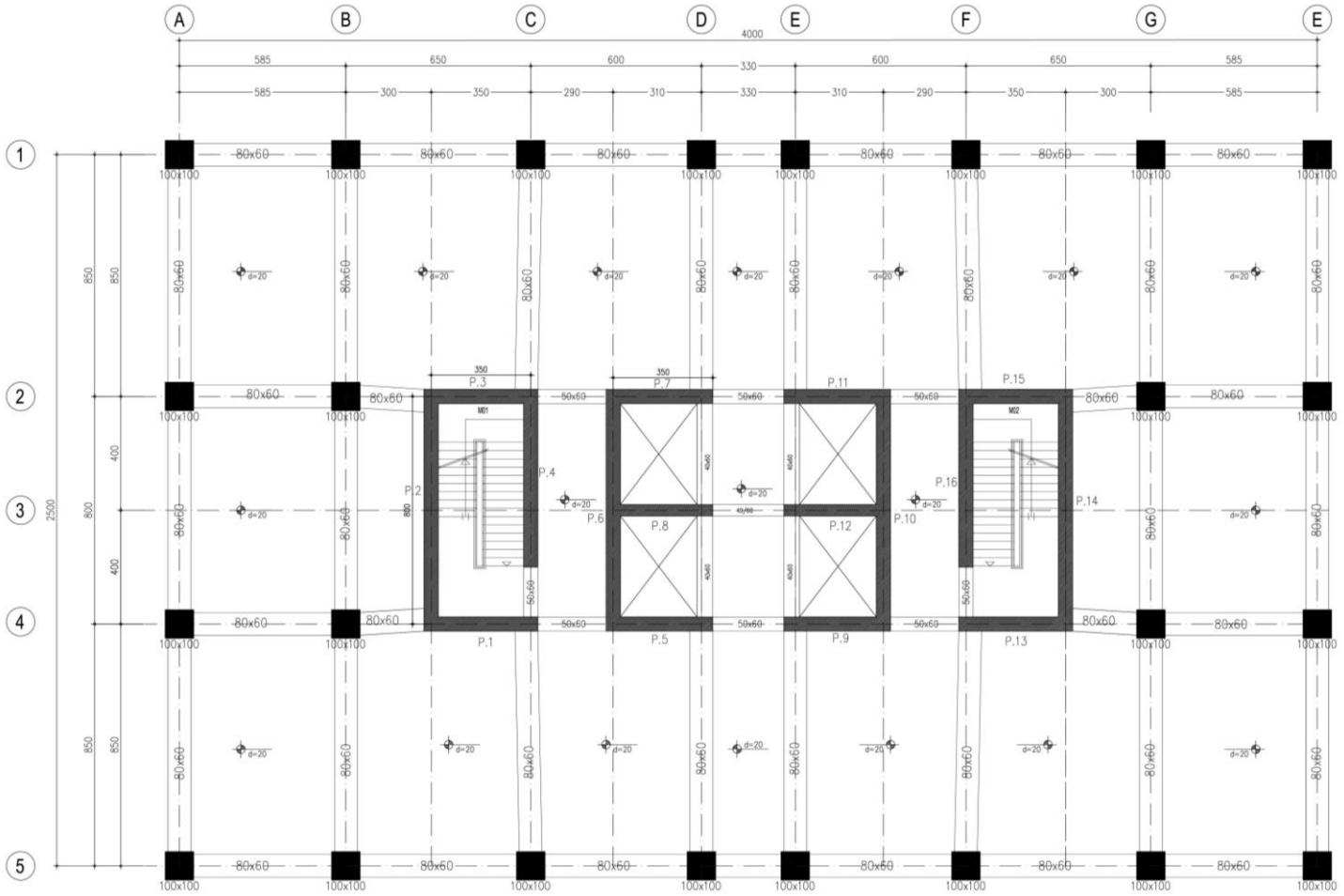

Figure 2.12. Typical floor plan of submodel 2B

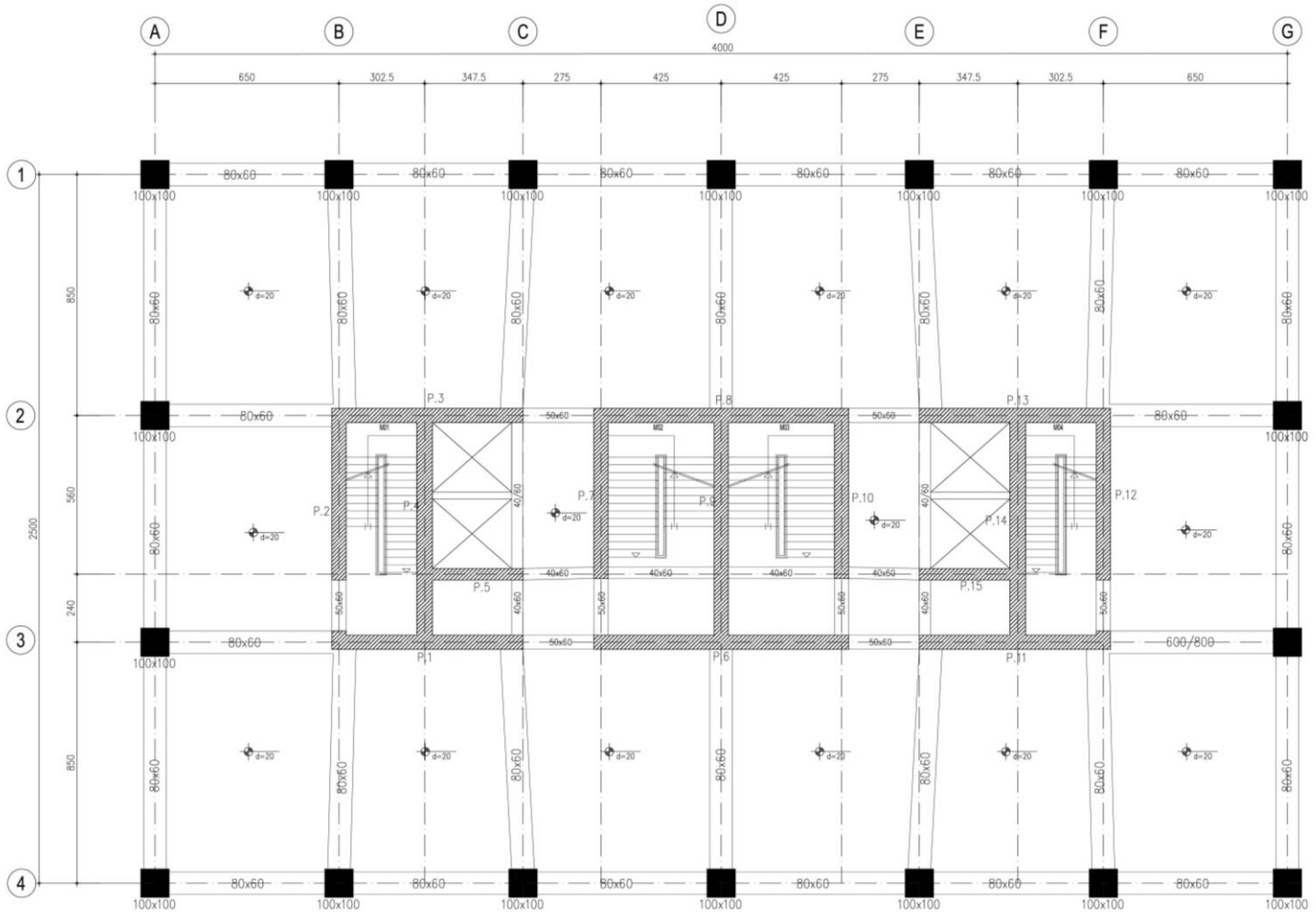

Figure 2.13. Typical floor plan of submodel 2C

3. DEVELOPMENT OF THE STRUCTURAL ANALYSIS MODELS

3.1. General

Analytical structural models are developed using Perform 3D software package (Computers and Structures, 2009). Visual representations of the 3D building models are presented in Figure 3.1 (Group-1) and Figure 3.2 (Group-2). Models of six different statistically representative tall buildings are developed with a similar modelling approach. Lateral load resisting system of each one of the bulding subtypes is composed of coupled core SW and columns. Hence, analytical models of the buildings included shear wall and column elements. It is essential to consider the contribution of the frame-shear wall interactions to obtain accurate results from nonlinear dynamic analyses (Ji et *al*, 2007). Slabs are not modelled because their effect on the global and local responses are negligible (PEER, TBI Task 12, 2011). The nodes at each floor are constrained by a rigid diaphragm assumption. Frame elements (beams and columns) are modelled with lumped plasticity approach, whereas fiber-based analytical models are utilized to model SW elements to consider spread plasticity. P-Δ effects are taken into account in nonlinear response history analyses (NRHA) while floor masses are assigned as lumped masses at the center of gravity.

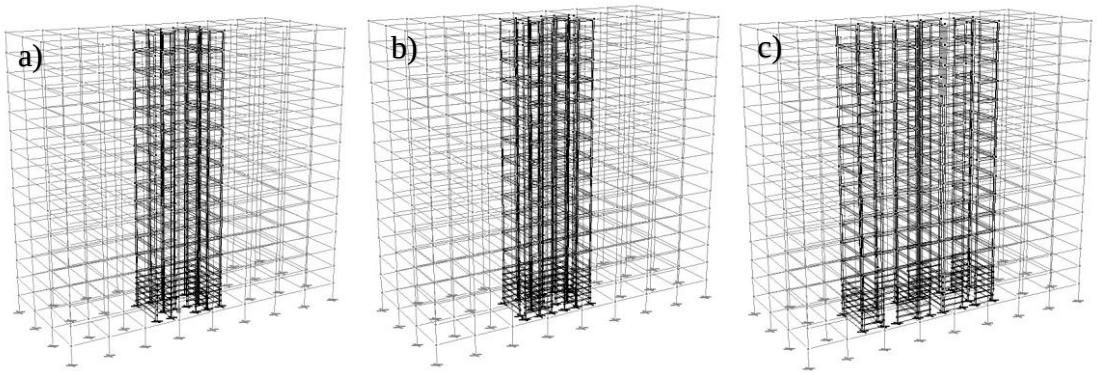

Figure 3.1. Analytical structural models of the first group buildings in Perform 3D. (a) Building 1A, (b) Building 1B and (c) Building 1C

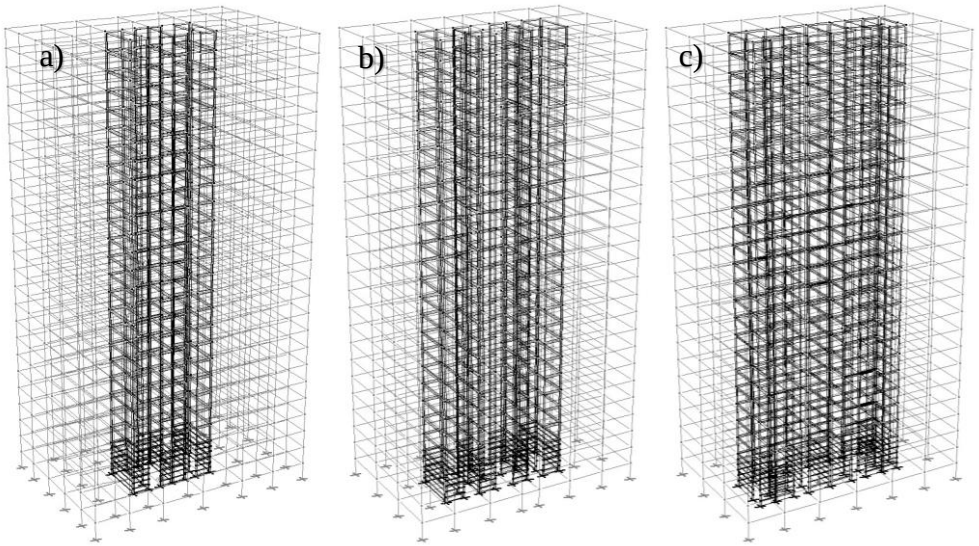

Figure 3.2. Analytical structural models of the second group buildings in Perform 3D. (a) Building 2A, (b) Building 2B and (c) Building 2C

3.2. Gravity Loading Criteria

Prior to the nonlinear dynamic analysis, a gravitiy loading case is set to simulate the initial state of the structure. For the contribution of gravity loads, different building codes specify different percentages of live loads. These percentages do not differ from each other significantly. Tall Buildings Initiative (TBI, 2010) notes that the live load reduction factor, L_{exp}, should be taken as 25% of the unreduced live load unless otherwise stated. According to the regulations of Turkish Earthquake Code (2007) live load reduction factors should be taken as 30% of the unreduced live loads for residential buildings. Hence for all building models gravity load combination is defined as:

$$W=G+0.3Q \tag{3.1}$$

where, G is the total dead load of the structure, and Q is the total live load of the structure.

3.2.1. Input Gravity Loads

Dead and live loads exerted on the buildings with their respective load descriptions are given in Table 3.1.

Table 3.1. Gravity loading definitions

Load Description	**Type of Loading**[†]	**Loading**
Perimeter (Exterior) Walls	SI Dead Load	3.80 kN/m^2 (Wall Area)
Inner Non-Structural Walls	SI Dead Load	2.50 kN/m^2
Overcoats	SI Dead Load	1.50 kN/m^2
Slabs[*]	SI Dead Load	4.64 kN/m^2
Uniform Live Loads	Live Load	2.50 kN/m^2 (Unreduced)

[*] Slab loads given in this table are for 20 cm thick RC flat slabs with a concrete density of 25 kN/m^3

[†] SI refers to "Superimposed".

3.2.2. Story Mass

In actual building behaviour, the mass is distributed through the entire structure and is excited during a ground shaking resulting in forces on members that occur as a consequence of the imposed displacements. This phenomenon can not be fully mimicked via analytical modelling because of the limitations in computer power. To this end, simplifications are made in line with the current practice and masses at each story are lumped at the center of gravity on both horizontal directions with the moments of inertia assigned as an angular quantity around the vertical axis. Mass is calculated from the gravity load combination given in Equation 3.1. For rectangular plane bodies, which in this case the slab diaphragms, the angular mass corresponding to the axis perpendicular to the slab's plane surface is calculated as the rotational moment of inertia of a rectangular plane. Table 3.2 lists the story mass of each model building.

Table 3.2. Resulting story mass for the model buildings

Building	**Mass in horizontal directions**	**Rotational Mass**
1A	2234.7 tons	640290 tons.m^2
1B	2276.4 tons	652250 tons.m^2
1C	2272.5 tons	651120 tons.m^2
2A	1938.0 tons	358180 tons.m^2
2B	2036.6 tons	377620 tons.m^2
2C	1948 tons	361190 tons.m^2

3.3. Effective Stiffness Definitions

Structural elements should posess realistic estimates of stiffnesses considering the expected level of excitation which can be related to any intensity measure of the ground motion. Definition of effective rigidity reflects both the effects of cracking and yielding of the RC sections. For linear analysis, member stiffnesses control the perdiods of the structure and the deformation demands. As for nonlinear analysis, accurate estimates of stiffnesses are necessary ingredients to reliably predict the yield deformations which affect the displacement ductility demands. Practical and accurate procedures are required to estimate the effective stiffnesses up to yielding of structural members (Figure 3.3).

Codes and design guidelines recommend effective stiffness definitions depending on the structural member type. This is mainly because the yield displacements vary for different structural members and loading conditions (axial loads being the most influential action) they are subject to. These recommendations are derived from both experimental and analytical studies of various researchers (e.g., Mehanny et al., 2001; Berry et al., 2004; Elwood and Eberhard, 2006).

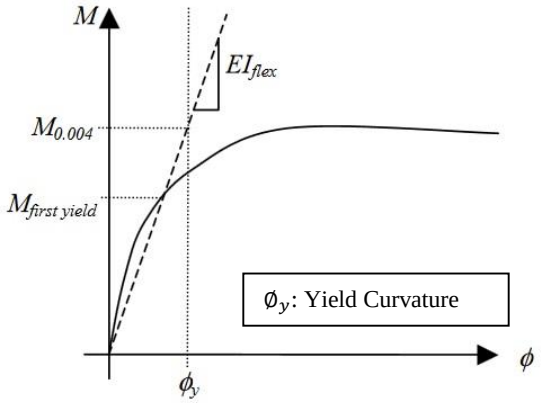

Figure 3.3. Effective flexural stiffness definition of a member. Slope of the dashed line (EI_{flex}) represents the effective stiffness

The effective stiffness parameters is implemented, for each building model based on the recommendations in LATBSDC (2014). Normally, LATBSDC recommends different levels of stiffness reduction factors depending on the intensity of the excitation (Table 3.3). However, a uniform modeling procedure was established so that engineering demand

parameters (EDPs) for all building models (Buildings 1A, 1B, 1C, 2A, 2B and 2C) could be compared (PEER, TBI Task 12, 2012). Thus, stiffness modifiers for different structural members are determined considering an MCE-level ground shaking.

Table 3.3. Reinforced concrete stiffness properties of structural elements according to LATBSDC (2014)

Element	**Servicability and Wind**	**MCE-Level Nonlinear Models**
Structural walls	Flexural – 0.9 I_g Shear – 1.0 A_g	Flexural – 1.0 E_c *, ** Shear – 0.5 A_g
Moment frame beams	Flexural – 0.7 I_g Shear – 1.0 A_g	Flexural – 0.35 I_g Shear – 1.0 A_g
Moment frame columns	Flexural – 0.9 I_g Shear – 1.0 A_g	Flexural – 0.5 I_g Shear – 1.0 A_g
Coupling Beams	Flexural – 0.5 I_g Shear – 1.0 A_g	Flexural – 0.2 I_g Shear – 1.0 A_g

* Modulus of elasticity is based on the following equation for C35 and C40 concrete grades:

E_c=5000$\sqrt{f'_c}$ MPa

** Nonlinear fiber elements automatically acount for cracking of concrete because the concrete fibers have zero tension stiffness.

3.4. Modelling of RC Shear Walls

Modelling methodology of SWs plays an essential role in systems whose lateral force resisting system primarily relies on this structural member. Majority of the RC tall buildings in Turkey are core wall-frame (CWF) systems where coupled RC shear walls are the main lateral load resisting structural elements. High-rise building database compiled within the framework of this thesis is a strong indicator of this fact.

3.4.1. Theoretical RC Shear Wall Models

SW elements act, in principle, as beam elements with bending, axial and shear deformations. There are a few ways to model SWs, such as

- Beam-column element model
- Fiber element model (e.g., Multiple-Verticle-Line-Element Model)

3.4.1.1. Beam-Column Element Model

Beam-column elements can be utilized for modelling of RC shear walls. This model is easy to implement and it is computationally less demanding. Yet the analyst should be aware of the crudeness of beam-column elements in theoretical accuracy to estimate structural response. This approach assumes shear wall members as frame elements with rigid end zones that stretch along the width of the SW member. Although it has been observed by various researchers that the beam-column assumption can yield reasonable estimates of structural response (e.g., Wallace, 2007; Orakcal and Wallace, 2006; Thomsen *et. al*., 2004), beam-column model fails to account for the migration of the neutral axis in a SW cross section.

3.4.1.2. Fiber Element Model

Member sections are discretized into many uniaxial concrete and steel layers through fiber element modelling approach that leads to more realistic representation of their mechanical properties. Figure 3.4 shows analytical representation of the multiple-vertical-line-element model (MVLEM; Vulcano et al., 1988).

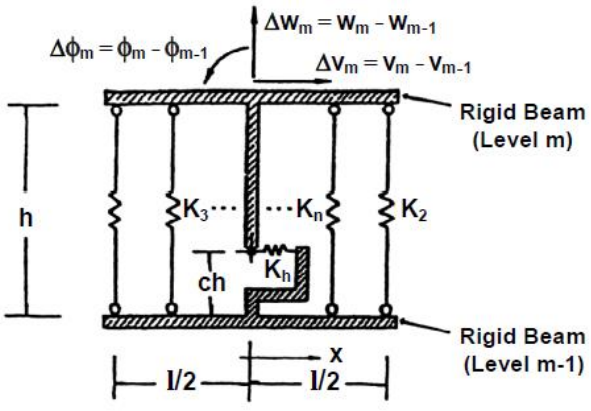

Figure 3.4. Multiple-vertical-line-element model (Vulcano et al., 1988)

The basic idea of fiber modelling was first introduced by Park et *al*. (1972) to model the cyclic behaviour of beams. Based on this method, Taylor (1977) proposed using uniaxial cyclic properties of concrete and reinforcing steel at each fiber on wall elements over the height of the wall member. This way, the shift in neutral axis of the wall element is

successfully captured, which is necessary to accurately represent the cyclic behaviour of SW. Recent studies have improved accuracy and reliability of the MVLE model by implementing refined cyclic material constitutive models that can better capure the hysteretic behviour of shear walls. (Orakcal et *al*., 2006; Massone et *al*., 2006; Kolozvari et *al*. 2012). Their models aim to capture the interaction between axial/flexural-shear behaviour in RC walls. Based on these studies Kolozvari et *al*. (2015) has proposed one of the most recent analytical MVLE model that considers shear-flexural interaction (Figure 3.5). This model is embedded into OpenSees structural analysis software (Open System for Earthquake Engineering Simulation, http://opensees.berkeley.edu).

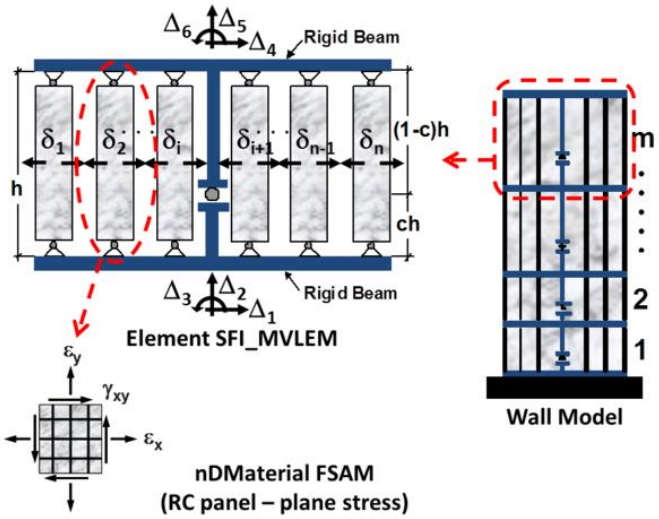

Figure 3.5. Shear-flexure interaction MVLE model proposed by Kolozvari et *al*. (2015)

Experimental studies carried out by various researchers (Hines et *al*., 1999; Orakcal et *al.*, 2006) indicated that in most SWs designed for yielding in flexure, shear crackings induce considerable shear deformations and stiffness loss in plastic hinge regions which consequently lead to an increase in overall deflection of walls. Therefore, the use of an axial/flexural-shear interaction SW model in NRHA can result in more accurate estimates of response parameters in exchange of additional computer run time. However, experimental verifications for these sophisticated models are still not convincing. Kolozvari et *al.* (2012) reported that their shear-flexure interaction MVLE model overestimates flexural deformations by approximately 30% and underestimates shear deformations by 30% to 40%. To this end, ongoing studies still refine the current MVLE models by considering complex

behaviours involved in the model formulations such as shear aggregate interlock relaionships. The current major limitations of multi spring (fiber) models are:

1) The adoption of Bernoulli hypothesis that suggests the plane sections remain plane, prevents the models from capturing the actual nonlinear strain profile. This is a poor assumption to make in shear walls because of their cross section geometry (large length to thickness ratio).
2) Inability to accurately take into account the complex axial/flexural-shear interaction
3) Inability to consider the effect of slabs on SW responses.

To facilitate a more realistic estimate of shear wall behaviour, an attemp is currently being made at the University of Canterbury (Sedgh and Dhkal, 2015): a new macro wall element is being developed constituting a number of fibers analysed based on material models. Although this new model seemingyly avoids all of the major drawbacks listed for the current MVLE models, it is still under development and further research is required to calibrate the model with experimental data.

3.4.2. RC Shear Wall Modelling in This Study

Reinforced concrete (RC) shear walls are modelled as fiber elements. Fiber elements used in modelling only represent the flexural force-deformation relationship of the longitudinal strips that are defined for each RC shear wall section. Shear stress-strain relationship of RC shear wall sections are introduced separately. In other words, the modelling of shear walls considers uncoupled axial/flexural-shear behaviour (Figure 3.6).

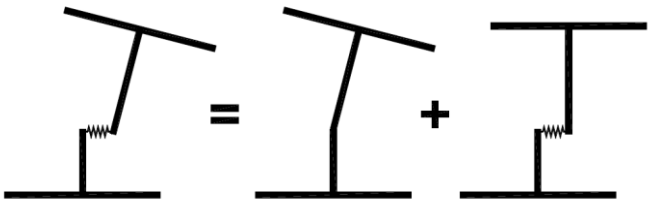

Figure 3.6. Representation of uncoupled shear and flexural responses (Orakcal et *al.*, 2006)

A fiber SW element is defined by a fiber cross section and segment length. The key aspect of a fiber segment is its behaviour when the fiber section becomes nonlinear through yielding of steel fibers and/or cracking and crushing of concrete. While modelling SW members, a beam element is used in the wall (see Figure 3.7) to introduce a moment-resisting connection between the wall and the beam. This is because the used SW elements has no in-plane rotational stiffness at its nodes. The beam elements utilized here are usually refered to as “imbedded beams”. The stiffness parameters of these beams are set to very large values to provide a near-rigid moment connection. The use of this *SW with imbedded beams* modelling approach yields fairly realistic estimates of the responses for slender CWF systems where majority of the torsional loading is resisted by in plane flexural behaviour of well distributed SWs across the building plan.

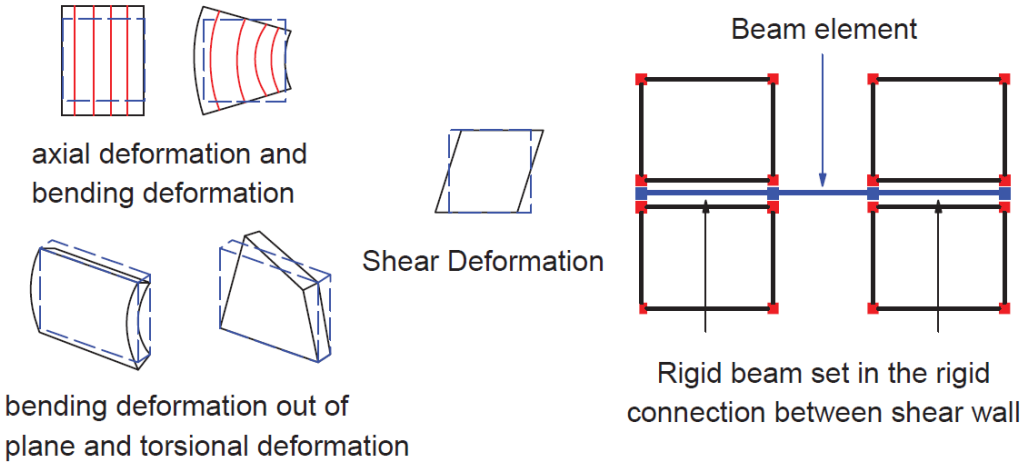

Figure 3.7. Fiber element model for shear walls in Perform 3D

It should also be noted that the out-of-plane bending behaviour of the SW elements are assumed elastic, requiring the assignment of an effective stiffness value for the nonlinear response history analysis. LATBSDC (2014) effective stiffness recommendations are adopted in assigning shear wall sections with out-of-plane elastic stiffness values (See Table 3.3). The following subsections further explain the modelling of shear walls under cyclic loading in model buildings.

3.4.2.1. Inelastic Shear Wall (Fiber) Sections

Geometrical and material properties of each filament (a uniaxial fiber strip) in a fiber SW section are defined manually at their respective locations. This way the property of each fiber is described individually. Therefore, the necessary distinction between the boundary zones and web area of SW cross-sections could be made in a more detailed manner. Figure 3.8 shows how the overall layout of concete and steel fibers are represented in a fiber model.

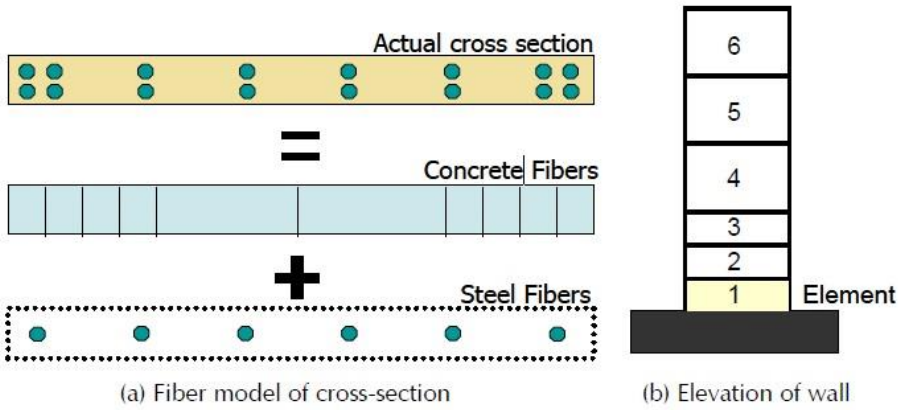

Figure 3.8. Fiber model idealization. (a) Cross-section of the fiber element, (b) Elevation of wall (ATC 72-1, 2010)

3.4.2.2. Flexural/Axial Layer: Constitutive Stress-Strain Relationships

For the stress-strain relationship of concrete in SW sections, the modified Mander (Mander *et al.*, 1988) model is adopted (See Figure 3.9). More complicated stess-strain relationships that would, for example, take into account the gradual crack closure (Chang and Mander, 1994) are disregarded due to the limitations in structural analysis software. However, the modified Mander model can still provide a reasonable stress-strain relationship in the uniaxial fibers of SW sections that would satisfy the overall objectives in this study. It should be noted that only the backbone force-deformation (F-D) curve is defined using the modified Mander model. The cyclic behaviour should also be represented in the fibers to account for the hysteretic loss in strength and/or stiffness.

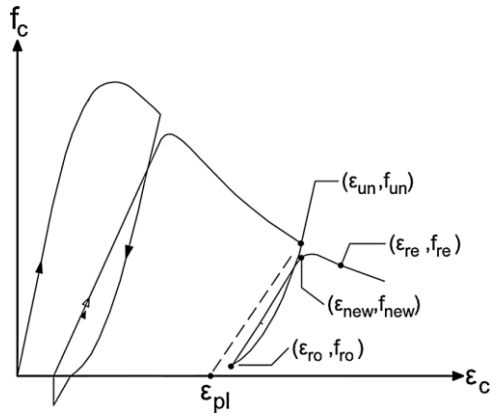

Figure 3.9. Modified Mander model for SWs (Mander et al., 1988)

Cyclic deterioration is defined as the hysteretic reduction in strength, stiffness or both as a function of the energy dissipated in a yielding component (ATC 72-1, 2010). Cyclic degredation of SW fibers is considered by implementing energy degredation factors (EDFs) to the material constitutive force-deformation relationships. These factors modify shape of the initial force-deformation backbone curve of uniaxial fibers depending on the level of deformation. Degredation in stiffness occurs between each cycle of loading as opposed to happening in-cycle. In other words, the initial F-D backbone curve remains an un-changing boundary for cyclic loading. The stiffness is modified by the EDFs after one full loading to simulate deterioration in subsequent cycles. Inherently, strength deterioration is not simulated by using this model. EDFs in this sense, represent the ratio between the area of the degraded hysteresis loop and the area under the backbone curve (non-degraded loop). They are defined for multiple deformation thresholds so that the stiffness degredation is simulated accordingly. Numerical values of the energy degredation factors might depend on the material (concrete or steel fibers) and configuration of the structural component. Evaluation of reinforced concrete and steel structural member databases suggest large variability in EDF values (Haselton and Deierlein, 2007; Lignos and Krawinkler, 2007; Lignos, 2008) but they should still be applied in structural modelling of such systems.

Considering the above arguement, hysteretic backbone stress-strain relationship of concrete is derived from the modified Mander model while cyclic degredation parameters are taken from the study of Görgülü and Taşkın (2014). In their study, Görgülü and Taşkın (2014) conducted a series of experiments on RC infill walls in Turkey and they calibrated the energy degredation factors in view of the test results. The formwork practice and SW

detailings observed in the building inventory are relatively similar to those represented by Görgülü and Taşkın (2014). Therefore, these EDFs are assumed to be consistent for the purposes of this study. Figure 3.10 shows the energy reduction factors adopted for concrete fibers of SW elements in building models. The letters Y, U, L, R and X in Figure 3.10 correspond to specific corner points in the idealized F-D relationships. Assumptions of these points together with the constitutive concrete stress-strain relationships used for different building submodels (1A, 1B, 1C, 2A, 2B and 2C) are presented in Appendix A.

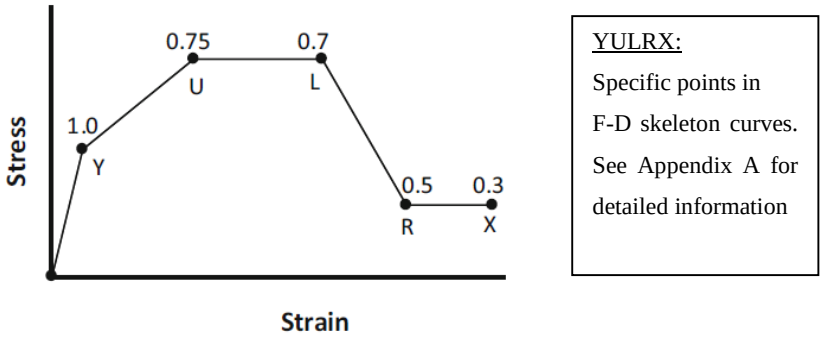

Figure 3.10. Calibrated "Energy Degredation Factors" for concrete (Görgülü and Taşkın, 2014)

A widely used and accepted constitutive model developed by Menegotto and Pinto (Menegotto and Pinto, 1973) is used to define the stress-strain relationship of reinforcement steel. The model is capable of representing the hyteretic behavior of reinforcement steel under cyclic loading with acceptable accuracy. Filippou et *al.* (1983) modified the Menegotto and Pinto model by considering its limitations. The modified model by Filippou *et al.* (1983) introduces Baushinger and pinching effects as well as isotropic strain hardening effect. This model is widely adopted by various researchers in their studies (e.g., Orakcal *et al.*, 2006). Figure 3.11 represents the stress-strain curves of Menegotto and Pinto (1983) and Filippou et *al.* (1983) models. In order to account for the cyclic degredation of the reinforcement steel, calibrated EDFs proposed by Görgülü and Taşkın (2014) are utilized for the commonly used S420 grade steel. EDFs are shown in Figure 3.12. Note that the factors of cyclic deterioration apply to the uniaxial hysteretic force-deformation relationship of reinforcing steel filaments in the SW fiber sections.

S420 grade reinforcement steel is the only steel grade used in the high-rise building models in this thesis. Therefore, only a single constitutive model for steel is defined, and is shown in Figure 3.13. Detailed explanations about the parameters of the idealized stress-strain curve are provided in Appendix A.

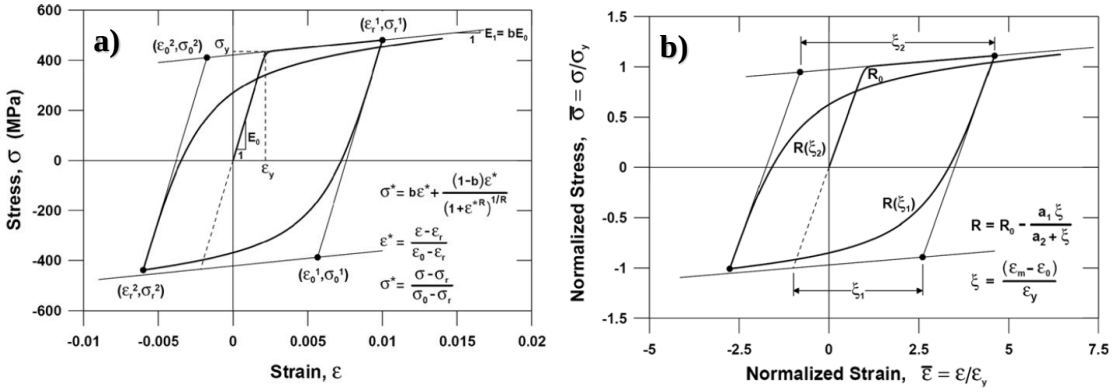

Figure 3.11. a) Menegotto and Pinto (1973) constitutive model for reinforcement steel, b) Modified version of Menegotto and Pinto (1973) by Filippou et al. (1983)

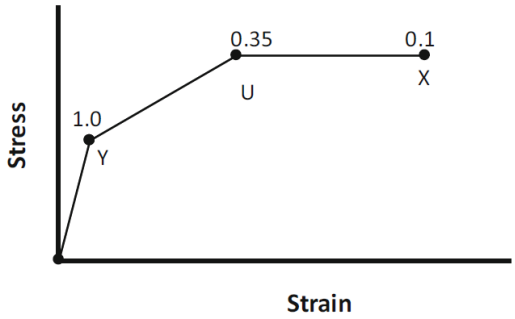

YUX:
Specific points in F-D skeleton curves. See Appendix A for detailed information

Figure 3.12. Calibrated energy degredation factors for steel constitutive model (Görgülü and Taşkın, 2014)

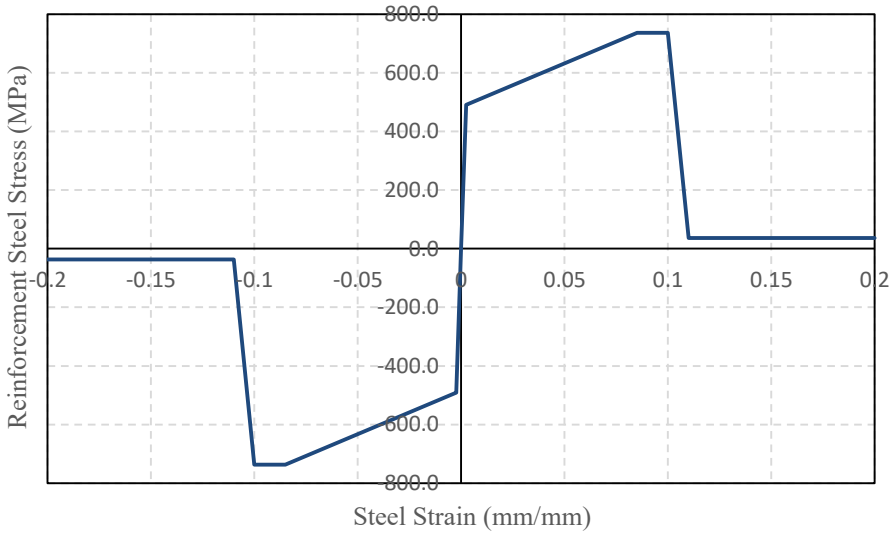

Figure 3.13. Expected stress-strain relationship of steel reinforcement used in all building models

3.4.2.3. Horizontal Layer: Shear Stress-Strain Relationships

Shear and flexural responses are uncoupled in the building models. Therefore a separate shear layer with a separate shear stress-strain relationship is introduced as a transverse spring in SW elements. Currently, shear stress-strain relationships are generally considered as linear in nonlinear structural analysis practice. However the actual shear stress-strain behaviour is not linear because of cracking of concrete. Thus, in this study, a trilinear curve is used to introduce shear force-deformation relationship where cracking of concrete is simulated Figure 3.14 shows two alternatives for defining shear F-D relationship in SWs recommended in ATC 72-1 (2010).

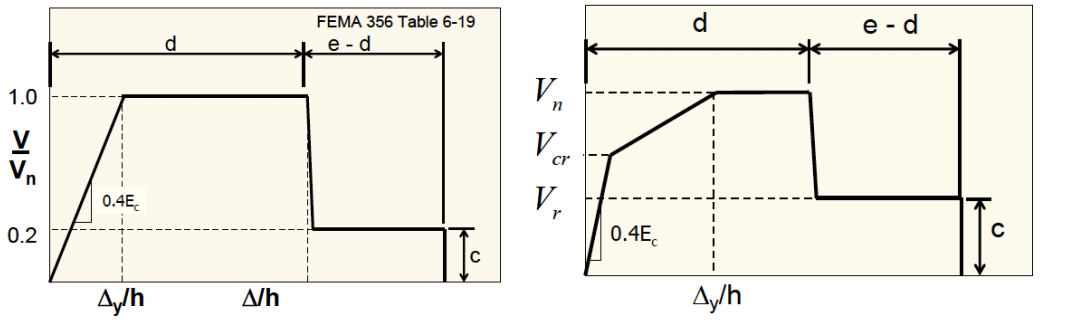

Figure 3.14. Shear force-deformation curves taken from PEER/ATC 72-1 (2010)

In Figure 3.14, V/V_n is the shear force on a SW section normalized to its ultimate shear force capacity V_n, V_{cr} is cracking strength, V_r denotes residual strength and Δ_y is yield deformation and h is height of the wall section.

In the last decade, significant developments have been made in understanding and analytically modelling of shear behavior for RC shear walls (e.g., Orakcal *et al.*, 2004; Orakcal *et al.*, 2006; Wallace, 2007; Kolozvari *et al.*, 2012; Tran and Wallace, 2012). As for the code requirements, ATC 72-1 (2010) presents a comprehensive guidance for analytical modelling of structural walls governed by shear behaviour. In this thesis, a set of publications and studies are investigated (e.g., Wallace, 2007; ATC 72-1, 2010; Gogus, 2010) to define the stress-strain relationship parameters for RC shear walls. The basis of the force-deformation parameters adopted in this study is determined from the study of Wallace (2007). These parameters are presented in Equations 3.2 and 3.3.

$$V_{cr} = 4\sqrt{f_c'}\left[1 + \frac{P_u/A_g f_c'}{4\sqrt{f_c'}}\right]^{1/2} < 0.6V_n \quad \gamma_{cr} = \frac{V_{cr}}{0.4E_c} \tag{3.2}$$

$$V_y = V_n = A_{cv}\left(\alpha_c\sqrt{f_c'} + \rho_n f_y\right) \quad \gamma_y = 0.004 \tag{3.3}$$

Here, P_u is axial load on the member, f_c' is the compressive strength of concrete, E_c is elastic modulus of concrete, A_{cv} is cross-sectional area of the wall, ρ_n is transverse reinforcement ratio in web of the wall section, $\alpha_c = 2.0$ when $h_w/l_w \geq 2.0$. Although it is not introduced in above expressions, Wallace (2007) acknowledges the increase of shear strength depending on the axial load level on shear wall sections. Several studies reported that the ultimate shear strength of walls is noticeably sensitive to their axial load levels ($P_u / A_g f_c'$) (Orakçal et *al.*, 2006; Wallace 2007; Elywood et *al*, 2007; Orakcal et *al.*, 2009). The experiments in these studies indicated that structural walls behave much stronger and stiffer under increasing axial load levels. Figure 3.15 illustrates the differences in RC shear wall response corresponding to changing axial load levels.

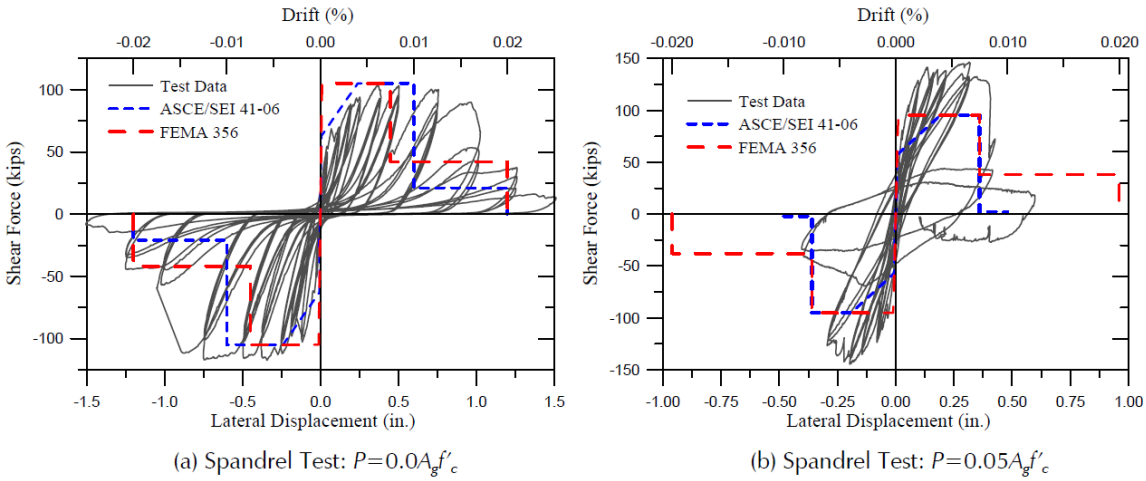

Figure 3.15. Shear force-deformation results of lightly reinforced wall piers for different axial load levels (Elwood et *al*., 2007)

Consequently, the following features are adopted for the analytical modelling of shear force-deformation relationship in RC shear wall sections:

1) A trilinear shear stress-strain relationship is defined for RC shear wall elements in all models to account for cracking of concrete under shear forces. The strength and strain parameters associated with cracking of concrete are calculated from Equation 3.2 and 3.3(Wallace, 2007).
2) An increased ultimate shear strength is used to take into consideration the axial load effects. The ultimate shear strength given in Equations 3.3 is increased by a factor of 1.5 in view of the recommendations of the above-mentioned studies.

For detailed explanations about analytical shear stress-strain relationship parameters and assumptions, the reader is referred to Appendix A.

3.4.3. Additional Modelling Assumptions of Shear Walls

3.4.3.1. Meshing of Shear Walls

The sizes of meshes in shear walls may significantly affect the structural response. The mesh sizes are particularly important for shear wall sections within the plastic hinge region in order to capture the local response accurately (Powell, 2007). It was also reported by various researchers that the global and local responses are sensitive to the dimensions of

shear wall fiber sections used in the analytical modelling of structures (Orakcal *et al.*, 2006; Salas, 2008). Flexural behaviour is represented better when the height to width ratio of shear wall sections are closer to unity (Powell, 2007) (see Figure 3.16). In view of this recommendation for meshing of shear walls, member sections are divided into three sub meshes in the first two stories to better capture the local strain profiles for seismic performance evaluations as presented in Chapter 5.

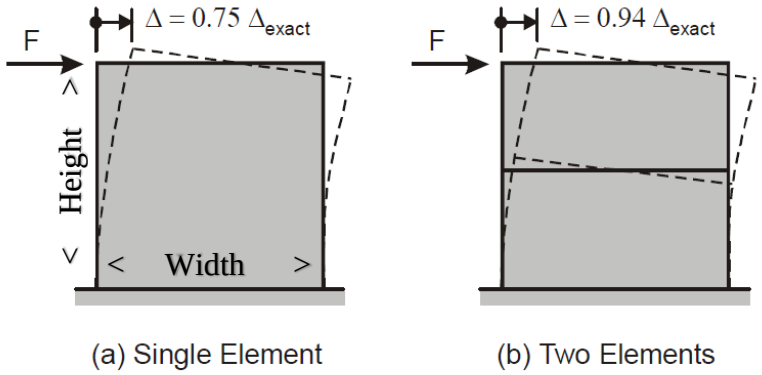

Figure 3.16. Importance of height-to-width ratio of meshes while modeling shear walls. Height-to-width ratios closer to unity should be preferred (Powell, 2007).

3.4.3.2. Deformation Capacities and Strength Loss

Although all materials and structural components have their analytically defined "ultimate" deformation capacities, force-deformation relationships that are used in the models are extended towards extreme displacements with very small residual strength values to retain the ability of gauging the local and global responses during severe shakings (i.e., earthquake ground motions with a return period of 10000 years). A sudden strength loss on force-deformation relationship may cause numerical instabilities in the anaylsis. Therefore, strength loss is introduced in a gradual manner in the sub elements of the analytical models. Figure 3.17 illustrates the recommendations for introducing strength loss with a less steeper degrading segment (dashed line). This modelling approach is adopted for all structural components whose force-deformation relationships are nonlinear.

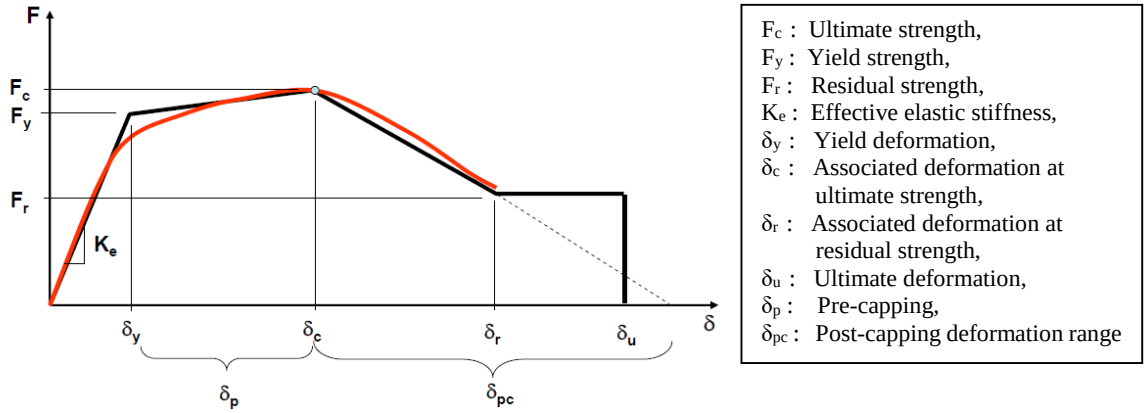

Figure 3.17. Proposed modelling approach for strength loss (ATC 72-1, 2010). The generic force and deformation quantities are denoted by *F* and *δ*.

3.4.3.3. Geometric Approximations

The cover concrete currounding concrete layers is not modelled for its complicated modelling nature. This lack of cover concrete (unconfined concrete layer) in buildings does not have any major impact on either local or global response parameters (PEER, TBI Task 12, 2011). Although the cover concrete is ignored in prediction of responses, weight of the cover concrete is considered in computation of the self weight of shear walls. Lastly, a geometrical approximation is being made in the analytical building models that the wall elements overlap at junction points of shear wall elements (see Figure 3.18). Analytical studies demonstrated that this simplification does not lead to a major impact on structural response parameters (Powell, 2007; PEER Task 12, 2011; van der Linde, 2015).

Figure 3.18. Geometrical approximation at the shear wall intersection points

3.5. Modelling of Frame Elements

Beam and column members of statistical high-rise building models are defined as inelastic components using lumped plasticity (point hinge) idealization, in which inelasticity

is assumed to concentrate at the member ends (Figure 3.19). Force-deformation relationship remain elastic before yielding in the hinges. A nonlinear force-deformation backbone curve is defined to describe the post-yield hysteretic behaviour of these end hinges. The main drawback of the lumped plasticity approach is its inability to consider the gradual stiffness deterioration of members or to account for the instantaneous interaction between axial force and bending moment during multi-step nonlinear response history analyses. However, plastic hinges are easy to implement and provide reasonably accurate estimates of average local responses while saving significant computer run times (Wallace, 2012).

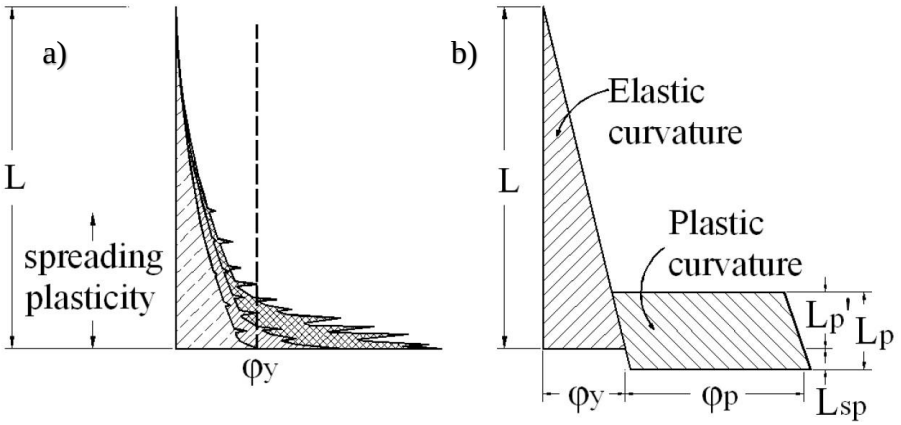

Figure 3.19. Lumped plasticity approach: a) actual curvature distribution, b) approximated curvature distribution (Fedak, 2012)

3.5.1. Beam Elements

Moment-curvature hinges are assigned at the ends of beam members in the analytical models. Axial load levels are taken as zero when sectional analyses are carried out to derive backbone curves of end moment versus curvature. Pre-yield (initial) stiffness parameters are adjusted to account for cracking of concrete in lieu of the proposed effective rigidity values presented in Table 3.3. The force-deformation relationships used in modelling of frame members (right panel in Figure 3.20) follow a certain pattern where each point on the curve is denoted by a certain letter (i.e., Y, U, L, R and X). In this study, component F-D backbone curves are defined to impose artificially extended ultimate deformation capacities with minimal residual strength values after the actual ultimate deformation is reached. The actual ultimate displacement capacity is denoted by the letter ‘L’ in Figure 3.20. This way the response history analysis continues even after a beam member has reached its ultimate

deformation capacity. This is an important modelling approach (already discussed in Section 3.4.3.2) and it is especially useful for collapse fragility assessment as it will be discussed in the following chapters. Continuation of structural analysis even after members reach their ultimate capacities leads to a better monitoring of structural behavior where structure features gradual strength and stiffness loss. Besides, termination of the structural analysis upon reaching the deformation capacity in a single component of a highly redundant building would not lead to its proper evaluation because the ground motion would not be fully exerted to the building model.

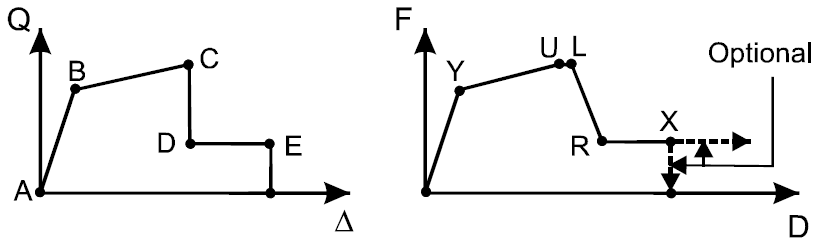

(a) FEMA-356 relationship (b) The relationship adopted in this study

Figure 3.20. Force-deformation relationship of frame components with strength loss (Powell, 2007)

While modelling the beam members, studies on the building inventory indicated that majority of link beams in the Turkish design practice are designed with the procedure adopted for the design of gravity beams. This observation is especially valid for buildings with less than 30 stories. As a consequence of such a design methodology, none of the beams can attain their ultimate shear strength values due to their confinement detailings. Hence, for beam elements, assigning of shear hinges deemed to be not necessary. Shear force gages are placed instead at mid-sections to monitor demand-over-capacity (D/C) ratios. Detailed force-deformation relationships obtained from section analyses for the model buildings are given in Appendix A.

3.5.2. Column Elements

Gravity columns are modelled as frame elements using lumped plasticity approach. Plastic hinges are placed at member ends where the sections are assumed to undergo plastic

deformations. Since the collapse mechanisms of column elements in all submodels are governed by flexural behaviour, shear hinges are not assigned to these elements. The demand/capacity ratios are measured to assess whether the shear capacity is reached for columns. Effective stiffness values are used to determine the pre-yield bending rigidity of members. Section analyses are carried out to derive axial load-bending moment (P-M-M) interaction curves that determine the yield surface for column elements. Note that different regions of the P-M-M interaction surface translate into different modes of yielding or failure (see Figure 3.21). Moment-curvature at the hinge ends are calculated accordingly depending which point on the P-M-M curve is attained. This way the effect of axial load on moment capacity and curvature ductility are considered. Appendix A presents force-deformation parameters for column members for each building submodel.

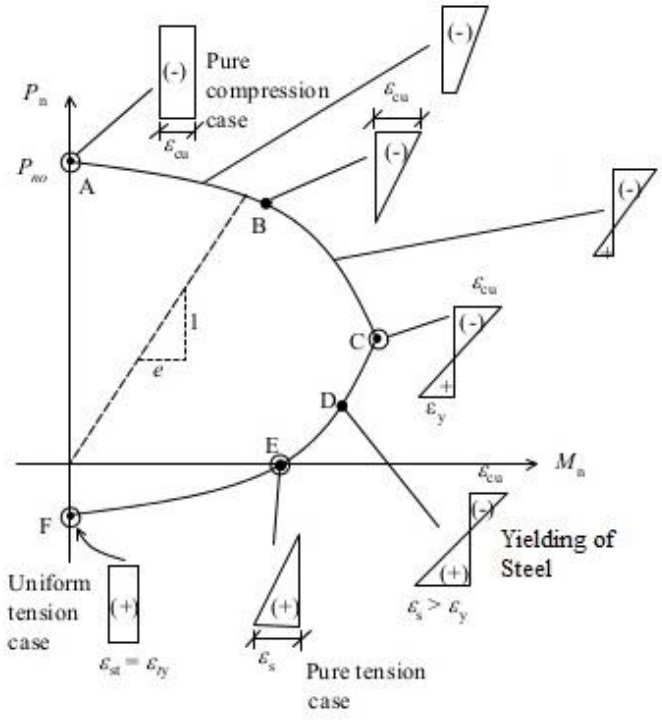

Figure 3.21. Typical axial load-bending moment interaction surface

3.6. Other Modelling Assumptions

There are other assumptions and simplifications for the analytical models by considering the potential in the computational capabilities of the computers in hand. These simplifications are deemed to be practical in exchange of little to no substantial effects on

the structural responses. This section presents other important structural modelling decisions and assumptions that need to be explained for a better vision on the structural analysis.

3.6.1. No-Slab Structural Models

None of the structural models include slabs as a force resisting component. Only their self weights are considered and included in the gravity load cases. Excluding slabs from analytical building models have several implications in terms of both local and global structural response quantities. Normally, slabs share some of the gravity loads with the beam members. They also introduce additional constraints onto the adjacent structural members which they are framing into. To this end, slabs essentially act as outriggers to increase overturning moments, shear demands and axial loads on vertical elements of structural systems. Hence, excluding slabs in structral models ultimately results in lower demands than the expected values. Experimental data studied by Schotanus and Maffei (2008) has shown that a “wall-only model” might estimate the system overturning moments and shear forces even as half of the actual response (Figure 3.22). Contraversially, it is also known that no-slab structural models better capture the inter-story drift engineering demand parameters (EDPs). This case is presented in Figure 3.23. Although models with or without slabs have their drawbacks, no-slab building models are preferred because:

1) Frame members (beam and colunmns) act as outriggers to resist moment rotations transfering a big portion of the actual outrigger forces to the shear walls. For this reason, the relative contribution of slabs to the shear and overturning moment demands in SWs become negligible.
2) Excluding slabs from the structural models saves a considerable computer run time.

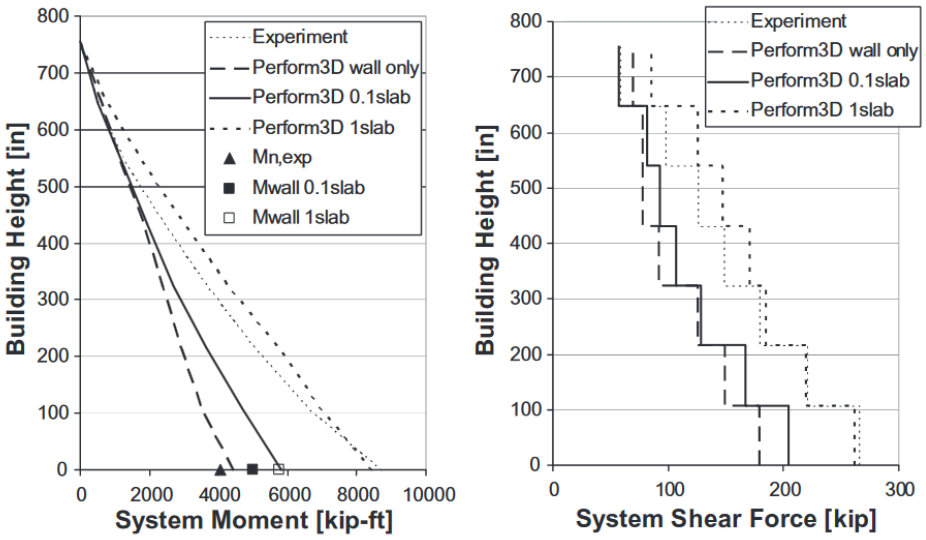

Figure 3.22. Comparison of peak moment (a) and peak story shear (b) envelopes for different modelling approaches under the same excitation (Schotanus and Maffei, 2008)

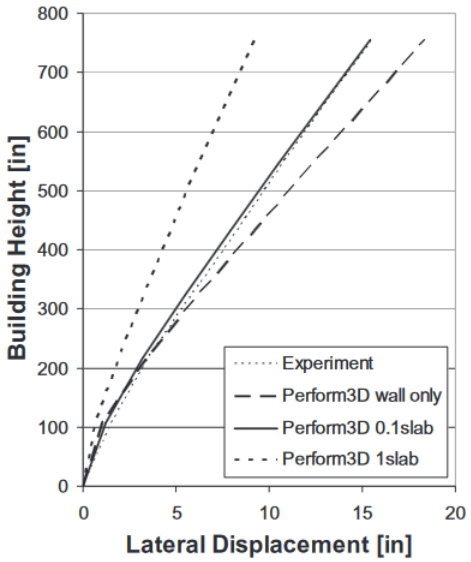

Figure 3.23. Comparison of peak displacement envelopes for the same excitation (Schotanus and Maffei, 2008)

3.6.2. Rigid Diaphram Assumption

Rigid diaphragm in a system distributes lateral forces to the vertical load resisting elements in direct proportion to their relative rigidities. It is based on the assumption that the diaphragm does not undergo deformations on itself and will cause each vertical element to

deflect the same amount (Figure 3.24). A flexible diaphragm, on the other hand, distributes the loads according to the tributary areas. Flexible diaphragm can be inevitable depending on the slab configuration in the structural system.

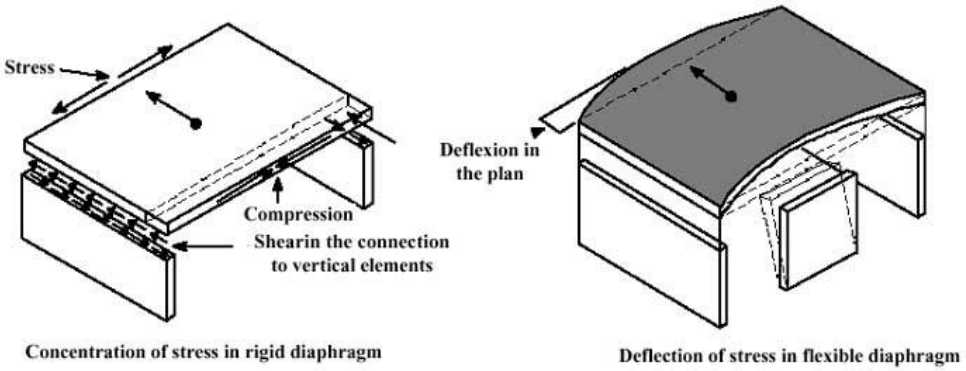

Figure 3.24. Difference in behaviour between a flexible and a rigid diaphram

A rigid diaphragm assumption saves computer run time significantly at the cost of disregarding deficiencies in slab systems, such as big openings due to poor design practices that might affect the accuracy of response parameters. The statistical survey on the high-rise building inventory indicated that slabs are usually continuous except within the elevator shafts, which does not have any significant implication in terms of slab continuity. To this end, accepting the practical time saving efficiency of such assumption, simplifications were made by assigning rigid diaphragm constraints each story for the building models. This way a significant computer run time is saved due to 960 nonlinear response history analyses performed on highly complex 3D models.

3.7. Viscous Damping

Viscous damping is a mechanical property in an elastic oscillatory system that absorbs the dynamic input energy to reduce the vibration amplitude. In nonlinear dynamic analysis of structures, viscous damping is usually assumed to account for elastic energy dissipation. Although the actual damping mechanism of a building system is not viscous, it is widely used because it is easy to model and integrate with the dynamic solution. As viscous damping only accounts for elastic energy dissipation, energy absorbtion beyond the elastic limits is done through hysteretic excusions of structural components. In general, two types of viscous damping are available: modal damping and Rayleigh damping. Elastic

vissous damping can be either defined as modal or Rayleigh damping in the dynamic response history analyses trat are discussed further in the following sections.

3.7.1. Modal Damping

Calculation of the damping matrix, [*C*], using modal properties (mode shapes and periods) can be done using Equation 3.4.

$$[C] = [\Phi^T]^{-1}[c_i][\Phi]^{-1} \tag{3.4}$$

Here, [Φ] is the matrix of eigenvectors and [c_i] is a diagonal matrix constituting damping coefficients for each mode. The subscripts *T* and *-1* refer to transpose and inverse matrix operations. The above equation can be written as given by Equation 3.5 following Chopra (2007).

$$[C] = [M]\left(\sum_{n=1}^{N} \frac{4\pi\xi_n}{T_n M_n}\phi_n\phi_n^T\right)[M] \tag{3.5}$$

In Equation 3.5 [*M*] is the diagonal mass matrix, T_n , ξ_n and Φ_n are the n^{th} mode period, critical damping and eigenvector, M_n $(= \Phi_n^T[M]\Phi_n)$ is the generalized mass for the n^{th} mode, and *N* is the number of modes included in the computations. Physical interpretation of modal damping suggests, that at any instant of time each mode is independently damped and vibrates independently with its own frequency. For all practical purposes, this can also be implemented to nonlinear response history analysis because each step in nonlinear analysis is assumed to be a linear 'event' at which the structural stiffness terms are recalculated instantaneously. Therefore, use of modal damping can be a reasonable alternative for nonlinear response history analysis. A modal damping of 2.5% of critical is assumed for the model buildings that is in line with the recommendations of ACI 72-1 (2011) and TBI (2010).

3.7.2. Rayleigh Damping

Rayleigh damping assumes that the structural damping matrix, [C] is proportional to mass matrix, $[M]$ and the stiffness matrix, $[K]$ of the structure with the proportionality constants of α_M and α_K as shown in Equation 3.6.

$$[C] = \alpha_M[M] + \alpha_K[K] \tag{3.6}$$

Here, damping ratio for the modes are calculated as a function of proportionality constants

$$\xi_n = \frac{\alpha_M T_n}{4\pi} + \frac{\alpha_K \pi}{T_n} \tag{3.7}$$

In the above expression, ξ_n is fraction of critical damping for the n^{th} mode with period T_n. The selection of reference modal periods (T_A and T_B) should account for the most significant modes dominating the overall structural behaviour. In a way, the expert prejudges the controlling modes and corresponding modal dampings in constructing the damping matrix in Rayleigh damping. As a rule of thumb, T_A and T_B is selected within the period range of 0.2 T_1 and T_1 for most cases where T_1 is the first mode period of the structure.

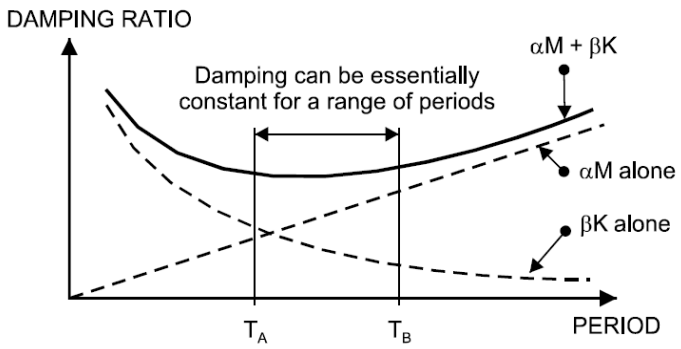

Figure 3.25. Variation of the damping ratio as a function of period (Powell, 2007)

3.7.3. Viscous Damping in Nonlinear Response History Analyses

A combination of modal and Rayleigh damping is used to define the viscous damping in model buildings. ATC 72-1 (2010) suggests that modal damping assumption is appropriate for damping the higher elastic modes. ATC 72-1 (2010) and TBI (2010) suggests

a viscous damping range of 1% to 5% that is based on the laboratory test results. In essence, these guidelines recommend the effective viscous damping for tall RC buildings to not exceed 2.5% of critical for the primary modes. A number of researchers, such as Hall (2005) and Charney (2006) has shown that, as structure components soften under seismic excitation, the damping forces occur across the components can result in force unbalances. This is a common problem when using stiffness damping because the damping forces do not generally reduce in proportion to the structural softening. It is also known that the mass-proportional damping terms of Rayleigh damping often lead to unrealistically large forces in buildings with spesifically large rigid body motion (Hall, 2005). The results of these studies suggest:

1) Stiffness-proportional damping tends to overdamp higher mode effects;
2) Mass-proportional damping underdamps higher modes;
3) Modal damping facilitates best control of damping for elastic and inelastic (elongated) periods.

For the above reasons, Rayleigh damping with the corner periods 0.2 T_1 and 1.5 T_1 is implemented in addition to modal damping for the building models. These corner periods represent the 'higher mode period' and 'elongated period' of buildings. A damping ratio of 0.25% of critical is specified for Rayleigh damping to prevent numerical problems such as force imbalances that may occur as certain elements soften due to nonlinear behaviour (ATC 72-1, 2010). The damping assumptions are summarized in Table 3.4.

Table 3.4. Damping assumptions for the nonlinear dynamic analyses

Damping Type	**Description**
Modal Damping	Damping ratio: 2.5% of critical for all modes
Rayleigh Damping	$T_{higher} = 0.2\ T_1$, damping ratio=0.25% $T_{elongated} = 1.5\ T_1$, damping ratio=0.25%

4. DEFINITION OF SEISMIC HAZARD AND GROUND MOTIONS FOR NONLINEAR RESPONSE HISTORY ANALYSIS

4.1. Probabilistic Seismic Hazard Assessment for Target Response Spectra

The aim of probabilistic seismic hazard assessment (PSHA) is to quantify uncertainties associated with the location, size and resulting ground motion intensity of future earthquakes and combine them to estimate the distribution of ground-motion intensity measures of interest at a specific site. Earthquake engineering practice is interested with the development of site specific ground motions for use in seismic demand analyses. There are four basic ingredients in PSHA: (1) seismic source characterization; (2) earthquake occurrence characteristics for each source; (3) ground motion prediction model; (4) quantification of the seismic hazard. Information obtained in the first three steps of PSHA is numerically integrated using a probabilistic model to attain probability of exceedence, or mean annual exceedence rates of various ground motion parameters for a given site. Kartal district (40.9°N ve 29.2°E) in Istanbul is selected as the reference site for PSHA. It is an area of high seismicity because of its location near the North Anatolian Fault (NAF) and its subsidiary branching segments across Marmara Region.

A recent study in Kandilli Observatory and Earthquake Research Institute (KOERI) forms the basis for PSHA and deaggregation calculations for the selected reference site in this study. Seismic sources considered for the PSHA are presented in Figure 4.1 as a combination of fault sources and background seismicity. The ground motion prediction equation (GMPE) of Campbell and Bozorgnia (2008) is used to derive the uniform hazard spectrum for eight return periods (inverse of mean annual exceedence rate). Campbell and Bozorgnia (2008) GMPE predicts ground motion intensity measures as orientation-independent geometric mean of the horizontal components (GMRotI50) (Boore et *al.*, 2006). Spectral accelerations and spectral displacements for eight return periods are shown in Figure 4.2. These return periods are: 43, 72, 150, 475, 1500, 2475, 5000 and 10000 years. The reference site is represented by a soil type having a shear wave velocity, V_{s30} = 500 m/s, which falls under soil type C category according to NEHRP provisions (FEMA, 2015). This

assumption is in agreement with the statistical survey carried out for the building inventory in this study.

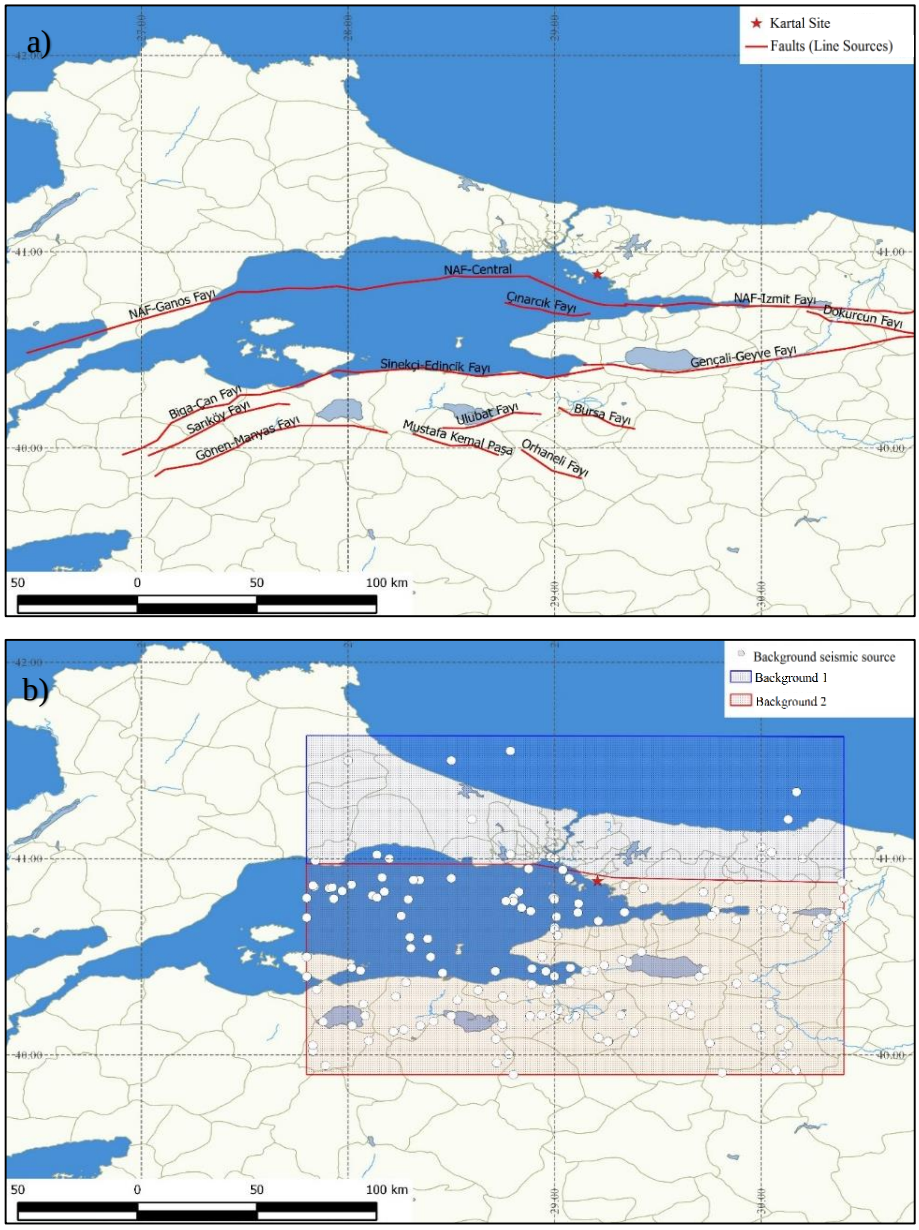

Figure 4.1. Seismic sources considered in PSHA: a) fault sources; b) background seismicity

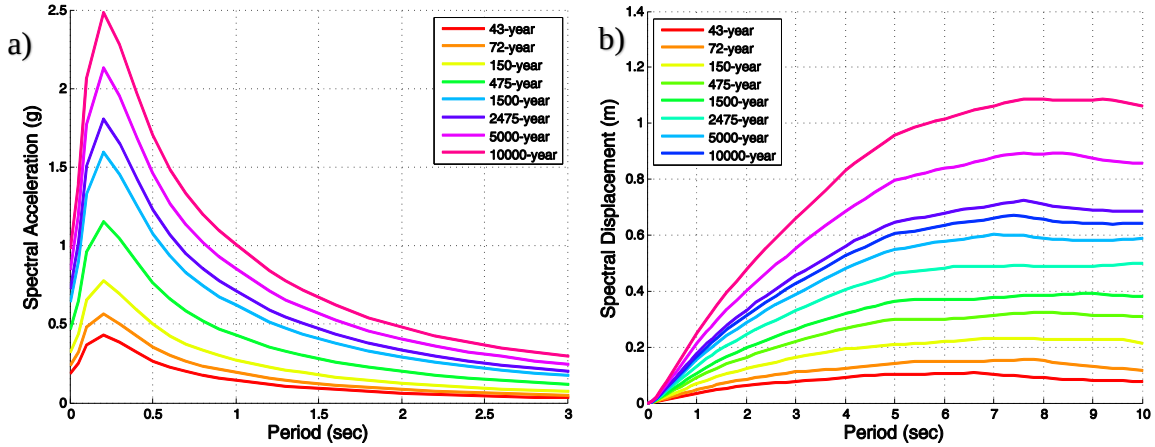

Figure 4.2. Uniform hazard spectral ordinates calculated using the Campbell and Bozorgnia (2008) GMPE at different return periods: (a) spectral acceleration; (b) spectral displacement

4.2. Conditional Spectrum for Ground Motion Selecting and Scaling

4.2.1. General

Fairly realistic distibutions of structural response parameters that are generally called as engineering demand parameters (EDPs) (e.g., maximum interstory drift ratios, peak floor accelerations) can be obtained from nonlinear response history analysis (NRHA) under earthquake ground motios. Ground motions used in NRHA are intended to represent a target seismic hazard level. To this end, ground motion record selection and scaling becomes important for a proper representation of hazard levels as well as to obtain reliable distributions of EDPs. Several different methods are adopted by various researchers in the past for the selection of ground motions for NRHA (Ji et *al.*, 2007; Jieng et *al*., 2012). Considering the current state of practice, Haselton et *al*. (2012) provide the most relevant and transparent methodologies for selection and scaling of accelerograms for performance-based seismic design. In this study, Conditional Spectrum (CS) that is defined in Lin et *al.* (2013) is used for describing the target hazard levels for scaling of accelerograms.

Conditional mean spectrum (CMS; Baker, 2011) and conditional spectrum (CS; Lin et *al.*, 2013) consider the cross correlation between the conditioning period and the other spectral periods. Therefore the target spectrum is spesifically tailored by considering the conditioning period. The conditioning period is generally considered as the fundamental

periof of the structural system while the scaling (ASCE, 2010; BSSC, 2015). The most contributing earthquake scenario at conditioning period for the target hazard level (obtained from deaggregation analysis: Bazzurro and Cornell 1999; McGuire 1995) and the cross correlation between the spectral orditanes at conditioning period and the rest of the periods are sufficient for computing CS and CMS. The major difference between CS and CMS is that the former diregards the inherent aleatory variability scaled ground motions. In other words, conditional spectrum includes conditional mean spectrum and the aleatory variability of ground motions about CMS. Figure 4.3a shows the concept of conditional mean spectrum for the conditioning period at T*=1.0s. Deaggregation analysis of UHS at T=1.0s yields a magnitude of M_w 7 and source-to-site distance of 12 km as the most contributing scenario (Figure 4.3b) for the 2475-year UHS (Figure 4.3a). The median ground motion for the most contributing earthquake scenario and its difference in terms of epsilon (see Equation 4.1) as well as the CMS is given in Figure 4.3a. The following section describes the computation of conditional spectrum that considers CMS as well.

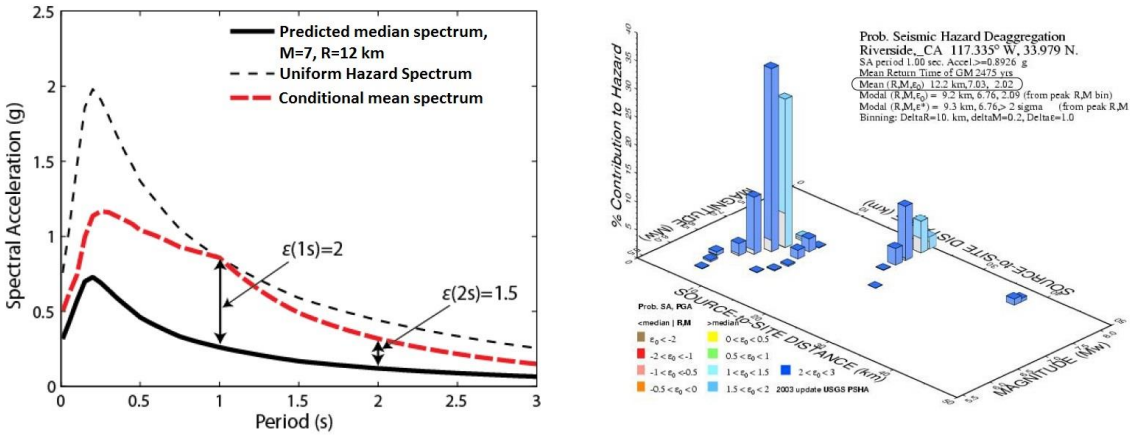

Figure 4.3. Seismic hazard data for an example site presented in Baker (2011). (a) Conditional mean spectrum for the example site. (b) Deaggregation information for Sa(1s) exceed with 2% probability in 50 years (computed using USGS interactive deaggregation tools)

4.2.2. Basic Computation of the Conditional Spectrum

The basic steps of computation of the CS involve: (1) input earthquake parameters (e.g., magnitude and distance information) similar to what is required by GMPEs; (2) definition of a conditioning period (T^*); (3) a ground motion predictive model to predict logarithmic mean and standart deviation of spectral acceleration for a specified hazard level; (4) a cross correlation model between spectral acceleration ordinates (e.g., Baker and Jayaram 2008) for a period range of interest (usually $0.2T^*$ and $1.5T^*$ where T^* is the conditioning period that is generally taken as the fundamental period of the structure for scaling). The computation steps are summarized in the following paragraphs (Lin et *al*., 2013b; Lin and Baker, 2015):

1. Given a specified return period compute the target UHS from PSHA. For the conditioning period, T*, determine the mean earthquake magnitude (M), distance (R) and other relevant parameters (e.g., site conditions, rupture mechanism: θ) of the most contributing earthquake scenario from deaggregation calculations.
2. Determine logarithmic mean, $\mu_{lnSa}(M, R, \theta)$ and standart deviation, $\sigma_{lnSa}(M, \theta)$ of spectral accelerations across a pre-determined period range using GMPE (e.g., Abrahamson et *al.*, 2008) employed in PSHA.
3. Calculate the epsilon parameter, $\varepsilon(T^*)$ at T^* from Equation 4.1 to determine the number of standart deviations between $\mu_{lnSa}(M, R, \theta, T^*)$ and $lnSa(T^*)$ obtained from UHS.

$$\epsilon(T^*) = \frac{lnSa(T^*) - \mu_{lnSa}(M, R, \theta, T^*)}{\sigma_{lnSa}(M, \theta)} \tag{4.1}$$

4. Compute the target conditional mean spectrum $\mu_{lnSa(T_i)|lnSa(T^*)}$ (Equation 4.2) by using a correlation model which determines the correlation coefficient between the spectral ordinates at T_i and T^* (i.e., $\rho(T_i , T^*)$ as well as $\epsilon(T^*)$. The development of correlation coefficient models is out of scope of this thesis but they simply establish the correlation between the epsilons of ground motions at different periods.

$$\mu_{lnSa(T_i)|lnSa(T^*)} = \mu_{lnSa}(M, R, \theta, T_i) + \rho(T_i, T^*)\epsilon(T^*)\sigma_{lnSa}(M, \theta, T_i) \quad (4.2)$$

Here, the $\mu_{lnSa(T_i)|lnSa(T^*)}$ indicates the mean values of lnSa(T_i) conditioned on lnSa(T*).

5. Calculate conditional standart deviation, $\sigma_{lnSa(T_i)|lnSa(T^*)}$ of logarithmic Sa(T_i), conditioned on lnSa(T*) by Equation 4.3.

$$\sigma_{lnSa(T_i)\,|\,lnSa(T^*)} = \sigma_{lnSa}(M, \theta, T_i)\sqrt{1 - \rho^2(T_i, T^*)} \quad (4.3)$$

When the conditional standart deviation is combined with the conditional mean spectral values, a full distribution of logarithmic Sa values by considering the ground motion aleatory variability at all periods is obtained. The proposed terminology for this distribution of mean and +/- one or two conditional standart deviations around the mean is 'Conditional Spectrum' (Baker and Lin, 2013).

4.3. Details of CS-Based Ground Motion Selection

Eight different return periods (reciprocal of mean annual exceedence rates) as described in Section 4.1 are used to assess the structural responses of model buildings. For each return period, the conditional spectrum is computed by considering the average of fundamental translational vibration periods (T^*) along buildings' principal directions. In other words, T^* is taken as $0.5(T_{1x}+T_{1y})$ where T_{1x} and T_{1y} represent the fundamental translational vibration periods along the orthogonal directions X and Y, respectively. Information of T^*, T_{1x} and T_{1y} are given in Table B.1 to Table B.6 in Appendix B. Consideration of average of fundamental periods along two principal directions as T^* for assessing building performance is proposed by Kohrangi et *al*. (2015). These researchers indicate that average fundamental period of principal building axes would yield more reliable building response in 3D nonlinear response history analysis.

CS for each building model is developed by deaggregating the hazard results at T* for eight return periods. The chosen return periods yield fairly seperated Sa(T^*) that, in a way, yields more consistent EDP distributions with increasing Sa(T*) (Kohrangi et *al*., 2015). Deaggregation is only done T^* values that belong to model buildings 1B, 1C, 2B and

2C. Deaggregation results of buildings 1B and 2B are used for building models 1A and 2A, respectively due to the similarity in corresponding T* values (see modal properties of the model buildings in Chapter 5.2). Thus, a total of 4x8 sets of CS are produced for record selection and scaling to study the structural behaviour of six model buildings. As the uniform hazard spectrum is developed from Campbell and Bozorgnia (2008) GMPE, the horizontal component definition of CS is GMRotI50 (or simply geometric mean).

Table 4.1 to Table 4.4 show the deaggregation results of return periods of interest. Note that mean magnitudes are almost identical and range between M_w 7.1 and M_w 7.3 for the considered return periods. The same observation is also valid for mean source-to-site distance parameters as their variation is between 16 km and 15 km for the entire return periods. These observations indicate that the hazard for Istanbul is dominated by a magnitude of M_w 7.3. The mean source-to-site distance range suggests that the Central Marmara fault segment is the prominent fault source in all cases. These observations are in agreement with the previous hazard studies conducted for Istanbul (e.g., Erdik et *al.*, 2004).

Table 4.1. Summary of mean M, R and ε values obtained from deaggregation at T*=1.46 sec (Building 1C)

Return Period (yrs)	Sa(T*)	Mean Magnitude	Mean Distance (km)	Mean Epsilon
43	0.102	7.13	18.76	-0.18
72	0.138	7.16	17.89	0.23
150	0.189	7.19	17.24	0.66
475	0.290	7.22	16.65	1.25
1500	0.410	7.25	16.34	1.75
2475	0.470	7.26	16.24	1.95
5000	0.558	7.27	16.14	2.20
10000	0.655	7.28	16.06	2.43

Table 4.2. Summary of mean M, R and ε values obtained from deaggregation at T*=1.64 sec (Building 1B)

Return Period (yrs)	Sa(T*)	Mean Magnitude	Mean Distance (km)	Mean Epsilon
43	0.090	7.13	18.77	-0.19
72	0.119	7.16	17.95	0.18
150	0.167	7.19	17.24	0.64
475	0.257	7.23	16.65	1.24
1500	0.365	7.26	16.34	1.74
2475	0.418	7.27	16.24	1.93
5000	0.499	7.28	16.14	2.19
10000	0.59	7.29	16.06	2.42

Table 4.3. Summary of mean M, R and ε values obtained from deaggregation at T*=2.0 sec (Building 2C)

Return Period (yrs)	Sa(T*)	Mean Magnitude	Mean Distance (km)	Mean Epsilon
43	0.08	7.14	18.79	-0.22
72	0.10	7.17	17.97	0.16
150	0.14	7.20	17.25	0.62
475	0.21	7.24	16.66	1.22
1500	0.30	7.27	16.34	1.72
2475	0.34	7.28	16.25	1.91
5000	0.41	7.29	16.14	2.17
10000	0.48	7.30	16.06	2.41

Table 4.4. Summary of mean M, R and ε values obtained from deaggregation at T*=2.50 sec (Building 2B)

Return Period (yrs)	Sa(T*)	Mean Magnitude	Mean Distance (km)	Mean Epsilon
43	0.06	7.14	18.81	-0.24
72	0.07	7.17	17.97	0.14
150	0.11	7.20	17.25	0.60
475	0.16	7.24	16.66	1.21
1500	0.23	7.27	16.34	1.71
2475	0.27	7.28	16.25	1.90

Table 4.4. (Continued)

Return Period (yrs)	Sa(T*)	Mean Magnitude	Mean Distance (km)	Mean Epsilon
5000	0.32	7.29	16.14	2.16
10000	0.38	7.30	16.06	2.40

The following record selection criteria are set based on the overall deaggregation results and considered soil condition at the site of interest,

- $300 \text{ m/s} \leq V_{s30} \leq 690 \text{ m/s}$
- $6.0 \leq M_w \leq 7.9$
- $15 \text{ km} \leq R_{rup} \leq 80 \text{ km}$

The chosen V_{s30} range covers V_{s30}=500 m/s that is chosen specific to this study (guided by the statistical studies on the building inventory. The magnitude and distance ranges are also consistent with the mean magnitudes and distances obtained from deaggregation results. None of the selected records contain pulse-like waveforms that are typical of recordings under the influence of directivity effects. This is because near-fault directivity effects are prominent for rupture distances less than 15 km (Silva, 1997). Mean distances computed from deaggregation are larger than 15 km for the considered cases. The ground motions are downloaded from PEER Strong Motion Database (http://peer.berkeley.edu). A total of 640 two-component horizontal ground motions are downloaded and they are subjected to the scaling procedure described in the following subsection.

4.4. Scaling of Ground Motions for NRHA

4.4.1. Ground Motion Selecting and Scaling Algorithm

A computationally efficient algorithm developed by Jayaram et *al*. (2011) is used in this study for selecting and scaling of ground motions using PEER NGA database. The matlab tool provided by the proponents of the algorithm can be accessed at http://web.stanford.edu/~bakerjw/gm_selection.html. It computes the conditional spectrum and selects and scales ground motions in accordance with the specified record selection

criteria by matching the target spectrum mean and variance. The multivariate normal distribution of lnSa(T_i) for a range of periods is parameterized in the first step of the algorithm. It then uses Monte Carlo based simulations to generate a number of realizations of response spectra from the multivariate normal distribution. For each simulated spectrum, a ground motion with similar response spectrum is selected by evaluating the sum of squared errors (SSE) between the Monte Carlo simulated response spectrum ($lnS_a^{(s)}(T_j)$) and the sample ground-motion response spectrum ($lnSa(T_j)$). Equation 4.4 shows the SSE expression where *P* is the number of discrete periods used in SSE.

$$SSE = \sum_{j=1}^{P} \left(lnS_a(T_j) - lnS_a^{(s)}(T_j) \right)^2 \tag{4.4}$$

A greedy optimization method is also built into the algorithm that, further improves the match between the sample and target means and variances upon its implementation. In this approach each ground motion response spectrum simulated in the previous step is replaced one by one to provide a better match between the target and the sample means and variances. If the replacement ground motion response spectrum does not deliver an improvement in the match, the original ground motion is kept.

Response spectra of selected and scaled ground motions at 2475-year return period (2% probability of exceedence in 50 years) using the algorithm of Jayaram et *al.* (2011) are shown in Figure 4.4a. The mean and variance of sample and target spectra at the period range of 0.1s to 10 are presented in Figure 4.4b and Figure 4.4c, respectively to demonstrate the match between the target and selected ground motion spectra. Response spectra of the selected ground motions for different conditioning periods listed in the previous section are presented in Appendix C. The scaled ground motions are compatible with the target spectra for period ranges of 0.1s to 10. The scaling is such that it satisfies the provisions required by ASCE/SEI 7-05 (ASCE, 2005: Chapter 21). This is explained further in the next section.

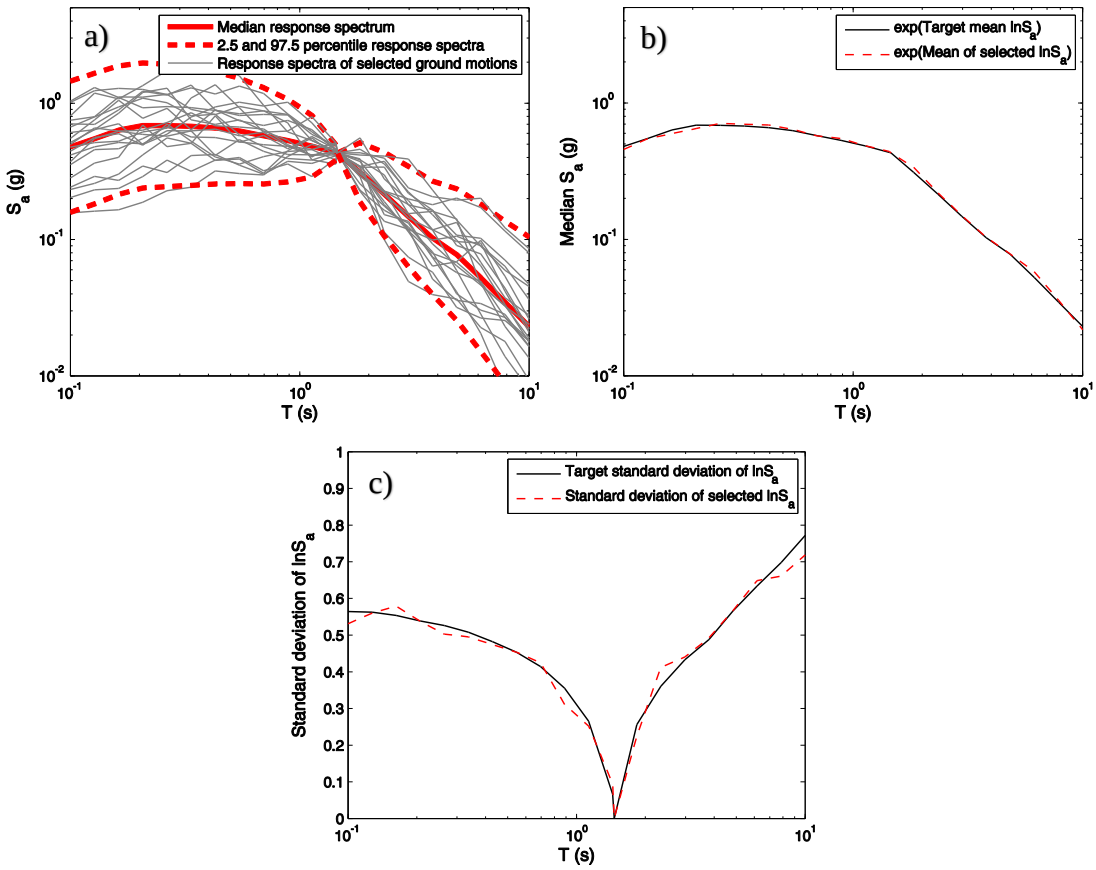

Figure 4.4. (a) Response spectra of the selected ground motions using CS anchored at T*=1.46s. (Building 1C) for return period 2475 years (2% probability of exceedence in 50 years) motion (b) Target and sample logarithmic means comparison. (c) Target and sample logarithmic standart deviations

4.4.2. Application of Ground Motions to Model Buildings

The horizontal component definition of target spectra used for scaling of records is geometric mean and the scaled horizontal components satisfy ASCE 7-05 (ASCE, 2005) provisions for 3D NRHA. In other words, the averages of response spectra computed from the square root of sum of squares (SRSS) of two scaled horizontal components are not less than 1.3 times the target response spectrum within the period range of interest. The period range of interest is taken as 0.1s to 10s in this study. The factor "1.3" accounts for the directional uncertainty of mutually perpendicular horizontal components in 3D analysis. It is common in practice to apply ground motion pairs in multiple orientations. Although neither ASCE, 7-05 (2005) nor ASCE 7-10 (2010) state specific rules for the ground motion orientations at far-field sites, it is usually necessary to apply the selected ground motion pairs

with two orientations (by switching the places of both-direction accelerograms) to obtain statistically more robust estimates of structural response. However in this study, the selected 20 ground-motion pairs at each return period are applied to the building models in 3D NRHA in a single orientation.

The horizontal ground motion records with sampling rates equal to or less than 0.005 seconds are down-sampled by a factor of 2 to speed up the computations. This procedure does not cause any significant effect on structural responses (PEER/TBI Task 12, 2011). Another reason behind this process is that the software used (Perform 3D) has a limt in terms of allowable number of acceleration data. The software can not perform response history analysis if the acceleration data is over 24000 time steps.

5. DYNAMIC BEHAVIOUR OF MODEL BUILDINGS

5.1. General

A total of 960 NRHA are performed on 6 different 3D high-rise building models. P-Delta effects are included in the analyses to better capture both local and global structural responses especially towards higher intensity shakings that would result in severe damage states or collapse of structures. Soil-structure interaction has not been taken into consideration in the structural analyses. The lateral modes and frequencies of vibration are obtained from modal analyses to evaluate dynamic characteristics of the model buildings. Engineering demand parameters (EDPs) attained from NRHA such as: (1) intenstory drift ratios (IDR); (2) maximum interstory drift ratios (MIDR); (3) core wall strains; (4) shear forces on core walls over building height are evaluated in the following subsections of this chapter. A probability based damage assessment procedure is presented in Section 5.4 to investigate the joint and conditional probability distributions of EDPs by considering the correlation among these EDPs.

5.2. Modal Analysis

It has been emphasized for many decades that the modal properties of buildings (e.g., modes and frequencies of vibration) have a significant influence on dynamic response of structures under periodic loading such as earthquake excitation (Clough, 1962; Rosenblueth, 1961). These properties often determine the damage patterns that structures likely to experience. The main dynamic properties of the model buildings derived from modal analyses are presented in the following sections. Detailed information about periods and effective mass factors associated with the first 10 lateral modes of vibration of the model buildings are given in Appendix B.

5.2.1. Dynamic Properties of the Model Buildings

Although the centers of mass and rigidity of all model buildings coincide, it is observed that torsional modes of vibration are apparently dominant in most cases. For the models 1A, 1B and 2C, the first modes of vibrations are torsional modes. These results may

suggest that torsional irregularities exist in majority of the core wall-frame tall building stock. The study by Ozmen (2002) has shown that torsional irregularity may exist in structures that are symmetric in terms of both plan geometry and stiffness distribution in plan. Özmen et *al.* (2012) and Inel et *al.* (2014) conclude that torsional irregularity increases (1) as the number of stories decrease and (2) as the SWs are located closer to the center of mass (Inel et *al.*, 2014; Ozmen et *al.*, 2014). In ASCE 7-10 (2010), torsional irregularity coefficient η_t is defined by

$$\eta_{\mathrm{t}} = \frac{\delta_{\max}}{\delta_{\mathrm{avg}}} \tag{5.1}$$

where δ_{max} and δ_{avg} are maximum lateral displacement and average of the displacements at extreme (corner) points of the structure at the n^{th} story under earthquake excitation. This formulation suggests that seismic torsion causes increased displacement at the corner points of the building and distress in the lateral load-resisting structural components. Miranda (2012) stated that the torsional effects are not easily observed unless full three-dimensional NRHA is conducted. Hence in this study, seismic torsional effects are aimed to be captured through inelastic nonlinear response history analyses.

The main dynamic characteristics of the submodels 1A and 2A are given in Figure 5.1 and Figure 5.2, respectively, to illustrate some of the differences in their dynamic properties. As indicated in the previous paragraph, building 1A has torsion dominant fundamental mode. Lesser number of stories and lesser torsional rigidity of building 1A with respect to building 2A may provoke prominent torsional mode in building 1A.

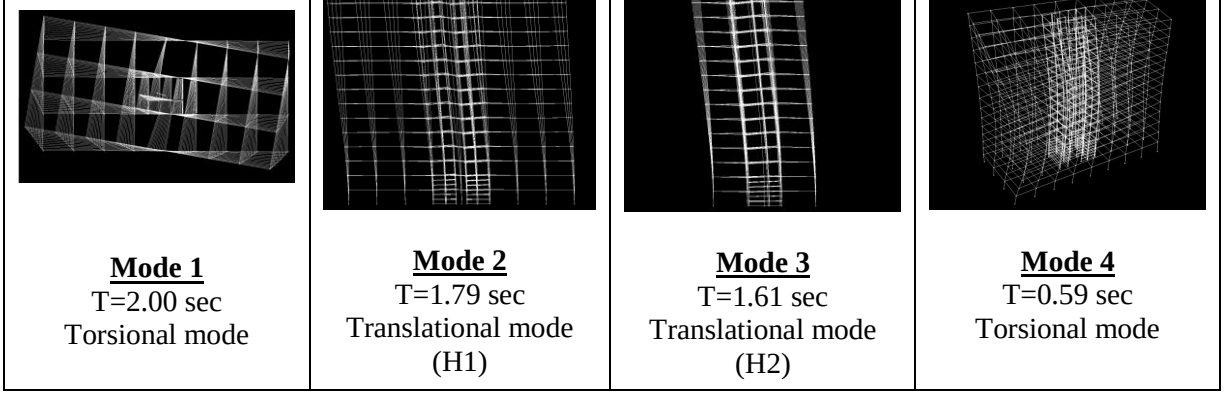

Mode 1	**Mode 2**	**Mode 3**	**Mode 4**
T=2.00 sec	T=1.79 sec	T=1.61 sec	T=0.59 sec
Torsional mode	Translational mode (H1)	Translational mode (H2)	Torsional mode

Figure 5.1. A summary of modal properties of building 1A.

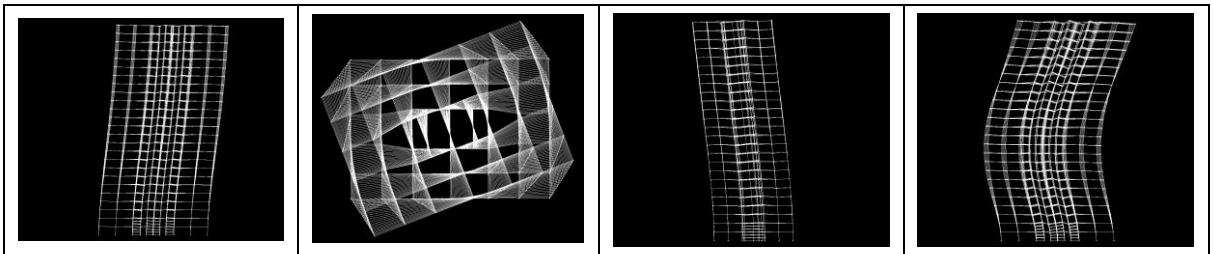

Mode 1	**Mode 2**	**Mode 3**	**Mode 4**
T=2.93 sec	T=2.28 sec	T=2.19 sec	T=0.59 sec
Translational mode (H1)	Torsional mode	Translational mode (H2)	Translational mode (H1)

Figure 5.2. A summary of modal properties of building 2A.

5.3. Earthquake Induced Structural Demand Assessment

Structural responses or the so called engineering demand parameters (EDPs) are calculated from NRHA for the model buildings. EDPs generally characterize building response in terms of interstory drift ratio, peak floor acceleration and inelastic component deformations such as strains and rotations (Moehle and Dierlein, 2004). In this study, the evaluated EDPs are: (1) interstory drift ratio (IDR), (2) maximum interstory drift ratio (MIDR) and (3) maximum shear wall strains. EDPs for the model buildings are calculated at multiple hazard levels (mimicked by different return periods) mentioned in Chapter 4. The engineering demands on the secondary structural elements such as beams, column and slabs are disregarded in this stud although further investigations on their behavior that might affect tall building behavior are strongly recommended for future studies.

5.3.1. Interstory Drift Ratios

The interstory drift ratios (relative lateral displacement between adjacent stories normalized by story height) are calculated for each structural model under subsequent hazard levels. The logarithmic mean values of each stripe analysis (20 analysis per stripe) as well as responses from individual ground motion excitation are presented in the following paragraphs to illustrate the relative difference in terms of average seismic demand and dispersion at increasing IM levels (Figure 5.3 and Figure 5.4). IDRs are computed in both principal directions of model buildings. At each story level, these interstory drift ratios are obtained by determining the absolute maximum of drift ratios computed from the entire duration of a ground motion. Thus, an IDR profile along the building height can be plotted for each individual ground motion as presented in Figure 5.3. Note that an IDR profile under a single excitation represents an envelope of the interstory drift ratio maxima along the building height where these drift values at each floor level may have occured at different time steps.

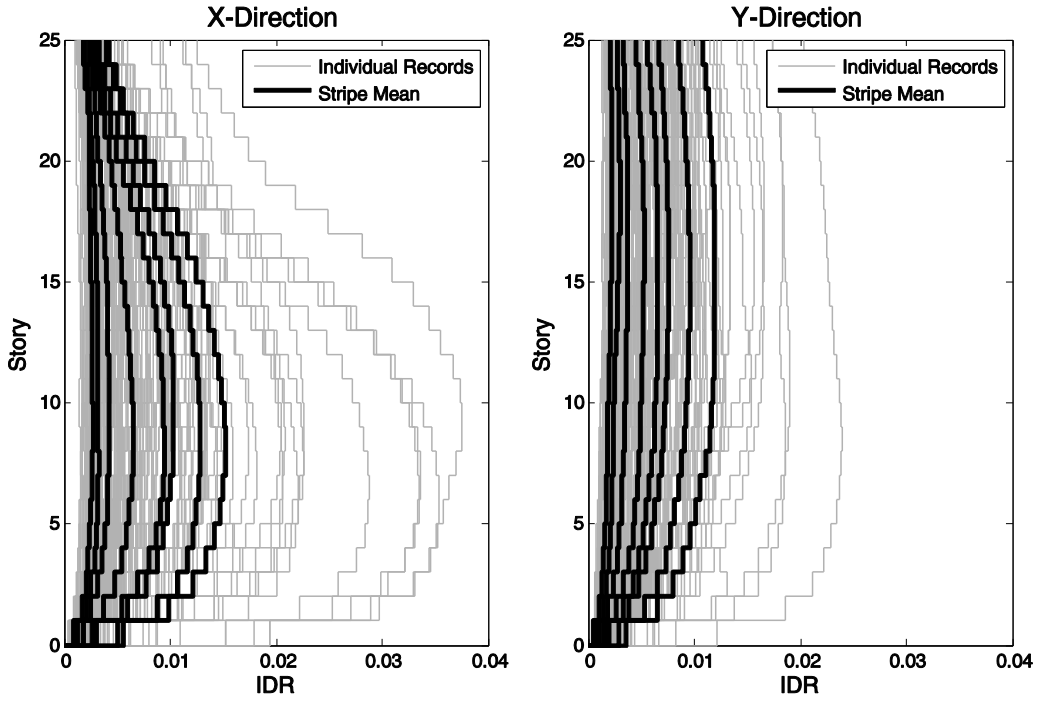

Figure 5.3. Interstory drift ratios in both principal directions of building 2A. Bold black lines represent the logarithmic mean of 20 responses for each return period. X- and Y-directions refer to long and short plan directions

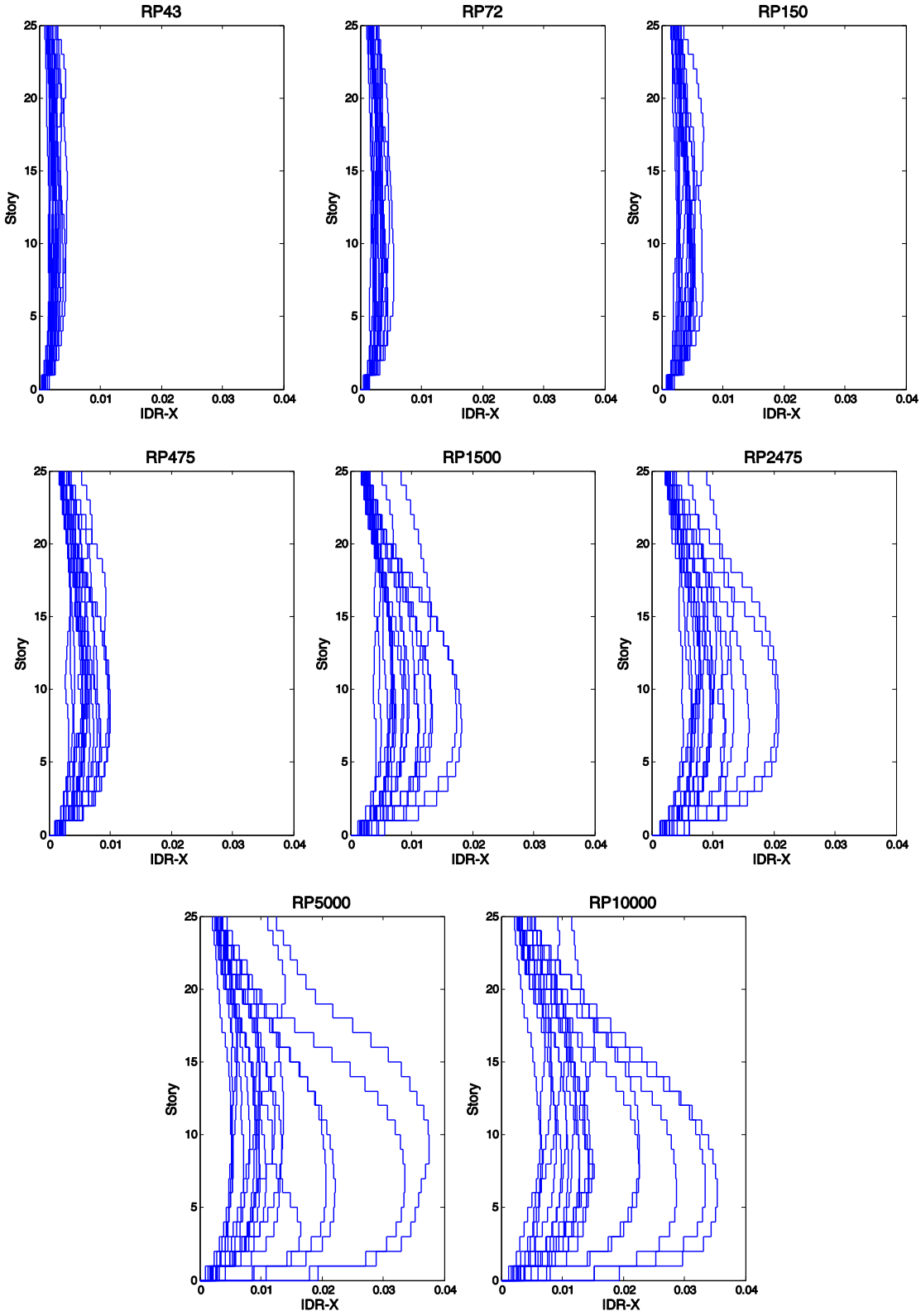

Figure 5.4. IDR-X distribution of building 2A for different hazard levels. Starting from top left corner IDR are plotted for sets of 20 ground motion excitations at increasing intensity measure levels (Return period 43, 72, 150, 475, 1500, 2475, 5000 and 10000-year shakings)

Under an earthquake excitation, interstory drift profiles of multi-story buildings vary in shape depending on several properties of buildings such as (1) number of stories; (2) type of lateral load-resisting system (e.g., moment resisting frame systems, core and outrigger systems, etc.). For example, an RC moment resisting frame system (MRF) and a core wall and frame system (CWF) having the same number of stories as well as identical first mode periods will experience different interstory drift ratio profiles along the building height. Given a uniform (regular) distribution of lateral load resisting member geometry and story height across stories, IDR reaches its maximum at the lower stories in MRF whereas the maximum IDR would most likely occur towards upper stories of a building dominated by CWF (Figure 5.5).

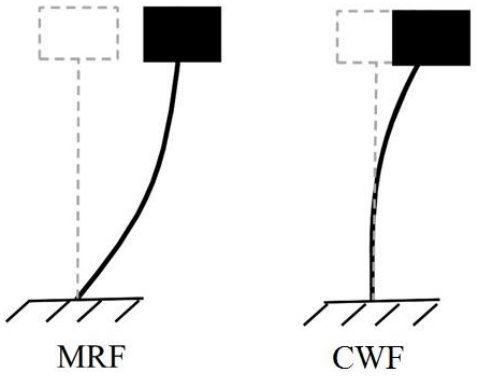

Figure 5.5. A simplified representation on displaced shapes of different structural systems (MRF versus CWF)

The interstory drift profiles of group-1 buildings suggest that the most extreme relative displacements occur around:

- 5^{th} to 10^{th} floors in long-direction
- Around 10^{th} floor in short-direction

In all cases, peak IDR values occur at lower stories in long-direction than short-direction. The intenstory drift maxima shift towards lower stories as the level of hazard (or the intensity of ground shaking) increases. Inherently, buildings suffer more damage with increasing ground motion intensity. Overall, 1B and 1C building models perform better when their maximum interstory drift ratios are compared to 1A building model. This is given in Table

5.1 that lists the average MIDR values of group-1 building models. Here, the term MIDR refers to the maximum of IDRs along the height of the building.

Table 5.1. The average maximum interstory drift ratio (MIDR) of group-1 buildings for increasing hazard levels.

Hazard Level (Return Period)	**Average MIDR**		
	1A	**1B**	**1C**
43-year	0.40%	0.41%	0.32%
72-year	0.49%	0.49%	0.43%
150-year	0.68%	0.69%	0.57%
475-year	0.96%	0.94%	0.89%
1500-year	1.35%	1.30%	1.19%
2475-year	1.47%	1.43%	1.29%
5000-year	1.84%	1.77%	1.54%
10000-year	2.09%	2.02%	1.73%

Relatively taller and slender group-2 buildings respond similarly to group-1 buildings under increasing hazard levels. The maximum interstory drift values are attained at proportionally lower stories as a result of higher mode and outrigger effects. Here, outrigger effect refers to the interaction between core walls and moment resisting frames in a building. Through this interaction, overturning stiffness and strength of the structure increase because the axial forces in distant columns supply additional lateral stiffness via beams (Figure 5.6). Moreover, Figure 5.7 is presented to illustrate the difference in terms of story levels at which the IDR maxima are observed between 1A (group-1) and 2A (group-2) buildings.

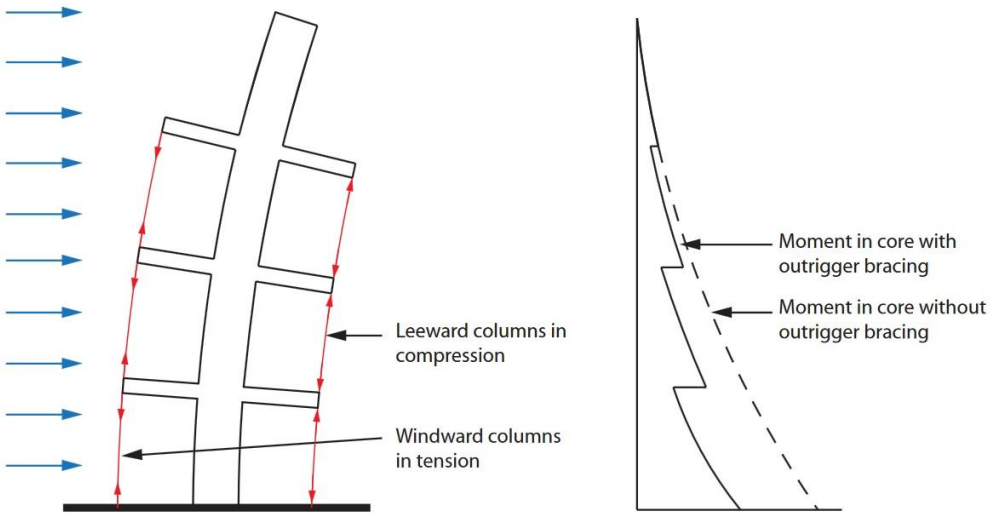

Figure 5.6. Interaction between core and outriggers (Taranath, 1998)

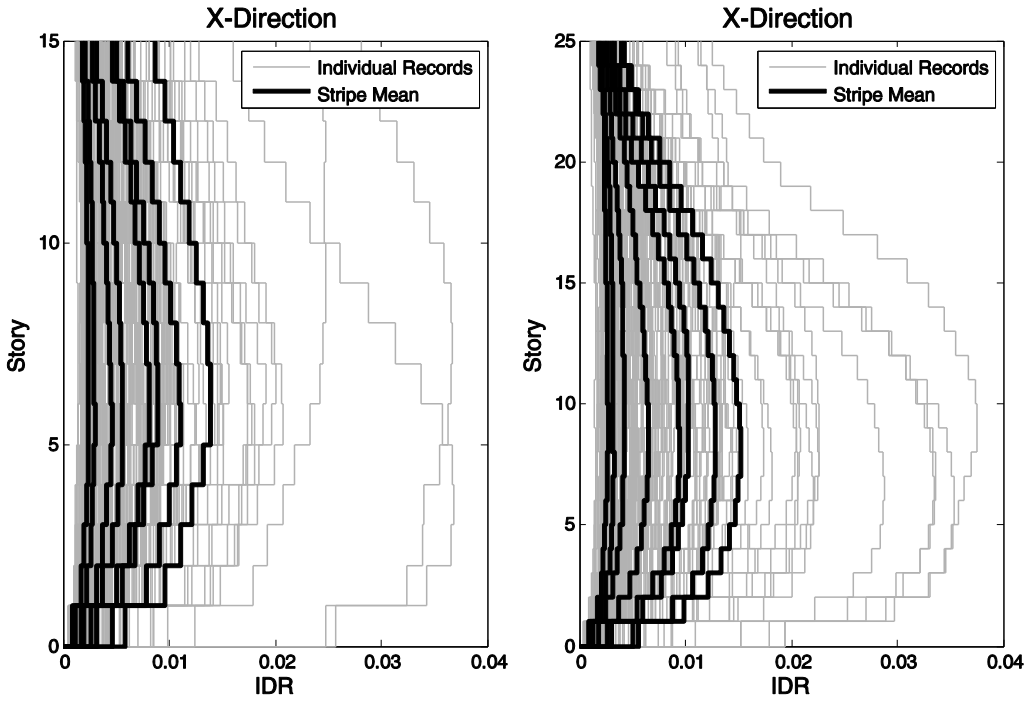

Figure 5.7. Difference in IDR shapes. a) IDR profile of 1A builing in long (X) -direction; b) IDR profile of 2A building in long-direction

Table 5.2. The average maximum interstory drift ratio (MIDR) of group-2 buildings for increasing hazard levels

Hazard Level (Return Period)	Average MIDR		
	1A	1B	1C
43-year	0.38%	0.37%	0.30%
72-year	0.48%	0.51%	0.39%
150-year	0.61%	0.66%	0.54%
475-year	0.88%	0.91%	0.87%
1500-year	1.20%	1.22%	1.14%
2475-year	1.35%	1.36%	1.21%
5000-year	1.73%	1.69%	1.47%
10000-year	2.06%	1.98%	1.62%

The nonlinear response history analyses indicate that the most extreme drift ratios are observed in X-direction (long-plan direction) for buildings 2A and 2B while the IDRs of 2C yield similar amplitudes in both principal directions. Similar to the responses of group-1 buildings, the peak amplitudes of IDRs shift towards lower stories with increasing hazard. As in the case of group-1 building models, the dispersion in IDR and MIDR distributions get larger as the hazard intensity increases. Table 5.2 lists the average MIDR values of group-2 building models at different return periods to complete the picture given for group-1 buildings in Table 5.1.

The nonlinear response history analyses of group-1 and group-2 buildings show that the MIDR values do not exceed 3% and 2% for 2475-year and 475-year return periods that are defined as maximum considerable (MCE) and design basis (DBE) ground shaking. These deformation limits are introduced in TBI (2011). The same guideline imposes 0.5% as the MIDR limit for servicibility performance level that is represented by 72-year return period ground motions. For ground-motions representing 72-year return period, the serviceability performance in terms of MIDR criterion is satisfied in many cases. The reader is refered to Appendix B for IDR plots obtained from entire NRHA. The following items are highlighted based on IDR and MIDR results:

- All model buildings show satisfactory performance under ground motions representing MCE (2475-year), DBE (475-year) and serviceability (72-year) hazard levels.
- Buildings having higher shear wall area ratios display better seismic performance in a global sense.
- IDRs tend to take larger values along long-direction (X-direction) for first two submodels of each group. As the shear wall distribution becomes more homogenous in both principal directions (last submodels in both groups: 1C and 2C), the difference in IDR distribution along these directions diminish.
- IDR profiles suggest a shift in peak IDR towards lower stories after 2475-year return period hazard. This shift is less frequent for 1C and 2C building models having larger shear wall areas.
- Dispersion in IDR as well as MIDR distribution increses as the ground motion intensity increases.

5.3.2. Core Shear Wall Behavior

Structural damage in shear wall members can be related to inelastic deformation parameters such as rotations and strains. Codes and guidelines (e.g., ASCE 41-13) impose a suite of quantative performance objectives to shear walls based on rotations. Although it is rarely utilized as a performance indicator in seismic codes, wall strains are frequently used to evaluate the damage levels in shear wall sections (e.g., PEER/TBI Task 12, 2010). Considering that design principles require structural systems failing under flexure, codes and guidelines dictate ductile failure mode for shear walls and do not allow shear capacity to dominate the failure. To this end, shear wall strains and shear forces are investigated herein to delineate the overall behaviour of core walls of the model buildings.

5.3.2.1. Shear Wall Strains

Studies have demonstrated that evaluating wall strains offer a more flexible viewport to the analyst to understand the flexural behaviour of shear walls (PEER/TBI Task 12, 2011). Tensile and compression strains are evaluated separately because limit states are different for strain values of concrete in compression and reinforcement steel in tension. In this study,

maximum wall strains are gaged at all corner points (nodes) over the height of bulding models. Strain gage labels are used on all core wall configurations to describe the locations where strain profiles are extracted. Figure 5.8 shows strain gage labels for 1A and 2A submodels whereas the strain gage labels of the other building models are presented in Appendix B. Strain profiles entailing individual responses (under each excitation) and their averages at each story level are derived from NRHA. Figure 5.9 shows maxima of shear wall strains for buildings 1A and 2A under MCE (2475-year) level shaking. Note that these plots include tension and compression maxima together to display tension and compression induced damages.

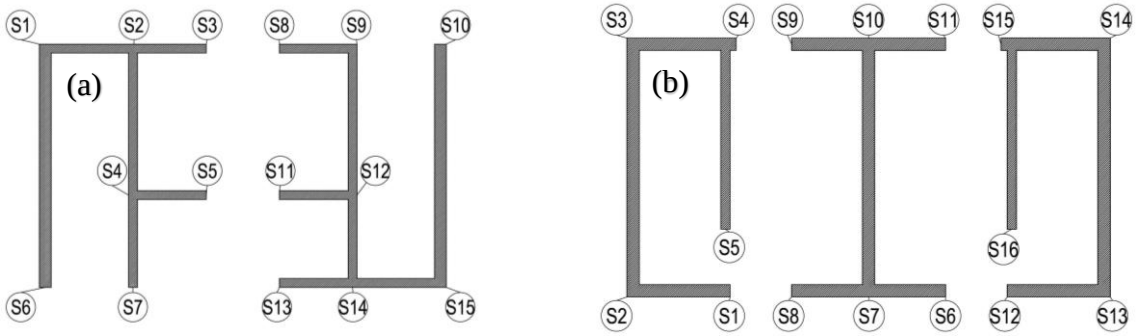

Figure 5.8. Illustration of strain gage locations where shear wall strain profiles are extracted. (a) Building 1A and (b) 2A

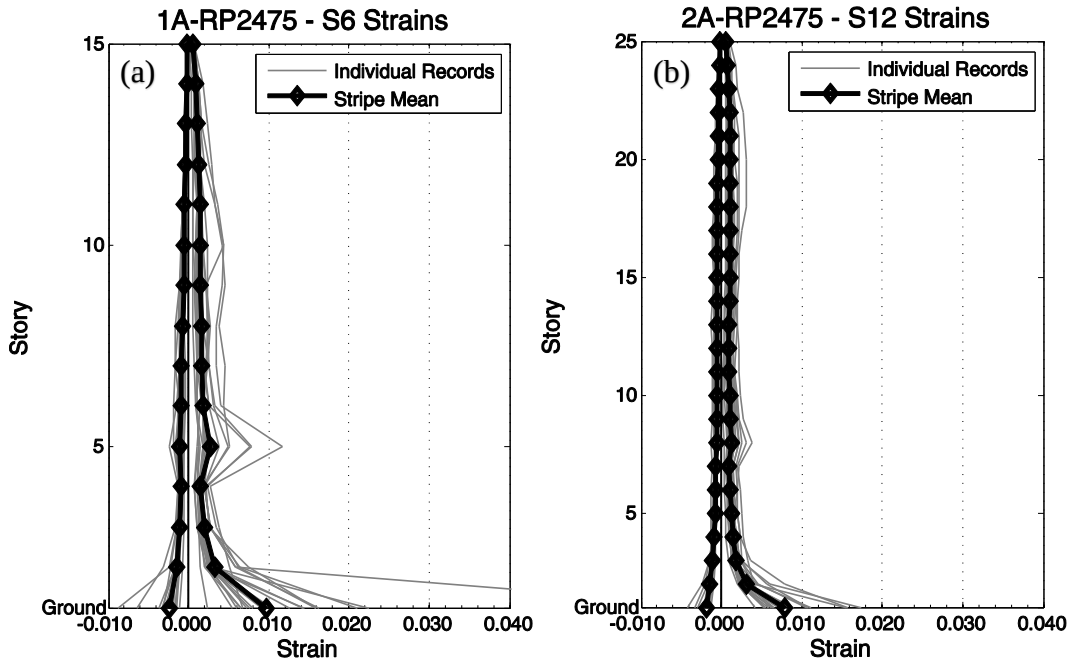

Figure 5.9. Distribution of shear wall strains at MCE level. (a) S6 profile of building 1A and (b) S2 profile of building 2A. Negative strains refer to compression and positive strains refer to tension

The distributions of maximum strain profiles for the entire model buildings are presented in Appendix D in CD format. Strain maxima attain peak values at the base level because of (1) the cantilever-like behavior of a core and outrigger system and (2) a first mode dominant dynamic response of the building models. Thus, flexural plastic hinges on core walls occur at base levels in almost all cases and they do not migrate to second floors. Yielding of longitudinal reinforcement steel is generally associated with a strain value of 0.01 for S420 steel grade, referring to "life safety" performance level, for example, in Turkish seismic code (TSC, 2007). It is also observed that tensile strains reach to considerable peaks at the 5^{th} story (group-1 buildings) and 8^{th} story (group-2 buildings) towards large return period ground motions. This observation is less frequent for group-2 buildings but it is quite apparent for group-1 buildings (See Appendix D). Note that the 5^{th} and 8^{th} stories mark floor levels at which reinforcement configurations change dramatically in group-1 and group-2 buildings, respectively (see Section 2.4.2). While the sudden change in confinement and longitudinal reinforcement configurations does not dramatically increase tensile strains for group-2 buildings, yielding of reinforcement steel is observed in group-1 buildings at the 5^{th} story as ground-motion intensity becomes higher (i.e., larger return periods). The following items are highlighted to summarize the states of strains on core walls in the building models:

- Core walls (in all model buildings) are expected to form plastic hinges at the ground-story level, provided that the ground motion intensity is severe enough.
- At story levels above ground story, shear walls do not undergo damage states beyond immediate occupancy level (0.01 under tension and 0.0035 under compression according to Turkish seismic code, 2007) where concrete does not reach to its ultimate compressive strength and/or reinforcement steel does not yield.
- The sudden change in the reinforcement configuration at the mid-stories (mimicked as the 5^{th} and 8^{th} stories in group-1 and group-2 buildings, respectively) leads to considerable increase in tensile strains at 5^{th} and 8^{th} stories of group-1 and group-2 buildings, respectively.
- Strain values at the corners of core-walll systems can be called as the most critical areas in terms of tension and compression.

5.3.2.2. Shear Force Distribution in Core Walls

Maximum shear force distributions along the height of walls are also investigated. Figure 5.10 and Figure 5.11 show the shear force distributions of building 2B along two principal axes computed at DBE (475-year) and MCE (2475-year) ground motions, respectively. Normalization for the story shear forces (in Figure 5.10) are done with respect to building weight. Plots similar to the ones given in Figure 5.10 and Figure 5.11 are presented in Appendix D for the rest of the building models. The story shear forces in core walls (Figure 5.10) increase steadily until an apparent yield base shear level is reached at the lower stories. Base shear versus top displacement curves (i.e., static pushover curves or hysteresis base shear versus base shear curves) are useful for determining approximate yield base shear levels of structures. However, these curves are not generated within the scope of this study.

Codes and guidelines do not provide shear deformation limits, but they include allowable shear forces (ultimate shear strength) to identify *brittle* failure mode. Codes (e.g., ACI 318-10, 2010) express allowable shear stress by considering the cumulative contribution of concrete and reinforcing steel (see Appendix A for detailed information on shear stress-strain relationships of shear walls). However it is known that reinforced concrete sections do not necessarily "fail" upon reaching their shear capacities. ATC 72-1 (2010) presents shear F-D relationships available in the literature to model nonlinear behaviour of shear walls for NRHA. In this study, inelastic shear constitutive models are built into the models to be able to better represent the overall dynamic behaviour of buildings.

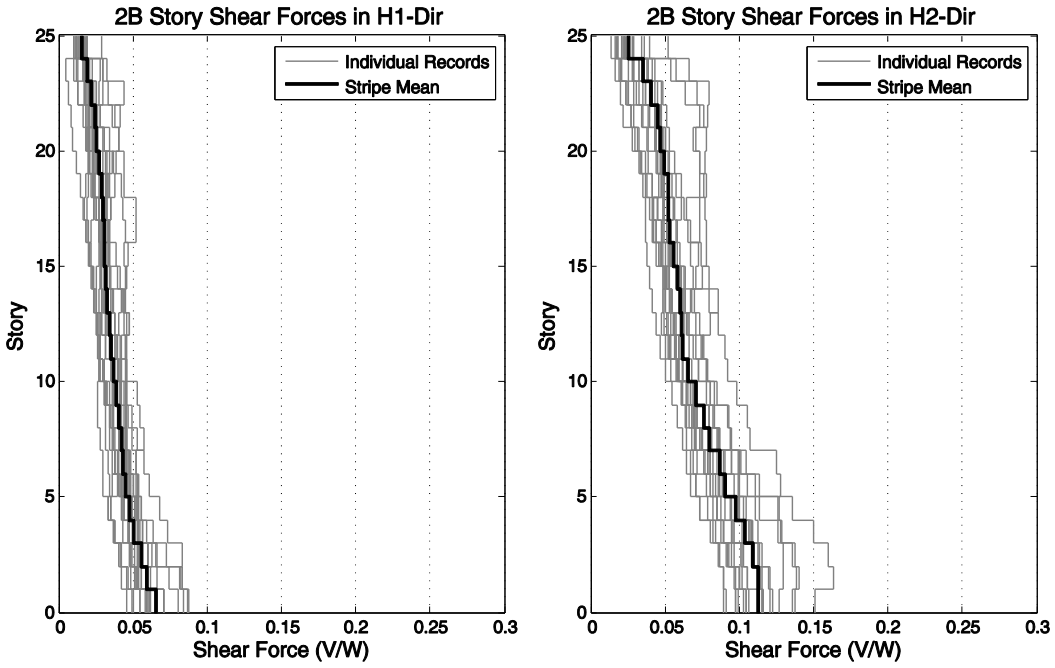

Figure 5.10. Distribution of normalized shear forces on core walls of building 2B at DBE (475-year) level. Bold black lines represent the arithmetic mean. H1 and H2 directions refer to long- and short-plan directions, respectively.

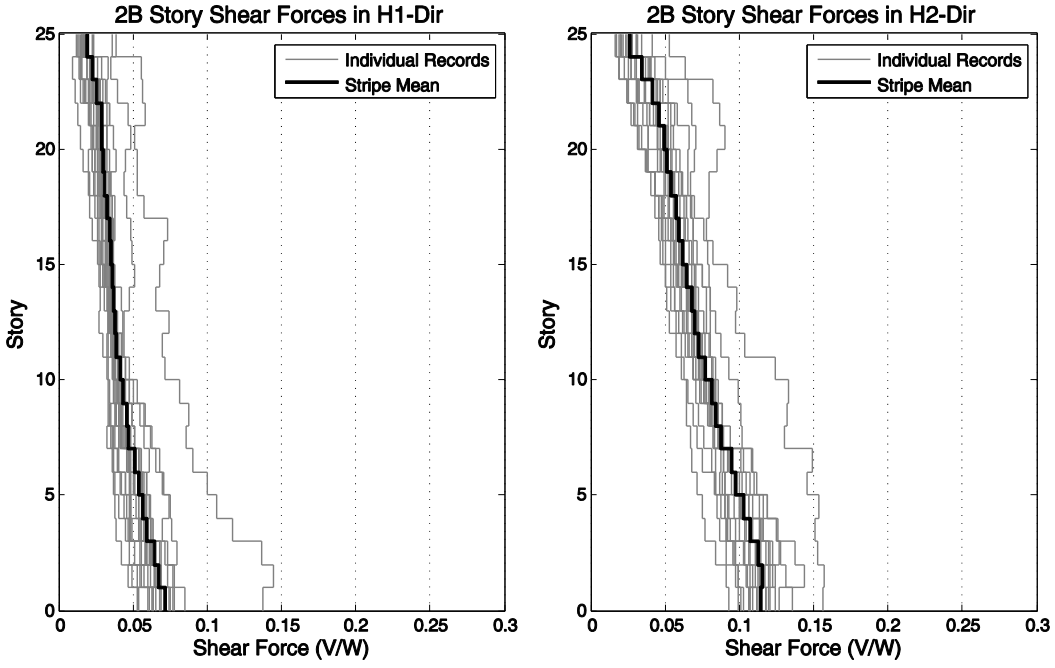

Figure 5.11. Distribution of normalized shear forces on core walls of building 2B at MCE (2475-year) level. H1 and H2 directions refer to long- and short-plan directions, respectively.

Distribution of the maximum shear forces of individual shear wall sections are also derived to investigate the local behavior of the shear walls. Figure 5.12 depicts shear force patterns of six different SW sections of building 2B. The notations to shear wall sections are already described in Chapter 2. Note that the shear forces in the wall section shown in Figure 5.12b do not keep increasing towards ground level but they are rather piled at the force level associated with cracking of concrete (i.e., 11880 kN for SW2 section of building 2B within the plastic hinge region) under seismic action. This behaviour is captured thanks to the nonlinear modelling of shear F-D relationships in shear walls. The sudden jump in shear forces is observed when the story above critical height has reached to cracking stress (Figure 5.12). Shear demands increase suddenly at the subsequent lower story because of the change in the reinforcement configuration (e.g., 8th story for group-2 buildings). As the first SW section below critical height cracks at a larger shear force, the demand takes a leap depending on the difference in cracking stresses between the two subsequent SW sections.

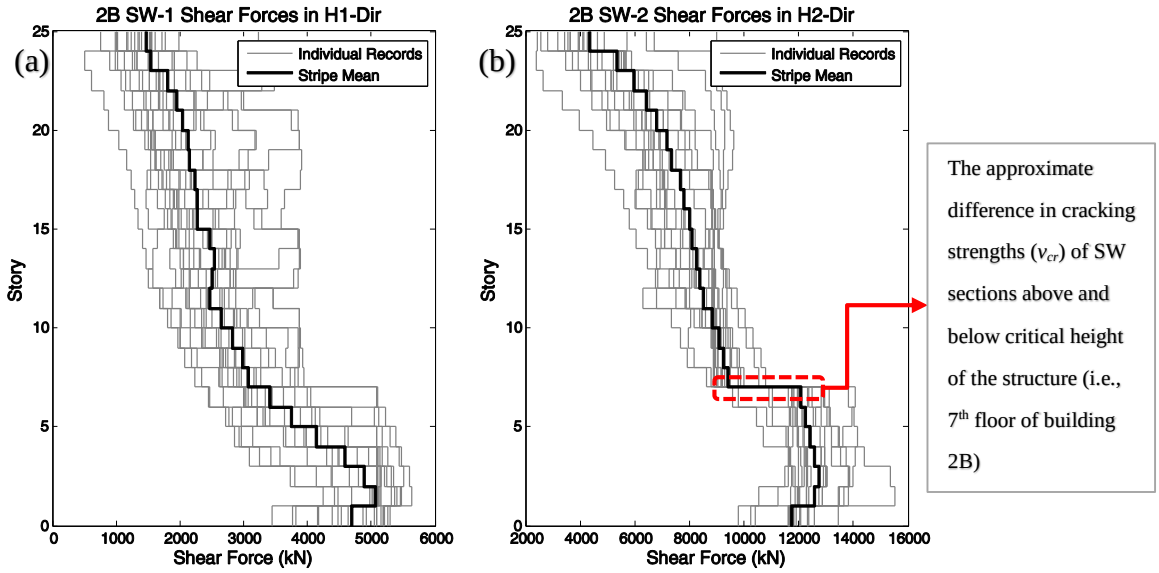

Figure 5.12. Comparison of shear force patterns of two different SW sections over the height of building 2B at DBE (475-year shaking) level. Bold black lines represent the arithmetic mean of individual responses.

Shear force distributions in critical shear wall sections (usually the wide web panels of individual cores, for example, SW-2 of building 2B) indicate that diagonal shear cracks occur along considerable heights of the buildings after 475-year return period hazard (DBE) level. In many cases, cracks in SW concrete propagate to 0.6 times the building height.

The above expressions emphasize the necessity of well-detailed (code complying) shear walls particularly in the plastic hinge regions of tall buildings. Shear force patterns on core walls as presented here provide insight to inelastic higher mode effects in tall buildings. Higher mode effects in such buildings result in large shear force demands especially above mid-height due to large moment reversals (Adebar et *al.* 2014). However, a contraversial study on cantilever shear walls by Dezhdar (2012) has shown that additional detailing at regions of high moment reversals are unnecessary because the curvature demands are relatively small above the plastic hinge regions provided that the NRHA consider proper modelling assumptions on shear wall behavior. It is a fact that accounting for cracking under flexure and shear actions through nonlinear modelling would lead to a significant increase in wall flexibility. Consequently, moment and shear demands in upper stories would reduce. Sample distributions of shear forces shown in Figure 5.10 to Figure 5.12 suggest that the shear walls of the first two stories (ground-level and the story above) attract the largest shear demands. This observation supports the fact that additional reinforcement is often not necessary above the critical height of tall shear wall buildings.

The average shear forces do not exceed the ultimate shear strength of SW sections (i.e., v_u = 1.5 v_n) in any building model at any hazard level. In terms of individual responses, the wide web panels of core wall configurations (generally parallel to the short-direction of buildings to increase the overturning stiffness in the more flexible short-direction) start to yield after 2475-year (MCE) return period ground motions. Here, yielding of a shear wall section means yielding of transverse steel under diagonal tension, provided other failure modes associated with crushing of concrete under diagonal compression, sliding shear and rocking are prevented. ACI 318-14 (2014) §11.5.4.3 sets an upper limit (maximum allowable in-plane shear stress in shear walls) for shear forces to guard against undesired diagonal compression failure in shear walls.

$$v_{max} = 0.83\sqrt{f_c'} \tag{5.1}$$

In Equation 5.1, v_{max} is the upper limit for shear stress in shear walls and f_c' is compressive strength of concrete. Note that v_{max} in above expression is calculated by assuming that shear forces are resisted by 0.8 times the length of a shear wall segment. In other words, shear stresses should be calculated using the effective wall cross-section area. The statistical

survey on the tall building inventory revealed that shear walls designed per Turkish seismic code (TSC, 2007) provisions inherit in-plane ultimate shear capacities (v_u) less than the upper limit given in Equation 5.1. This means that ductile response can be presumedly achieved in shear walls of the building models.

5.4. Probabilistic Damage Assessment

5.4.1. General

Engineering seismology and earthquake engineering use probability theory in topics such as PSHA, ground motion selection and scaling, evaluation of EDPs, generation of fragility functions. PBEE framework leads to the generation of large sets of data requiring probabilistic approach to evaluate this information. To this end, probabilistic calculations quantify outcomes of seismic demand analysis to represent structural response in a probabilistic framework. The computations in this section rely on the use of various probability concepts such as continuous random variables, jointly distributed (multivariate) random variables and conditional distributions. Seismic performance of core walls and the relationship between shear wall strains and interstory drift ratio (IDR) parameters are evaluated through probability calculations for each submodel in the following paragraphs to picture the overall dynamic behaviour of target building stock.

5.4.2. Evaluation of Seismic Performance of Core Walls

An extensive probabilistic framework is presented here to assess seismic performance of core walls by evaluating shear wall strains. Probabilistic expressions entail the likelihood of critical SW sections reaching to certain damage states in terms of confined concrete in compression and reinforcing steel in tension. A *critical* SW section refers to a member where in one of its corner nodes, the average of strain values (see bold lines in Figure 5.9) are maximum with respect to other nodes at a given floor. This way, strain EDPs always show the most critical sections at each floor in terms of tension and compression separately.

The maxima of shear wall strains are measured at the corner nodes of core walls in all building models. Repeating the measurements for 8 return periods, each containing 20

pairs of horizontal ground motions, strain EDPs form a data matrix of [8 x 20 x 15] for group-1 buildings and [8 x 20 x 25] for group-2 buildings. The numbers 15 and 25 in the above calculations refer to story numbers in group-1 and group-2 buildings, respectively. These EDPs are evaluated at multiple *story-return period* combinations by assuming their distributions are lognormal (Equation 5.2). Here, $P(EDP \geq edp)$ denotes the probability that the component, SW section in this implication, reaches or exceeds a demand level:

$$P(EDP \geq edp) = 1 - \Phi\left(\frac{\ln(edp) - x_m}{\beta}\right) \tag{5.2}$$

In Equation 5.2 Φ denotes the standart normal (Gaussian) cumulative distribution function, x_m represents logarithmic mean of the strain data, and β is the logarithmic standart deviation. Note that the lognormal distribution is often used in representing the distribution of structural response parameters because it fits the data (e.g., Porter et *al*., 2007; Aslani, 2005). In this study, maxima of shear wall strains constitute suits of 20 data under multiple return period-story pairs. Confined concrete and reinforcing steel strain tresholds are determined to seperately compute probabilies of observing different damage states for wall sections in tension and compression. The damage state thresholds (performance limits) are set in accordance with the provisions of Turkish seismic code (TSC, 2007) and are listed in Table 5.3. Note that the unconfined web concrete of SW sections are not evaluated since strains are not measured at web nodes. Although, based on engineering judgement, crushing of web concrete is not expected before crushing of the extreme confined concrete fibers in boundary regions in ductile designs, it is still recommended for future studies to investigate damage states of unconfined web regions of core walls.

Table 5.3. Performance criteria (damage states) for shear walls in terms of strains

Performance Levels	Confined Concrete in Compression	Reinforcing Steel in Tension
Immediate Occupancy (IO)	$\varepsilon < 0.0035$	$\varepsilon < 0.01$
Life Safety (LS)	$0.0035 \leq \varepsilon < 0.0135$	$0.01 \leq \varepsilon < 0.04$
Collapse Prevention (CP)	$0.0135 \leq \varepsilon < 0.018$	$0.04 \leq \varepsilon < 0.06$
Collapse (C)	$\varepsilon \geq 0.018$	$\varepsilon \geq 0.06$

The limit state notations given in Table 5.3 are widely used and accepted in the building provisions. The descriptions of these limit states are given below using ASCE 41-13 (2013) definitions:

- Immediate Occupancy (IO): Minor diagonal cracking of walls.
- Life Safety (LS): Some boundary element cracking and spalling and limited buckling of reinforcement. Damage around openings. Some crushing and flexural cracking.
- Collapse Prevention (CP): Major flexural or shear cracks and voids. Sliding at joints, extensive crushing and buckling of reinforcement. Severe boundary element damage.

Probability of damage states are obtained from cumulative distribution functions (CDFs) of shear wall strains using Equation 5.2. These computations are done from expressions given in Equation 5.3:

$$\begin{aligned} P(IO) &= 1 - P(EDP \geq edp_{IO}) \\ P(LS) &= P(EDP \geq edp_{IO}) - P(EDP \geq edp_{LS}) \\ P(CP) &= P(EDP \geq edp_{LS}) - P(EDP \geq edp_{IO}) \\ P(C) &= P(EDP \geq edp_{CP}) \end{aligned} \tag{5.3}$$

Here, "*edp"* terms with subscripts *IO, LS, CP* denote performance limits (or damage state tresholds) in strains (see Table 5.3). Figure 5.13 illustrates this probability computation. Here, probability values at each performance limit (shown with dashed lines) are computed from the expressions given in Equation 5.3. For example, in the case of ground-story tensile strain distributions (Figure 5.13b) for building 1A subjected to ground motions representing 475-year return period, the probability of damage states are computed as follows:

$$P(IO) = 1 - 0.4 = 0.6$$

$$P(LS) = 0.4 - 0 = 0.4$$

$$P(CP) = 0 - 0 = 0$$

$$P(CP) = 0 - 0 = 0$$

The above values indicate that there is a large probability that the critical shear wall segment of building 1A in tension will satisfy *immediate occupancy* or *life safety* performance levels while probability of observing *collapse prevention* and *collapse* damage states in tension are practically zero. For the compression strain distributions of the same core wall section, the probability of *IO* is 98% whereas the probability of other damage states are practically none. When compared to probabilities of damage due to tension and compression, for this particular case, the probability of observing core wall damage due tension is more likely. Such calculations are repeated at every *return period-story* pair of all building models to obtain the final probability distributions that are discussed next.

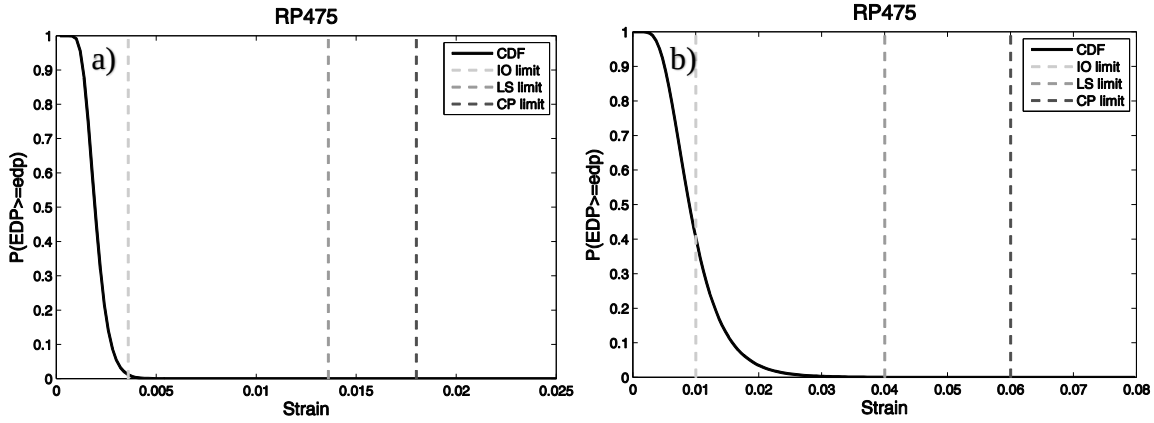

Figure 5.13. Lognormal CDF of a) compression strains; b) tensile strains of the most critical first story SW section (node) in building 1A at 475-year return period event

The probability distributions of damage states in tension and compression are delivered with two different 3D histogram format for different perception purposes. The first format, given in Figure 5.14 and Figure 5.15, shows the probability of observing the damage states (*IO*, *LS*, *CP* and *C*) in critical shear wall sections across all floor levels. These figures show the migration of damage from one state to another along the building height at a given return period. For example, the given case (building 1A under 475-year and 2475-year return period ground motions) indicates that the critical SW section will mainly experience IO performance level along the building height under tension (Figure 5.14) and compression (Figure 5.15) strains. The observed performance is shifted to LS at ground story with increasing level of hazard (i.e., from 475-year to 2475-year) that is more prominent in tensile (steel) failure. The second histogram format shows damage state probabilities at each floor level under multiple hazard levels (Figure 5.16). The histograms in Figure 5.16 display

similar information as in Figure 5.14 and Figure 5.15 but from a different perspective. The tensile and compression failures happen to occur at ground level with very large probabilities. These failure states fall into IO and LS performance levels, where the latter performance level is likely to occur at larger return periods (475-year or above). The plots in this figure also correspond to building 1A. Appendix B displays similar plots for the rest of the building models. The following section summarizes the overall observations from these probabilistic calculations.

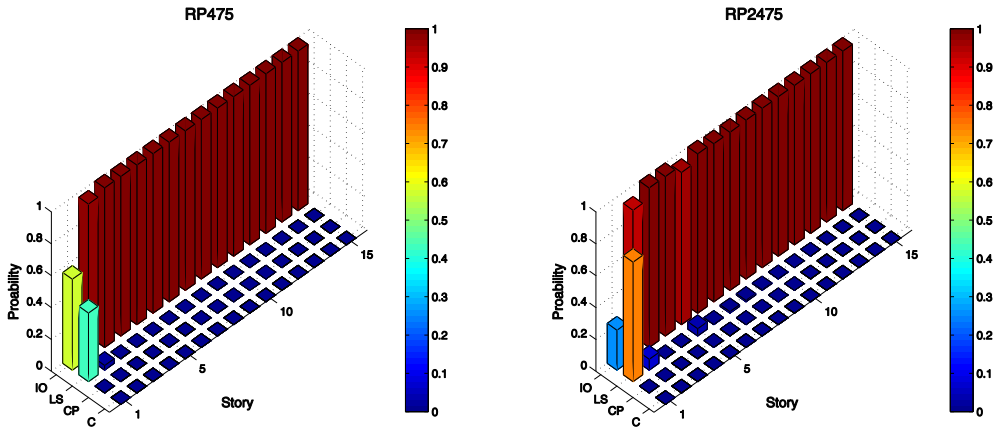

Figure 5.14. Damage state probabilities of critical SW sections in terms of reinforcing steel tensile strains for building 1A at DBE (475-year) and MCE (2475-year) levels

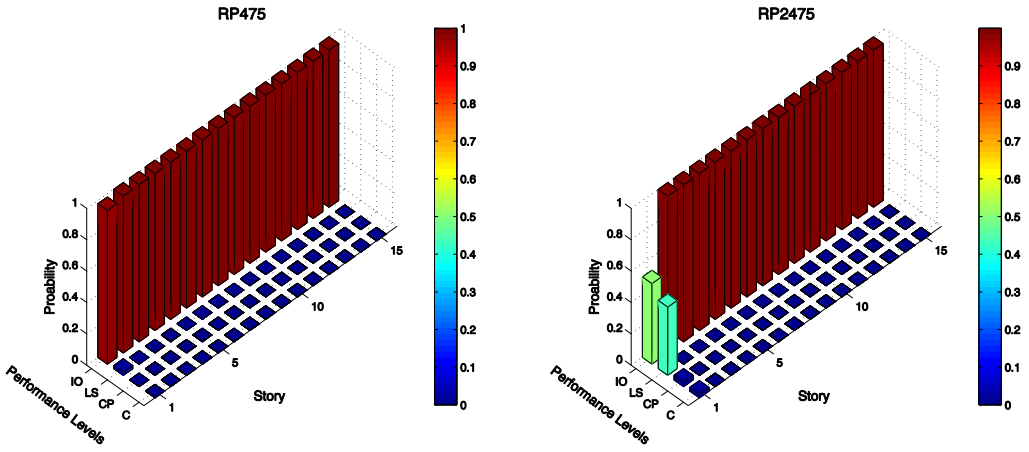

Figure 5.15. Damage state probabilities of critical SW sections for confined concrete under compression for building 1A at DBE (475-year) and MCE (2475-year) levels

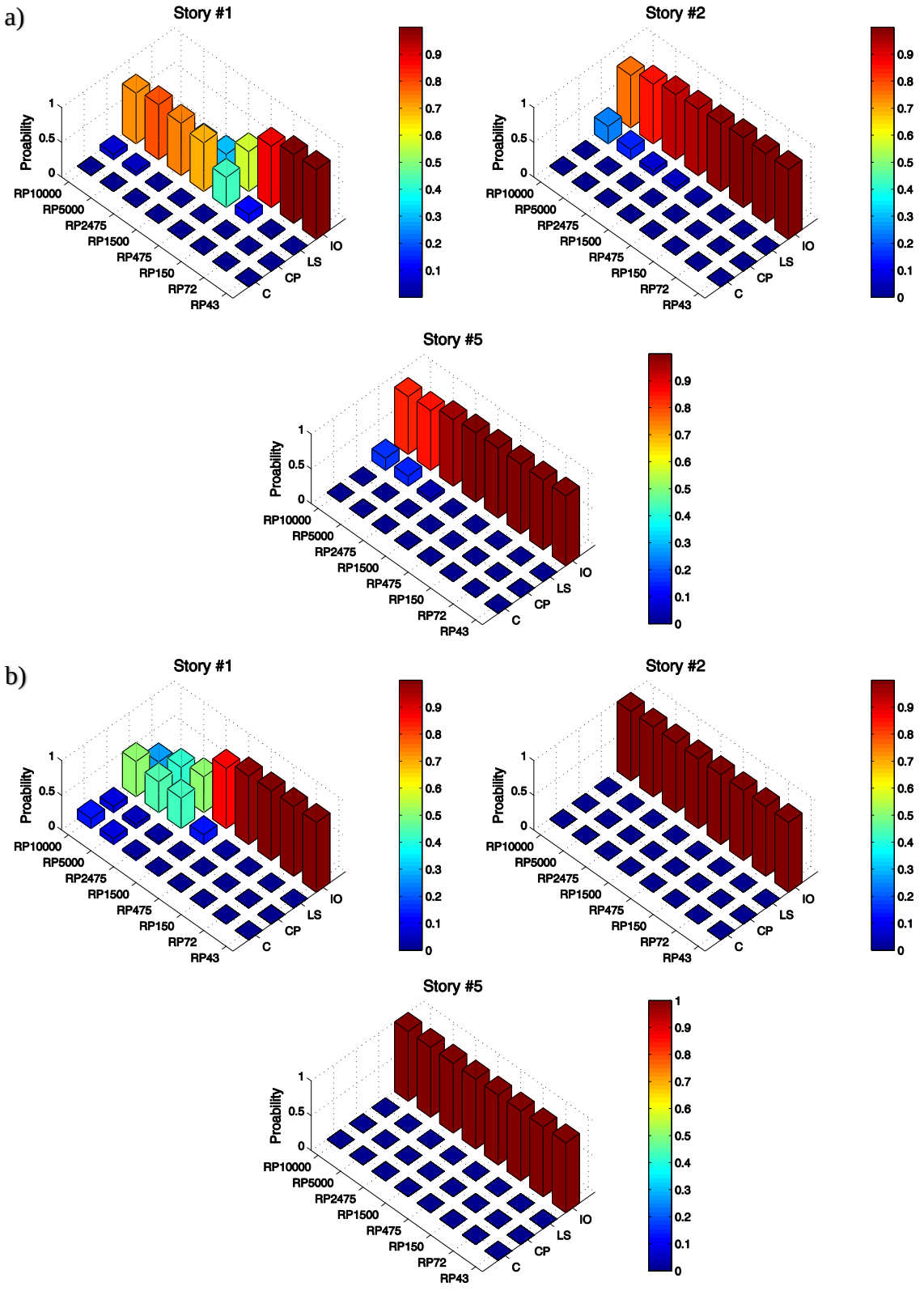

Figure 5.16. Damage state probabilities of critical SW sections at 1st, 2nd, 5th stories. (a) Reinforcement in tension and (b) confined concrete under compression for building 1A.

5.4.2.1. Group-1 Buildings

Group-1 buildings (represented by 15-story submodels) show an overall satisfactory performance on the basis of flexural core wall limit states (i.e., tensile and compression strains) while building 1C with the highest SW area ratio displays a superior performance over buildings 1A and 1B. Core walls in all group-1 models remain in *immediate occupancy* damage state in terms of concrete compression strain by retaining compression strains under 0.0035 (approximate strain value at the ultimate compressive strength of concrete fibers) for return periods up to 475 years. The shear walls of 1A and 1B models at the base levels experience yielding of reinforcement after 150-year return periods whereas yielding of steel initiates after 475-year DBE level in building-1C SWs. Towards higher hazard levels (1500-year return period or larger), ground story critical SW sections form plastic hinges at higher rate. However the core wall concrete at the base levels appear to be less critical in all group-1 buildings up to 2475-year (MCE) return period. Table 5.4 lists the probabilities of the ground-story shear wall damage states under MCE level ground motion are for group-1 buildings.

Table 5.4. Probabilities of the critical ground-story SW damage states of group-1 buildings at MCE level

Performance Level	Building		
	1A*	1B*	1C*
Immediate Occupancy	(25% | 52%)	(57% | 63%)	(68% | 98%)
Life Safety	(74% | 42%)	(42% | 36%)	(32% | 2%)
Collapse Prevention	(1% | 3%)	(1% | 1%)	(0% | 0%)
Collapse	(0% | 3%)	(0% | 0%)	(0% | 0%)

* Probability information is given as ($P_{tension}$ | $P_{compression}$)

Observations on tensile and compressive strain levels and damage (performance) levels indicate superior performance of building 1C that has the largest SW area ratio. The crushing of concrete under compression is very unlikely for this building submodel at MCE level advocating that larger SW area ratios prevent brittle damage. The *collapse prevention* performance level is unlikely to be observed for group-1 models at MCE level. Although

SW concrete remains in *immediate occupancy* state at stories above the ground level, yielding of reinforcement steel is seldomly observed at 2nd and 5th story levels with probabilities less than 10% under MCE level. These obervations indicate that group-1 buildings show ductile damage pattern at MCE level ground motions.

5.4.2.2. Group-2 Buildings

Probability computations of group-2 buildings show similar outcomes to those of group-1 buildings. Building-2C having larger shear wall area ratio demonstrates superior performance with respect to buildings 2A and 2B but the performance differences between these submodels are rather small. The computed probabilities of group-2 buildings suggest that core wall damage states (performance levels) exceed *immediate occupancy* only at the ground stories. The confined concrete of critical shear wall sections do not reach to their ultimate compressive strength levels before the ground motion demands reach to DBE levels. Table 5.5 lists the probabilities of performance levels for the ground-story core walls of group-2 buildings at 2475-year return period (MCE level):

Table 5.5. Probabilities of the critical ground-story SW damage states of group-2 buildings at MCE level

Performance Level	Building		
	2A*	2B*	2C*
Immediate Occupancy	(62% | 86%)	(52% | 93%)	(72% | 93%)
Life Safety	(38% | 14%)	(47% | 7%)	(28% | 7%)
Collapse Prevention	(0% | 0%)	(1% | 0%)	(0% | 0%)
Collapse	(0% | 0%)	(0% | 0%)	(0% | 0%)

* Probability information is given as ($P_{tension}$ | $P_{compression}$)

Above the ground level of structures, the probabilities that critical SW sections to reach to *life safety* damage state is less than 5%. This observation suggests that flexural damage in shear walls occurs only at the ground story. The probabilities listed in Table 5.5 indicate that the *life safety* performance level is dictated by the yielding of reinforcing steel in all building submodels for group-2 buildings.

5.4.3. Relationship Between Core Wall Strains and Interstory Drift Ratios

Structural damage usually involves more than a single parameter and probability distributions of single variables do not deliver the entire damage picture. To this end, joint probability distributions of multiple variables should be considered for a realistic portrayal of structural damage. In this stuy, the interaction between shear wall strains and interstory drift ratios is saught with a probabilistic framework to fully characterize the damage in the tall building groups of interest. Thus, log-normal bivariate distribution of shear wall strains and interstory drift ratios are developed because these two variates are assumed to be log-normally distributed.

Given two log-normally distributed random variables X and Y (representing the two EDPs of interest), their joint probability density function $f_{X,Y}(x, y)$ is written as:

$$f_{X,Y}(x, y)dx\,dy = P(x < X \leq x + dx \;\cap y < Y \leq y + dy) \tag{5.4}$$

The log-normal joint PDF of variables *X* and *Y* is given in Equation 5.5

$$f_{X,Y}(x, y) = \frac{1}{2\pi\sigma_X\sigma_Y\sqrt{(1-\rho^2)}}\; exp\left\{-\frac{z}{2(1-\;\rho^2)}\right\} \tag{5.5}$$

where ρ is the correlation coefficient between *X* and *Y*, and

$$\mathrm{z} = \frac{(\log(x)-\mu_x)^2}{\sigma_x^2} - \frac{2\rho(\log(x)-\mu_x)\big(\log(y)-\mu_y\big)}{\sigma_x\sigma_y} + \frac{(\log(y)-\mu_y)^2}{\sigma_y^2} \tag{5.6}$$

In Equation 5.6 $\mu_x$and μ_y are the logarithmic mean, σ_x and σ_y are logarithmic standart devations of the variables *X* and *Y*. A visual representation of joint probability distribution of core wall strain and IDRs is presented in Figure 5.17 for a particular story of a building submodel and return period. The volume under a specific region of this distribution gives the joint occurrence probability of X and Y within that region. Consequently, the volume under the entire distribution is 1.0 consistent with the total probability theorem.

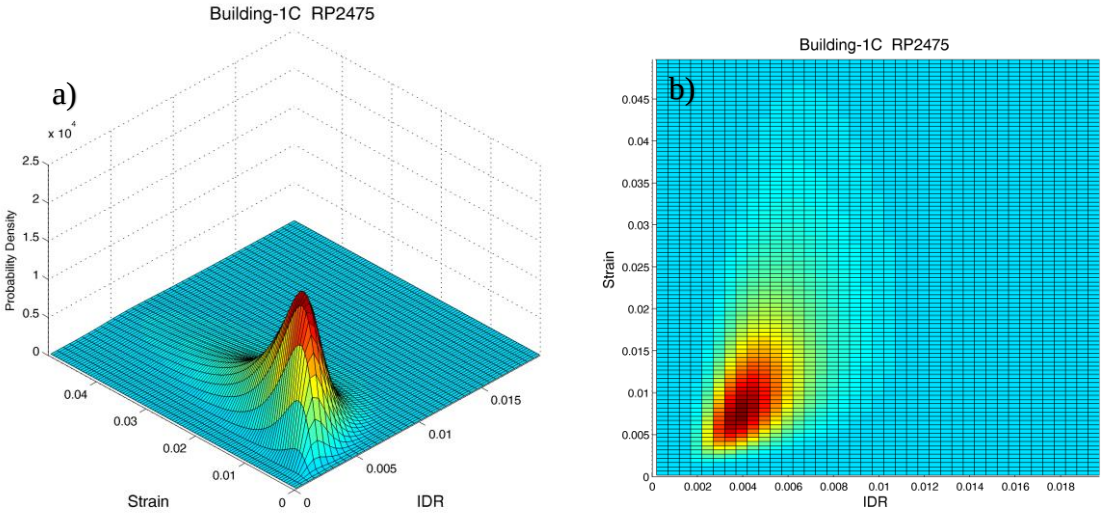

Figure 5.17. A sample joint probability distribution of shear wall strain and IDR datasets of Building 1C. The story is chosen as ground level and dataset is computed from the ground motions of 2475-year return period

The joint probability density functions of *shear wall strain-IDR* data pairs are generated at multiple *story-return period* pairs. The surface of these distributions are then divided into regions marked by the performance limits of shear wall strains and interstory drift ratios. The strain performance levels are already presented in previous subsection (Table 5.3), while IDR limits are adopted from the recommendations of Ghobarah (2004) for ductile shear wall buildings. These IDR limits are 0.8%, 1.5% and 2.5% marking immediate occupancy, life safety and collapse prevention performance levels. An impotant note about the IDR data is that they are the vectorial resolution of IDR values in both principal directions: $\sqrt{({IDR_{H1}}^2 + {IDR_{H2}}^2)}$. The vector-based definition of IDR is consistent with the shear wall strains that are computed as the vector resultant of core wall strains in both principal directions.

The joint PDF surfaces are divided into 4*4=16 sub-regions. The main objective lying under this practice is as follows:

1) To express the prominent performance indicator (either shear wall strain or IDR) governing the level of damage at a given story level,

2) To delineate transitions between different damage states and their levels at at different return periods of earthquake induced hazard.

Figure 5.18 illustrates the probability computations of different performance regions (16 regions as previously indicated). The dashed lines shown on the plan view of a given joint PDF (Figure 5.18a) repreent performance limits discussed in the previous lines. The alphanumeric labels given in Figure 5.18b is used to represent performance regions. For example, A1 region denotes that shear walls are in *immediate occupancy* damage state while IDR at the given story shows *life safety* performance level. Similarly, B1 region indicates that shear walls are in life safety while IDRs are at "immediate occupancy".

The volumes under each region are calculated to obtain the probabilities of performance regions. Note that A1, A4 and A6 regions of damage dominated by IDR whereas B1, B4 and B6 are regions of damage dominated by shear wall strains. The diagonal performance (damage) regions are equally dominated by shear wall strains and IDRs.

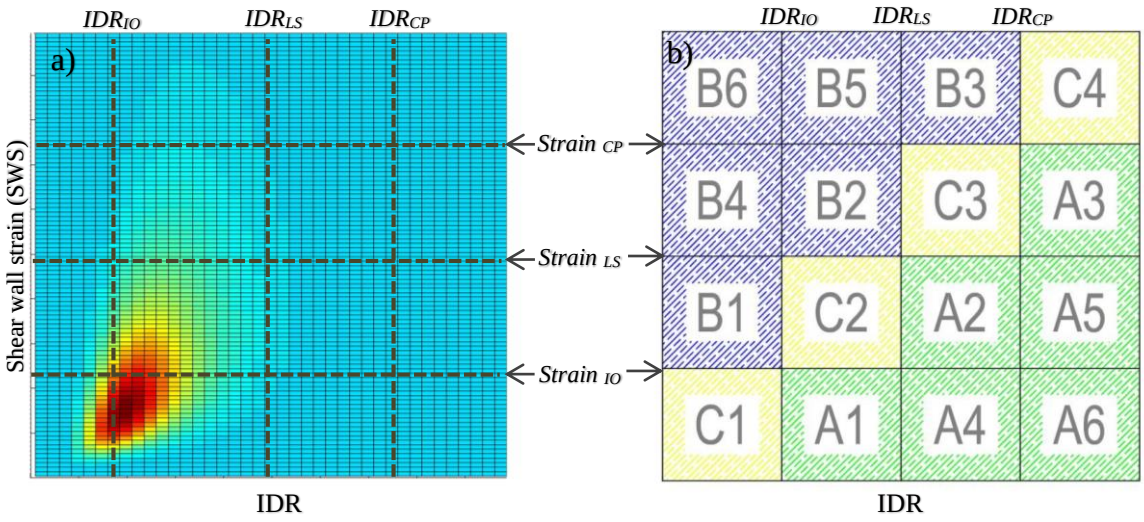

Figure 5.18. Representation of performance region definitions with their labelings (regions are not drawn to scale)

The outcomes of above computations are presented as probabilities, and they are given for all building models. Figure 5.19 shows two sample vertical bar plots displaying the performance region probabilities at 475- and 2475-year return periods. The vertical bar heights and their colors are associated with probability of observing a certain damage region contributed by shear wall strain and IDR. Although the computed probabilities differ from

one model to the other, certain trends can be immediately observed: a) the performance level is governed by flexural shear wall damage state at ground story levels (large B1 probabilities at the ground story indicating *LS* performance for shear walls) and b) for stories above the ground level the damage is dominated by IDR because both histograms show probabilities of A1 and A4: *LS* and *CP* performance levels for IDR and *IO* for shear walls. Similar calculations are performed across all return periods and are presented in Appendix B to picture the change in probability depending on the ground motion intensity level. In the following subsection, a comperative performance assessment of group-1 and group-2 buildings is given in terms of joint PDFs.

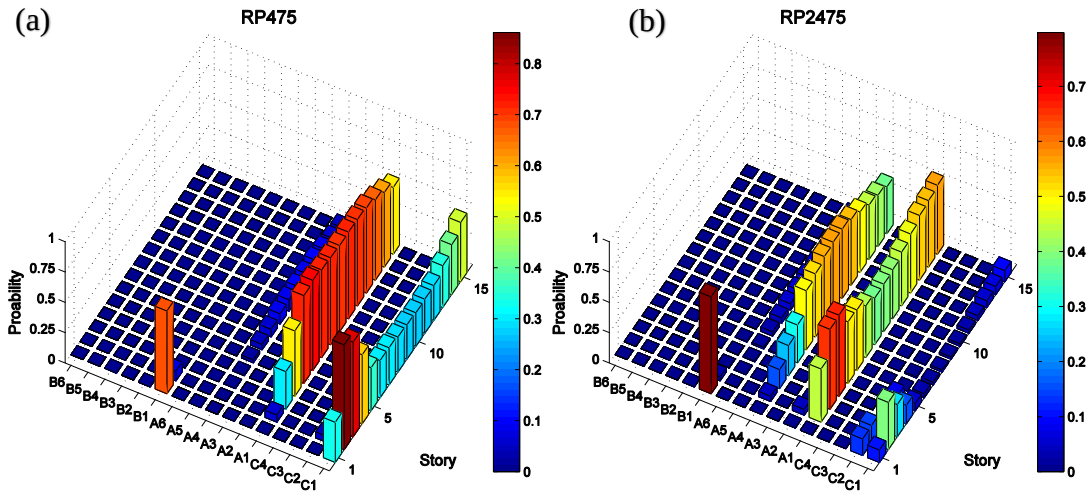

Figure 5.19. Probabilities of performance regions calculated from the joint PDF of corewall tensile strains versus IDRs at (a) DBE level and (b) MCE level for building 1A.

5.4.3.1. Overview of the Performance Region Probabilities of Model Buildings

Although the distribution of different performance region probabilities along the building heights do not differ significantly from one model to another, several different tendencies are observed. They are summarized in the following lines:

1) C1 probabilities (*IO* performance level for IDR and shear wals) are prominent along the height of group-1 and group-2 building models for ground motions with return periods up to 475 years.

2) For 475- to 2475-year return periods, large B1 and C1 probabilities at the ground story of the buildings suggest *IO* or *LS* performance for shear wall strains and *IO* for IDRs.
3) A1 and A4 performance regions represent the largest probabilities above the ground story of the buildings indicating *LS* or *CP* performance level for IDRs and *IO* for shear walls under 475-year return period.
4) A4 and A6 bars gain in height with increasing ground motion intensity level (particularly after 1500- to 2475-year return periods). Distribution of the probabilities of these performance regions along the building heights indicate that A4 and A6 probabilities reach to their highest values in mid-to-upper stories.
5) It is observed that there is a shift in the mid to upper story probabilities towards less critical performance regions in terms of IDR particularly in group-2 buildings (e.g., a shift in the vertical bar heights from A6 to A4, or from A4 to A1, or from A1 to C1: Figure 5.20)

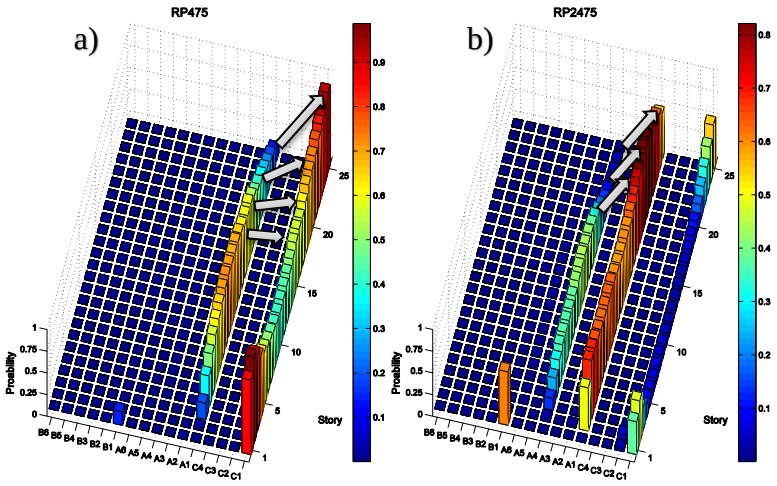

Figure 5.20. Illustration of the shift (shown by arrows) in the performance region probabilities towards less critical performance levels (damage states) for IDR in building 2A. (a) 475-year return period and (b) 2475-year return period.

6. FRAGILITY ASSESSMENT

6.1. General

There are various ways to assess the seismic performance of structures. Fragility curves, in this context, have become more tools of the seismic performance assessment. By definition, fragility curves are continuous structural response functions that express the probability of exceeding predefined damage states for a range of ground motion intensity levels. In this subsection, an overall review of existing fragility calculation methodologies is delivered to cover the approaches that are employed for the generation of fragility curves.

One simple method of obtaining fragility curves is to utilize expert judgement. Relying on expert opinion is often inevitable in regions where empirical data is limited, or where the fragility components are difficult to model. Several researchers contributed to the establishment of a systematic framework that relies on expert opinion to develop expert-based fragility functions (Von Winterfeld, 1989; Winkler et al. 1992). Expert-based fragility curves are first reported in ATC-13 (ATC, 1985) using the opinions of 58 experts for 40 different structure classes whose data were collected by ATC surveys.

Fragility functions can also be generated by observing post-earthquake structural damage. Sets of data are compiled in view of these observations and they are used with statistical procedures to develop fragility curves. This method may not be desirable because the data usually pertain to particular earthquakes making it disadvantageous for large-scale, general implications. An eartly study following this approach is carried out by Whitman et *al.* (1974) where the researchers investigated the structural damage of 5-story (masonry and reinforced concrete) buildings after 1971 the San Fernando earthquake, California. It was concluded by the researchers that this method inherits a major drawback that is the difficulty of forming a systematic rationale for evaluating structural damage specific to structural components.

Another alternative for developing fragilities is to use experimental data (e.g., Constantinou et *al*., 2000). Although there is an increasing trend in adopting this procedure for fragilities, there are limitations for its use both in time and monetary perspectives. Testing

large scale experimental models is not practical in most cases and it is very expensive as well as time consuming to perform parametric studies on such laboratory models.

Analytical approaches are widely and most commonly used procedures to develop fragility curves because they follow a systematic procedure by defining a transparent and direct relationship of each computational step under PBEE framework (e.g., Ji et *al.*, 2007). The analytical approaches entail the use of numerical building models to investigate structural performance they inherently require large suits of input data to compute accurate fragilities at the cost of a higher computational effort. In this study, an analytical approach (Baker, 2014) is adopted to produce fragility functions. Probabilities of exceeding certain performance limits for all building submodels are presented at multiple earthquake scenarios to achieve a qualitive understanding of structural damage for the target high-rise building stock.

6.2. Damage States and Performance Indicators

The maximum inter-story drift ratios are used as EDPs to develop the probability of exceedence rates for discrete damage levels. MIDR is a widely used global parameter that correlates well with structural damage (HAZUS-MH: FEMA, 2003). Besides, the discussions in the previous chapter suggest that IDRs govern the structural damage for stories other than the ground story. Note that it is important to define meaningful limit states for structural damage. The proposed structural performance limits by various studies change for different types of structures. Distributions of damage, failure modes of structural members, flexibility or overall ductility of different systems are among the factors that affect these performance limits. There are recommendations available in building codes, seismic guidelines and individual studies for performance levels in terms of interstory drift ratios. ASCE/SEI-41 (2006) provisions suggest the following performance criteria for tall shear wall structures:

- 0.5% for “Immediate Occupancy*”* (*IO*)
- 1.0% for “Life Safety*”* (*LS*)
- 2.0% for “Collapse Prevention*”* (*CP*)

The SEAOC Blue Book (SEAOC, 1999) lists performance levels for tall shear wall structures at *Negligible Damage, Minor-to-Moderate Damage, Moderate-to-Major Damage* and *Collapse Prevention* levels. The suggested MIDR values for these performance levels are: 0.4%, 0.9%, 1.4%, 2.1%, respectively, for RC shear wall structures. However, the code-recommended (by ASCE or SEAOC) MIDR limits tend to be on the conservative side and they might not necessarily imply reaching these performance limits. Less conservative MIDR limits are available in the literature based on analytical and experimental results. Ghobarah (2004) proposed MIDR limit states similar to those given in SEAOC (1999) by adopting a less conservative performance limit for *collapse*. These limits associated with different damage levels are given below.

- 0.4% for "Light Repairable Damage"
- 0.8% for "Irreparible Damage"
- 1.5% for "Severe Damage"
- 2.5% for "Collapse"

Figure 6.1 presents the base shear versus roof drift (maximum roof displacement normalized by building height) relationship given in Ghobarah (2004). In this figure, roof drifts are related to a suite of damage state expressions that are associated with structural behaviour. Note that these damage states (performance levels) are only valid if the building of interest does not undergo brittle failure modes.

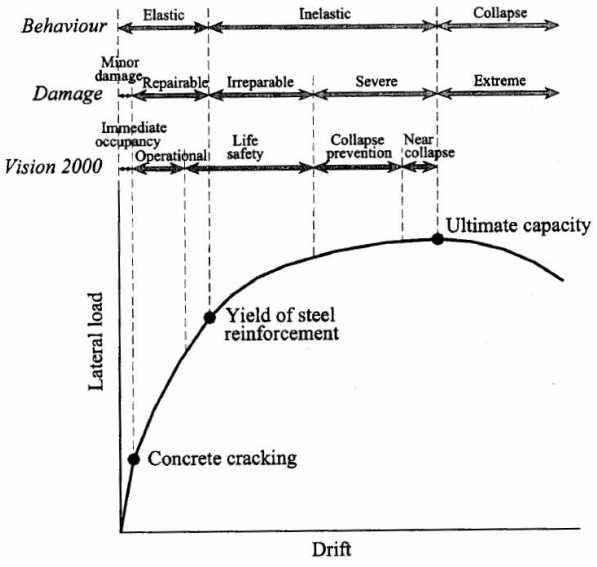

Figure 6.1. Typical levels of structural performance (damage states) by Ghobarah (2004)

In the light of above discussions MIDR limits suggested by Ghobarah (2004) are used to describe the damage states in fragility computations of tall building inventory. Considering the performance levels of Ghobarah (2004) *repairable damage* refers to a state of damage where flexural and shear cracks start to occur in concrete. '*Irreparable Damage*' is associated with the onset of yielding in longitudinal steel in structural members. Plastic hinges start to form in shear walls at the base of the structure. '*Severe Damage*' state translates into exceedence of capacity for lateral load carrying elements of the building or partial collapse.

6.3. Development of Analytical Fragility Curves

As discussed previously, fragility curves represent the probability of exceeding certain damage levels as a function of ground motion IM. There are few methods available for collecting damage versus ground motion IM data to develop analytical fragility curves. A fairly straightforward procedure is proposed by Vamvatsikos and Cornell (2002) that is called as incremental dynamic analysis (IDA). IDA is a computer intensive procedure and it performs a series of nonlinear response history analyses by using multiple ground motion records. Each ground motion within a suite is scaled incrementally by considering a preselected ground motion IM (e.g., PGA, spectral acceleration at fundamental period, etc.) The building is analysed via NRHA after each incremental scaling and the interested EDPs versus scaled ground motion IMs are collected until the collapse of subject building. The procedure is repeated for the entire ground motion recordings in the dataet to collect relevant data (ground motion IMs versus EDPs of interest) for fragility.

Estimating fragility parameters from IDA is fairly straightforward. The ground motion IMs and corresponding EDPs of interest at which collapse occurs comprise tha dataset from which the logarithmic mean and standart deviations for fragilities are calculated. Method of moments (Method A in Porter et *al.*, 2007) is widely used to estimate these parameters. Equation 6.1 and 6.2 presents the computation of logarithmic mean ($\ln\hat{\theta}$) and standart deviation ($\hat{\beta}$) using the method of moments. Obviously, the observed structural data are assumed to fit a lognormal distribution in these calculations.

$$\ln\hat{\theta} = \frac{1}{n}\sum_{i=1}^{n} IM_i \tag{6.1}$$

$$\hat{\beta} = \sqrt{\frac{1}{n}\sum_{i=1}^{n}\left(ln\left(IM_i/\hat{\theta}\right)\right)^2} \tag{6.2}$$

Incremental Dynamic Analysis is not utilized in this study because it is mainly intended to develop collapse fragilities. The objective of this thesis is to develop fragilities for various damage states. The computational burden is the other reason for not utilizing IDA for fragilities. The last reason for not utilizing IDA Is the inherent scaling strategy of this procedure that brutally enforces the ground motions to attain very large amplitudes to observe collapse. Such large scalings of ground motion amplitudes may be arguable in terms of seismological features of ground motions. The procedure used for collecting analytical fragility development is explained in the following section.

6.3.1. Multiple Stripes Analysis

This study uses multiple stripe analysis (MSA) for collecting damage versus ground motion IM data to develop analytical fragilities. The method can be incorporated with CS-based ground motion scaling. The ground motions scaled via CS-based target spectrum at various hazard levels would not yield extreme ground-motion amplitudes that one might expect from IDA-based scaling (see discussions in the above paragraphs). Besides, the scaled ground motions would represent specific hazard levels that might be more proper in PBEE-oriented engineering practice (e.g., Jayaram et *al.*, 2012; Kohrangi, 2015).

The MSA method is used together with the procedure proposed by Baker (2014) to develop analytical fragilities for different damage states. The procedure by Baker (2014) is suitable for CS-based ground motion scaling. The probability distribution that the structure reaches or exceeds a certain damage level is assumed to be lognormal. This assumption is observed to yield reasonable fits for fragility curves of various damage states in studies by different researchers (Porter et *al.*, 2006; Mwafy et *al.*, 2015). The lognormal cumulative

distribution to compute the probability of exceeding a damage state, P(*DS*>*ds* | *IM*=*im*), given a ground motion IM, *im*, is presented in Equation 6.3.

$$\mathrm{P}(DS > ds \mid IM = im) = \Phi\left(\frac{\ln(im/\theta)}{\beta}\right) \tag{6.3}$$

In Equation 6.3 Φ(.) represents the standart normal cumulative distribution function, θ is the median (logarithmic mean) of the fragility function and β is the logarithmic standart deviation of ln*IM* . Baker (2014) indicates that the maximum likelihood method (MLE) is the most appropriate statistical tool to fit a fragility curve to the observed data. One remark regarding the superiority of MLE in comparison with an alternative procedure such as the sum of the squared errors (SSE) method is that the former recognizes the variance of the observed fractions of exceeding a damage state. This way the fragility function can take values greater than zero for IM levels where fractional observations take zero values. This particular feature of MLE considers the probability of observing damage at such ground motion IM levels that can be overlooked by SSE.

For a given intensity level IM=*im*, the likelihood of observing z_j exceedence of a damage level out of n_j ground motions having *IM = im* is given by the binomial distribution (Equation 6.4).

$$P(z_j \; occurences \; in \; n_j \; ground \; motions) = \binom{n_j}{z_j} p_j^{\,z_j} \left(1 - p_j\right)^{n_j - z_j} \tag{6.4}$$

Here, p_j is the probability of a ground motion with *IM = im* will lead to exceedence of a certain damage state for the considered structure. For multiple, *m* intensity levels, the product of the binomial probabilities gives the final probability. Since different sets of ground motions are selected for different levels of ground motion intensities, the assumption of independant observations would validate taking the products of likelihoods at each IM level, for computing the overall likelihood as shown in Equation 6.5.

$$Likelihood = \prod_{i=1}^{m} \binom{n_j}{z_j} p_j^{\,z_j} \left(1 - p_j\right)^{n_j - z_j} \tag{6.5}$$

The estimates of the fragility function paramers θ and β are denoted as $\hat{\theta}\ and\ \hat{\beta}$. They are obtained by maximizing the likelihood function given in Equation 6.5 after substituting Equation 6.3 for p_j. Logarithm of the likelihood is maximized since it is numerically easier to do so. This is given in Equation 6.6.

$$\{\hat{\theta},\hat{\beta}\} = \text{argmax}_{\theta,\beta} \sum_{j=1}^{m} \left\{ ln\binom{n_j}{z_j} + z_j \ln\Phi\left(\frac{\ln(im_j/\theta)}{\beta}\right) + (n_j - z_j)\, ln\left(1 - \Phi\left(\frac{\ln(im_j/\theta)}{\beta}\right)\right)\right\} \tag{6.6}$$

6.3.2. Fragility Curves of the High-Rise Building Stock

The fragility curves are developed for multiple damage states for all building submodels. Fractions at each IM stripe analysis are represented by different symbols to display the agreement between these fractions and the continuous fragility functions. The fragility functions represent the probability of exceeding different damage states, as a function of IM. Note that the chosen IM for fragilities is the target spectral acceleration at the average of fundamental periods along two principal directions of the building models. This is already discussed in Chapter 4 while describing the CS-based scaling of ground motions. Fragilitiy curves for group-1 and group-2 buildings are presented in Figure 6.2 and Figure 6.3, respectively.

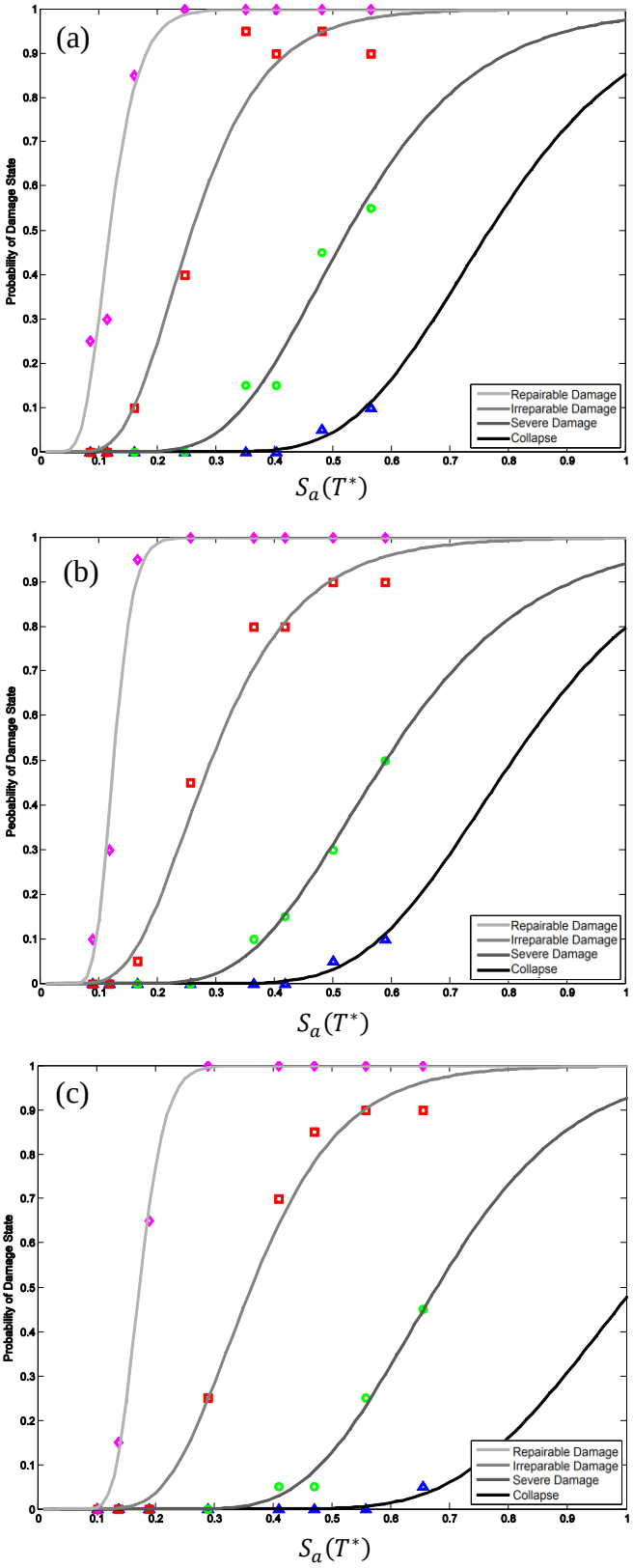

Figure 6.2. Fragility curves of damage states for (a) building 1A, (b) building 1B and (c) building 1C. In the x-axes, $T^* = 0.5(T_{1x} + T_{1y})$.

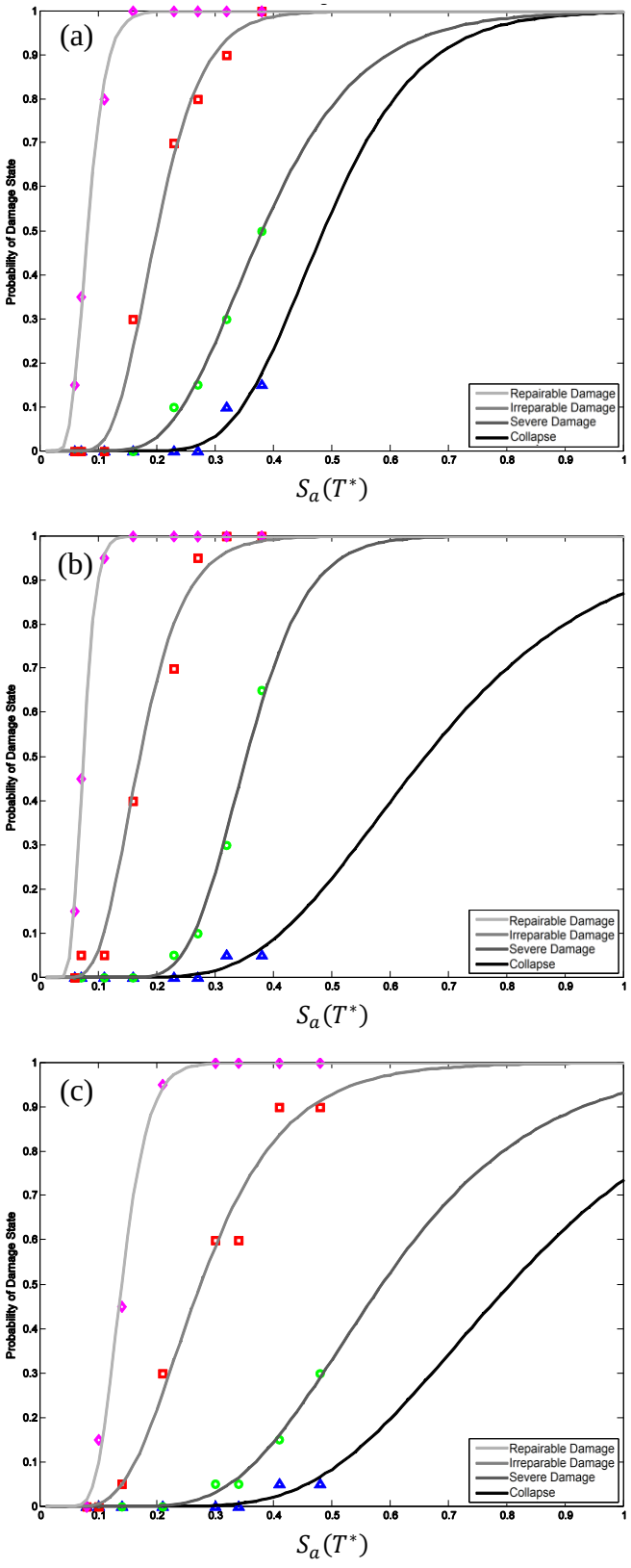

Figure 6.3. Fragility curves of damage states for a) building 2A, (b) building 2B and (c) building 2C. In the x-axes, $T^* = 0.5(T_{1x} + T_{1y})$.

6.4. Multiple-Level Seismic Performance Evaluation

A probabilistic, multiple-level seismic performance assessment procedure conveys information about the capacity of a building for fulfilling certain performance levels based on a set of acceptance criteria under multiple ground motion intensities. Earthquake ground motions can be generalized as frequent, occasional, rare and maximum considered (or maximum credible) as a function of hazard return periods 25, 75, 250 to 800 and 800 to 2500 years respectively (SEAOC, 2003). In this study, probability of observing damage states are evaluated at 43-, 72-, 475- and 2475-year return period seismic hazard levels. Because modern seismic codes define different performance objectives at these levels of ground shaking. Table 6.1 lists the hazard levels and their classifications that are used for structural performance assessment of tall buildings considered in this study.

Table 6.1. Quantatively described ground motion intensity levels

Ground motion Classification	**Return Period**	**Exceedence Probability**
Frequent	43-year	69% in 30 years
Occasional (operational)	72-year	50% in 50 years
Rare (design basis)	475-year	10% in 50 years
Maximum Considered	2475-year	2% in 50 years

The probabilities of observing pre-determined damage states (*no damage*, *repairable damage*, *irreparable damage*, *severe damage* and *collapse*) are computed from fragility functions in the previous section. A range of all probable damage states are covered where, according to the total probability theorem, the sum of probabilities of observing all damage states equals to 100%. The distribution of these damage state probabilities for the investigated tall building stock are presented in Figure 6.4 to Figure 6.7.

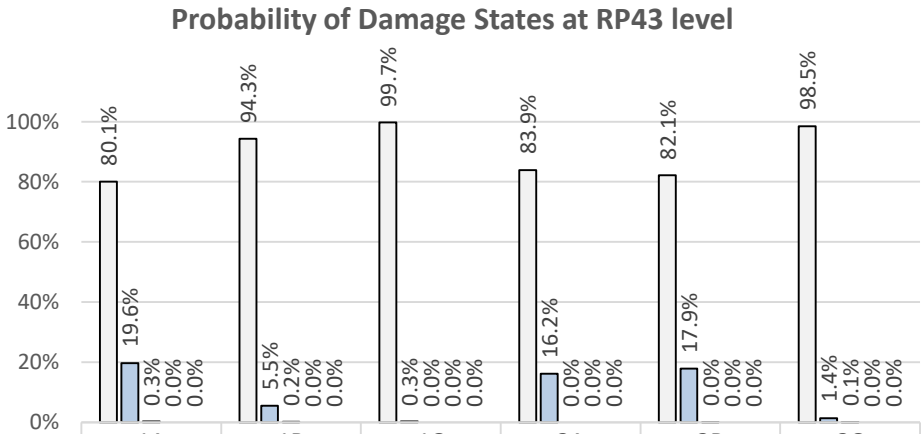

	1A	1B	1C	2A	2B	2C
No Damage	80.1%	94.3%	99.7%	83.9%	82.1%	98.5%
Repairable Damage	19.6%	5.5%	0.3%	16.2%	17.9%	1.4%
Irraparable Damage	0.3%	0.2%	0.0%	0.0%	0.0%	0.1%
Severe Damage	0.0%	0.0%	0.0%	0.0%	0.0%	0.0%
Collapse	0.0%	0.0%	0.0%	0.0%	0.0%	0.0%

Figure 6.4. Probabilities of damage states for the investigated building inventory under 43-year (frequent) ground shaking

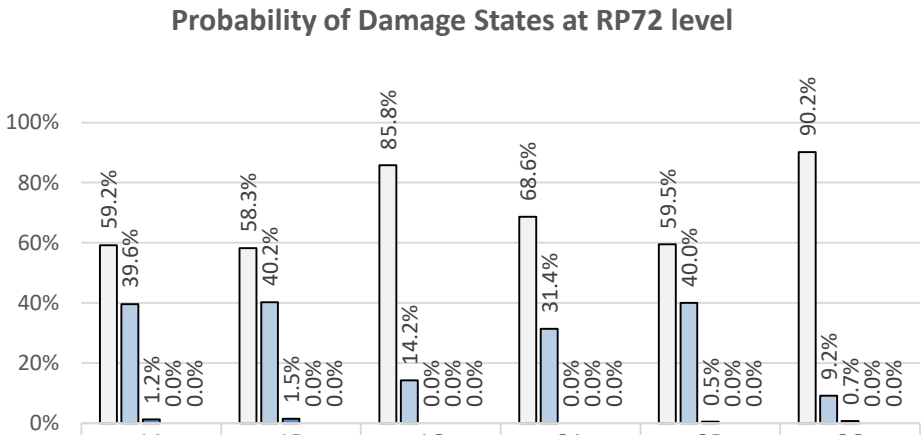

	1A	1B	1C	2A	2B	2C
No Damage	59.2%	58.3%	85.8%	68.6%	59.5%	90.2%
Repairable Damage	39.6%	40.2%	14.2%	31.4%	40.0%	9.2%
Irraparable Damage	1.2%	1.5%	0.0%	0.0%	0.5%	0.7%
Severe Damage	0.0%	0.0%	0.0%	0.0%	0.0%	0.0%
Collapse	0.0%	0.0%	0.0%	0.0%	0.0%	0.0%

Figure 6.5. Probabilities of damage states for the investigated building inventory under 72-year (operational) ground shaking

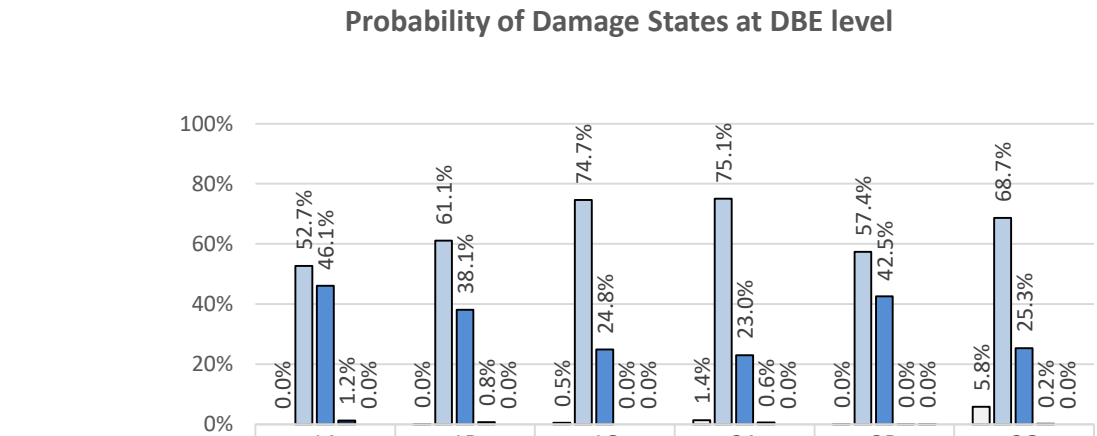

	1A	1B	1C	2A	2B	2C
No Damage	0.0%	0.0%	0.5%	1.4%	0.0%	5.8%
Repairable Damage	52.7%	61.1%	74.7%	75.1%	57.4%	68.7%
Irraparable Damage	46.1%	38.1%	24.8%	23.0%	42.5%	25.3%
Severe Damage	1.2%	0.8%	0.0%	0.6%	0.0%	0.2%
Collapse	0.0%	0.0%	0.0%	0.0%	0.0%	0.0%

Figure 6.6. Probabilities of damage states for the investigated building inventory under 475-year (DBE) ground shaking

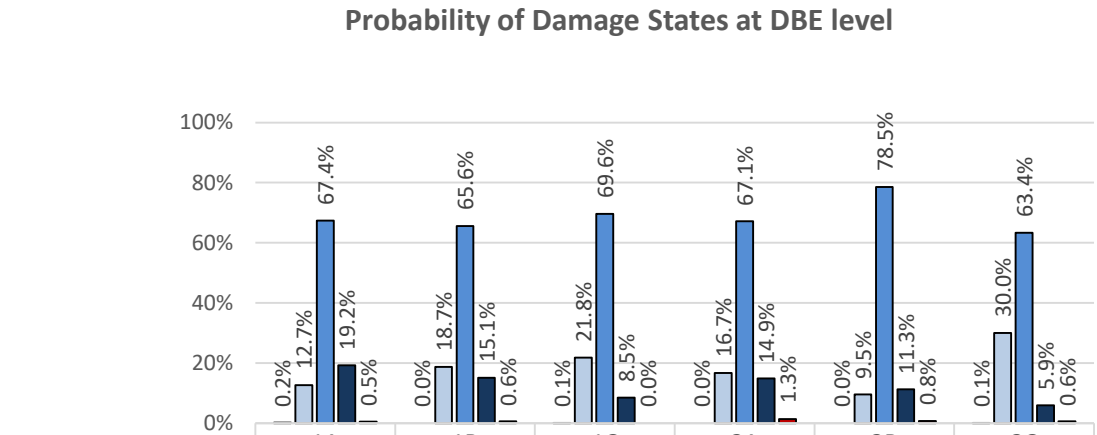

	1A	1B	1C	2A	2B	2C
No Damage	0.2%	0.0%	0.1%	0.0%	0.0%	0.1%
Repairable Damage	12.7%	18.7%	21.8%	16.7%	9.5%	30.0%
Irraparable Damage	67.4%	65.6%	69.6%	67.1%	78.5%	63.4%
Severe Damage	19.2%	15.1%	8.5%	14.9%	11.3%	5.9%
Collapse	0.5%	0.6%	0.0%	1.3%	0.8%	0.6%

Figure 6.7. Probabilities of damage states for the investigated building inventory under 2475-year (MCE) ground shaking

The following observations can be made from the computed damage state probabilities in Figure 6.4 to Figure 6.7:

1) The probability of observing no damage is significant (over ~60%) under 43-year and 72-year ground motions for group-1 and group-2 buildings. Inherently, no damage probability is larger under 43-year ground motions.
2) No damage performance level is followed by repairable damage state under 43-year and 72-year ground motions. The probability of observing repairable damage decreases and probability of observing no damage increases with increased SW area ratio under 43-year and 72-year ground motions.
3) State of observing no damage is almost null under DBE (475-year) level ground shaking. The investigated buildings would damage when they are subjected to DBE level ground motions and the probability of observing repairable damage is larger than the probability of observing irreparable damage. Similar to 43-year and 72-year ground motions SW area ratio plays a role in observing larger probabilities of repairable damage.
4) There is no systematic effect of story number on the observed damage states. However, this observation can be particular to the IDR-based fragilities and results might change upon the derivation of similar fragilities for SW strains.
5) The probability of irreparable damage is significant regardless of SW area under 2475-year (MCE level) ground motions. The consequential monetary loss could be significant for such tall buildings ubder MCE level ground shakings. The investigated building inventory would experience severe damage at this ground shaking level that might also imply significant engineering roles which should be the topic of future studies. The increased SW area decreases observing severe damage probability.

7. SUMMARY AND CONCLUSIONS

7.1. Summary

High-rise reinforced concrete (RC) buildings in the metropolitan cities of Turkey having 10 to 30 stories are investigated within the scope of this thesis. A building inventory is compiled including blueprints of tall buildings from densely populated areas of cities such as Istanbul, Ankara, Bursa and Mersin. Buildings in the inventory are investigated thoroughly by undertaking a statistical survey over their key structural properties. A hierarchical methodology is adopted for the categorization of these buildings. They are evaluated under two major groups: Group-1 and Group-2. 10 to 20 story core wall-frame buildings are mimicked by 15-story group-1 building models whereas 20 to 30 story buildings are represented by 25-story models. Each major group contains three submodels. Shear wall configurations are used to develop these submodels under two major groups. Core shear wall area (normalized by plan dimensions) information in both orthogonal axes of the structures are used to determine the subcategorization. All building models are intended to represent tall building design and constructuion practice in Turkey.

The building models are subjected to nonlinear response history analyses (NRHA) by considering the PSHA studies in Akkar et al. (2015). All models are assumed to be located in a highly seismic prone region that is chosen as Kartal district in Istanbul (40.9°N and 29.2°E). A total of 640 two-component horizontal ground motions from PEER-NGA database are used for NRHA. The conditional spectrum (CS: Lin et *al.*, 2013) is used as the target spectrum in scaling of ground-motion at different hazard levels (return periods). The ground motion selection and scaling algorithm developed by Jayaram et *al.* (2011) is utilized for this process. 20 pairs of mutually perpendicular horizontal accelerograms are scaled for the pre-selected return periods: 43, 72, 150, 475, 1500, 2475, 5000 and 10000 years. A total of 960 nonlinear response history analyses (NRHA) are performed on six 3D nonlinear structural models. Engineering demand parameters (EDPs) obtained from NRHA are evaluated to provide performance level statistics about the dynamic behaviour of the building stock under multiple hazard levels (ranging from 43-year to 10000-year return period). Analytical fragility functions are generated using multiple stripes analysis (MSA)

method proposed by Baker (2014). Probability distributions of intenstory drift ratios (IDRs) and shear wall strains, their correlations and joint as well as conditional probabilities are developed to seek the governing EDP in tall buildings to identify different damage states. The fragility curves are developed for multiple damage states using maximum interstory drift ratio (MIDR) as the damage indicator. A multiple-level seismic performance assessment is carried out using fragility data to assess whether if the investigated tall building stock fulfils certain performance criteria at different return period ground motions.

7.2. Conclusions

The following conclusions can be highlighted from this study:

1) MIDR-based fragilities indicated that Group-2 buildings (20 to 30 stories), in most cases, show slightly better performance with respect to Group-1 buildings (10 to 20 stories).
2) In general, increase in shear-wall area ratio implies better performance of tall buildings.
3) The nonlinear response history analyses indicate that the plastic hinges are generally located at the ground level on core shear walls.
4) In the majority of cases, tensile strains in reinforcing steel dominates the overall performances of the core shear walls. This observation indicate that the core walls principally deform under flexural mode as expected. Crushing of concrete is generally observed after 2475-year return period ground motions.
5) Shear force demands on shear walls can attain large values at heights significantly above ground level where the plastic hinging occurs on the core walls. Beyond 475-year return period shaking, diagonal shear cracks occur in web shear wall panels of the core wall configurations multiple stories above ground level. The validity of this information is sensitive to the nonlinear modelling assumptions in shear force-deformation relationships of core wall sections. The complex nature of axial/flexural-shear force interaction inherent in these structural members make the realistic modelling of shear walls difficult. In this study, flexure-shear force interaction is disregarded.

6) Probabilistic damage state assessments showed that MIDR-based performance levels indicate more critical damage in the building models compared to the performances achieved based on shear wall strains.
7) The tall shear wall buildings designed and constructed in Turkey generally comply with the performance criteria set for MIDR (PEER, 2010; ASCE, 2010) for frequent (43-year), occasional (72-year) and design basis (475-year) ground motion. However, the structural analyses suggest that the tall buildings in Turkey would most likely experience irreparable and severe damage under ground shakings corresponding to maximum considered earthquake (MCE, 2475-year). The observation suggests that monetary losses can be significant for tall buildings in Turkey under MCE level ground shaking.
8) It is observed that the sudden change in reinforcement configuration of the shear walls above plastic hinge regions can cause undesirable yielding of reinforcement in shear walls at these floor levels. Therefore, this design practice is discouraged based on the findings in this study.

7.3. Recommendations for Future Studies

In this study, the characteristics and dynamic behavior of tall RC core wall-frame buildings are investigated. Given the conclusions drawn, following items are outlined as recommendations for future studies:

1) Only the core wall-frame building class is investigated within the context of this thesis. However, the Turkish tall building stock is not solely composed of this building class. Therefore similar studies encompassing other tall building classes can provide further information to be able to make a comperative assessment of vulnerabilities of different tall building classes.
2) The results of NRHA depend on the adopted ground-motion selection and scaling procedure. In this study, a scalar ground-motion intensity measure, $Sa(T^*)$, is used. The parameter T^* is the average of translational fundamental periods, T_{1x} and T_{1y} along the two orthogonal directions (note that some of the building models are dominated by torsional modes). The conditioning period (T^*) significantly impacts spectral shape of the target spectrum. Therefore, considering only the first two

translational modes of tall buildings in determining the target spectra may not lead to monitoring the whole structural response. To this end, the use of vector-based intensity measures can be useful.

3) Although it is still limited by most of the current structural analysis software packages, modelling of axial/flexural-shear interaction in shear walls can result in significant discrepancies in structural responses compared to modelling assumptions relying on uncoupled axial/flexural-shear behavior. This case is demonstrated by various researchers. Therefore, it should be investigated by using more sophisticated models that are capable of appropriately mimicking this phenomenon in shear walls.

REFERENCES

Abrahamson, N.A., and Silva, W., "Summary of the Abrahamson & Silva NGA ground-motion relations". *Earthquake spectra, 24(1), 67-97,* 2008.

Abrahamson N.A, Bozorgnia Y., Boore D., Atkinson G., Campbell K., Silva, W., Chiou, B., Idriss, I.M., Youngs R., "Comparisons of the NGA ground-motion relations*". Earthq Spectra 24(1):45–66,* 2008.

Adebar, P., Mutrie, J.G., DeVall, R. and Mitchell, D., "Seismic design of concrete buildings: The 2015 Canadian Building Code", *In Proc. of 10th Nat. Conf. on Earthquake Eng,* 2014.

Akkar, S., Çağlar, N.M., Odabaşı, Ö., "Earthquake Induced Damage Assessment and Demolition Procedures for Tall Buildings", *project funded by the Ministry of Environment and Urban Urbanization,* 2015.

Aslani, H., "Probabilistic Earthquake Loss Estimation and Loss Disaggregation in Buildings", *Doctoral Thesis, Stanford University, Stanford, CA,* 2005.

ACI, "Building Code Requirements for Structural Concrete and Commentary", *ACI 318-08, American Concrete Institute, Farmington Hills, Michigan,* 2008.

ACI, "Building Code Requirements for Structural Concrete and Commentary", *ACI 318-11, American Concrete Institute, Farmington Hills, Michigan,* 2011.

ASCE, "Minimum Design Loads for Buildings and Other Structures, ASCE/SEI 7-05", *American Society of Civil Engineers, Reston, Virginia,* 2005.

ASCE, "Minimum Design Loads for Buildings and Other Structures, ASCE/SEI 7-10", *American Society of Civil Engineers, Reston, Virginia,* 2010.

ASCE 41-13, “Seismic Evaluation and Retrofit of Existing Buildings”, 2013.

ATC 72-1, “Modeling and Acceptance Criteria for Seismic Design and Analysis of Tall buildings”, *Technical report,* 2010.

Azak T. E., Ay, B.Ö., Akkar, S., “A statistical study on geometrical properties of turkish reinforced concrete building stock”, *Second European conference on earthquake engineering and seismology, Istanbul Aug. 25-29,* 2014.

Bal, İ. E., Crowley, H., Pinho, R., & Gülay, F. G., “Detailed assessment of structural characteristics of Turkish RC building stock for loss assessment models*”, Soil Dynamics and Earthquake Engineering, 28(10), 914-932*, 2008.

Berry, M., Parrish, M. and Eberhard, M., “PEER Structural Performance Database User’s Manual”, *Pacific Earthquake Engineering Research Center, Univ. of California, Berkeley,* 2004.

Boore, D. M., Watson-Lamprey, J., and Abrahamson, N. A., “Orientation-independent measures of ground motion”, *Bulletin of the seismological Society of America, 96(4A), 1502-1511,* 2006.

Boore, D. M., Atkinson, G. M., “Ground-motion prediction equations for the average horizontal component of PGA, PGV, and 5%-damped PSA at spectral periods between 0.01 s and 10.0 s”, *Earthquake Spectra, 24(1), 99-138*, 2008.

Calvi, G.M., Pinho, R., Magenes G., Boomer J.J., Restrepo-Velez L.F. and Crowley H., “Development of seismic vulnerability assessment methodologies over the past 30 years”, *ISET Journal of Earthquake Technology, 43(3):75-104*, 2006.

Campbell, K. W., & Bozorgnia, Y., “NGA ground motion model for the geometric mean horizontal component of PGA, PGV, PGD and 5% damped linear elastic response spectra for periods ranging from 0.01 to 10 s”, *Earthquake Spectra, 24(1), 139-171*, 2008.

Charney, F.A., “Unintended consequence of modeling damping in structures: Rayleigh damping”, *Procedures of 17th Analysis and Computation Specialty Conference, American Society of Civil Engineers.,* 2006.

Chiou, B. J., & Youngs, R. R., “An NGA model for the average horizontal component of peak ground motion and response spectra”, *Earthquake Spectra, 24(1), 173-215,* 2008ç

Clough R. W., “Earthquake analysis by response spectrum superposition”, *Bull. Seism. Soc. Am., 1962, 52 (3) 647-660,* 1962.

Constantinou, M.C., Tsopelas, P., Hammel, W., and Sigaher, A.N., “New Configurations of Fluid Viscous Dampers for Improved Performance”, *Passive Structural Control Symposium, Tokyo Institute of Technology, Yokohama, Japan,* 2000.

Cornell, C.A., and Krawinkler, H., “Progress and challenges in performance assessment ”, *PEER Center News, 3(2), 4p,* 2004.

Elwood, K.J., Eberhard, M.O., “Effective Stiffness of Reinforced Concrete Columns”, *Research Digest No. 2006-1, A publication of the Pacific Earthquake Engineering Research Center,* 2006.

Elwood, K.J., Matamoros, A.B., Wallace, J.W., Lehman, D.E., Heintz, J.A., Mitchell, A.D., Moore, M.A., Valley, M.T., Lowes, L.N., Comartin, C.D., and Moehle, J.P., “Update to ASCE/SEI 41 concrete provisions,” *Earthquake Spectra, Vol. 23, No. 3, pp. 493-523,* 2007.

Fedak, L. K., “Evaluation of plastic hinge models and inelastic analysis tools for performance-based seismic design of RC bridge columns”, *In Masters Abstracts International (Vol. 51, No. 01),* 2012.

FEMA, H. M., “MR3 Technical Manual”, *Multi-hazard Loss Estimation Methodology Earthquake Model, HAZUS-MH,* 2003.

FEMA-440, “Improvement of nonlinear static seismic analysis procedures”, *ATC-55 Draft, Washington D.C.,* 2005.

FEMA, “NEHRP Recommended Seismic Provisions for New Buildings and Other Structures”, *Building Seismic Safety Council, Washington, D.C.,* 2015.

Ghobarah, A., “On drift limits associated with different damage levels*”, In International workshop on performance-based seismic design (Vol. 28). Dept. of Civil Engineering, McMaster University*, 2004.

Görgülü, O. and Taşkın, B., “Numerical simulation of RC infill walls under cyclic loading and calibration with widely used hysteretic models and experiments”, *Bull Earthquake Eng (2015) 13:2591–2610 DOI 10.1007/s10518-015-9739-9,* 2014.

GRM İletişim ve Bilişim, “Türkiye kapsamında ve özellikle İstanbul’da mevcut yüksek binaların fiziksel envanterinin hazırlanması”, 2015.

Hall, J.F., “Problems encountered from the use (or misuse) of Raleigh damping”, *Earthquake Engineering and Structural Dynamics, Vol. 35, No. 5, pp. 525-545,* 2005.

Hanks, TC., Kanamori, H., “A moment magnitude scale”, *J. Geophys. Res., 84B (1979), pp. 2348-2350,* 1979.

Haselton, C.B., and Deierlein G.G., “Assessing Seismic Collapse Safety of Modern Reinforced Concrete Moment Frame Buildings”, *PEER Report 2007/08, Pacific Earthquake Engineering Research Center, University of California, Berkeley, California,* 2007.

Jayaram, N., Lin, T., Baker, W., “A Computationally Efficent Ground-Motion Selection Algorithm for Matching a Target Response Spectrum Mean and Variance”, *Earthquake Spectra: August 2011, Vol. 27, No. 3, pp. 797-815,* 2011.

Ji, J., Elnashai, A. S., & Kuchma, D. A., “Seismic fragility assessment for reinforced concrete high-rise buildings”, *MAE Center CD Release 07-14,* 2007.

Liel, A. B., Haselton, C. B., Deierlein, G. G., & Baker, J. W., "Incorporating modeling uncertainties in the assessment of seismic collapse risk of buildings", *Structural Safety, 31(2), 197-211,* 2009.

Mehanny S.S.F., Kuramoto H., Deierlein G.G., "Stiffness modeling of RC beam-columns for frame analysis", *ACI Structural Journal 98(2): 215–225,* 2001.

Taranath, B., "Steel, concrete, and composite design of tall buildings", *McGraw-Hill Professional,* 1998.

Thomsen, I. V., Wallace, J. H., and Wallace, J. W., "Displacement- Based Design of Slender RC Structural Walls – Experimental Verification", *J. Struct. Eng., ASCE, Vol. 130, No. 4, 2004, pp 618~630,* 2004.

Kolozvari, K., Tran, T., Wallace, J. W. and Orakcal, K., "Modeling of cyclic shear-flexure interaction in reinforced concrete structural walls", *15th World Conference on Earthquake Engineering, Lisbon, Portugal,* 2012.

Kolozvari, K., Orakcal, K. and Wallace, J. W., "Shear-Flexure Interaction Modeling for Reinforced Concrete Structural Walls and Columns under Reversed Cyclic Loading", *PEER Report No. 2015/12,* 2015.

Laplace, P. S., "Leçons de mathématiques données à l'École normale en 1795". *Oeuvres complètes de Lapalace. Tome XIV, 10-177,* 1812.

LATBSDC, "An Alternative Procedure for Seismic Analysis and Design of Tall Buildings Located in the Los Angeles Region. Los Angeles, CA", 2014.

Lignos, D.G., and Krawinkler, H.,, "A database in support of modeling of component deterioration for collapse prediction of steel frame structures", *ASCE Structures Congress 2007, Long Beach, California,* 2007.

Lignos, D.G., "Sidesway Collapse of Deteriorating Structural Systems under Seismic Excitations", *Ph.D Thesis, Department of Civil and Environmental Engineering, Stanford University, Stanford, California,* 2008.

Lin, T., and Baker, J.W., "Conditional Spectra", *Encyclopedia of Earthquake Engineering DOI 10.1007/978-3-642-36197-5_386-1,* 2015.

Lin, T., Haselton, C., and Baker, J. W., "Conditional spectrum based ground motion selection. Part I: Hazard consistency for risk-based assessments", *Earthquake Engineering & Structural Dynamics, 41(11):1549—1568,* 2013a.

Lin. T., Harmsen S.C., Baker J.W., Luco N., "Conditional Spectrum computation incorporating multiple causal earthquakes and ground-motion prediction models", *Bull Seismol Soc Am 103(2A):1103–1116,* 2013b.

Mander, J.B.; Priestley, M.J.N., Park, R., "Theoretical Stress-Strain Model for Confined Concrete", *J. Struct. Eng., 10.1061 / (ASCE) 0733-9445 (1988) 114:8 (1804), 1804-1826,* 1988.

McGuire, R. K. (2004). "Seismic hazard and risk analysis". *Earthquake Engineering Research Institute, 2004.*

Menegotto, M. and Pinto E., "Method of Analysis for Cyclically Loaded Reinforced Concrete Plane Frames Including Changes in Geometry and Non-Elastic Behavior of Elements under Combined Normal Force and Bending*", Proceedings, IABSE Symposium on Resistance and Ultimate Deformability of Structures Acted on by Well-Defined Repeated Loads, Lisbon, Portugal,* 1973.

Sarja, A., "Integrated life cycle design of materials and structures", *CIB World Congress, Gävle, Sweden, June, vol. 8, p. 13,* 1998.

Orakcal, K. and Wallace, J. W., "Modelling of slender reinforced concrete walls", *13th World Conference on Earthquake Engineering, 18(1):141- -143,* 2004.

Orakcal, K. and Wallace, J. W., “Flexural Modeling of Reinforced Concrete Walls - Model Calibration,” *ACI Structural Journal, Vol. 103, No. 2, 2006, pp. 196~206*, 2006.

Orakcal, K., Massone, L. M., and Wallace, J. W., “Analytical modeling of reinforced concrete walls for predicting flexural and coupled-shear flexural responses”, *Pacific Earthquake Engineering Research Center, College of Engineering, University of California, Berkeley*, 2006.

Özmen, G., Girgin, K., Yavuz, D., “Torsional irregularity in multi-story structures”, *Int J Adv Struct Eng (2014) 6: 121. doi:10.1007/s40091-014-0070-5*, 2012

Pitilakis, K.D., Crowley, H. and Kaynia, A.M. (ed.), “SYNER-G: Typology Definition and Fragility Functions for Physical Elements at Seismic Risk”. *Springer Dordrecht Heidelberg New York London. doi:10.1007/978-94-007-7872-6,* 2014

Porter, K., Kennedy, R., and Bachman, R., “Creating fragility functions for performance-based earthquake engineering”, *Earthquake Spectra, 23(2), 471-489,* 2007.

Powell, G. H., “Detailed Example of a Tall Shear Wall Building Using CSI's Perform 3D Nonlinear Dynamic Analysis”, *Computers & Structures Educational Services,* 2007.

Power, M., Chiou, B.S.-J., Abrahamson, N., Bozorgnia, Y., Shantz, T., and Roblee, C., “An overview of the NGA project”. *Earthquake Spectra 24,3 – 21,* 2008.

Rosenblueth, E., “Earthquake resistant design”, *Appl. Mech. Rev., 1961,14 (12), 923-926,* 1961.

SEAOC Blue Book, Revised Interim Guidelines, *Performance-Based Seismic Engineering,* Structural Engineers Association of California, USA, 2003.

Silva, W., “Characteristics of vertical strong ground motions for applications to engineering design” *(No. Technical Report),* 1997.

Massey, F. J., "The Kolmogorov-Smirnov Test for Goodness of Fit", *Journal of the American Statistical Association. Vol. 46, No. 253, 1951, pp. 68–78,* 1951.

Mwafy, A., Nadeem, H. and Khaled, E.S., "Seismic performance and cost-effectiveness of high-rise buildings with increasing concrete strength*", The Structural Design of Tall and Special Buildings 24.4 (2015): 257-279,* 2015.

Park, R., Kent, D.C. & Sampson, R.A., "Reinforced concrete members with cyclic loading", *Journal of the Structural Division, 98(7): 1341-1360,* 1972.

Porter, K., Kennedy, R., Bachman, R., "Creating Fragility Functions for Performance-Based Earthquake Engineering", *Earthquake Spectra, Volume 23, No. 2, pages 471–489,* 2007.

Schwartz, D. P. and Coppersmith, K. J., "Fault behavior and characteristic earthquakes: Examples from the Wasatch and San Andreas fault zones". *Journal of Geophysical Research: Solid Earth, 89(B7), 5681-5698,* 1984.

Tran, T., Wallace, J., "Experimental Study of Nonlinear Flexural and Shear Deformations of Reinforced Concrete Structural Walls", *15th World Conference on Earthquake Engineering, Lisbon, Portugal,* 2012.

Turkish Earthquake Code, *Specification for structures to be built in disaster areas,* Ministry of Public Works and Settlement Government of Republic of Turkey, 2007.

Von Winterfeld, D., "Eliciting and Communicating Expert Judgments: Methodology and Application to Nuclear Safety", *Joint Research Centre, Commission of the European Communities,* 1989.

Wallace, J. W., "Slender Wall Behavior and Modeling", *PEER/EERI Technical Seminar Series, New Information on the Seismic Performance of Existing Concrete Buildings, 2006. See www.eeri.org/,* 2006.

Wallace, J. W., “Modelling Issues for Tall Reinforced Concrete Core Wall Buildings”. Geotechnical, Geological and Earthquake Engineering, 17:279—307, 2007.

Wallace, J. W., “Modelling Issues for Tall Reinforced Concrete Core Wall Buildings”, *Struct. Design Tall Spec. Build., 16, 615-632,* 2012.

Whitman, R.V., Reed, J.W., and Hong S.T., “Earthquake Damage Probability Matrices”, *Proceedings of the 5th World Conference on Earthquake Engineering, Rome, 2531–2540*, 1974.

Winker RL, Hora, S.C. and Baca, R.G., “The Quality of Experts’ Probabilities Obtained Through Formal Elicitation Techniques”, *Center for Nuclear Waste Regulatory Analyses CNWRA. San Antonio (TX), USA*, 1992.

APPENDIX A: NONLINEAR MODELLING INPUT

Modelling inputs such as material stress-strain relationships, plastic hinge moment-rotation backbone curves, P-M-M relationships of column elements are presented in this section. Expected material strength values are used according to the recommendations of LATBSDC (2014). The expected material strength values are given in Table A.1.

Table A.1. Expected material strengths (LATBSDC, 2014)

Material	**Strength**	**Value**
Concrete	Compressive Strength	$1.30\,f'_c$
Reinforcing Steel	Yield Strength	$1.17\,f'_y$
	Ultimate Strength	$1.50\,f'_y$

A.1. Unconfined Concrete Stress-Strain Relationship

Unconfined concrete stress-strain curves follow Modified Mander (Mander *et al*. 1988) model. Input parameters for the constitutive models are shown in Table A.2. Stress-strain relationships of unconfined concrete are given in Figure A.2. Points on the idealized curves are defined such that the actual backbone curve can be represented with sufficient accuracy. The *Y, U, L, R* and *X* points together create five linear segments of the uniaxial stress-strain relationship of materials (Figure A.1). *DX* points on the curves are defined as very large values to prevent termination of NRHA upon reaching a deformation limit in a single structural member. Therefore, *DX* is taken as 0.1 for unconfined (web region) concrete.

Table A.2. Material properties of the concrete grades used

Concrete Grade*	***Nominal f 'c***	***Expected f 'c***	***Expected Ec †***
C35	35 MPa	45.5 MPa	29303 MPa
C40	40 MPa	52 MPa	30850 MPa

* Grade C35 concrete is used in "Group 1" buildings and Grade C40 concrete is used in "Group 2" buildings

† Modulus of elasticity is based on the following equation:

$E_c = 40000\sqrt{f'_c} + 10^6$ (ksi) for $f'_c > 6000\ psi\ (\approx 41\ mpa)$

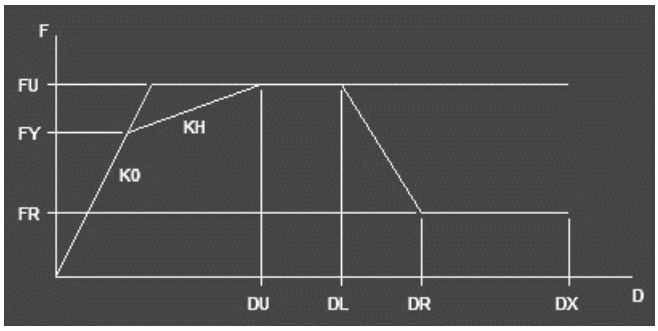

Point A (FY, DY): (0.6 fcc/Ec , 0.6 fcc)

Point B (FU, DU): (0.9 εcc, fcc)

Point C (FL, DL): (1.1 εcc, fcc)

Point D (FR, DR): (εcu, 0.05fcc)

Figure A.1. Unconfined concrete stress-strain relationship, Perform 3D idealization points.

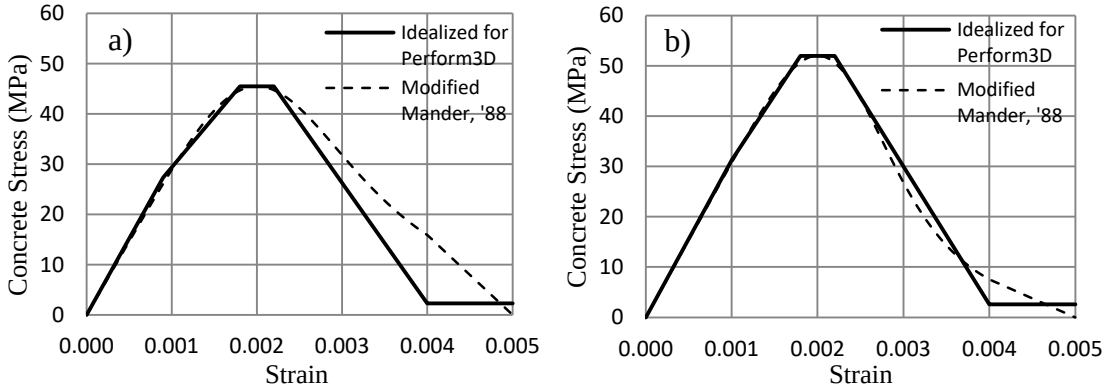

Figure A.2. Expected stress-strain relationship for unconfined concrete. a) C35 Grade b) C40 Grade

A.2. Confined Concrete Stress-Strain Relationship

Confined concrete stress-strain relationships are calculated for the boundary zones of shear walls for all building models. The modified Mander (Mander et *al*., 1988) is used for all cases. Various parameters of the constitutive model for confined concrete stress-strain backbone curve are presented in Table A.3. The points on the idelized stress-strain backbone

curve are defined according to Figure A.3. Here, the maximum deformation (denoted with *DX*) is taken as 0.1. Stress-strain relationships of the confined concrete are given in Figure A.4 and Figure A.5.

Table A.3. Constitutive model parameters for confined (in boundary zones of shear walls) concrete

Building Model	**Parameter**	**Value**
1A	e_{cc}	0.0044
	e_{cr}	0.0166
	ρ_x	0.64%
	ρ_y	0.45%
1B	e_{cc}	0.0042
	e_{cr}	0.0157
	ρ_x	0.50%
	ρ_y	0.50%
1C	e_{cc}	0.0040
	e_{cr}	0.0161
	ρ_x	0.52%
	ρ_y	0.50%
2A	e_{cc}	0.0036
	e_{cr}	0.0135
	ρ_x	0.46%
	ρ_y	0.42%
2B	e_{cc}	0.0041
	e_{cr}	0.0150
	ρ_x	0.56%
	ρ_y	0.50%
2C	e_{cc}	0.0039
	e_{cr}	0.0117
	ρ_x	0.40%
	ρ_y	0.33%

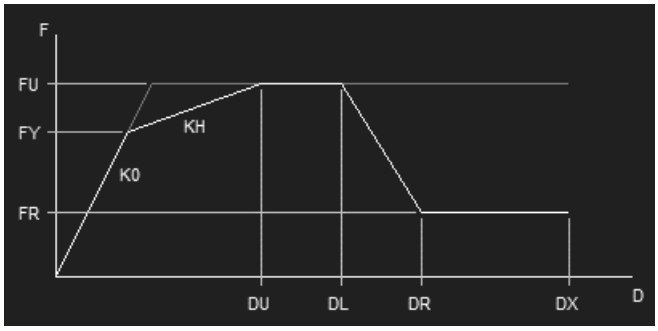

Point A (FY, DY): (0.6 f_{cc}/E_c , 0.6 f_{cc})

Point B (FU, DU): (0.75 εcc, f_{cc})

Point C (FL, DL): (1.2 ε_{cc}, f_{cc})

Point D (FR, DR): (0.9 ε_{cr}, f_{cc})

Figure A.3. Concrete stress-strain relationship, Perform 3D idealization points

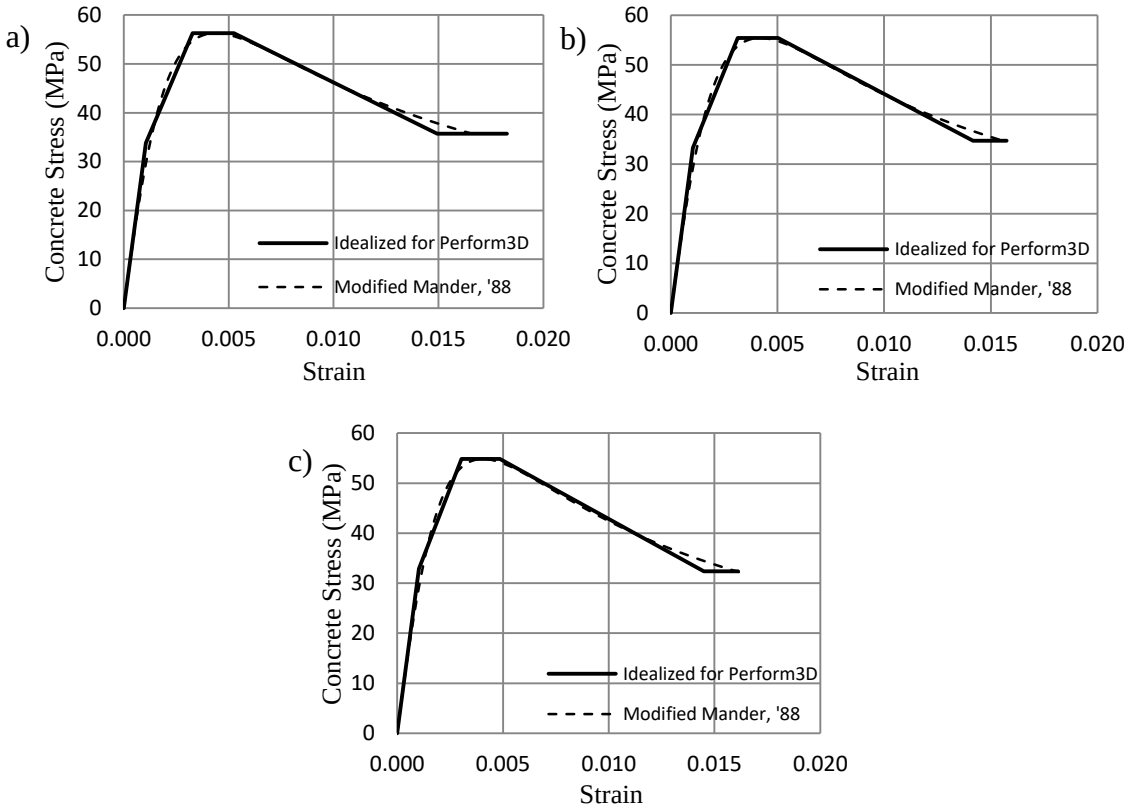

Figure A.4. Expected stress-strain relationship for confined concrete. a) Building 1A b) Building 1B c) Building 1C

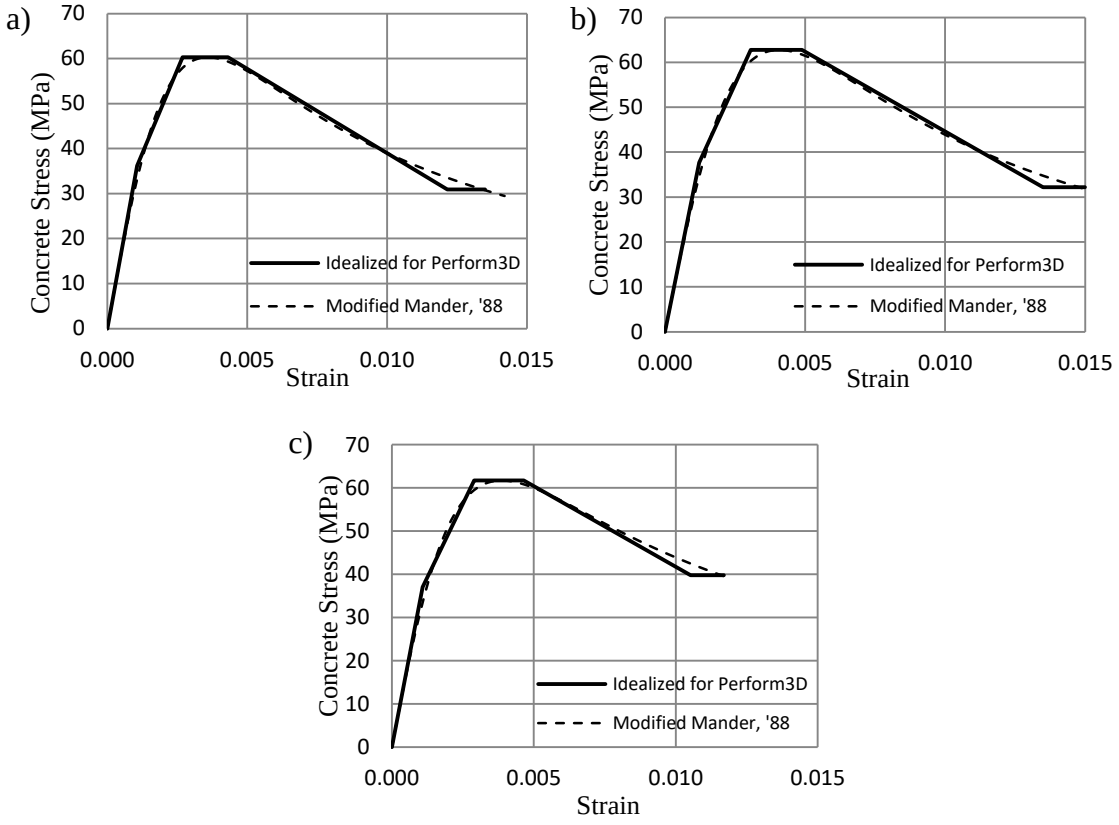

Figure A.5. Expected stress-strain relationship for confined concrete. a) Building 2A b) Building 2B c) Building 2C

A.3. Shear Stress-Strain Relationship of Concrete

The recommendations of ATC 72-1 (2010) and Wallace (2007) are utilized to construct shear stres-strain backbone relationships of shear wall members. Shear force-deformation curves include a pre-cracked linear segment, with an uncracked shear stiffness up to the strength at cracking V_{cr}, followed by a post-cracked segment with an effective shear stiffness up to the yield strength, V_n. The strength at cracking ν_{cr} is defined by Equation A.1.

$$\nu_{cr} = 4\sqrt{f'_c}\left[1 + \frac{P_u/A_{web}}{4\sqrt{f'_c}}\right]^{1/2} < 0.6\nu_n \qquad \text{(A.1)}$$

Here, f'_c is compressive strength of concrete (ksi), A_{web} is cross-sectional area of the web (in^2), P_u is average axial load on wall sections (in^2). The cracking strain is defined as:

$$\gamma_{cr} = \frac{v_{cr}}{G_c} \tag{A.2}$$

$$G_c = \frac{E_c}{2(1+\nu)} \tag{A.3}$$

In above expressions, $\nu = 0.2$. The nominal shear strength v_n is defined as:

$$v_n = \left(\alpha_c \lambda \sqrt{f'_c} + \rho_t f_y\right) \tag{A.4}$$

where, α_c is equal to 2.0 for $h_w / l_w \leq 2.0$, λ is 1.0 for normal weight concrete, ρ_t is transverse reinforcement ratio in direction of the shear force, f_y is the nominal yield strength of S420 reinforcing steel.

Orakcal et *al.* (2009) reported that axial loads on shear wall sections result in a much stronger and stiffer response. The proponents of this study state:

- The yield strength is observed as 1.75 times the nominal shear strength if $P_u/A_g f'_c \geq 0.010$.
- The yield strength is observed as 1.50 times the nominal shear strength if $P_u/A_g f'_c \leq 0.010$.

For simplicity, the amplification factor for the yield strength is defined as 1.5 times the nominal shear strength, v_n , calculated per ACI 318-11 (2011). The points on the force-deformation curve are defined by Equation A.5 and A.6.

Cracking : $$v_{cr} = 4\sqrt{f'_c}\left[1 + \frac{P_u/A_{web}}{4\sqrt{f'_c}}\right]^{1/2} < 0.6 v_{cu} \, , \gamma_{cr} \tag{A.5}$$

Yield: $$v_{cu} = 1.5 v_n \ , \ \gamma_y = 0.004 \tag{A.6}$$

The maximum shear strain γ_{max} is defined by ACI 318-11 (2011) as 0.015. In this thesis, the maximum shear strain before loss of strength, is defined as, $\gamma_{max} = 0.0135$. Input shear stress-strain backbone curves are shown in Figure A.6.

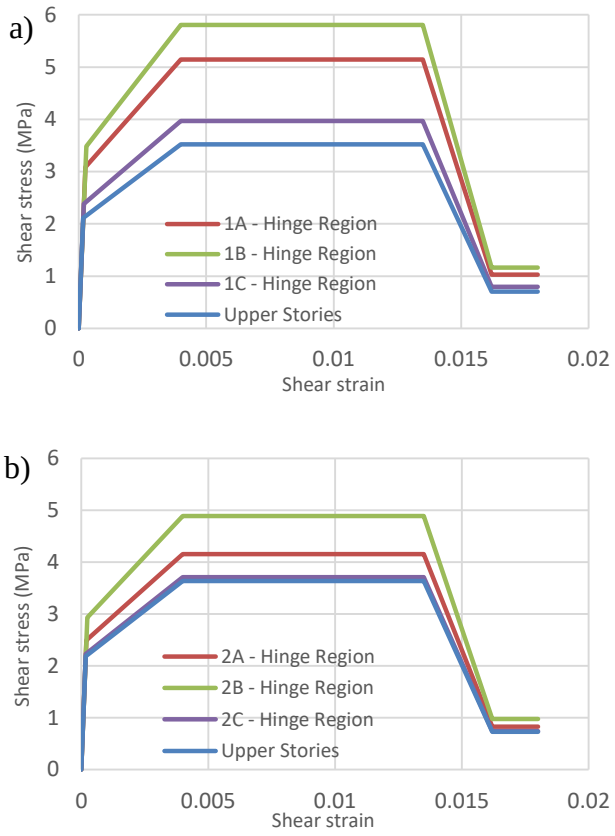

Figure A.6. Shear stress strain relationships of a) Group-1 buildings b) Group-2 buildings

A.4. Stress-Strain Relationship of Reinforcement Steel

S420 grade steel is used for the rebars in all building models. S420 grade steel refers to a nominal yield strength of 420 mPA, and a nominal ultimate strength of 550 mPA. Miscellenous parameters of the constitutive model are presented in Table A.4. Expected strength values are used for the analyses. Expected stress parameters are defined in accordence with the recommendations of LATBSDC (2014). The expected yield stress $f_{y,exp}$ is proposed to be 1.17 times the nominal yield stress f_y. And the expected ultimate stress $f_{u,exp}$ is defined to be 1.5 times the expected yield stress. The input stress-strain relationship is based upon Menegotto and Pinto constitutive model (Menegotto and Pinto, 1973). Figure A.7 shows the uniaxial stress-strain relationship of steel.

Table A.4. Constitutive model parameters for S420 grade reinforcement steel

Steel Grade	***f_{sy} (mPA)***	**ε_{sy}**	**ε_{sh}**	**ε_{su}**	***f_{su} (mPA)***
S420	420	0.0021	0.008	0.10	550

ε_{sy}: Yield strain
ε_{sh}: Onset strain of strain hardening
ε_{su}: Ultimate strain

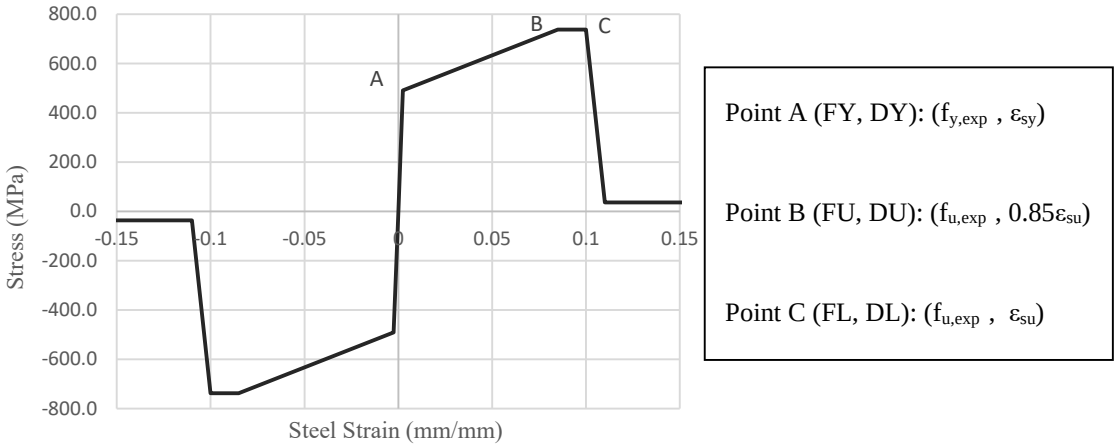

Figure A.7. Reinforcement steel stress-strain relationship

A.5. Moment-Curvature Relationships in Plastic Hinges

Nonlinear moment-curvature (M-K) relationship of beam and column plastic hinges at the member ends are presented in this subsection. Section analyses are carried out to obtain M-K relationship using frame member properties (i.e., cross-section geometry, reinforcement configuration and material force deformation relationships) given in Section 2.3.2. Figure A.8 shows the M-K relationships for all frame members in the submodels. The column M-K relationships in Figure A.8 are given under an axial loading that is 0.25 times the maximum axial load (in compression) that the sections can withstand. Note that during a NRHA, the M-K curves for column hinges are calculated considering the point attained on the yield surface of the member. This way, the effect of axial load on columns is taken into account.

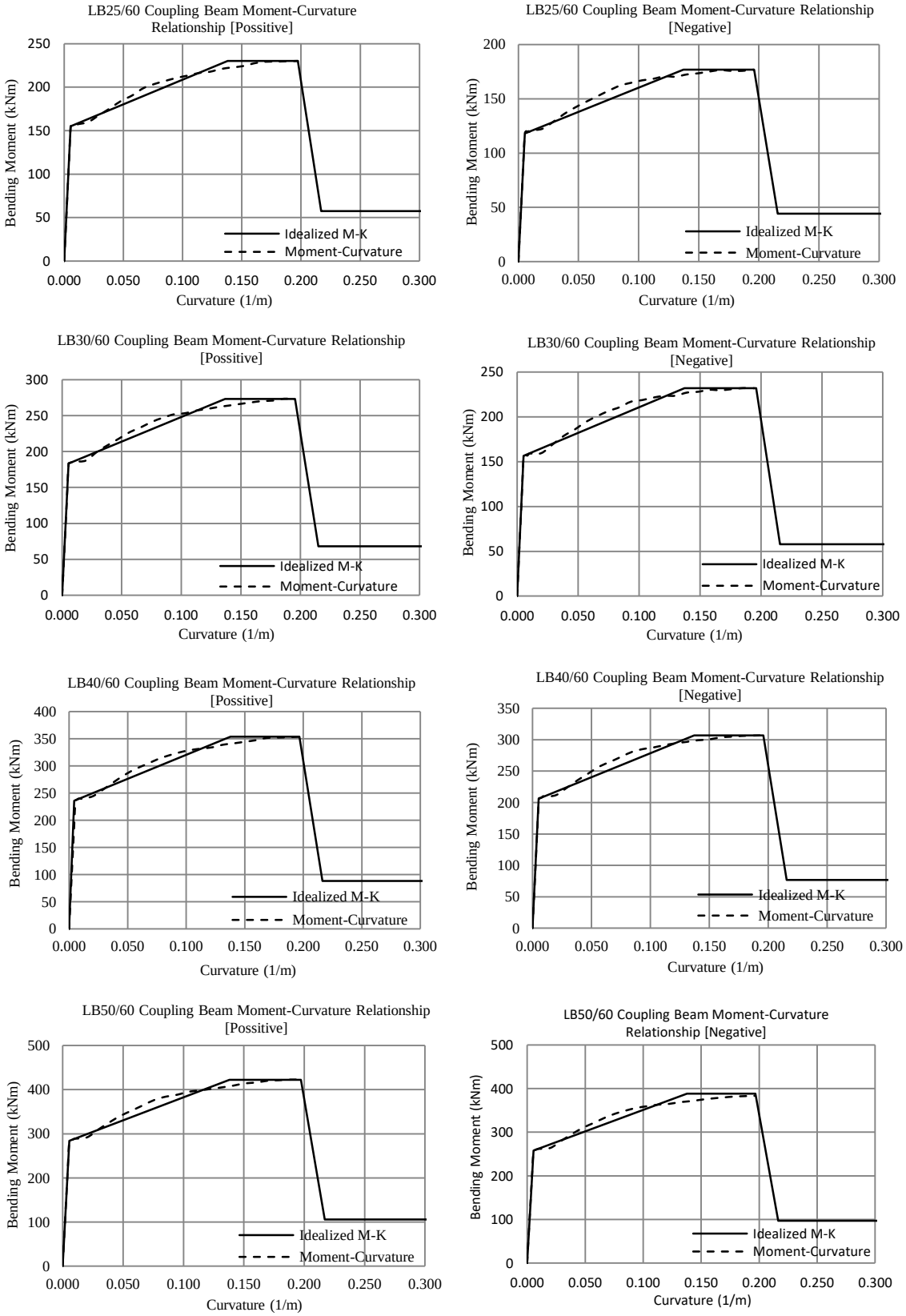

Figure A.8. Moment-Curvature relationships of all structural frame elements, obtained from section analyses

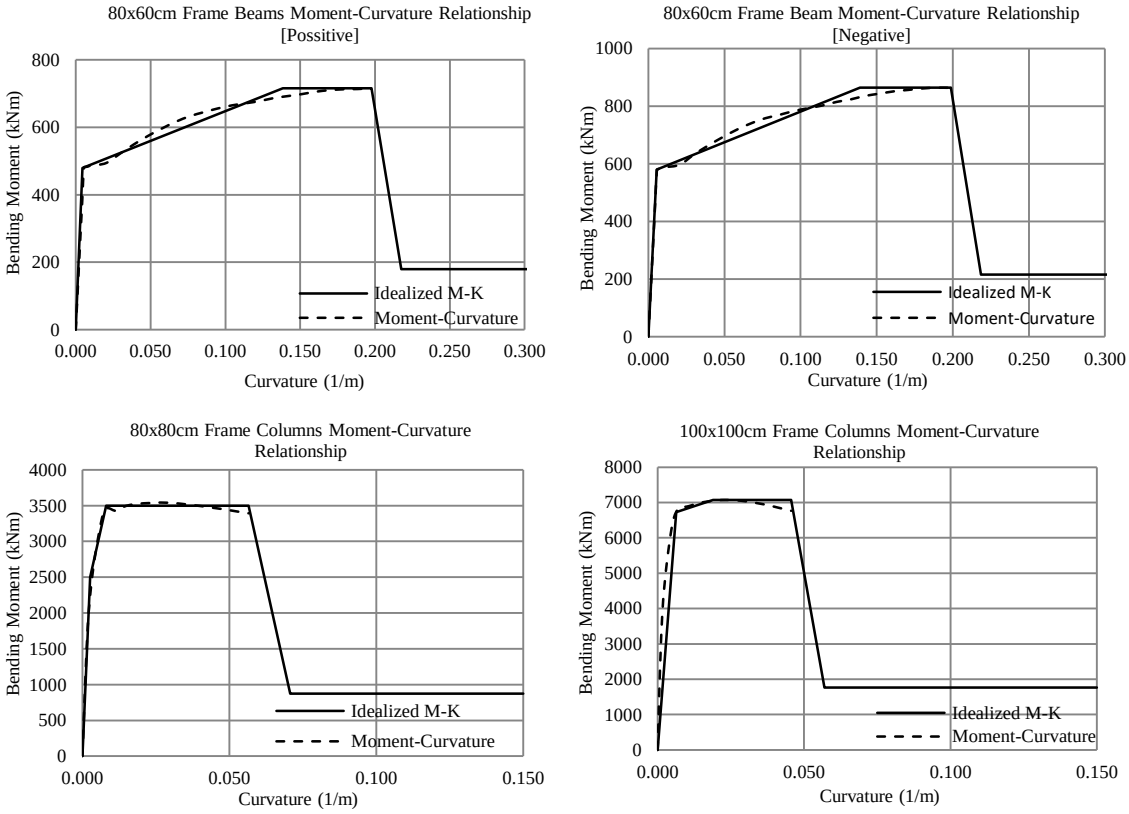

Figure A.8. Moment-Curvature relationships of frame elements obtained from section analyses (cont'd)

APPENDIX B: STRUCTURAL RESPONSES

Modal Properties of the Model Buildings

Table B.1. Modal properties of the building 1A

		Effective Mass Factors	
Mode	T (sec)	H1	H2
1	2.00	0.200	0.024
2	1.79	0.496	0
3	1.61	0.006	0.639
4	0.59	0.014	0.002
5	0.47	0.143	0
6	0.34	0	0.188
7	0.30	0.003	0.003
8	0.22	0.056	0
9	0.19	0	0
10	0.14	0	0.068

Table B.2. Modal properties of the building 1B

		Effective Mass Factors	
Mode	T (sec)	H1	H2
1	2.20	0	0
2	1.81	0.700	0
3	1.47	0	0.670
4	0.64	0	0
5	0.46	0.160	0
6	0.33	0	0.196
7	0.32	0	0
8	0.21	0.060	0
9	0.20	0	0
10	0.15	0	0.063

Table B.3. Modal properties of the building 1C

		Effective Mass Factors	
Mode	T (sec)	H1	H2
1	1.66	0.578	0.010
2	1.54	0.097	0
3	1.25	0.012	0.658
4	0.41	0.044	0
5	0.40	0.12	0
6	0.28	0	0.20
7	0.19	0	0
8	0.17	0.064	0
9	0.13	0	0.061
10	0.12	0	0

Table B.4. Modal properties of the building 2A

		Effective Mass Factors	
Mode	T (sec)	H1	H2
1	2.93	0.721	0
2	2.28	0.005	0
3	2.19	0	0.673
4	0.85	0.122	0
5	0.68	0.003	0
6	0.52	0	0.173
7	0.41	0.050	0
8	0.35	0.002	0
9	0.25	0.002	0
10	0.23	0	0.064

Table B.5. Modal properties of the building 2B

		Effective Mass Factors	
Mode	T (sec)	H1	H2
1	2.72	0.687	0
2	2.24	0	0.639
3	2.15	0.012	0.010
4	0.73	0.137	0
5	0.54	0.004	0
6	0.46	0	0.19
7	0.33	0.056	0
8	0.25	0	0
9	0.19	0.005	0.056
10	0.19	0.026	0.011

Table B.6. Modal properties of the building 2C

		Effective Mass Factors	
Mode	T (sec)	H1	H2
1	2.22	0.163	0
2	2.05	0	0.647
3	1.90	0.511	0
4	0.56	0.040	0
5	0.45	0.127	0
6	0.42	0	0.197
7	0.25	0.015	0
8	0.20	0.048	0
9	0.18	0	0.065
10	0.15	0.008	0

MODE SHAPES

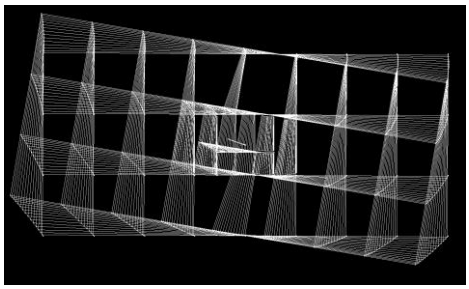

Mode 1

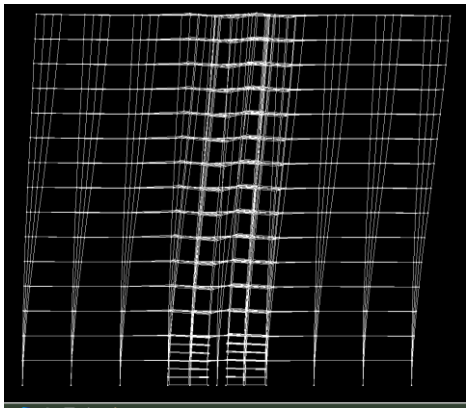

Mode 2

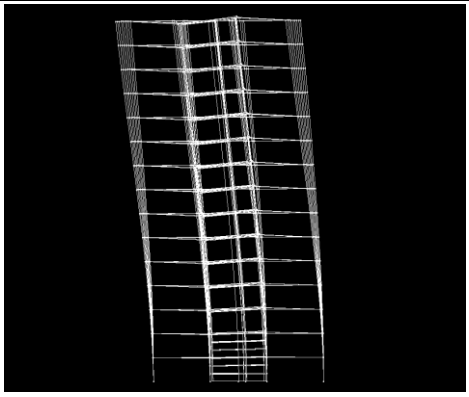

Mode 3

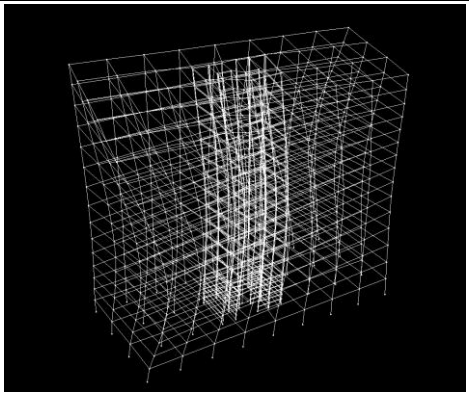

Mode 4

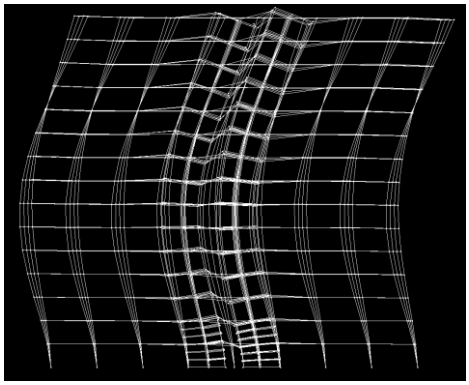

Mode 5

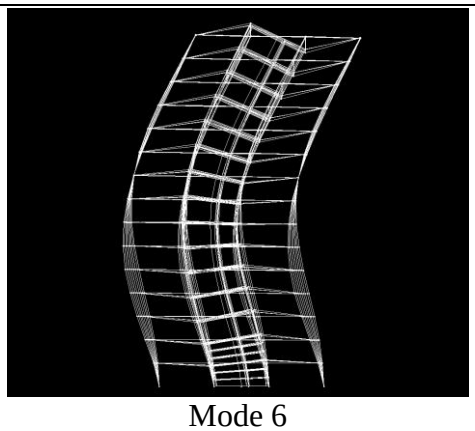

Mode 6

Figure B.1. Mode shapes of the building 1A

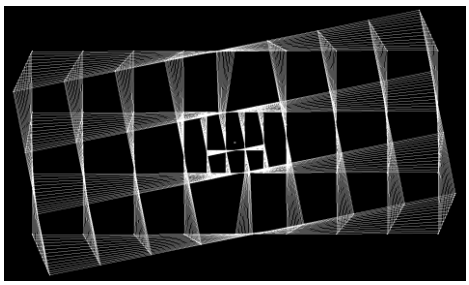

Mode 1

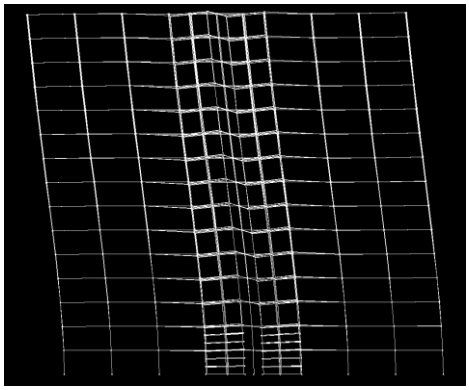

Mode 2

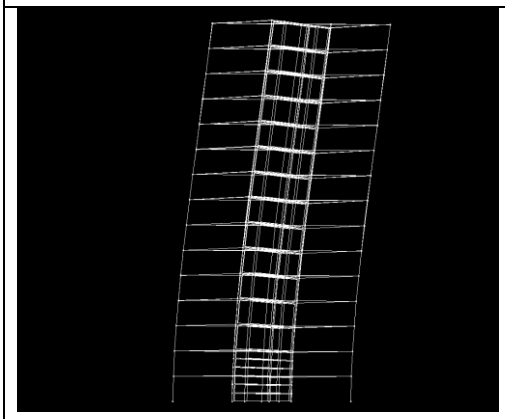

Mode 3

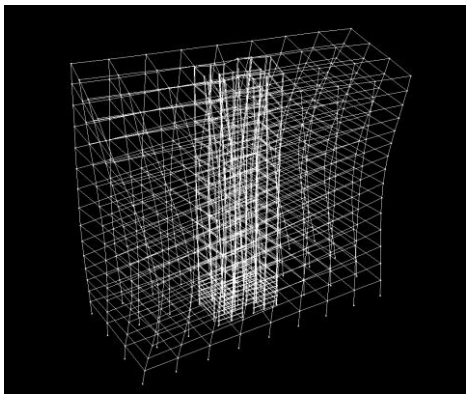

Mode 4

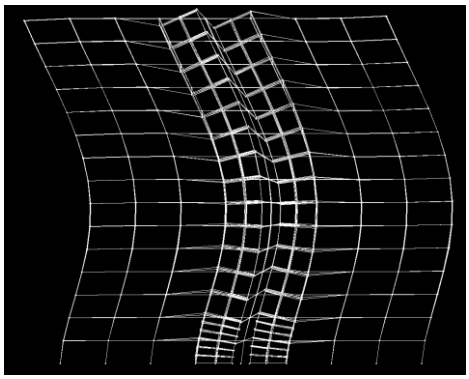

Mode 5

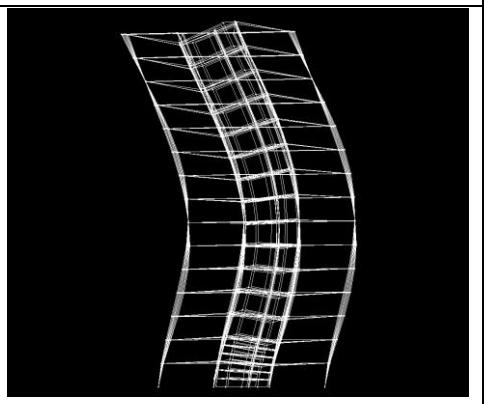

Mode 6

Figure B.2. Mode shapes of the building 1B

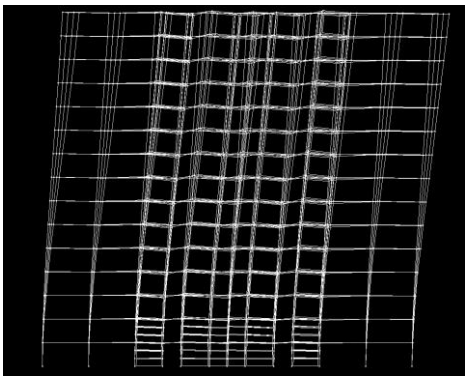

Mode 1

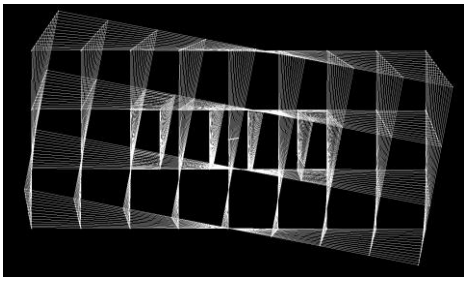

Mode 2

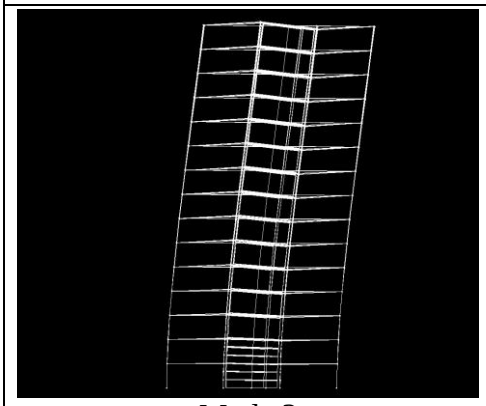

Mode 3

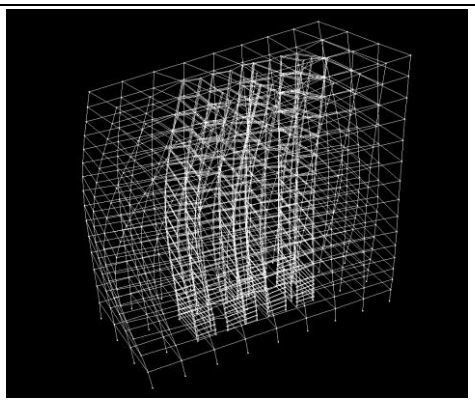

Mode 4

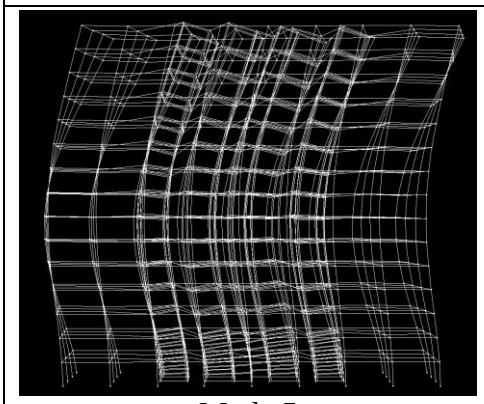

Mode 5

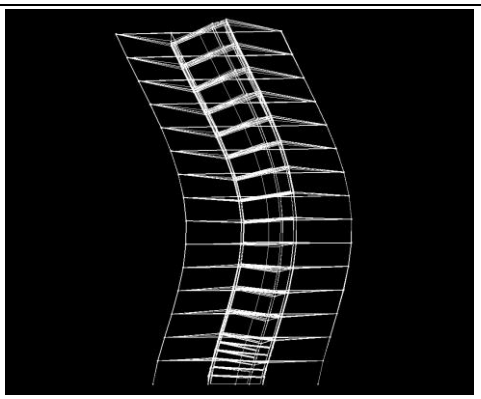

Mode 6

Figure B.3. Mode shapes of the building 1C

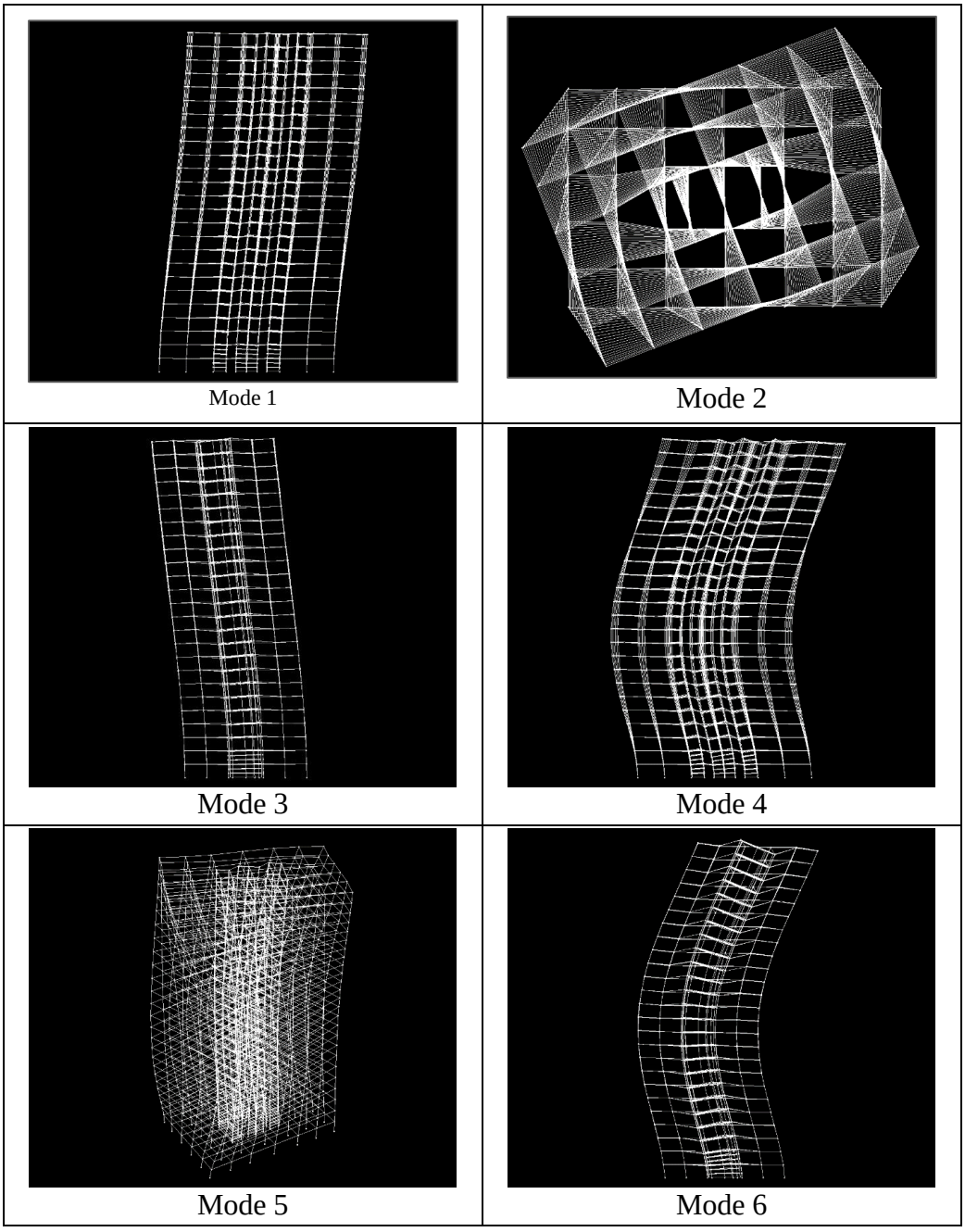

Figure B.4. Mode shapes for the building 2A

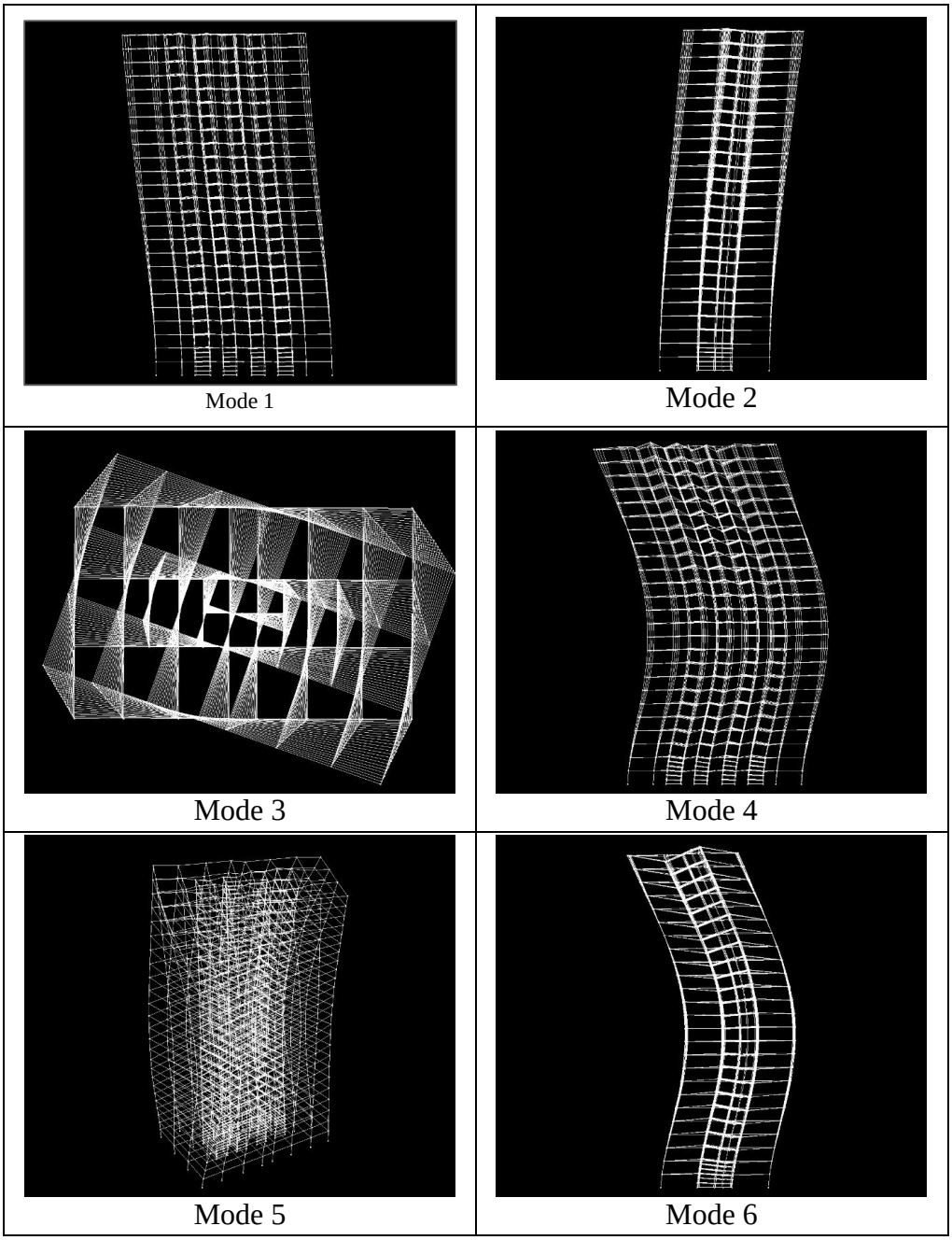

Figure B.5. Mode shapes for the building 2B

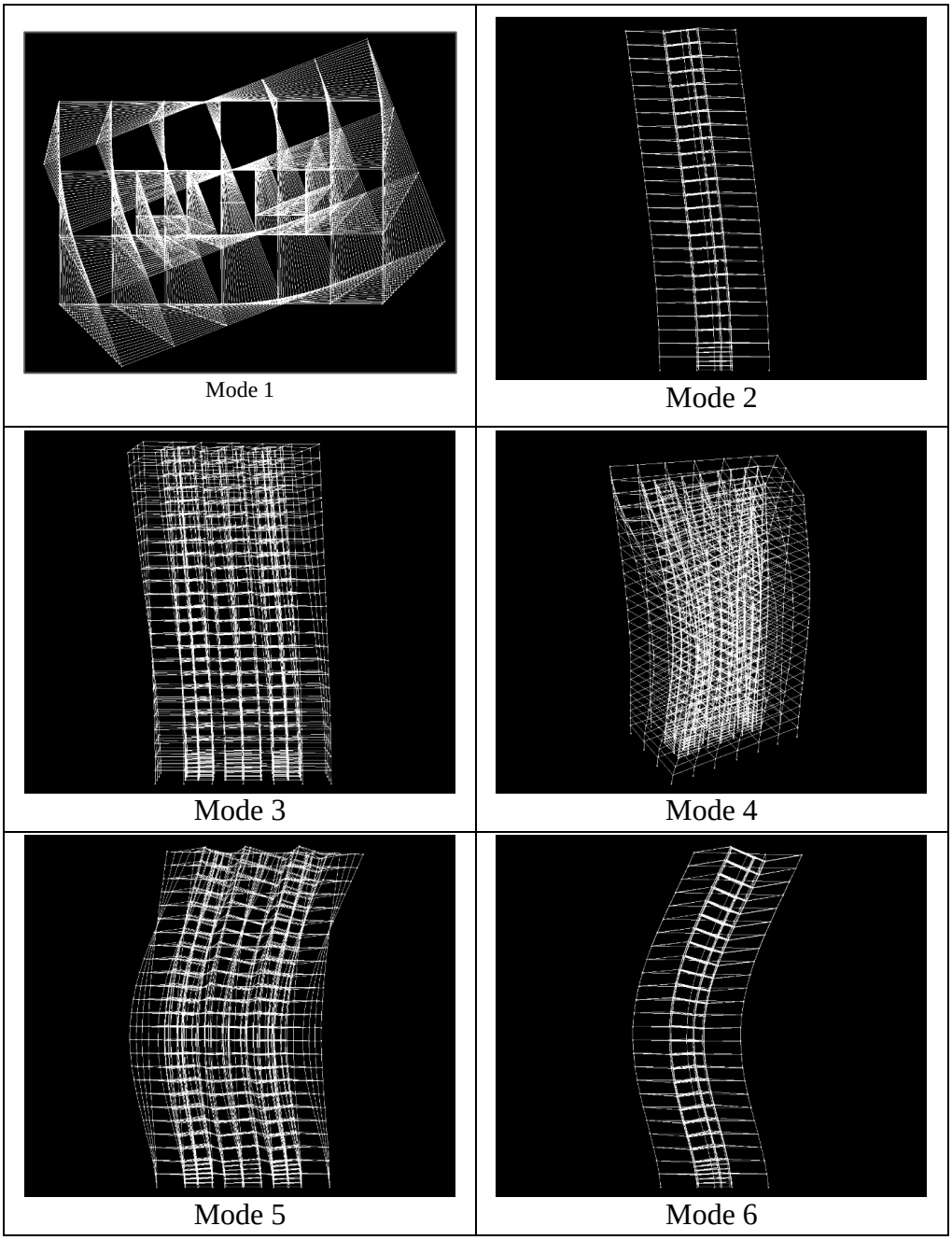

Figure B.6. Mode shapes for the building 2C

INTERSTORY DRIFT RATIOS

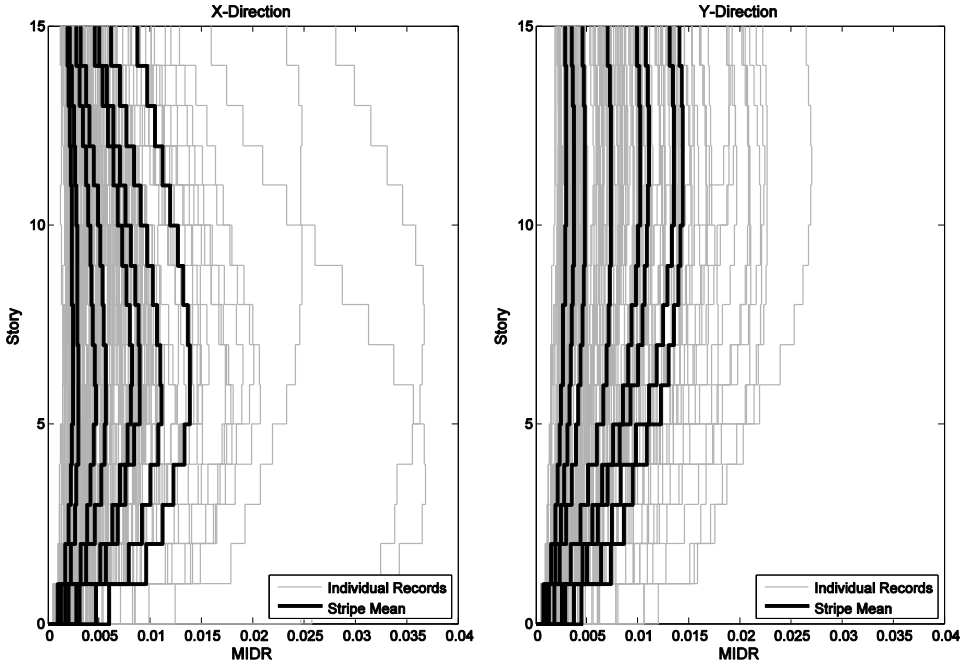

Figure B.7. IDR profile in both principal directions of the building 1A. Bold black lines represent the mean of individual responses for each return period

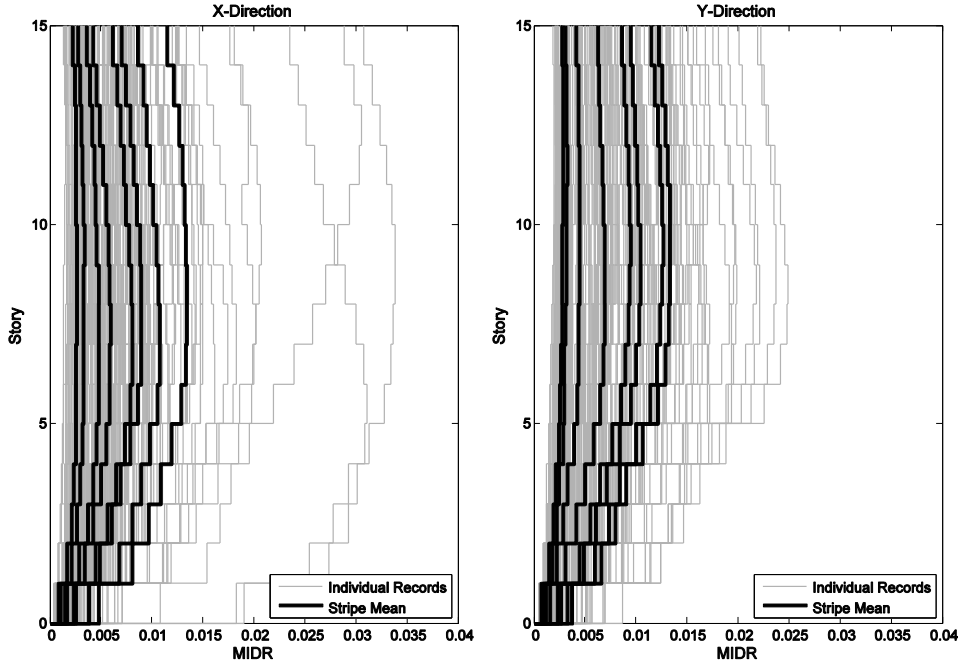

Figure B.8. IDR profile in both principal directions of the building 1B. Bold black lines represent the mean of individual responses for each return period

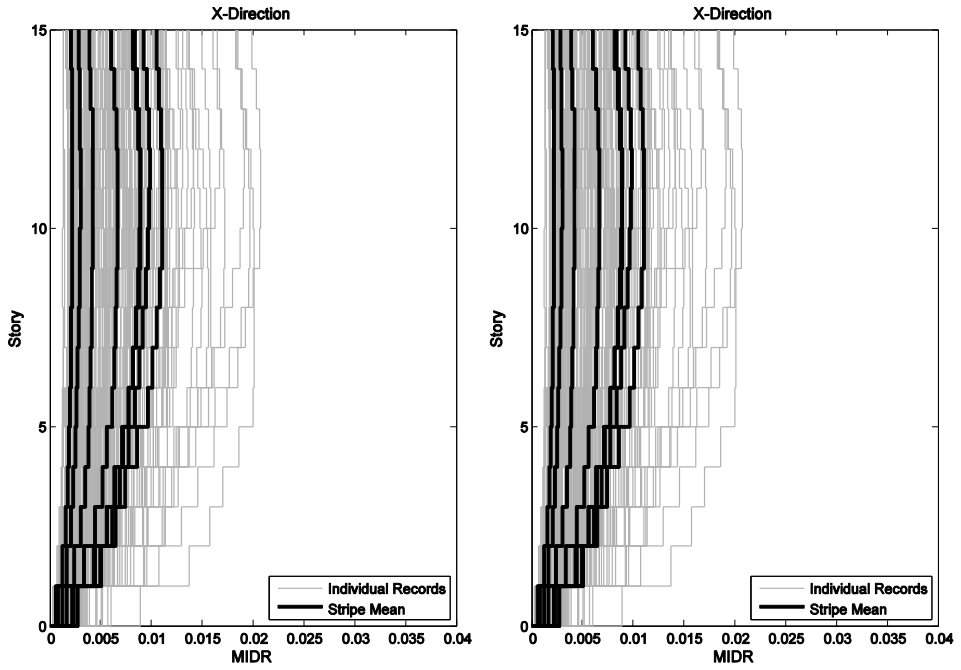

Figure B.9. IDR profile in both principal directions of the building 1C. Bold black lines represent the mean of individual responses for each return period

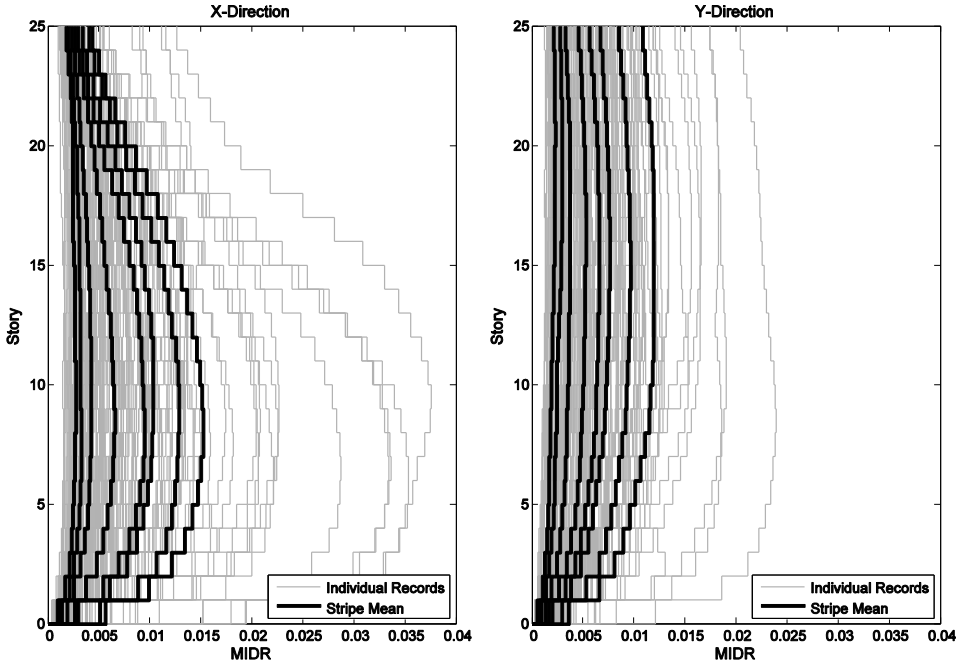

Figure B.10. IDR profile in both principal directions of the building 2A. Bold black lines represent the mean of individual responses for each return period

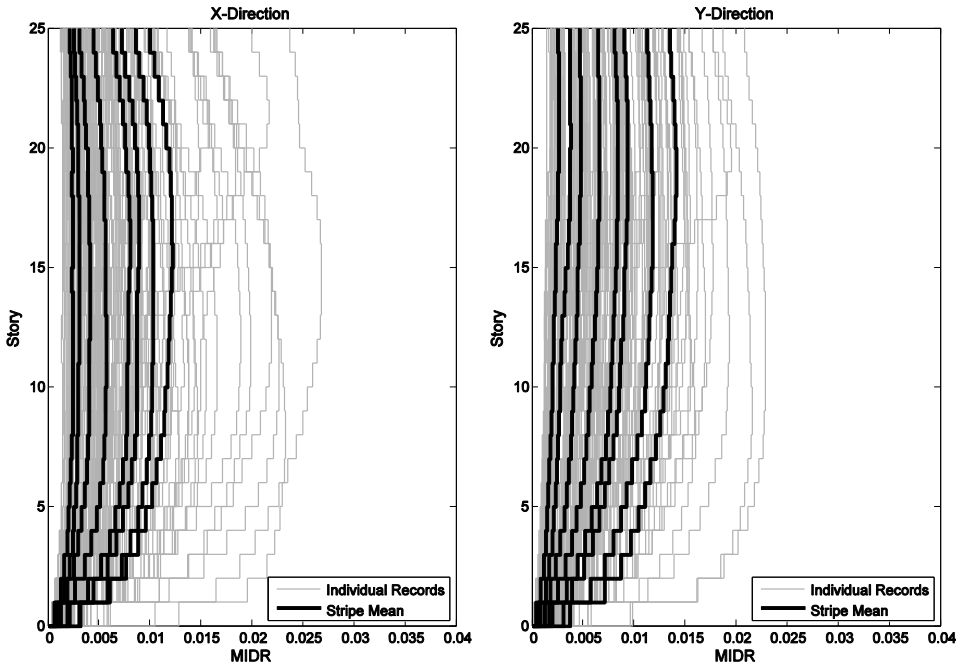

Figure B.11. IDR profile in both principal directions of the building 2B. Bold black lines represent the mean of individual responses for each return period

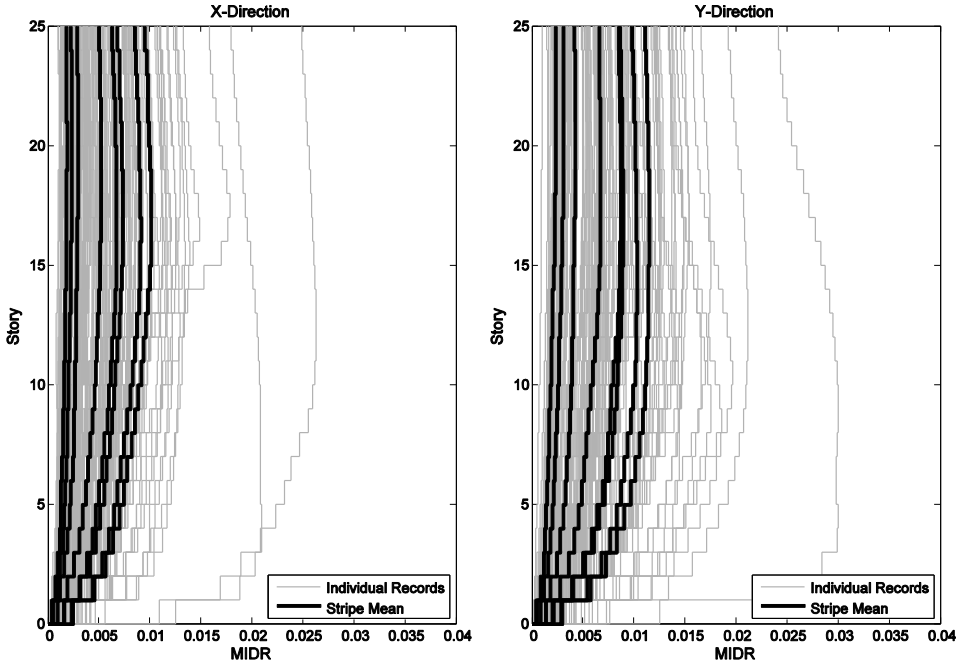

Figure B.12. IDR profile in both principal directions of the building 2C. Bold black lines represent the mean of individual responses for each return period

PROBABILITY DISTRIBUTIONS OF DAMAGE STATES

1A BUILDING

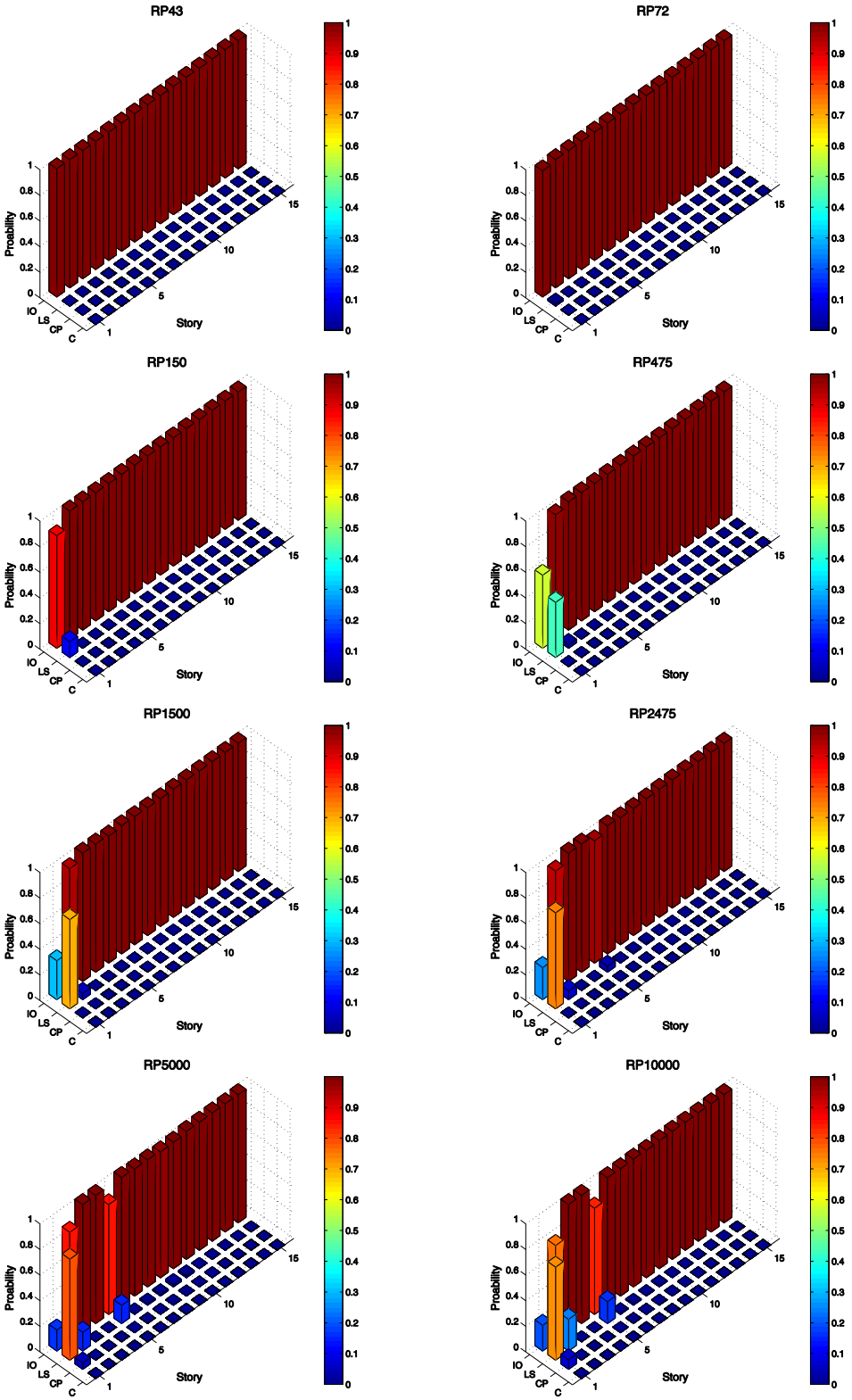

Figure B.13. Damage state probabilities of critical SW sections in terms of reinforcing steel tensile strains for building 1A at all hazard levels

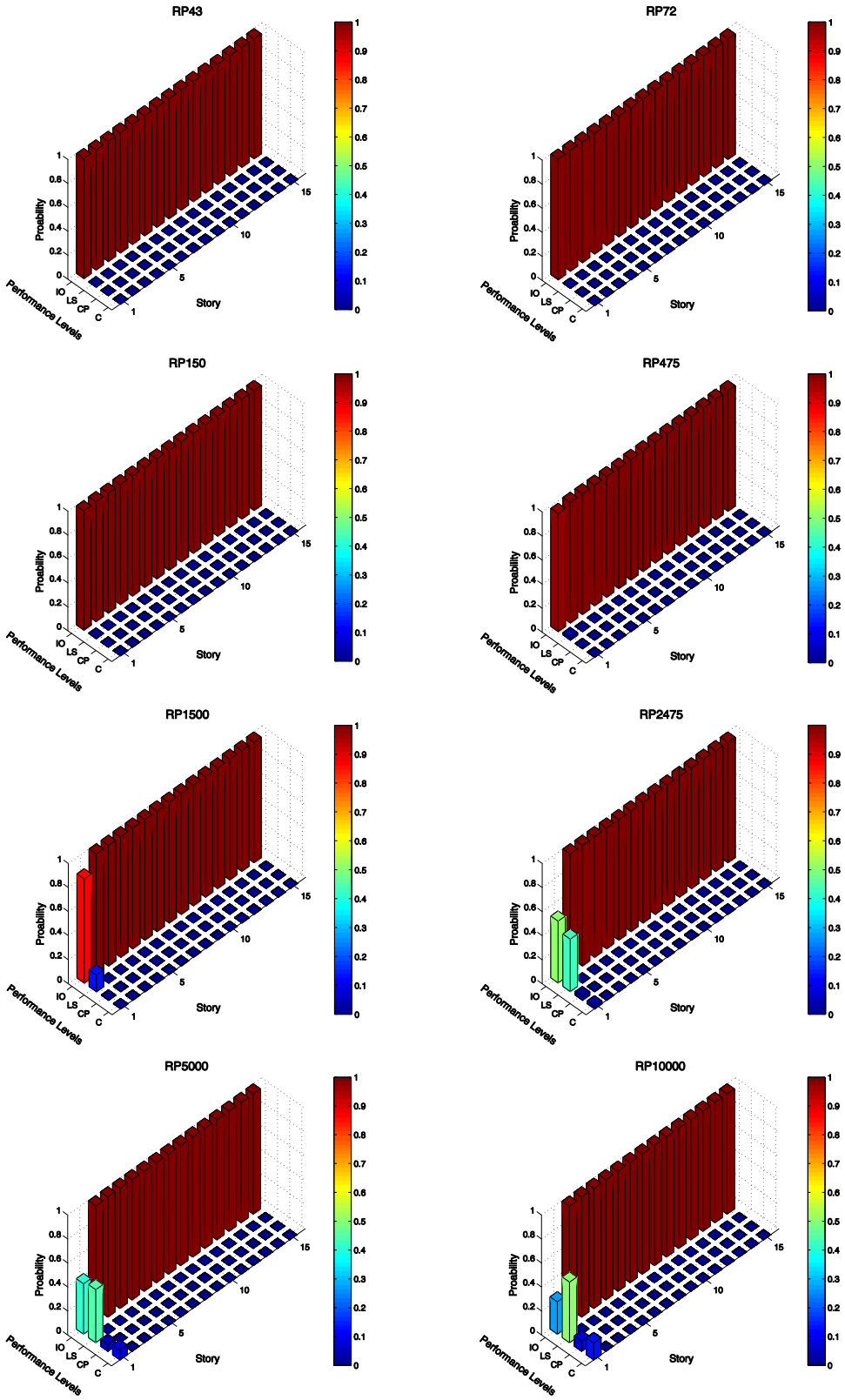

Figure B.14. Damage state probabilities of critical SW sections in terms of confined concrete under compression for building 1A at all hazard levels

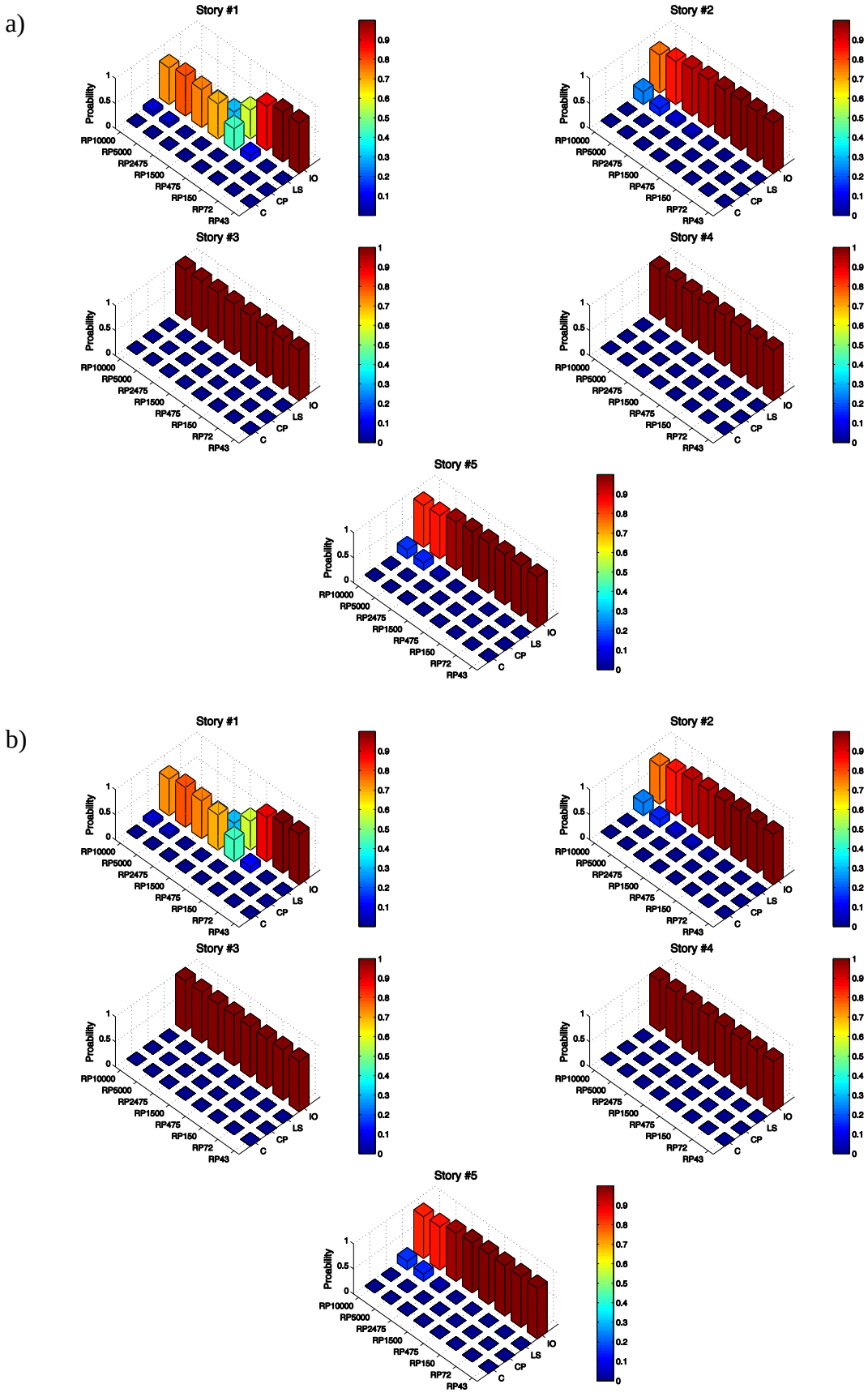

Figure B.15. Damage state probabilities of critical SW sections at 1st to 5th stories. (a) Reinforcement in tension and (b) confined concrete under compression for building 1A.

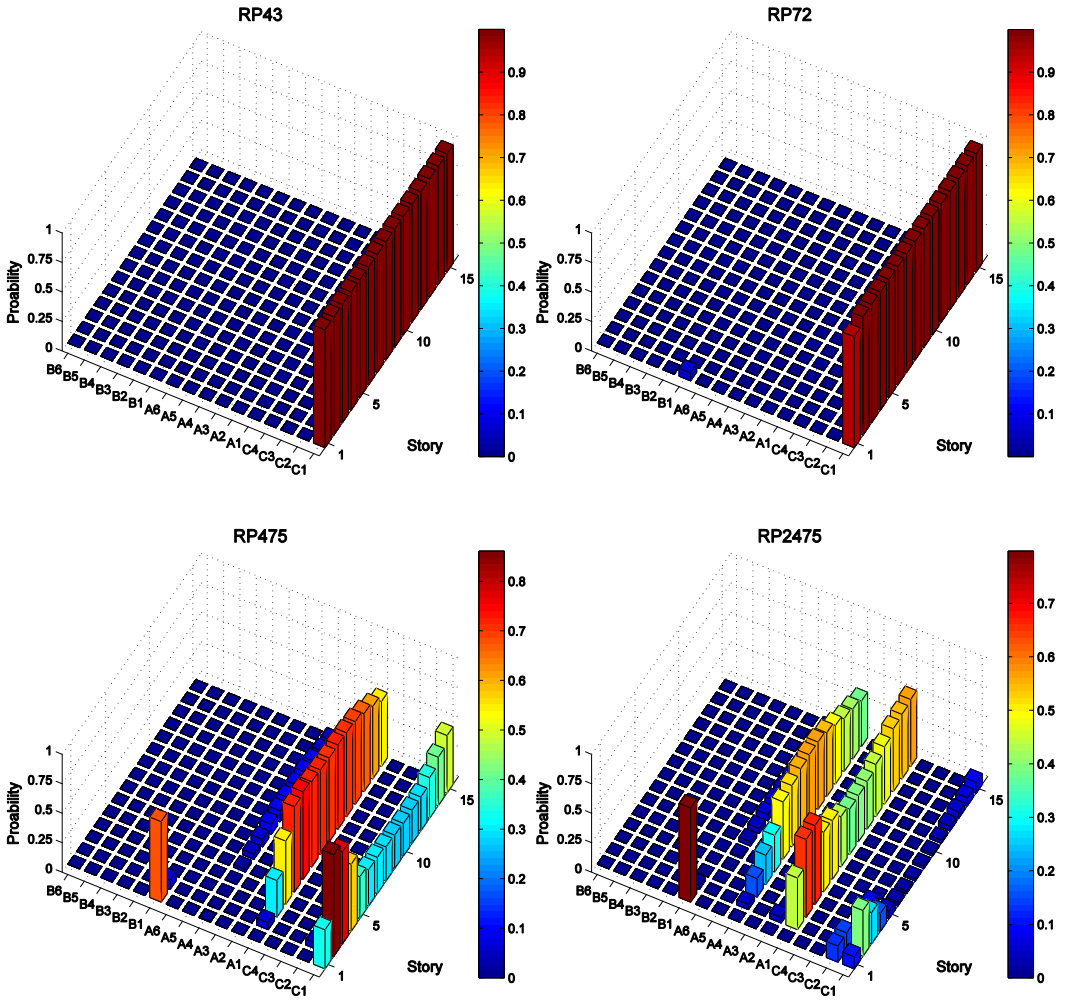

Figure B.16. Probabilities of performance regions calculated from the joint PDF of shear wall tensile strains versus IDRs at 43-, 72-, 475- and 2475-year return periods for building 1A

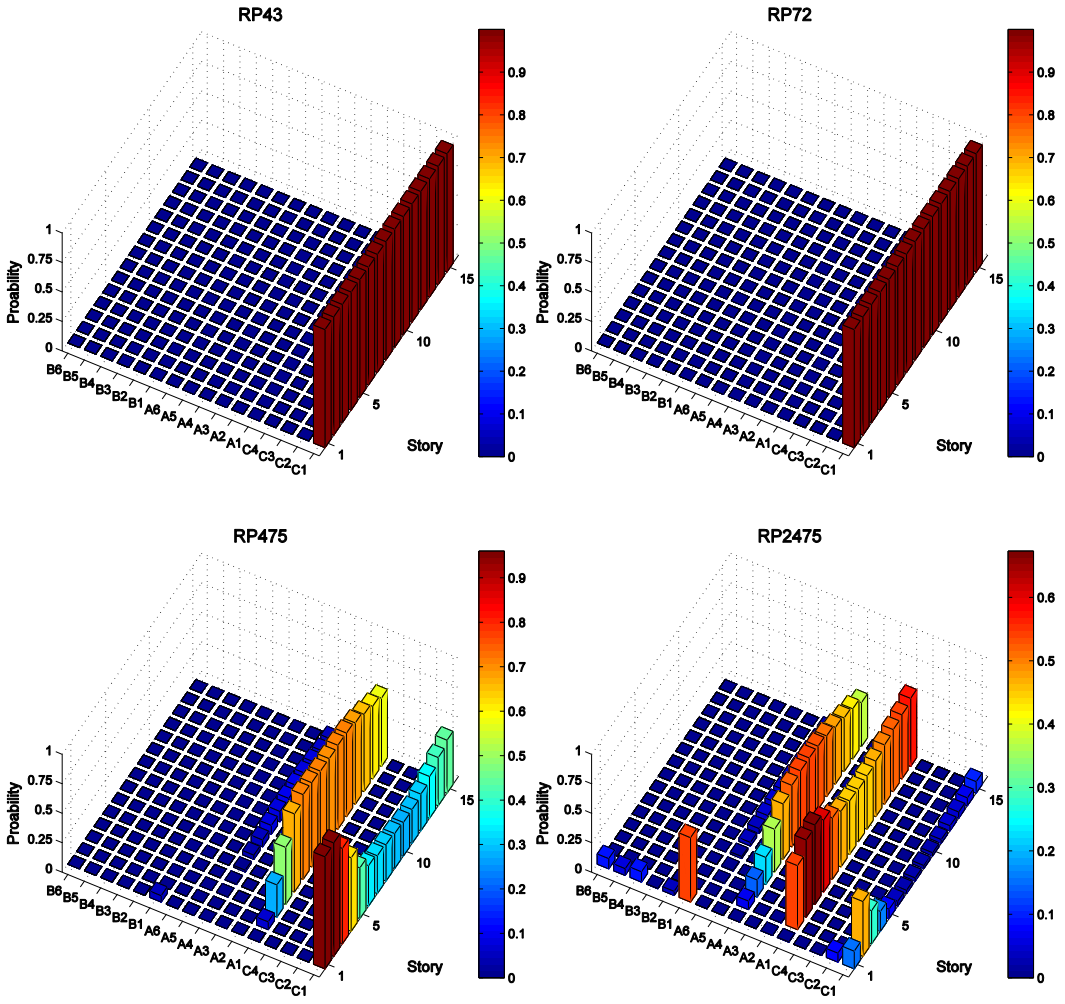

Figure B.17. Probabilities of performance regions calculated from the joint PDF of shear wall compression strains versus IDRs at 43-, 72-, 475- and 2475-year return periods for building 1A.

1B BUILDING

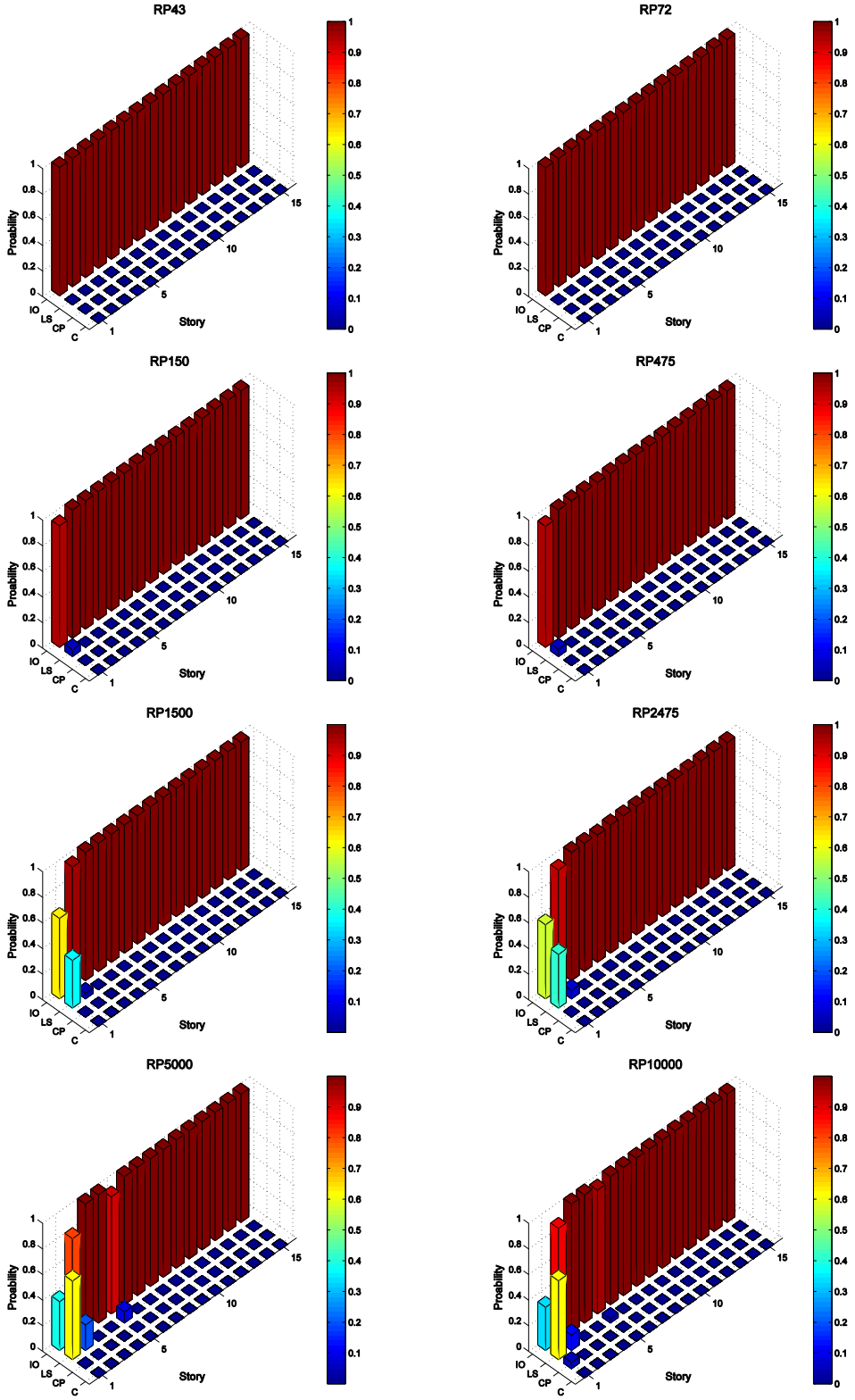

Figure B.18. Damage state probabilities of critical SW sections in terms of reinforcing steel tensile strains for building 1B at all hazard levels

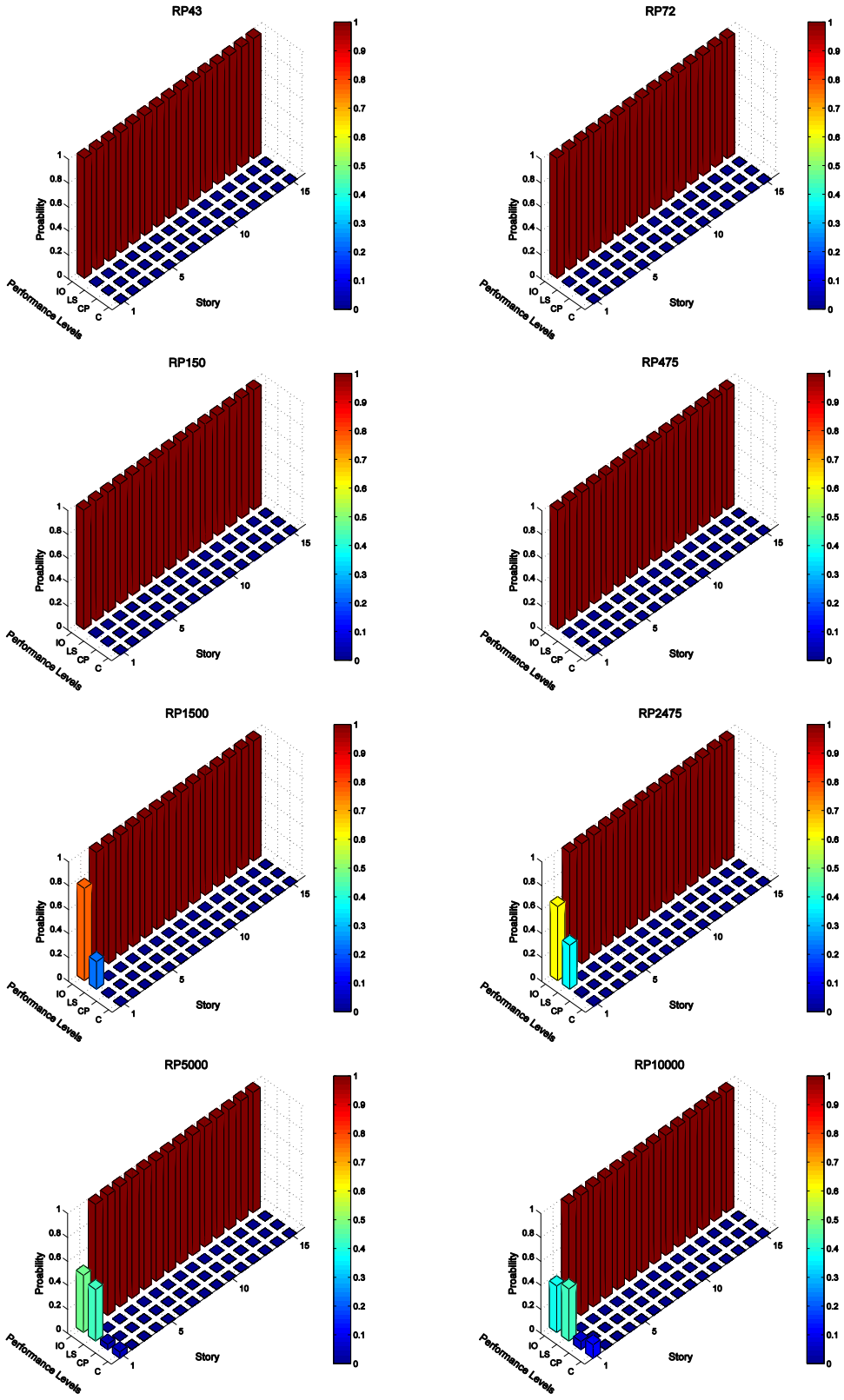

Figure B.19. Damage state probabilities of critical SW sections in terms of confined concrete under compression for building 1B at all hazard levels

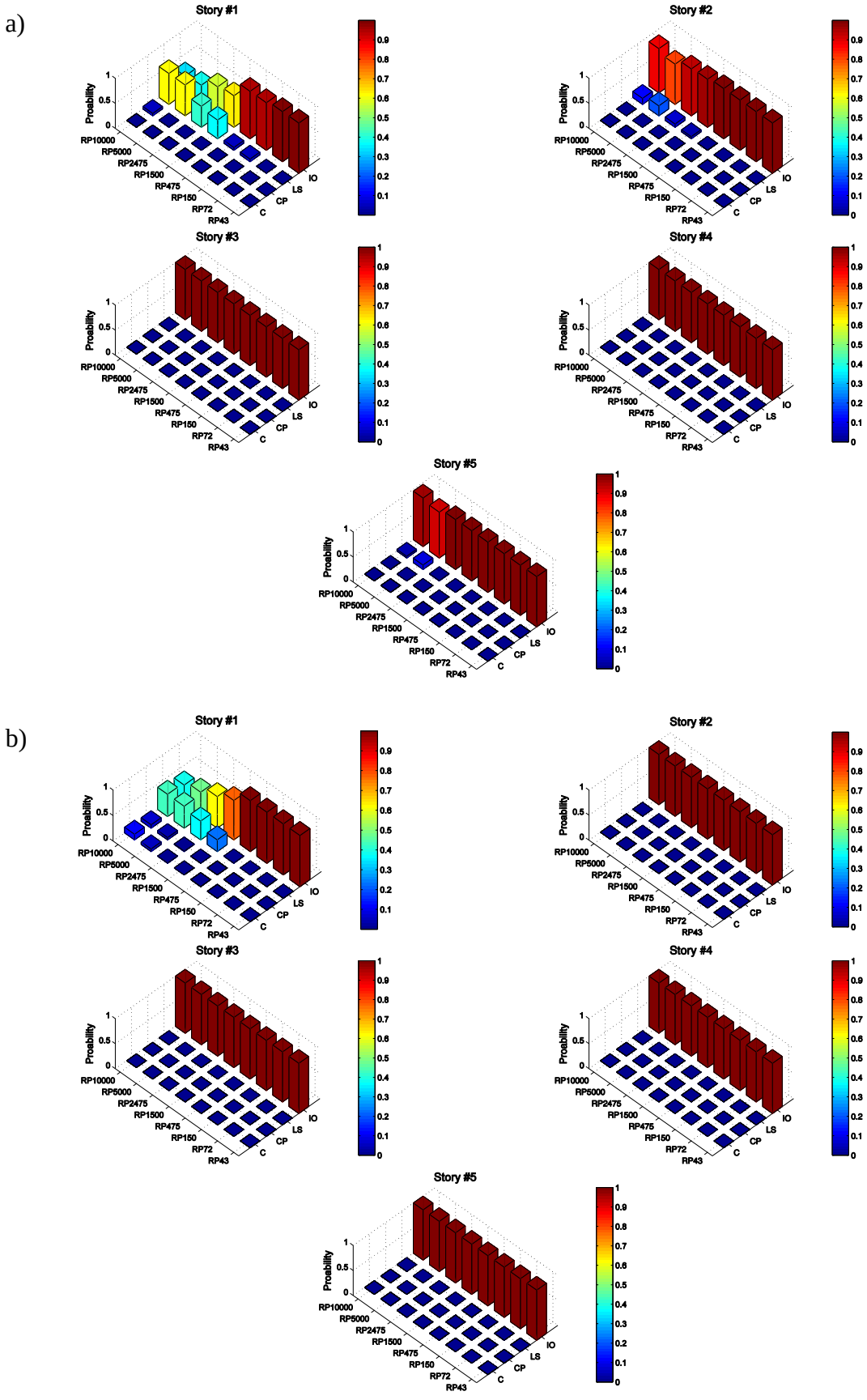

Figure B.20. Damage state probabilities of critical SW sections at 1st to 5th stories. (a) Reinforcement in tension and (b) confined concrete under compression for building 1B.

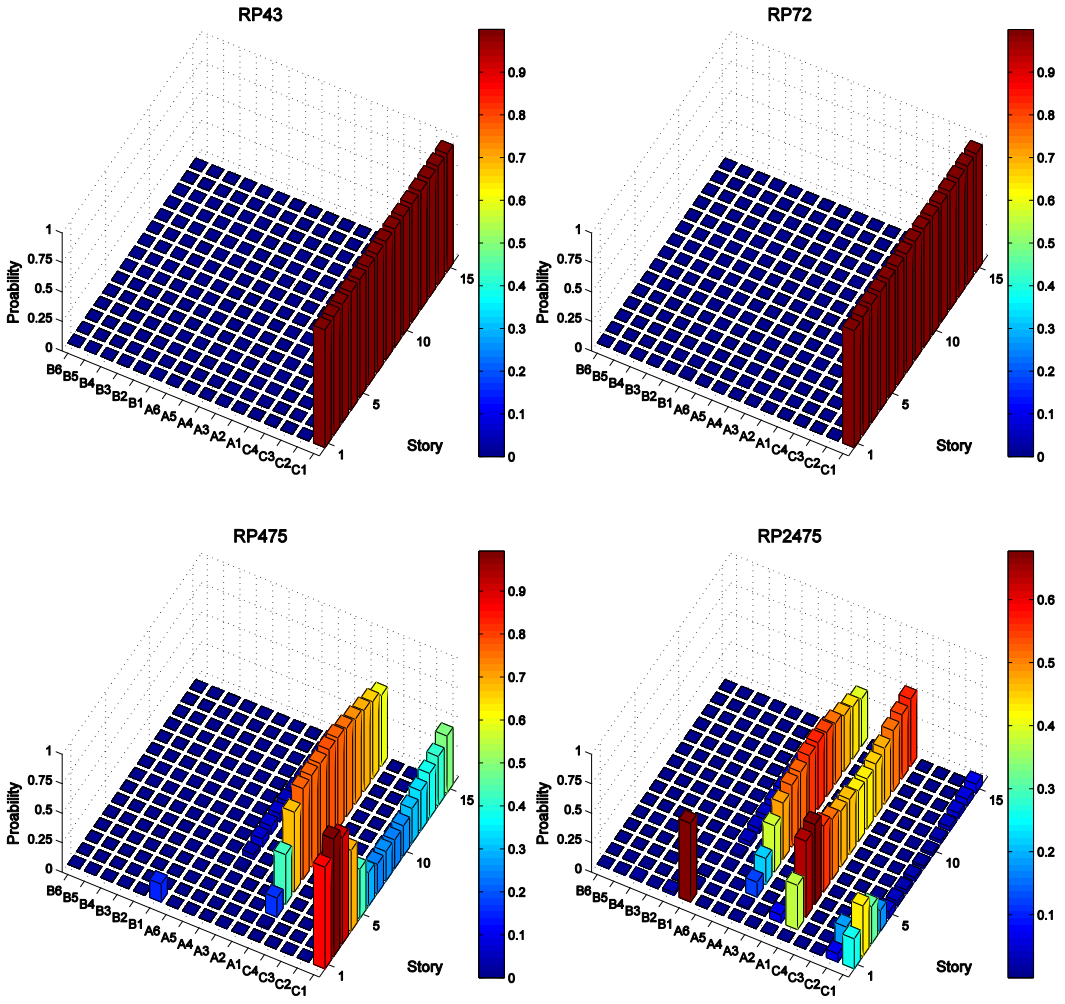

Figure B.21. Probabilities of performance regions calculated from the joint PDF of shear wall tensile strains versus IDRs at 43-, 72-, 475- and 2475-year return periods for building 1B

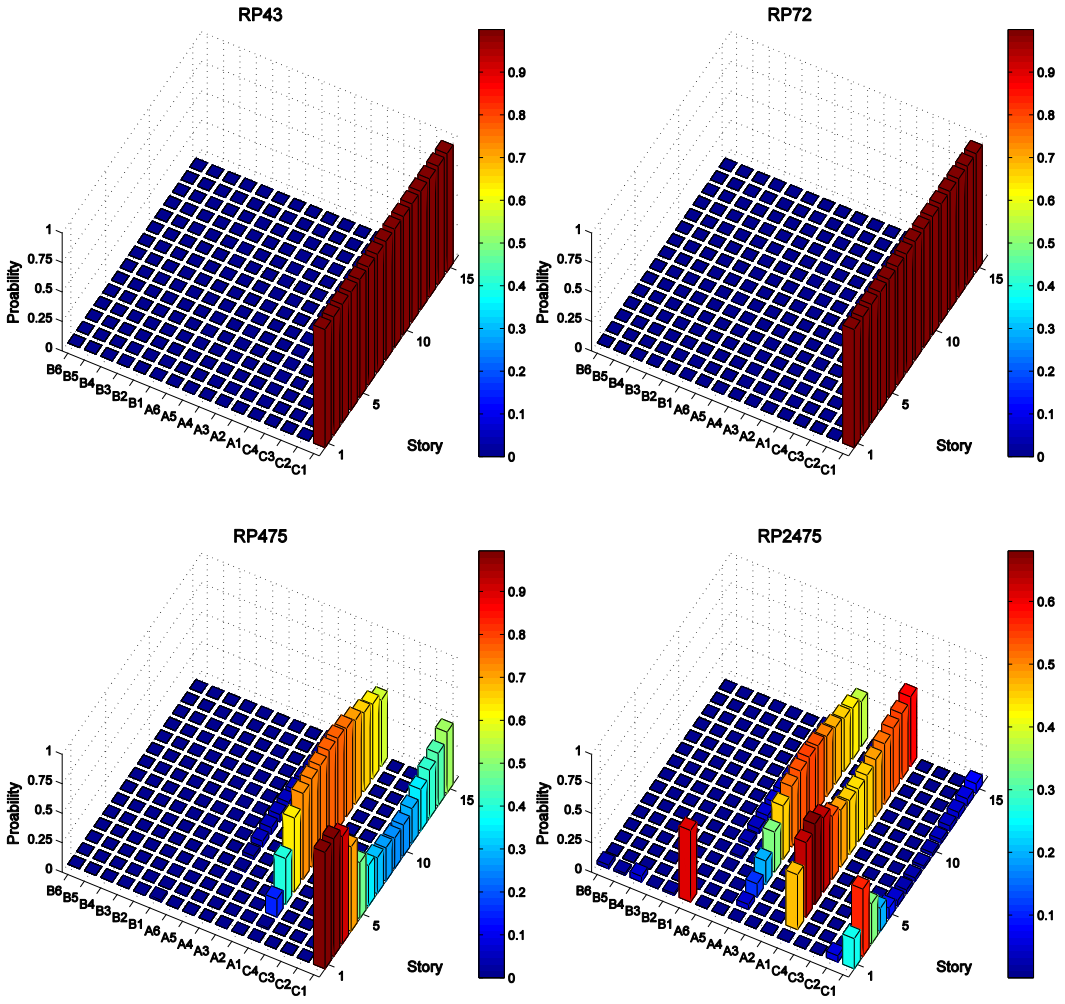

Figure B.22. Probabilities of performance regions calculated from the joint PDF of shear wall compression strains versus IDRs at 43-, 72-, 475- and 2475-year return periods for building 1B

1C BUILDING

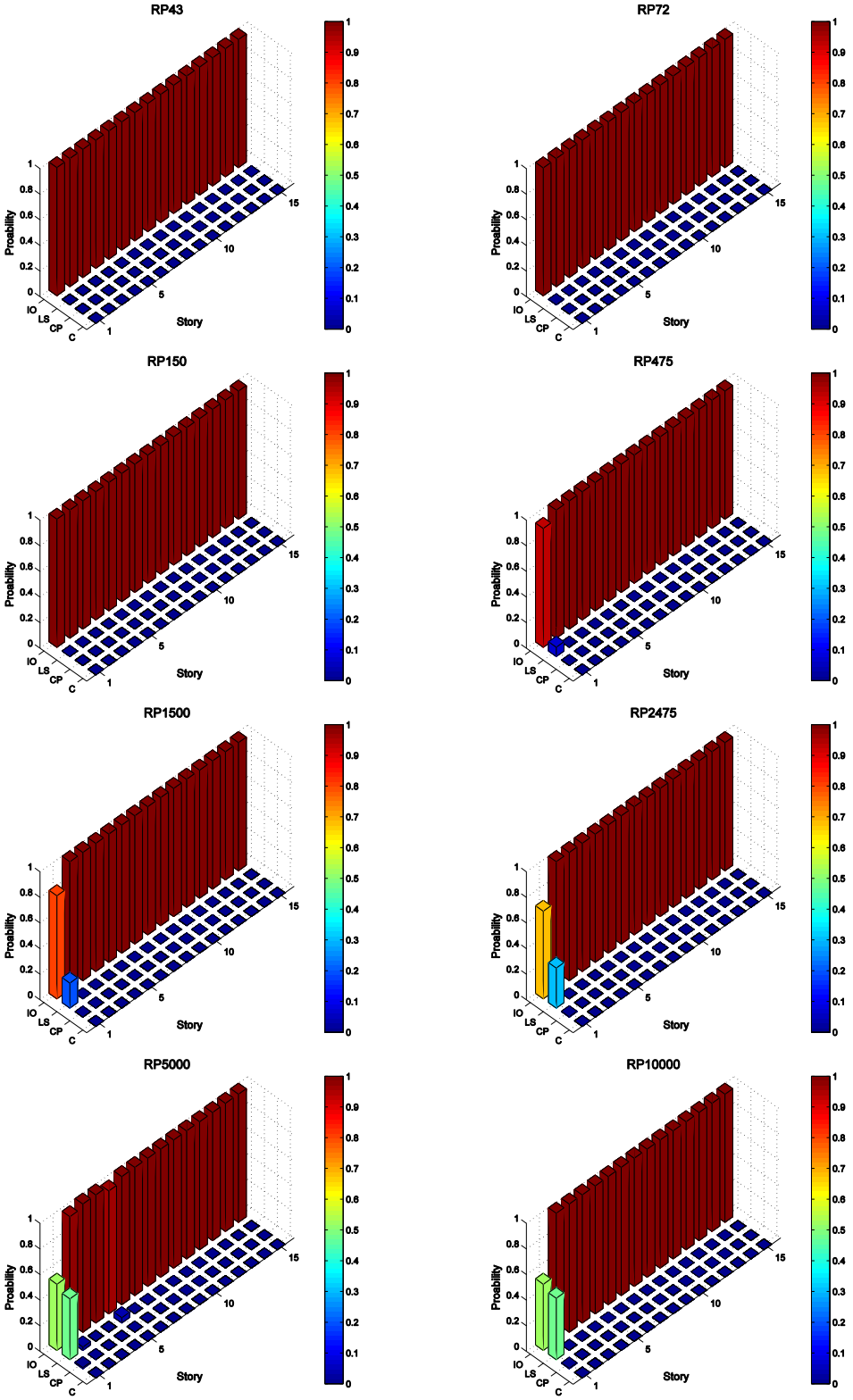

Figure B.23. Damage state probabilities of critical SW sections in terms of reinforcing steel tensile strains for building 1C at all hazard levels

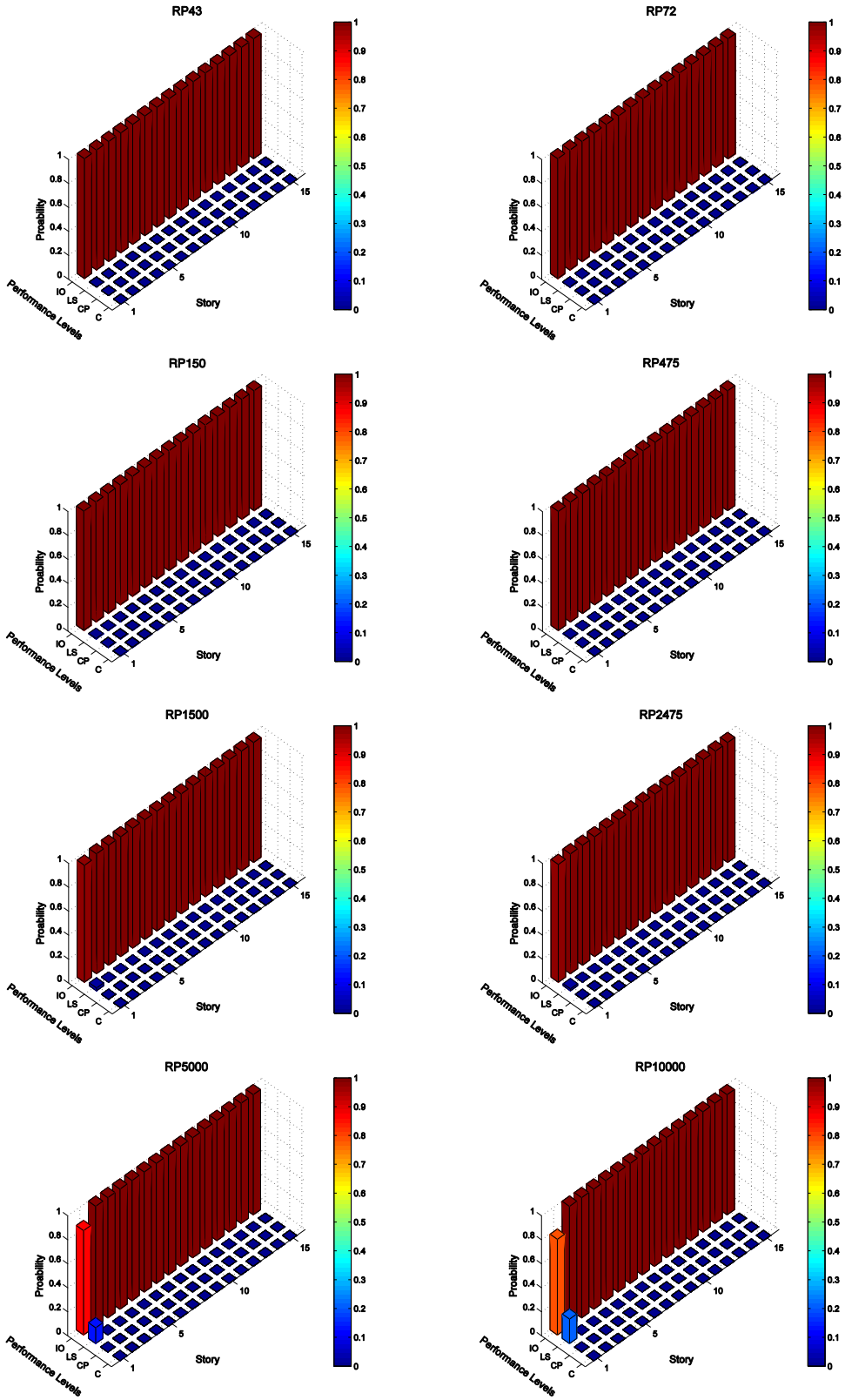

Figure B.24. Damage state probabilities of critical SW sections in terms of confined concrete under compression for building 1C at all hazard levels

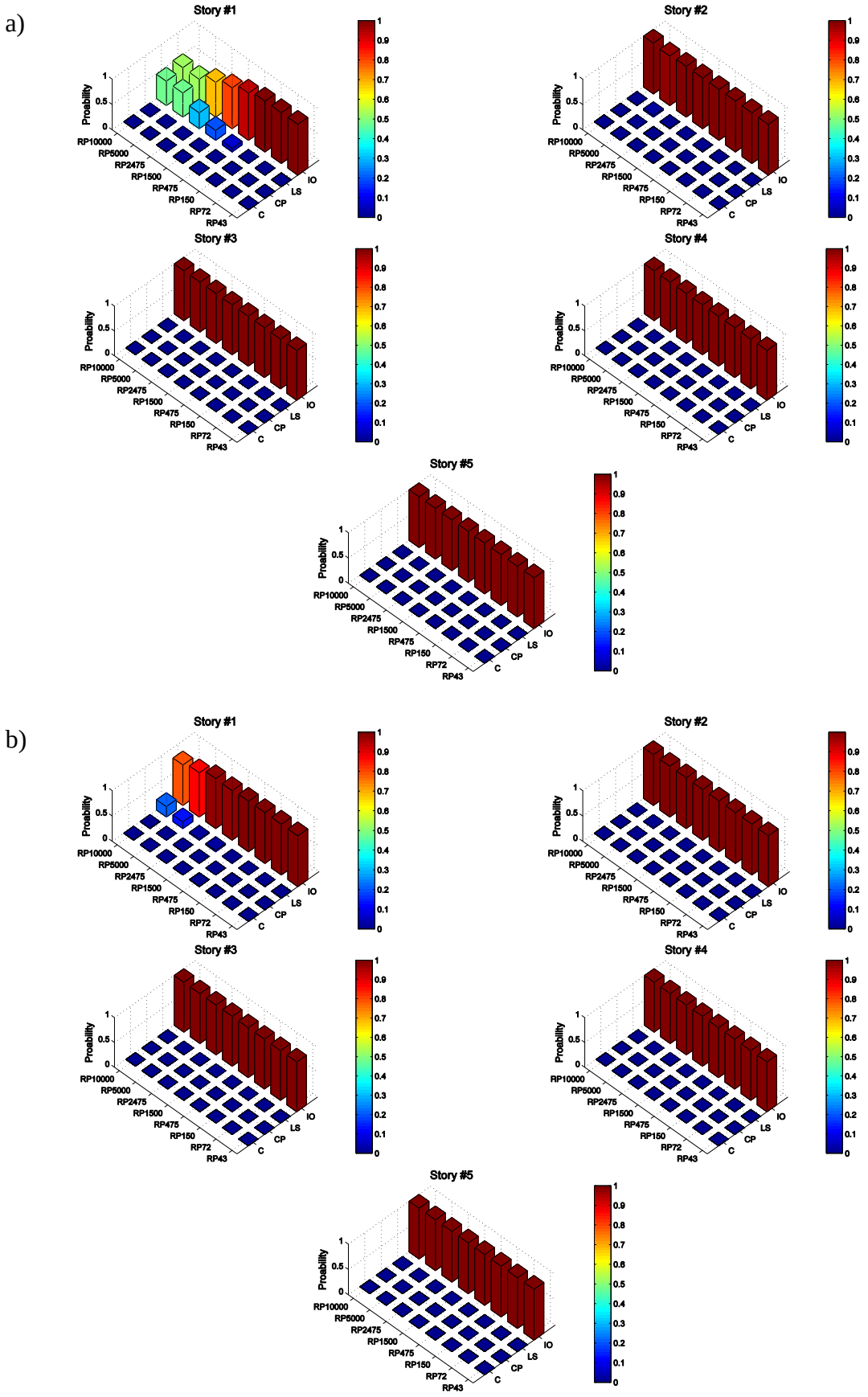

Figure B.25. Damage state probabilities of critical SW sections at 1st to 5th stories. (a) Reinforcement in tension and (b) confined concrete under compression for building 1C.

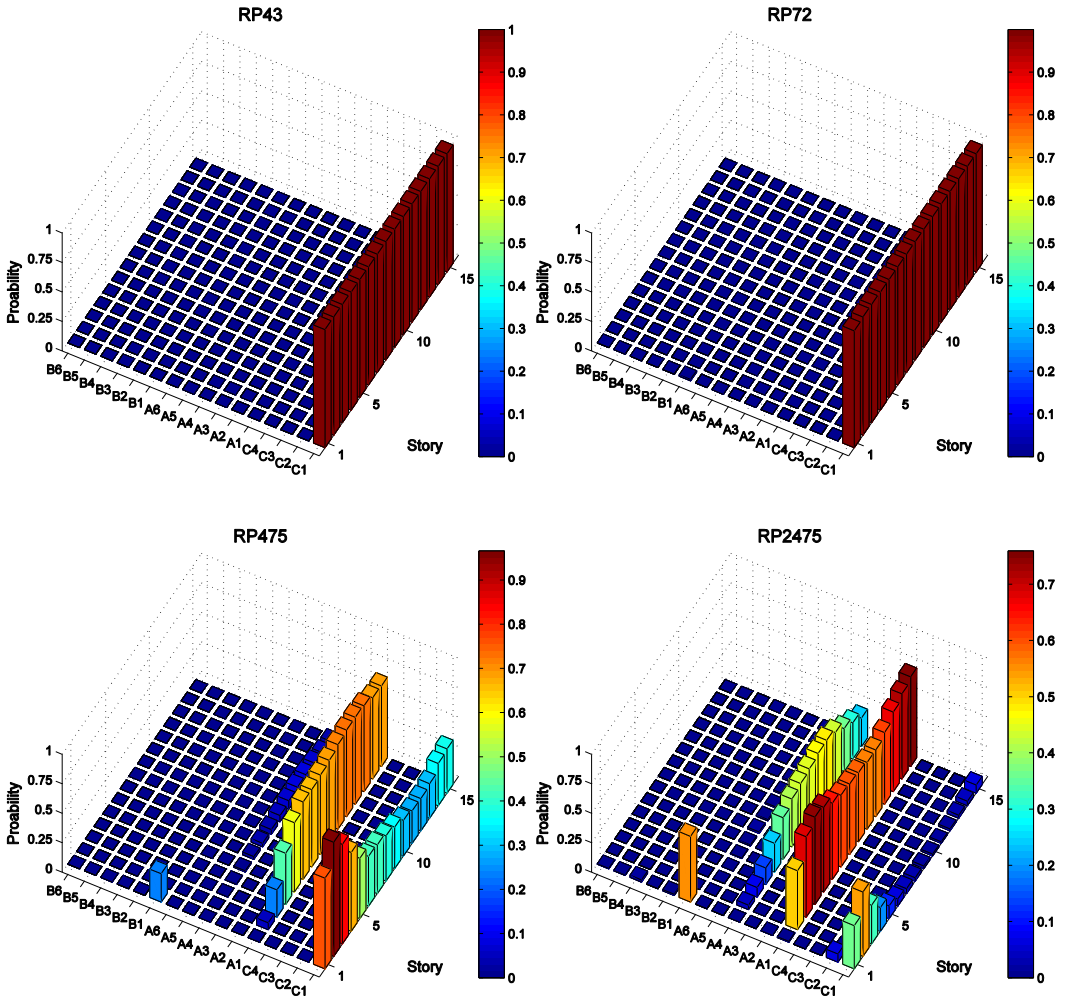

Figure B.26. Probabilities of performance regions calculated from the joint PDF of shear wall tensile strains versus IDRs at 43-, 72-, 475- and 2475-year return periods for building 1C

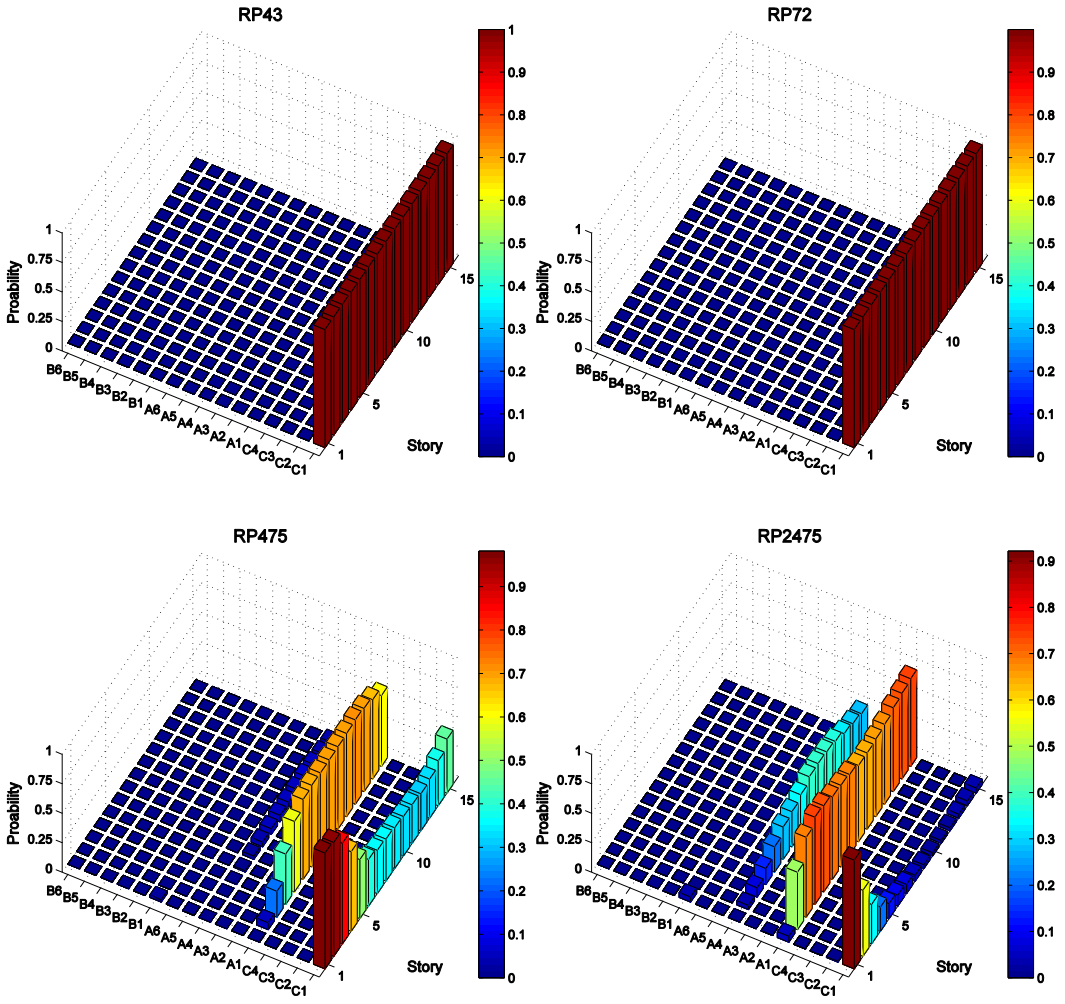

Figure B.27. Probabilities of performance regions calculated from the joint PDF of shear wall compression strains versus IDRs at 43-, 72-, 475- and 2475-year return periods for building 1C

2A BUILDING

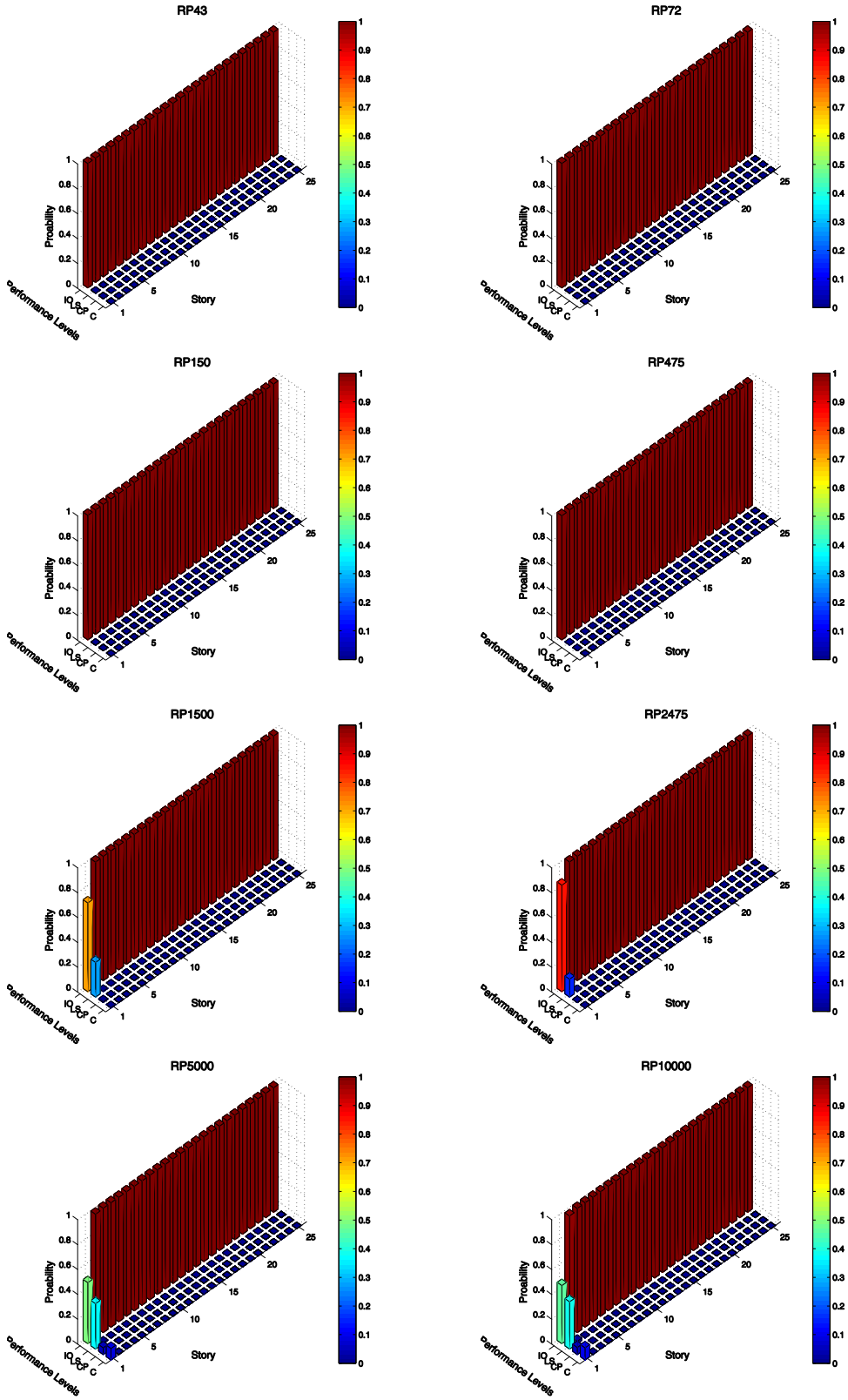

Figure B.28. Damage state probabilities of critical SW sections in terms of reinforcing steel tensile strains for building 2A at all hazard levels

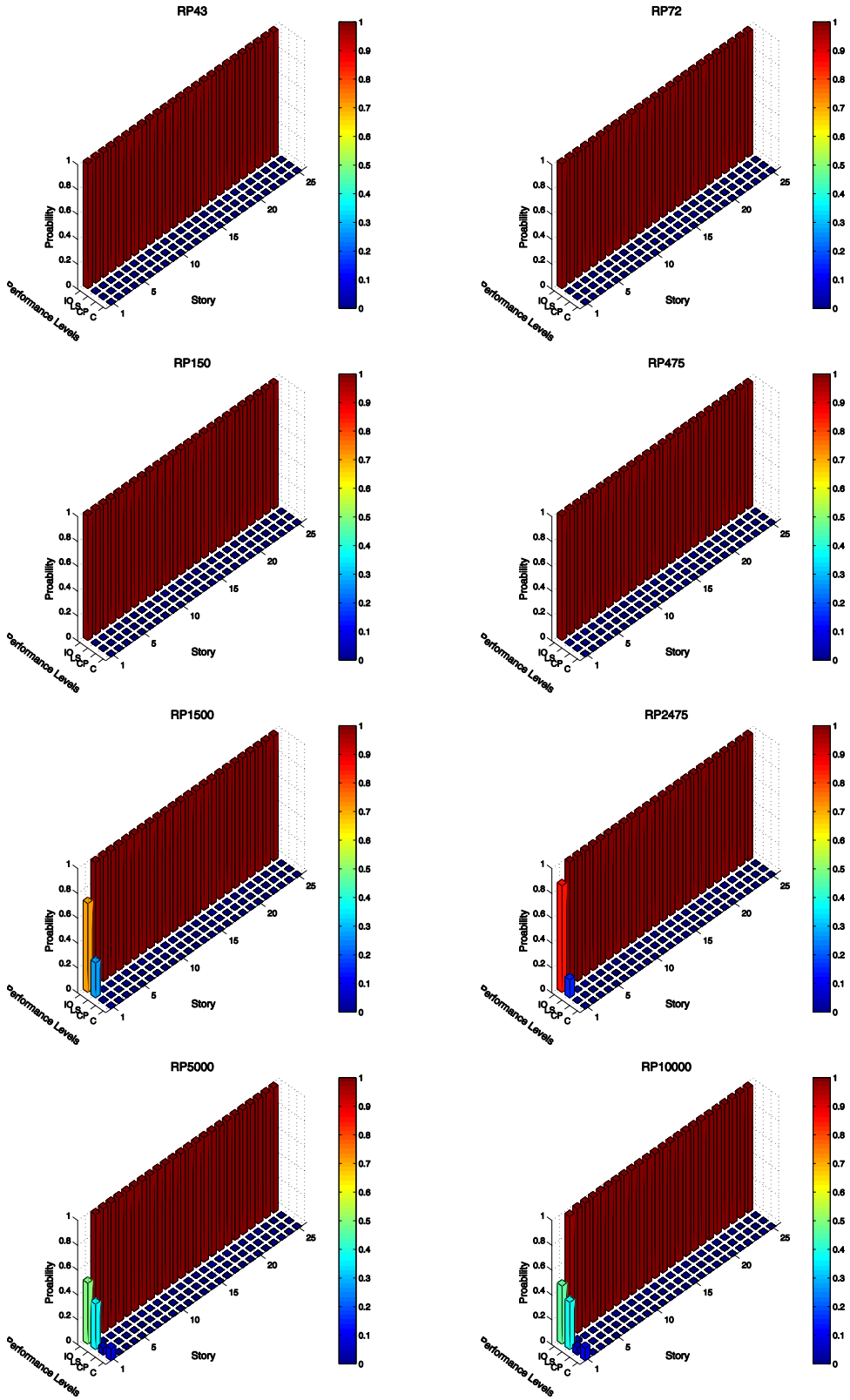

Figure B.29. Damage state probabilities of critical SW sections in terms of confined concrete under compression for building 2A at all hazard levels

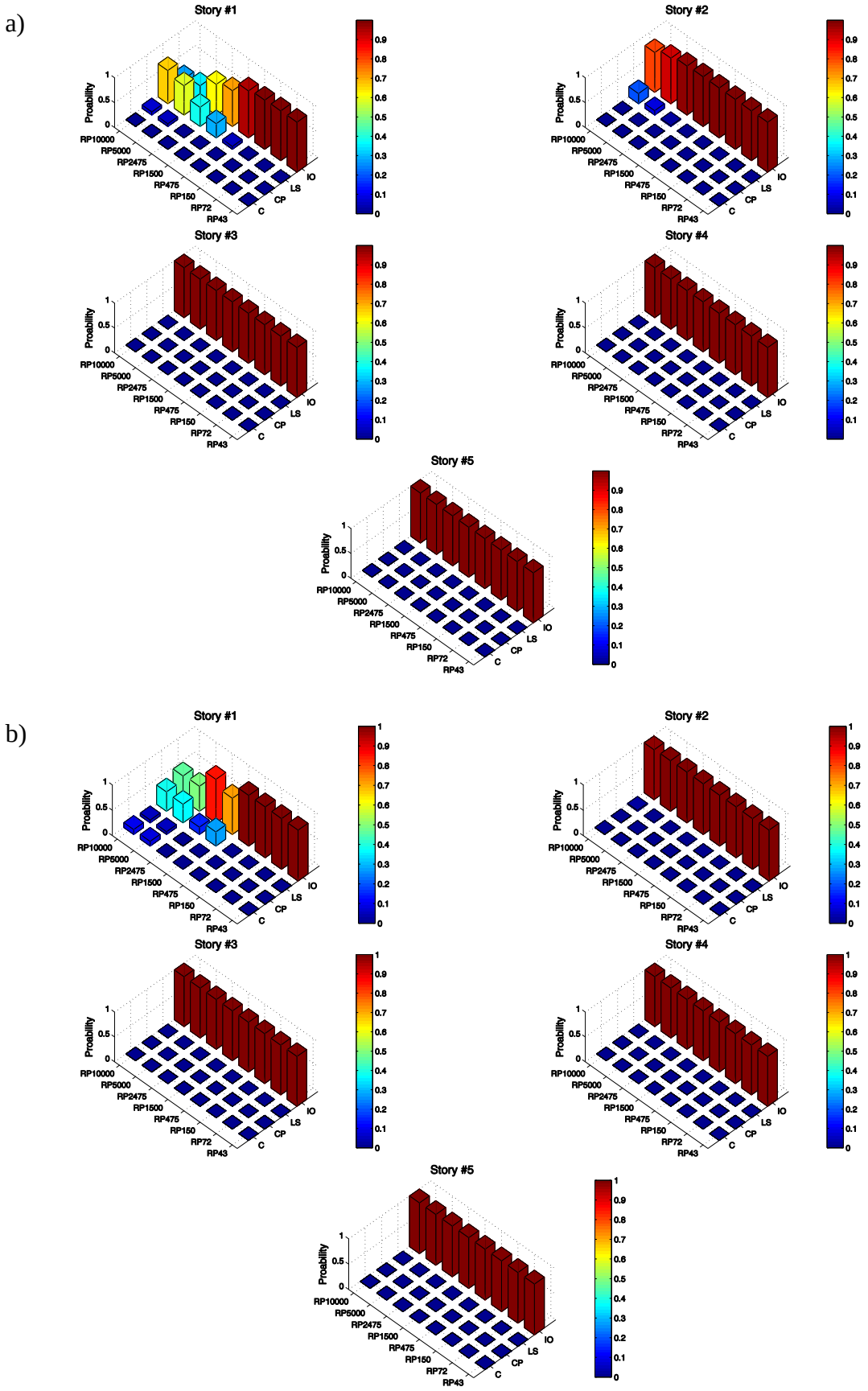

Figure B.30. Damage state probabilities of critical SW sections at 1st to 5th stories: (a) reinforcement in tension and (b) concrete in compression for building 2A

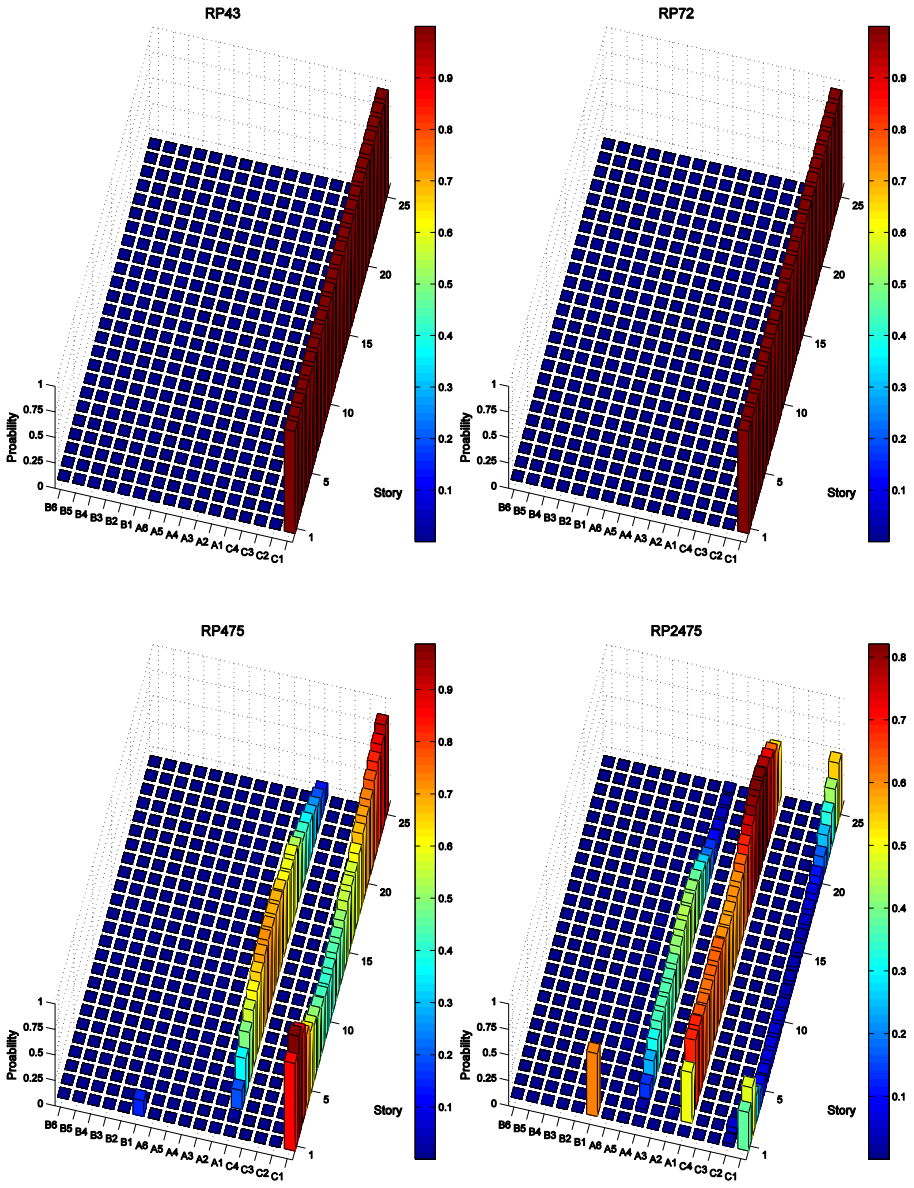

Figure B.31. Probabilities of performance regions calculated from the joint PDF of shear wall tensile strains versus IDRs at 43-, 72-, 475- and 2475-year return periods for building 2A

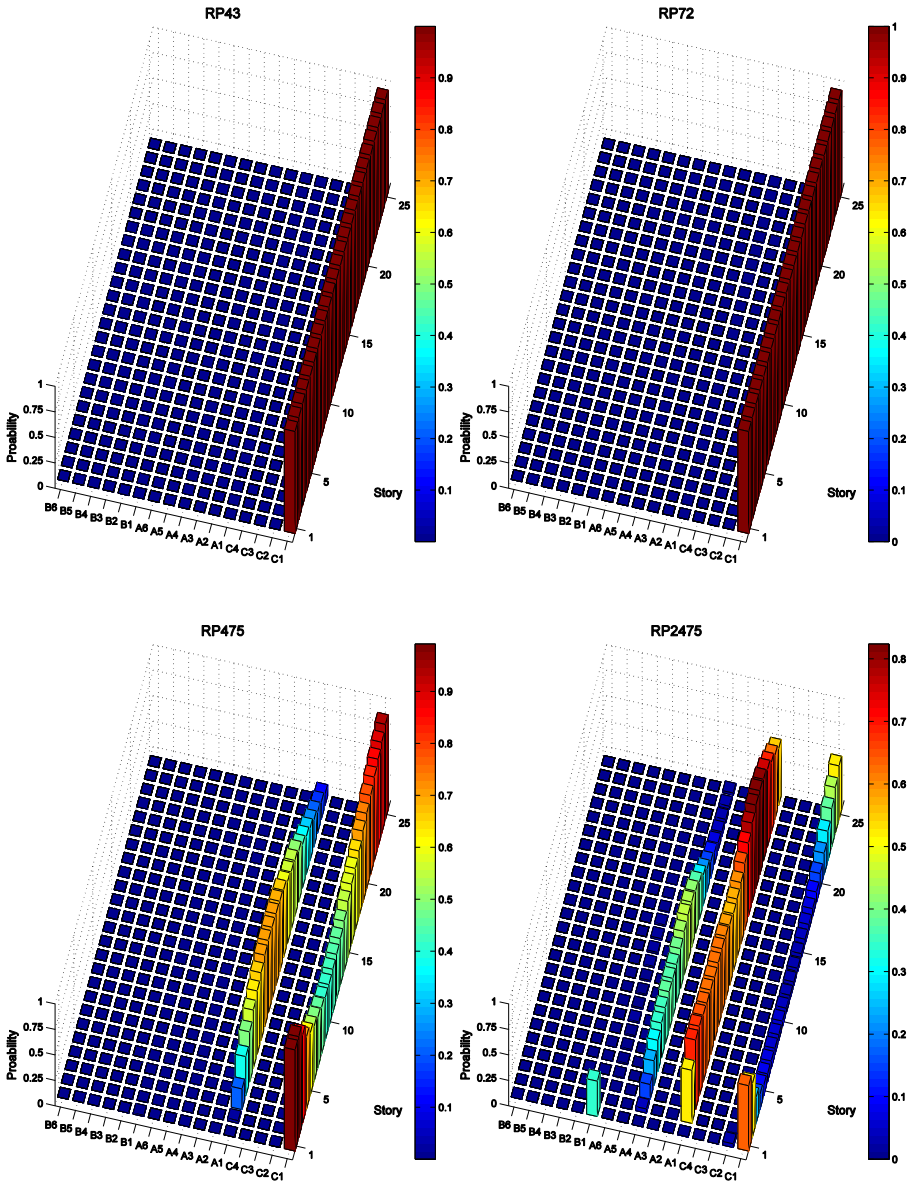

Figure B.32. Probabilities of performance regions calculated from the joint PDF of shear wall compression strains versus IDRs at 43-, 72-, 475- and 2475-year return periods for building 2A.

2B BUILDING

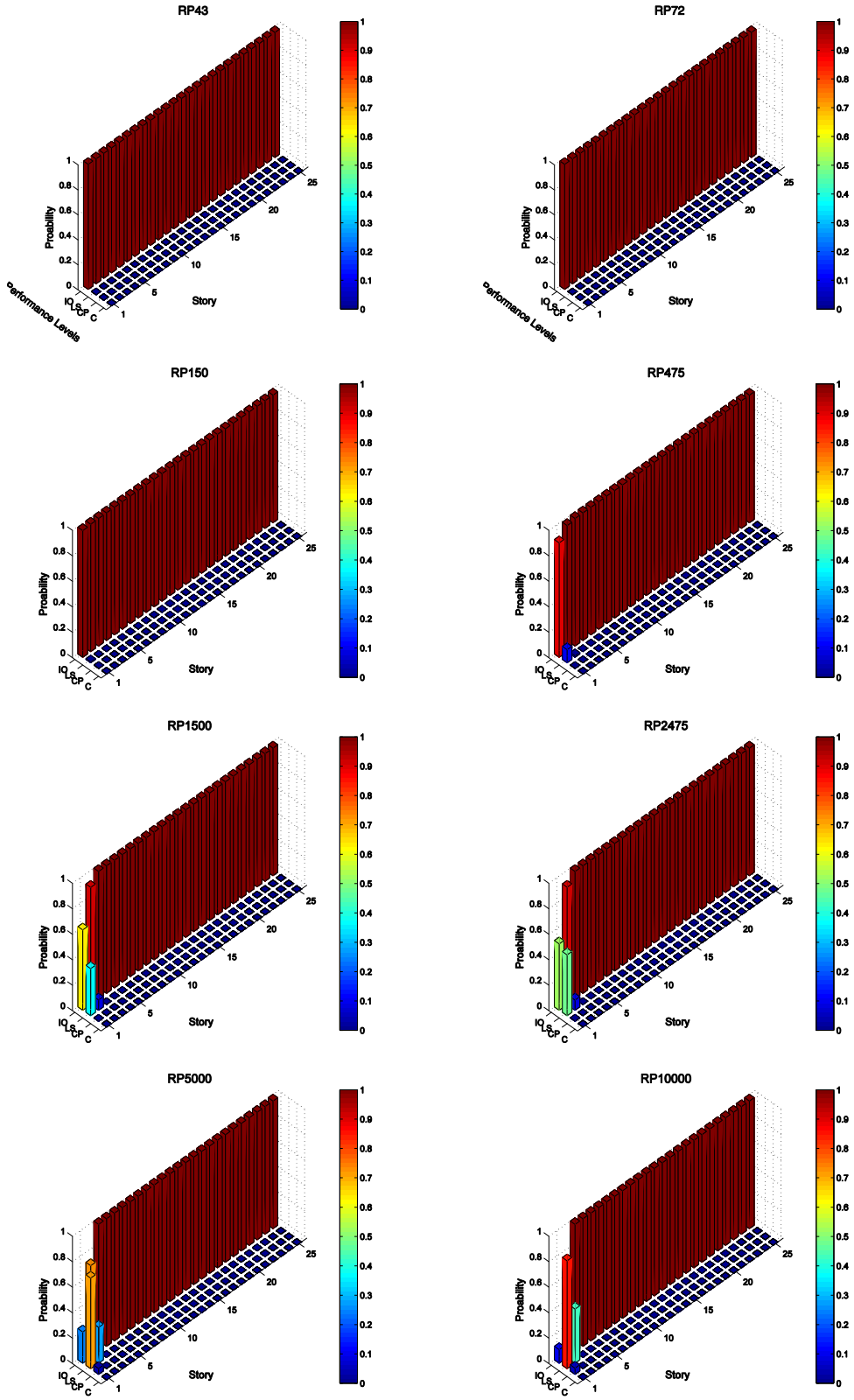

Figure B.33. Damage state probabilities of critical SW sections in terms of reinforcing steel tensile strains for building 2B at all hazard levels

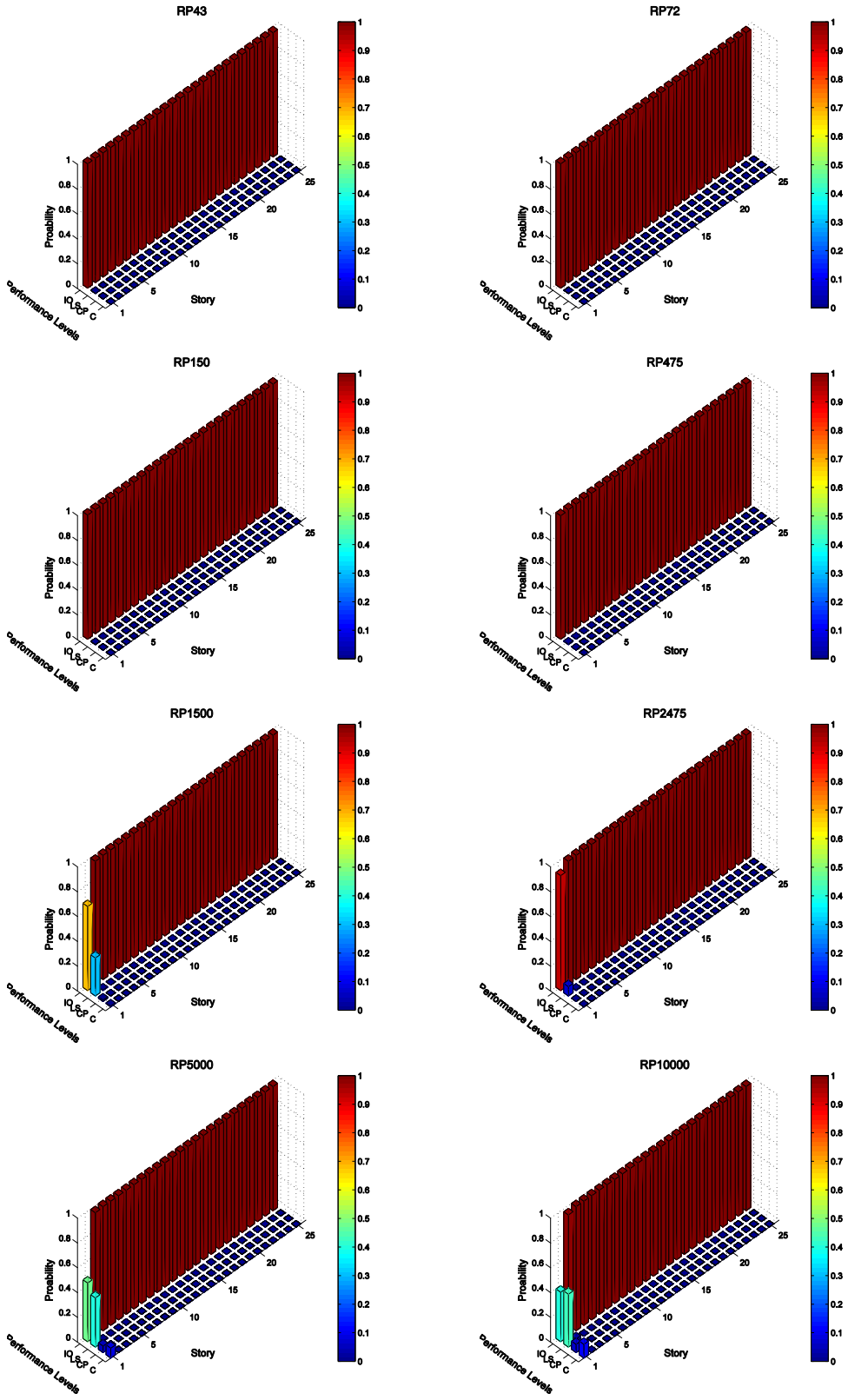

Figure B.34. Damage state probabilities of critical SW sections in terms of confined concrete under compression for building 2B at all hazard levels

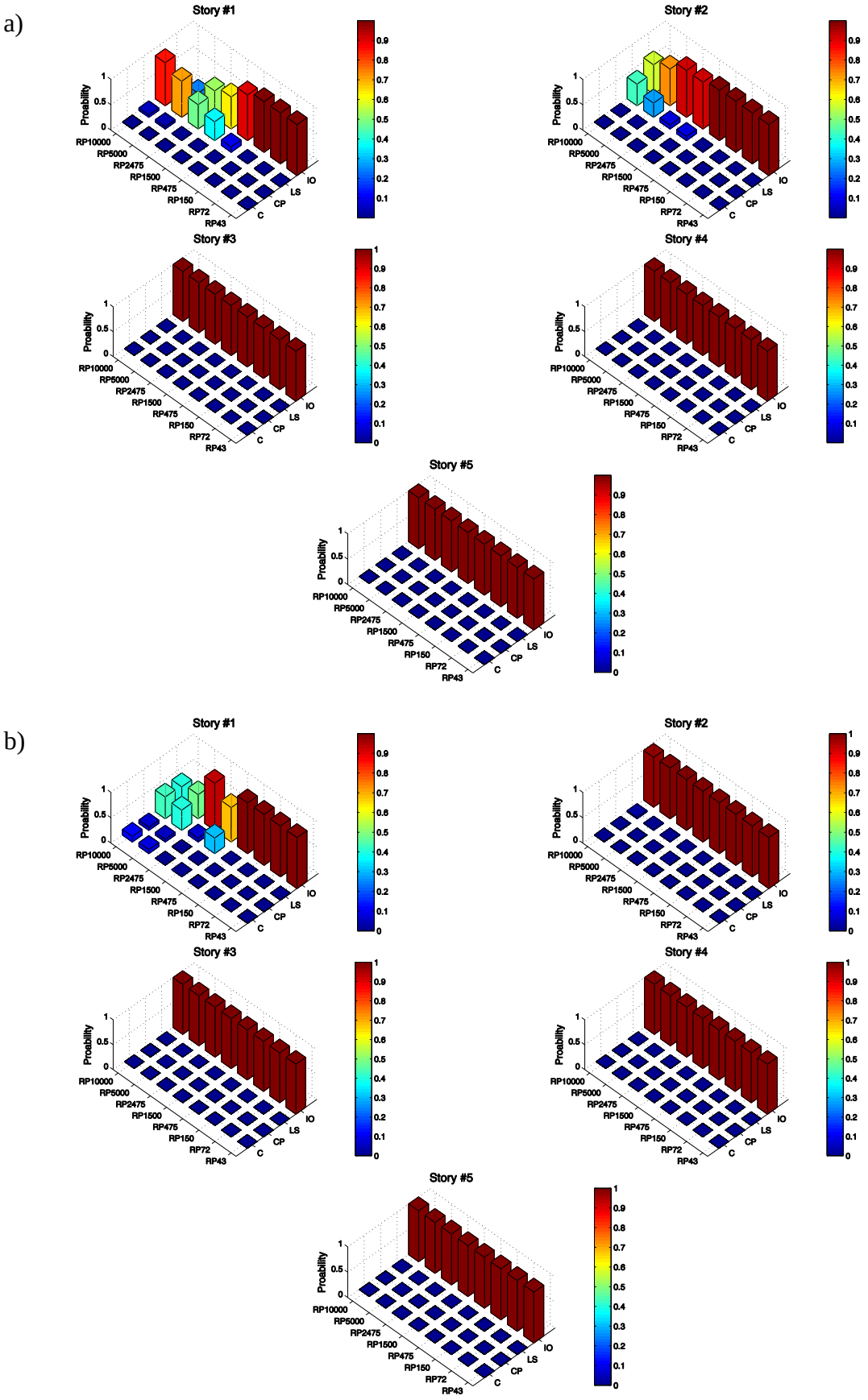

Figure B.35. Damage state probabilities of critical SW sections at 1st to 5th stories. (a) Reinforcement in tension and (b) concrete in compression for building 2B.

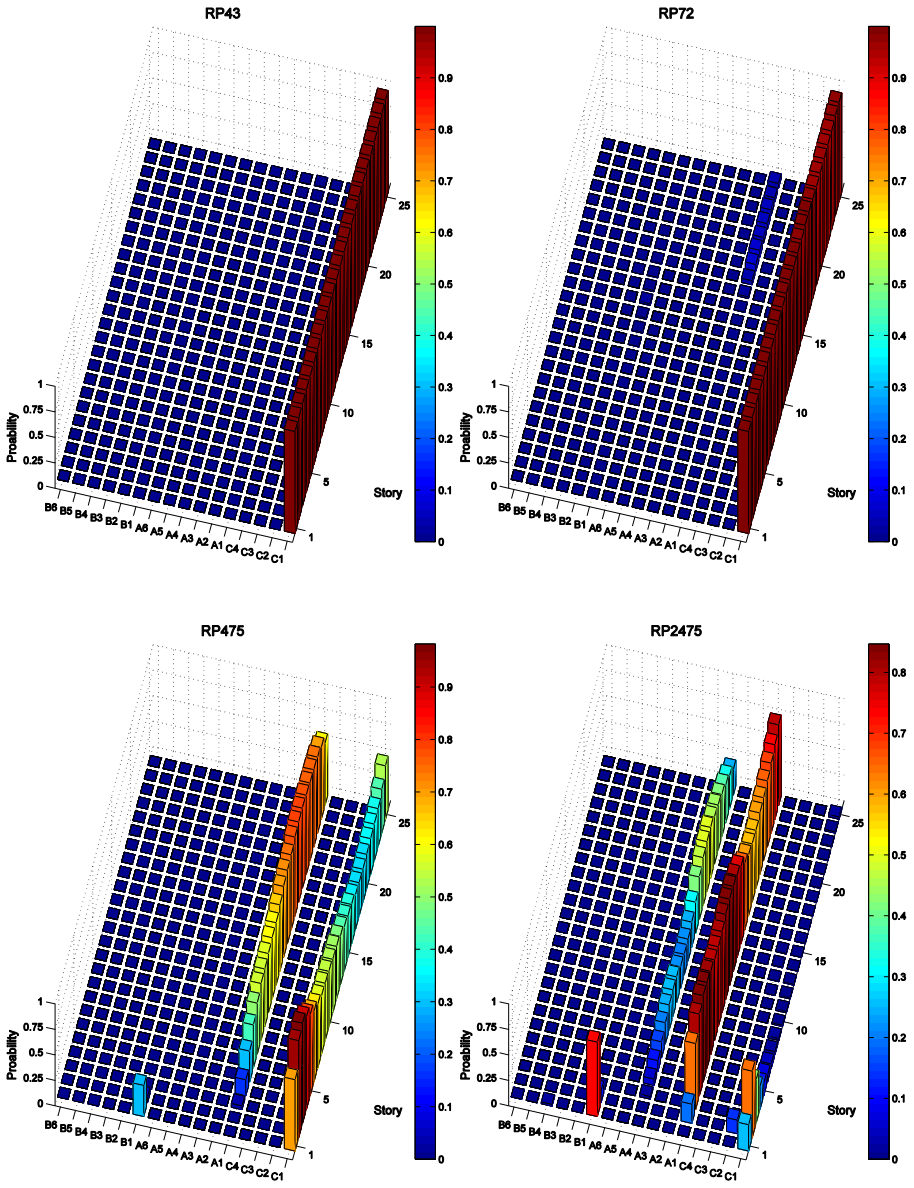

Figure B.36. Probabilities of performance regions calculated from the joint PDF of shear wall tensile strains versus IDRs at 43-, 72-, 475- and 2475-year return periods for building 2B

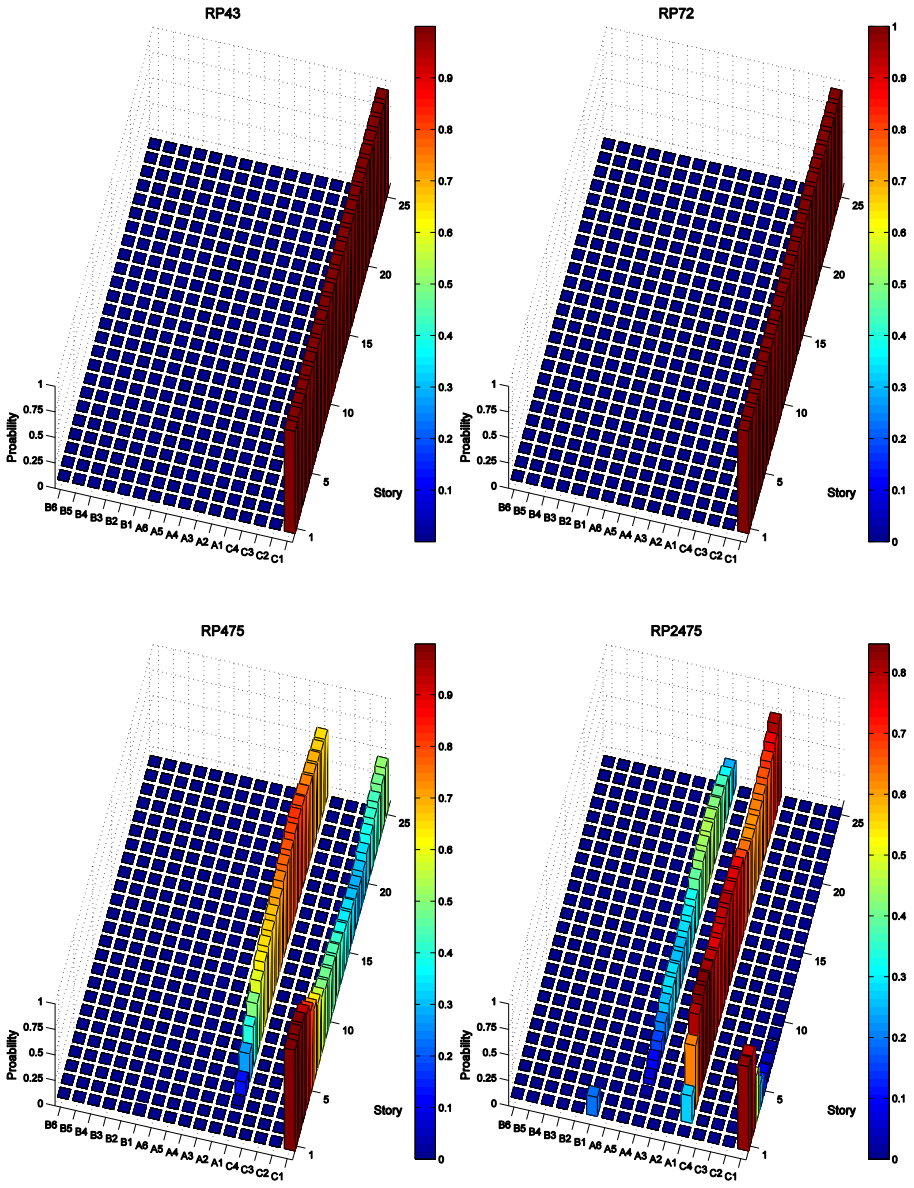

Figure B.37. Probabilities of performance regions calculated from the joint PDF of shear wall compression strains versus IDRs at 43-, 72-, 475- and 2475-year return periods for building 2B.

2C BUILDING

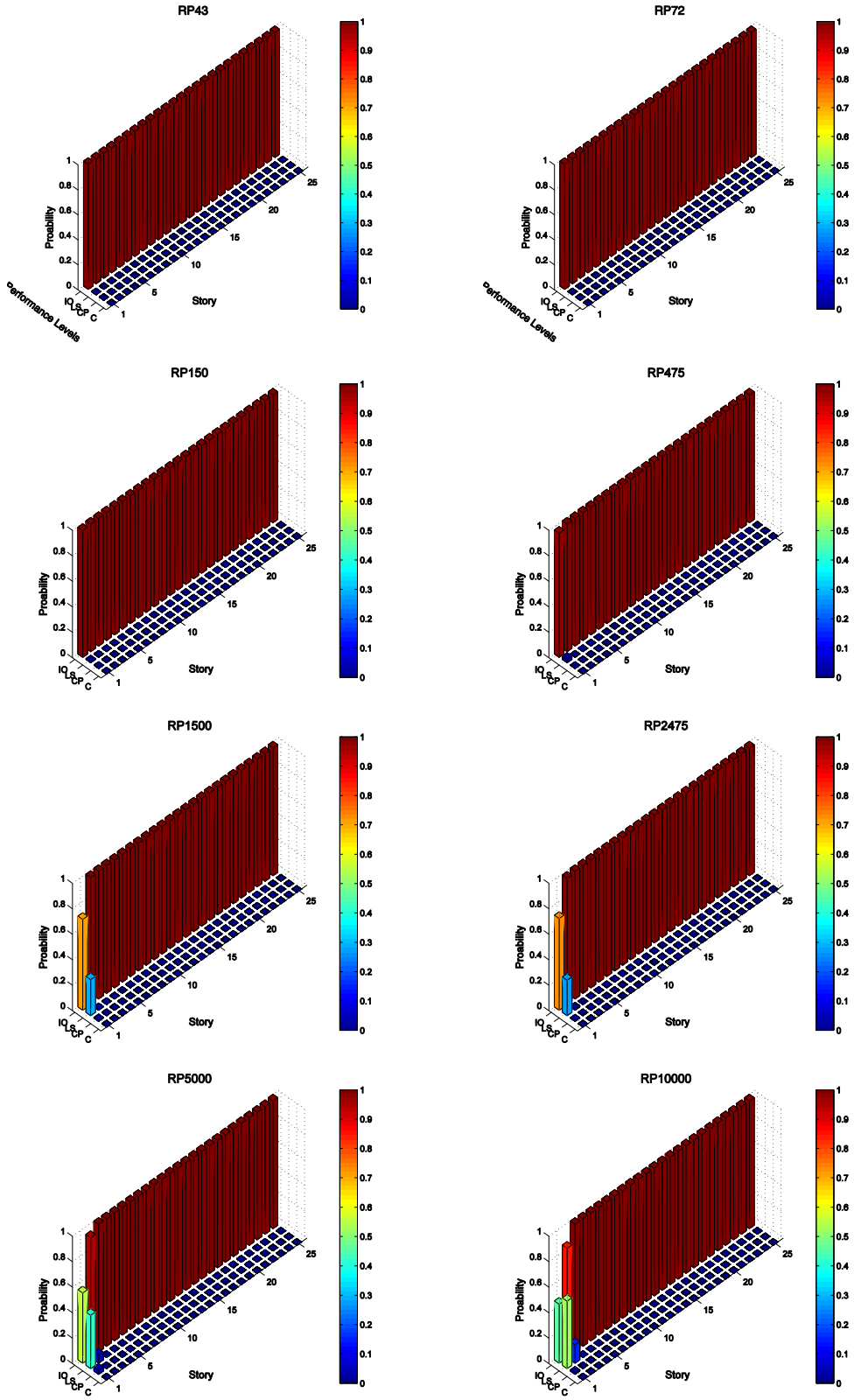

Figure B.38. Damage state probabilities of critical SW sections in terms of reinforcing steel tensile strains for building 2C at all hazard levels

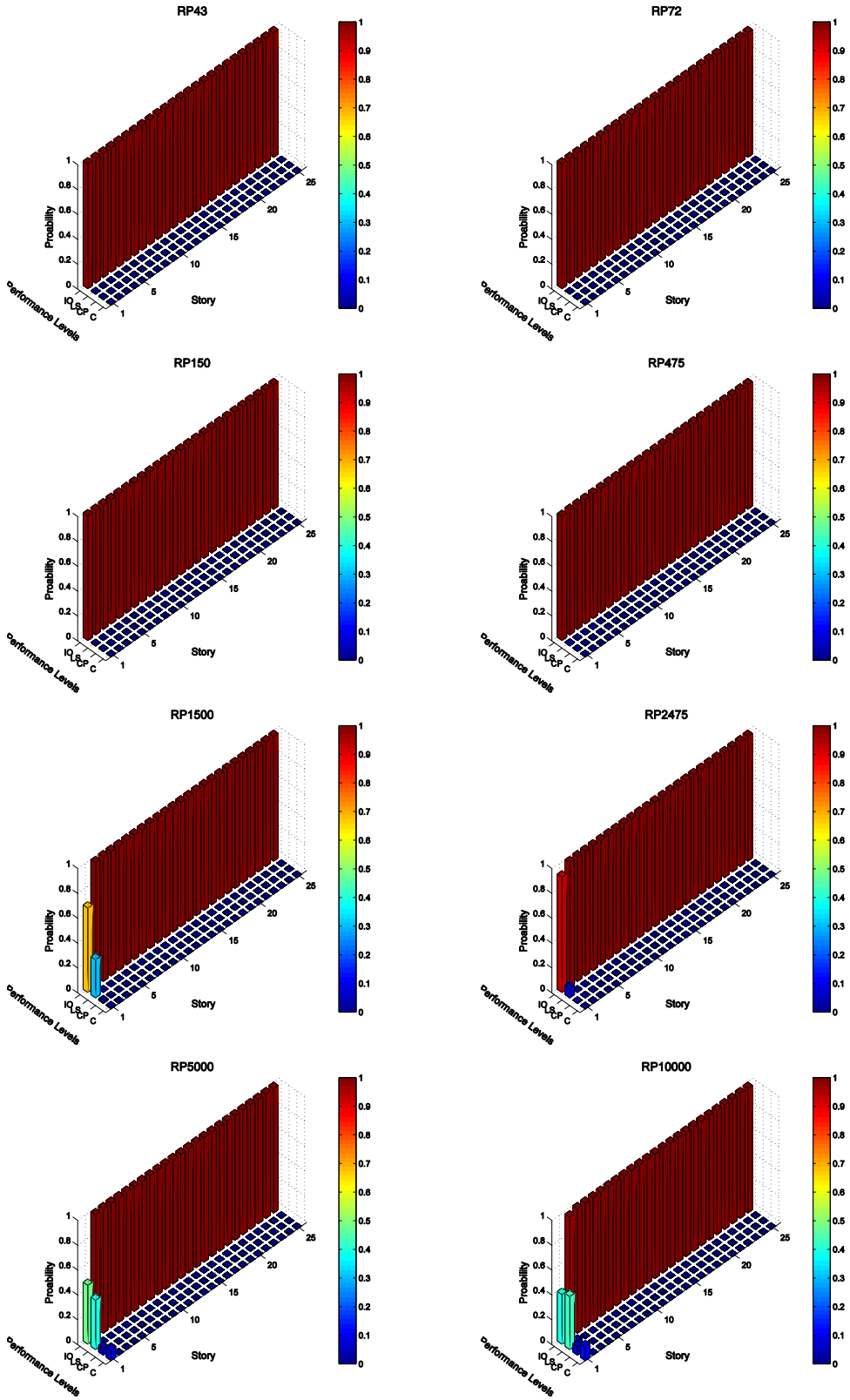

Figure B.39. Damage state probabilities of critical SW sections in terms of confined concrete under compression for building 2C at all hazard levels

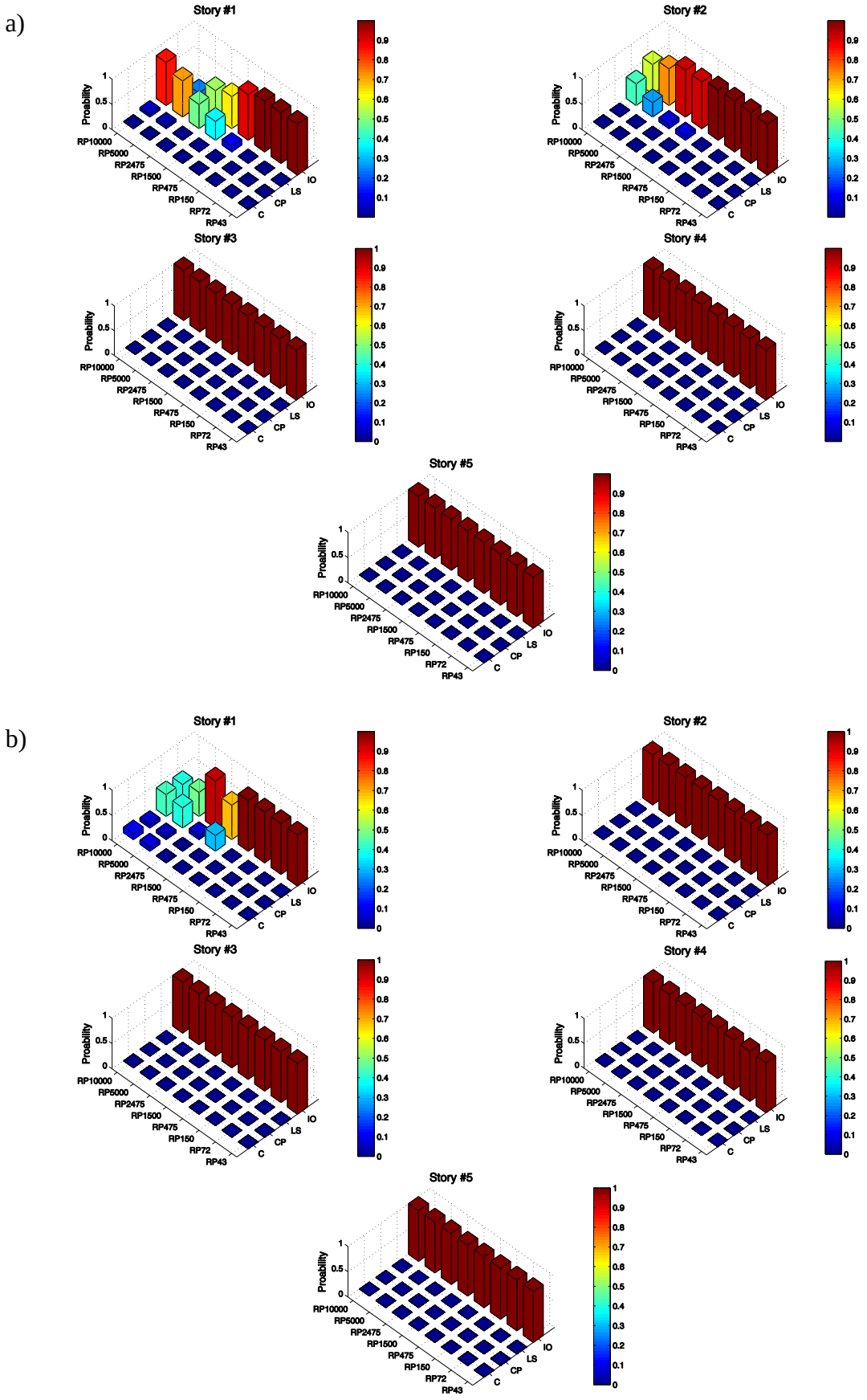

Figure B.40. Damage state probabilities of critical SW sections at 1st to 5th stories. (a) Reinforcement in tension and (b) concrete in compression for building 2C.

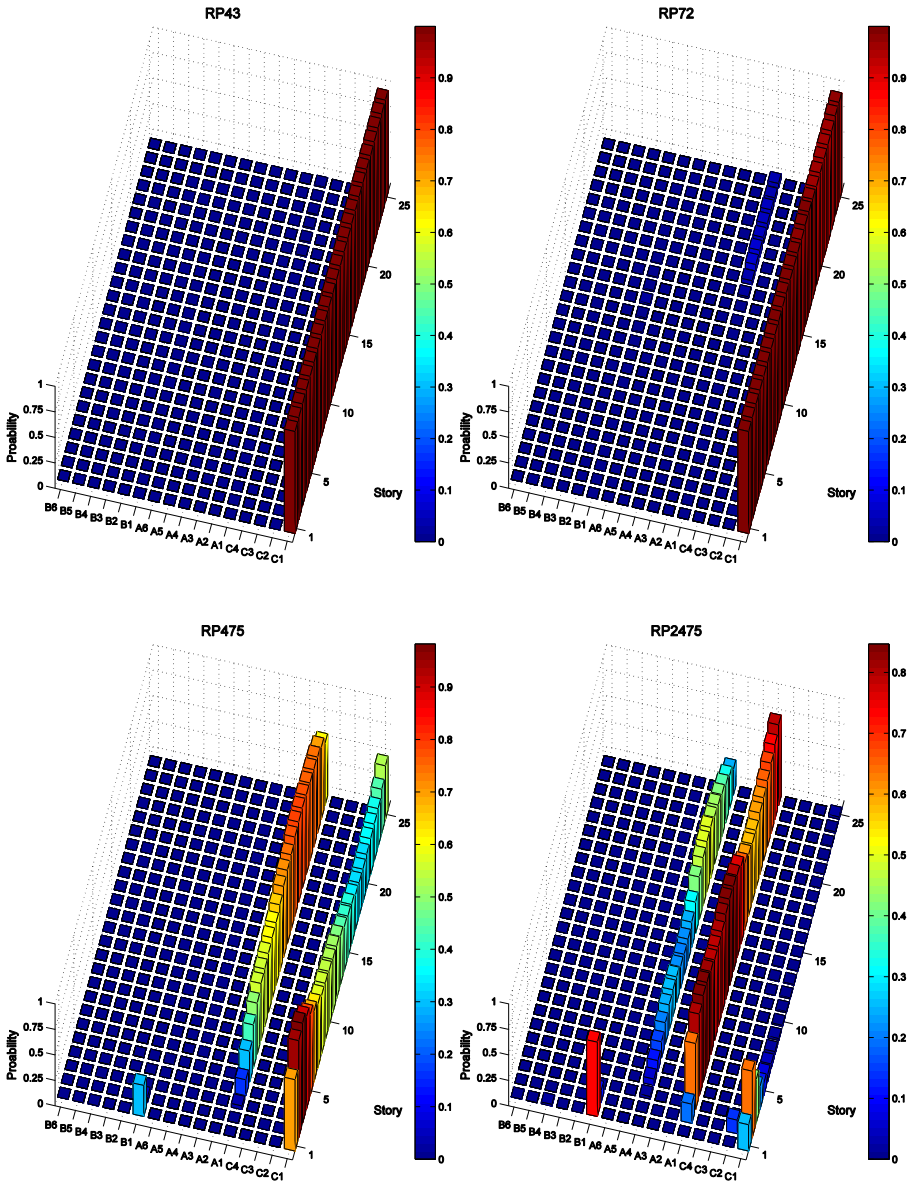

Figure B.41. Probabilities of performance regions calculated from the joint PDF of shear wall tensile strains versus IDRs at 43-, 72-, 475- and 2475-year return periods for building 2C

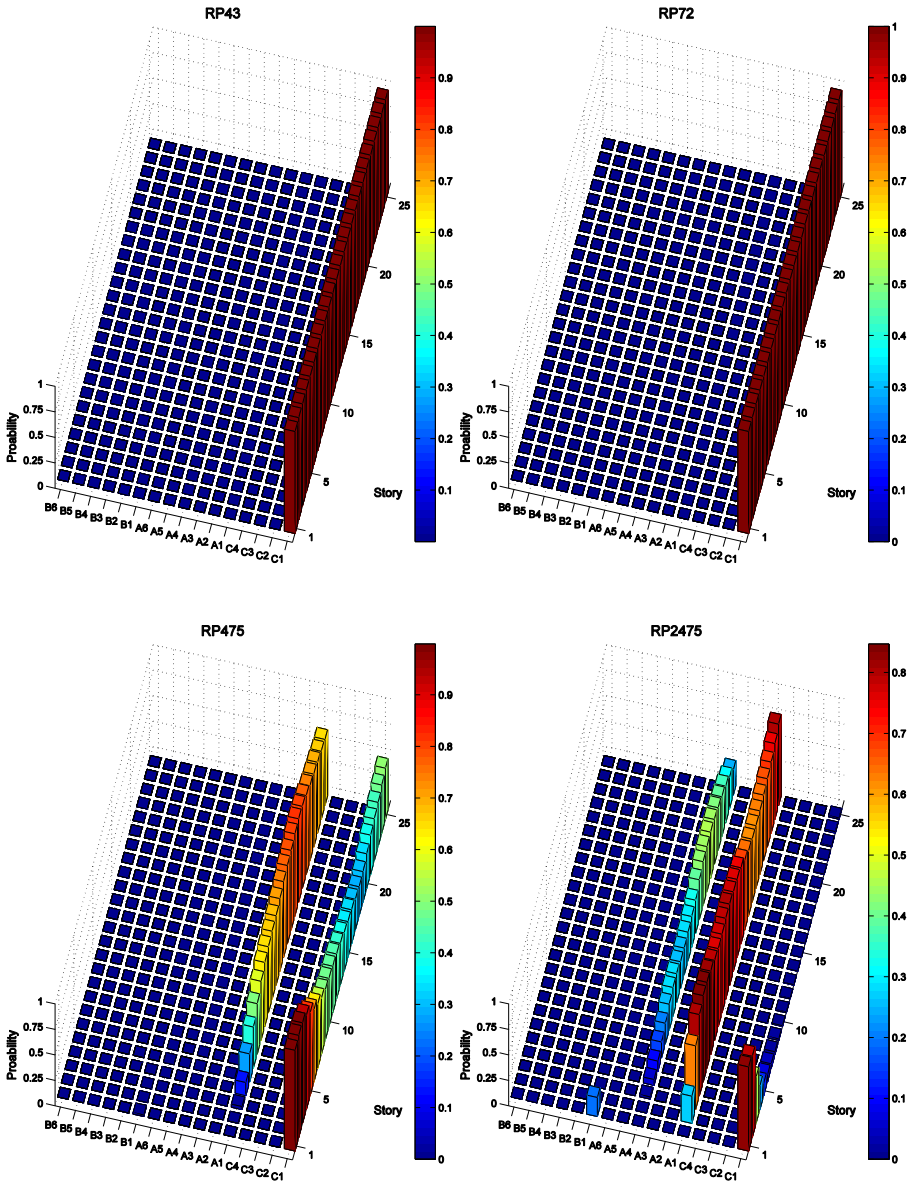

Figure B.42. Probabilities of performance regions calculated from the joint PDF of shear wall compression strains versus IDRs at 43-, 72-, 475- and 2475-year return periods for building 2C.

APPENDIX C: GROUND MOTION INPUT

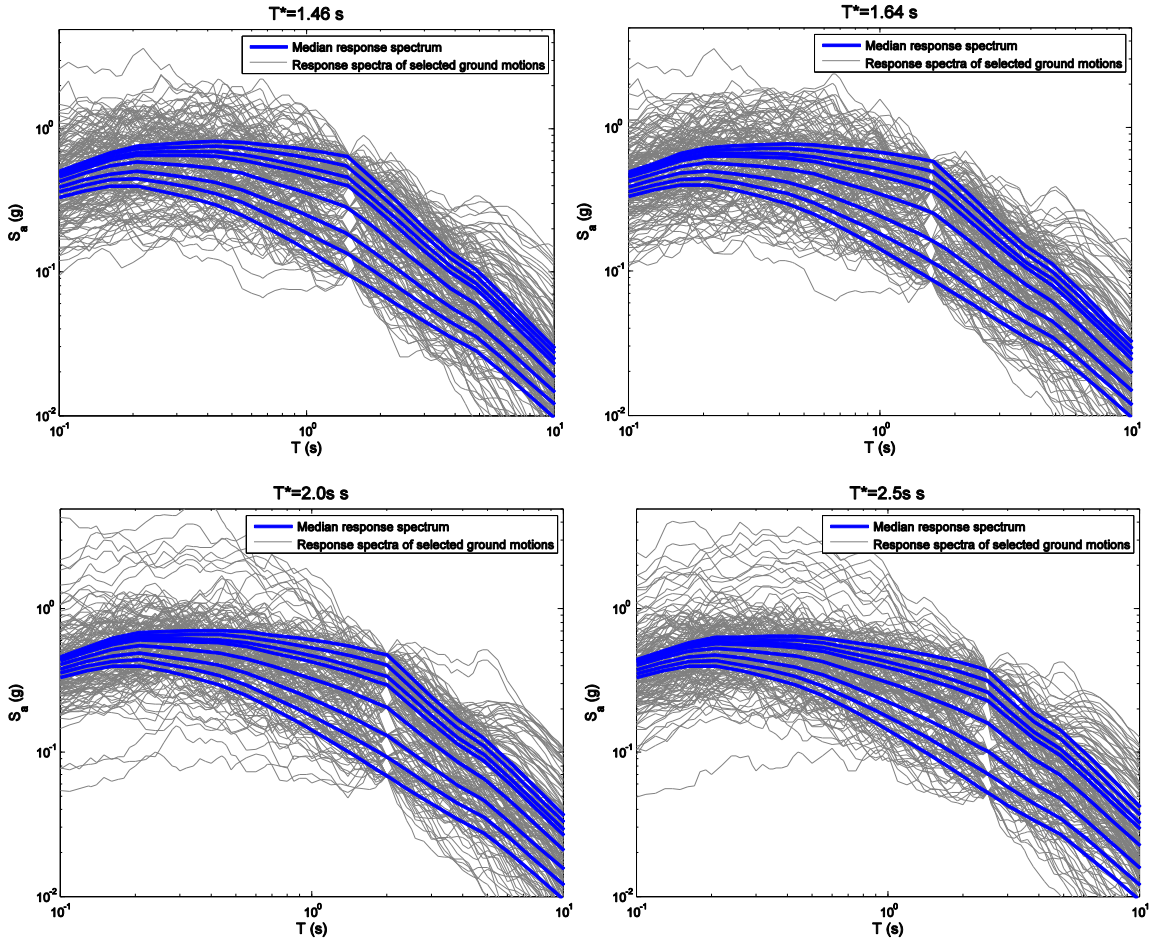

Figure C.1. Response spectra of the selected ground motions